UNIVERSITY OF CALIFORNIA
SANTA CRUZ

SIGNATURES OF THE LATE TIME CORE-COLLAPSE SUPERNOVA ENVIRONMENT

A dissertation submitted in partial satisfaction of the
requirements for the degree of

DOCTOR OF PHILOSOPHY

in

ASTRONOMY AND ASTROPHYSICS

by

Luke Forrest Roberts

September 2012

The Dissertation of Luke Forrest Roberts
is approved:

Professor S. Woosley, Chair

Professor E. Ramirez-Ruiz

Professor S. Reddy

Tyrus Miller
Vice Provost and Dean of Graduate Studies

Table of Contents

List of Figures

Abstract

Signatures of the Late Time Core-Collapse Supernova Environment

by

Luke Forrest Roberts

The hot and dense proto-neutron star (PNS) born subsequent to core-collapse in a type II supernova explosion is an intense source of neutrinos of all flavors. It emits the $3-5\times10^{53}$ ergs of gravitational binding energy gained during collapse as neutrino radiation on a time scale of tens of seconds as it contracts, becomes increasingly neutron-rich and cools. While the supernova explosion mechanism and associated accretion of material is expected to influence the neutrino emission at early time (i.e. $t \lesssim 1\,\mathrm{s}$ post bounce) the late time neutrino signal is shaped by the properties of the PNS, such as the nuclear equation of state (EoS), neutrino opacities in dense matter, and other microphysical properties that affect the cooling timescale by influencing either neutrino diffusion or convection. Detection of significant numbers of late time supernova neutrinos will provide a direct window into the properties of nuclear matter and neutron stars, if the neutrino signal can be modeled accurately. The average emitted neutrino energies also strongly affect nucleosynthesis in the neutrino driven wind, neutrino induced nucleosynthesis further out in the star, and the patterns of neutrino oscillations outside of the PNS.

This thesis examines a number of aspects of this environment. First, the equations of spherically symmetric general relativistic radiation hydrodynamics are discussed, a new code for calculating neutrino transport in PNSs is described, and first results from this code are presented. It is found that the NDW is neu-

tron rich for at least a few seconds, in contrast to other recent work. This change in the expected wind electron fraction is traced to the correct treatment of the nucleon dispersion relations in an interacting medium and turns out to be influenced by the sub-nuclear density symmetry energy. Late time convection in PNSs is also studied. It is found that the density dependence of the symmetry energy may affect the duration of convective activity, which is imprinted in the neutrino luminosity evolution.

The second part of the thesis focuses on the neutrino driven wind (NDW) which is blown from the surface of the PNS. Time-dependent hydrodynamic calculations of the NDW are presented, which include accurate weak interaction physics coupled to a full nuclear reaction network. Using two published models of PNS neutrino luminosities, predictions of the contribution of the NDW to the integrated nucleosynthetic yield of the entire supernova are made. For the neutrino luminosity histories considered, it is found no r-process occurs in the most basic wind scenario because the NDW entropy is too low, the dynamical timescale is too long, and the wind electron fraction is too high. It is possible that the wind produces the $N = 50$ closed shell isotopes, but this depends on the neutrino luminosities employed. The effect of a secondary heating source on the wind is then considered. The general characteristics of a secondary heating source required to produce r-process nucleosynthesis are discussed. Then gravitoacoustic power excited either by convection or g-mode oscillations of the PNS is considered as a possible source of this heating. It is found that this a viable mechanism for increasing the wind entropy and decreasing the the dynamical timescale to values that are favorable for the r-process, when the neutrino spectra found in the first part of the thesis are assumed.

Acknowledgments

First, I want to thank my advisor, Stan Woosley, for his advice and support over my graduate career at UCSC. I am grateful for the great freedom he gave me to pursue projects that I found interesting at any particular time, that he was always willing to take the time to discuss anything I was working on, and for his valuable insights into the problems I was working on. I am also very happy to acknowledge those who have collaborated with me on the work presented in this thesis: Sanjay Reddy, Gang Shen, Vincenzo Cirigliano, Rob Hoffman, and Jose Pons. Additionally, I would like to acknowledge people who I collaborated with during my time at UCSC on work that is not part of this thesis: Enrico Ramirez-Ruiz, Dan Kasen, and William Lee. Particularly, I would like to thank both Sanjay and Enrico for many useful discussions and their advice.

During most of my time at UCSC, I was mainly supported by an NNSA/DOE Stewardship Science Graduate Fellowship (DE-FC52-08NA28752), for which I am very grateful. I would also like to acknowledge support from the University of California Office of the President (09-IR-07-117968-WOOS), the National Science Foundation (AST-0909129), and the DOE SciDAC Program (DEFC-02-06ER41438), all of which supported me through my advisor Stan Woosley.

I would also like to thank my family and Nicole Kinsman for their encouragement, their support, and not being too embarrassed that I was still a student at 28 years old.

Chapter 1

Introduction

Recorded observations of supernovae go back almost two millennia, when Chinese astronomers observed and recorded the galactic supernova SN 185 (Green & Stephenson 2003). Modern observations of supernovae began in the late 1800s and the rate of electromagnetic supernova detection has increased exponentially over the late modern era, especially with the advent dedicated supernova surveys (Filippenko et al. 2001). In 2010 alone, close to one thousand supernovae were detected (Barbon et al. 2010). Supernovae are observed to shine with luminosities over $10^{41}\,\mathrm{erg\,s^{-1}}$ over timescales of months and spectroscopic observations have shown that there are two distinct classes of supernovae, type I and type II (Minkowski 1941), which are mainly characterized by the presence or absence of hydrogen in their spectra. Additionally, the only observed extra-solar neutrinos were emitted from a supernova (Hirata *et al.* 1987, Bionta *et al.* 1987), making supernovae the only observed "multi-messenger" events in the universe.

The massive release of energy associated with supernovae led Baade & Zwicky (1934) to conjecture that supernovae are powered by the collapse of a normal

star to a (then recently theorized and as yet unobserved) neutron star. This supposition has held up for type II (as well as type Ib and Ic) supernovae and was the first clue that the physics of supernovae might be intimately related to nuclear physics. A convincing picture of the connection between supernovae, the evolution of massive stars, nuclear physics, and the origin of the elements was described in the seminal work of Burbidge et al. (1957) and Cameron (1957). Stars much more massive then the sun transmute the hydrogen initially found in their interiors to heavier and heavier elements through various stages of nuclear burning (hydrogen, helium, carbon, neon, oxygen, and silicon burning, see Woosley et al. (2002) for a modern detailed description of the evolution of massive stars) until nuclei around iron are formed in the core. Nuclei near iron have close to the maximal binding energy per nucleon and therefore cannot be burned to provide an energy source to support the star against collapse. Rather, electron degeneracy pressure supports the core against collapse until it reaches the effective Chandrasekhar mass. The inner regions of the star then collapse inward until the center reaches supra-nuclear densities, at which the infall is halted by neutron degeneracy and the repulsive part of the nuclear interaction. The core releases most of its gravitational binding energy ($\sim 3 \times 10^{53}$ erg) in the form of MeV neutrinos on a timescale of seconds. Supersonically in falling material impacts on this newly stiffened core and creates a shock wave which propagates out into the star and eventually serves to expel most of the stellar mass (Colgate & White 1966). The ejected material is enriched in elements formed through nuclear burning both during the stars quiescent life and during the supernova explosion itself. These newly formed elements are ejected and mixed into the interstellar medium, from whence the next generation of stars is formed.

This theoretical picture of core collapse supernovae has been verified in a number of ways: supernova progenitors have been identified as massive stars in archival data (Smartt 2009), the nucleosynthetic yields from massive stars have had success explaining the observed abundances of most of the isotopes in our solar system as well as the evolution of elemental abundances with metallicity (when combined with other nucleosynthetic sources) (Timmes et al. 1995), pulsars have been observed to be associated with supernova remnants (Large et al. 1968), and neutrinos emitted from the inner most regions of a supernova have been observed (Hirata *et al.* 1987, Bionta *et al.* 1987) with emission timescales and average energies in general agreement with theoretical predictions (Lattimer & Yahil 1989, Loredo & Lamb 2002).

Although supernovae have been detected for over a hundred years and the general theoretical picture of core collapse supernovae has been observationally confirmed, there a number of significant open questions concerning the innermost regions of core collapse supernovae:

1. *How is the gravitational binding energy of the compact object coupled to the outer layers of the star?* Although supernovae clearly blow up in nature, the details of how the energy gained from binding the inner compact object gets transmitted to the outer layers of the star and unbinds them are uncertain. Initially, it was thought that the shock which formed after bounce would continually propagate outwards and unbind the star (Colgate & White 1966), but dissociation of iron behind the shock saps it of energy and causes it to stall. Therefore, for the explosion to occur, some mechanism must operate which re-energizes the shock. The favored mechanism for this is neutrino heating in the convectively unstable region behind the shock (Bethe & Wil-

son 1985). Although this neutrino re-heating mechanism has been studied for almost three decades, there is still significant uncertainty concerning the efficacy of this mechanism (c.f. Janka 2012). This is a challenging problem because it is inherently multi-dimensional, general relativistic, involves radiation hydrodynamics, and the microphysics is uncertain. Additionally, MHD mechanisms for exploding supernovae have also been proposed, as magnetic fields are expected to be large in at least some fraction of supernovae (c.f. Meier et al. 1976, Burrows et al. 2007).

2. *What are the detailed properties of the emitted neutrinos?* Direct detection of supernova neutrinos is a rare event; it has only occurred once. Still, it is quite possible that a galactic core-collapse supernova will be seen with neutrino detectors in the lifetime of the author of this thesis, assuming current estimates for the Type II supernova rate for the Milky Way. Given that neutrinos have been observed from a supernova, the interesting aspect of new neutrino observations will be what they can tell us about the details of the inner most regions of a core-collapse supernova. There were not enough neutrino detections from SN 1987A ($\sim$ 24), to determine much detail of the cooling process (Lattimer & Yahil 1989, Loredo & Lamb 2002), though limits were placed on the properties of weakly interacting particles (Keil et al. 1997). If a similar core collapse supernova were to occur today, modern neutrino detectors would see thousands of events. Detailed modeling of the neutrino emission is required if anything is to be learned about the central engine of core collapse supernovae from the detection of neutrinos from a nearby event.

   If the shape of the neutrino spectrum is well understood, the late time core-

collapse supernova neutrino signal will give an estimate of the neutron star radius via $L_\nu \propto r^2 T^4_{\nu,\mathrm{eff}}$ (c.f. Hüdepohl *et al.* 2010), which would complement other measurements of neutron star radii and constrain the nuclear equation of state (Steiner et al. 2010). Additionally, the early neutrino emission may be correlated with the structure of the progenitor star and put constraints on models of massive stellar evolution (O'Connor & Ott 2012). The rate of PNS cooling also has the potential to put limits on exotic physics, such as axions (Keil et al. 1995), the presence of quark matter or a Kaon condensate in the PNS core (Pons et al. 2001a;b), as well as possible extensions of the standard model using data already in hand from SN 1987A.

It is also possible that current neutrino detectors with upgrades or next generation neutrino detectors will be able to observe the diffuse background of neutrinos produced by supernovae over the lifetime of the universe (Horiuchi et al. 2009). Predictions for the diffuse MeV scale neutrino background density depend significantly on the the integrated spectrum of neutrinos emitted in core-collapse supernovae (Woosley et al. 1986, Ando 2004). The integrated neutrino emission is dominated by PNS evolution, so that accurate modeling of PNSs can also contribute to understanding the diffuse supernova neutrino background.

Additionally, the neutrino emission from the "photosphere" of PNSs gives the initial conditions for the study of both matter-induced and neutrino-induced neutrino oscillations (Duan et al. 2006). The differences between the spectra various neutrino flavors, especially $\bar{\nu}_e$ and $\bar{\nu}_{\mu,\tau}$, can significantly affect the impact of flavor evolution in the nearly free streaming regime (Keil et al. 2003). The rise time of the supernova neutrino burst may be affected

by the neutrino mass hierarchy, so that observations of supernova neutrinos could distinguish the heretofore unknown neutrino mass hierarchy (Serpico et al. 2012).

The evolution of PNSs is described by the Kelvin-Helmholtz cooling of the collapsed, shock heated remnant of a core-collapse supernova. Similarly to the explosion mechanism itself, the cooling phase is fundamentally a radiation hydrodynamics problem (although the regions important for neutrino emission are not very *dynamic* after bounce). Theoretical predictions of post-bounce neutrinos have existed for more than 25 years (Burrows & Lattimer 1986, Mayle et al. 1987, Keil & Janka 1995, Pons et al. 1999, Fischer *et al.* 2010, Hüdepohl *et al.* 2010, Roberts et al. 2012). Over time, the treatment of radiative transfer and neutrino microphysics in simulations has become increasingly sophisticated, moving from the equilibrium flux limited diffusion (EFLD) and greatly simplified neutrino physics (Burrows & Lattimer 1986) to full solutions of the Boltzmann equation (Fischer *et al.* 2010) with more realistic microphysics (Hüdepohl *et al.* 2010, Roberts 2012). Still, there is significant physics that is not included in these models which may affect the neutrino emission, leaving much work to be done (Roberts & Reddy 2012).

3. *What nucleosynthesis is expected from the inner most supernova ejecta?*

Another important reason for studying the late time core-collapse environment is the impact neutrinos have on supernova nucleosynthesis. The site where r-process nuclei above A=90 have been synthesized remains a major unsolved problem in nucleosynthesis theory (e.g., Arnould et al. 2007). Historically, many possibilities have been proposed (see Meyer 1994), but

today, there are two principal contenders - neutron star mergers (Lattimer et al. 1977, Freiburghaus et al. 1999, Roberts et al. 2011) and the NDW (e.g. Woosley et al. 1994, Witti et al. 1994a, Thompson et al. 2001, Wanajo et al. 2001, Arcones et al. 2007). Observations of ultra-metal-poor stars suggest that many r-process isotopes were already quite abundant at early times in the galaxy (Cowan et al. 1995, Sneden et al. 1996, Frebel et al. 2007), suggesting both a primary origin for the r-process and an association with massive stars, both of which favor the NDW of NSNS mergers.

Charged current neutrino interactions in the wind blown from the surface of PNSs determine the electron fraction of the ejected material and thereby constrain its nucleosynthesis. Current uncertainties in the relative energies of the electron neutrinos and anti-neutrinos emitted from PNSs are in fact large enough to allow for the possibility of both neutron-rich and proton-rich conditions in the innermost supernova ejecta, which may be favorable for either r-process (Woosley et al. 1994) and νp-process nucleosynthesis (Fröhlich et al. 2006, Pruet et al. 2006), respectively. Some recent work points to the wind ejecta being proton rich at all times (Hüdepohl *et al.* 2010, Fischer *et al.* 2010), but this conclusion is far from certain (Roberts 2012, Roberts & Reddy 2012, Martínez-Pinedo et al. 2012).

The neutrino driven wind (NDW) that emanates from young neutron stars was first studied by Duncan et al. (1986), but without an eye towards possible nucleosynthesis in this environment. It was first suggested that the NDW might be responsible for r-process nucleosynthesis in Woosley & Hoffman (1992) and Meyer et al. (1992). The first dynamical models of the NDW showed conditions that were very favorable for r-process nucleosynthesis

(Woosley et al. 1994), but subsequent core-collapse supernova models that followed the wind phase were unable to reproduce the conditions found in that work and the r-process did not obtain (Witti et al. 1994a). Analytic models of the wind found that in the simplest scenario the NDW was not conducive to r-process nucleosynthesis (Qian & Woosley 1996, Hoffman et al. 1997, Thompson et al. 2001). In reality, the PNS environment is likely significantly more complicated than is assumed in these models of the wind. Strong magnetic fields can alter the dynamics of the wind (Metzger et al. 2007) and Alfven waves can heat the material in the wind, increasing the entropy and making conditions more favorable for the r-process (Suzuki & Nagataki 2005a). It is also possible that acoustic waves could provide a similar augmentation of neutrino heating.

Additionally, the average energies of μ and τ neutrinos also significantly affect the neutrino spallation rates that determine nucleosynthetic yields of the ν-process (Woosley et al. 1990), which may be responsible for a number of rare isotopes. The average energies of these are strongly affected by the inclusion of detailed neutrino physics, so that more accurate modeling of the neutrino emission is required to see if the ν-process is operative as imagined (Heger et al. 2005).

This thesis focuses on understanding some of the physics that influences late time supernova neutrino emission and on the details of how this neutrino emission affects the nuclear composition of the inner most material ejected in the supernova (i.e. questions 2 and 3 above), but eschews the important question of the supernova mechanism itself.

In **Chapter 2**, a spherically symmetric, general relativistic, multi-group neu-

trino transport code for PNS evolution is described. The basic equations of general relativistic stellar structure coupled to the equations of moment based radiative transfer are described. A simplified method for angle and energy dependent radiative transfer in a curved space-time is then discussed as a way to close the moment equations of radiative transfer. Numerical aspects of the code are then discussed and some test problems are described. This code is then used to model the evolution of young neutron stars over a period of about one minute. The generic features of PNS evolution are described, such as the evolution of the internal structure and evolution of the neutrino emission. The importance of the treatment of charged current neutrino interaction rates in the PNS is then discussed, specifically in relation to the expected neutrino driven wind electron fraction. A comparison is also made to a model of PNS evolution which uses a simplified method for radiative transfer that has been employed in many previous studies. The chapter concludes with a discussion of the integrated neutrino emission from the neutron star.

In **Chapter 3**, the physics of the charged current response in matter at sub-nuclear densities is discussed with an eye towards its affect on electron neutrino and anti-neutrino transport in the outer layers of a PNS. It is found that the nuclear symmetry energy can affect the electron fraction of the NDW when only mean field affects are considered in the charged current response. Possible modifications of the response due to collective modes and multi-particle hole excitations are also discussed.

In **Chapter 4**, neutrino emission from a PNS is modeled using equilibrium flux limited diffusion to study its sensitivity to the nuclear equation of state, neutrino opacities, and convective instabilities at high baryon density. It is found that

the time period and spatial extent over which convection operates is sensitive to the behavior of the nuclear symmetry energy at and above nuclear density. When convection ends within the PNS, there is a break in the predicted neutrino emission that may be clearly observable

In **Chapter 5**, dynamical models of NDWs including integrated nucleosynthesis are described. It is found that the simplest models are incapable of producing r-process nucleosynthesis, but it is possible that the NDW might be responsible for the production of ^{87}Rb, ^{88}Sr, ^{89}Y, and ^{90}Zr (although this is sensitive to the assumed neutrino luminosities).

In **Chapter 6**, a possible extension of the NDW model to include a source of heating in addition to neutrinos is discussed, which allows for r-process nucleosynthesis in marginally neutron rich NDWs. It is proposed that gravitoacoustic waves emanating from the PNS could naturally provide such a heating source. Therefore, assuming the NDW electron fractions predicted in chapter 2, it is found that it is at least plausible (once again) that the NDW is a source of r-process nuclei, but the uncertainties are quite large.

Chapter 2

A New General Relativistic Multi-Group Proto-Neutron Star Evolution Code

This work has been published in the Astrophysical Journal as (Roberts 2012).

Abstract

A new code for following the evolution and emissions of proto-neutron stars during the first minute of their lives is developed and tested. The code is one dimensional, fully implicit, and general relativistic. Multi-group, multi-flavor neutrino transport is incorporated that makes use of variable Eddington factors obtained from a formal solution of the static general relativistic Boltzmann equation with linearized scattering terms. The timescales of neutrino emission and spectral evolution obtained using the new code are broadly consistent with previous results. Unlike other recent calculations, however, the new code predicts that the neutrino-driven wind will be characterized, at least for part of its existence, by

a neutron excess. This change, potentially consequential for nucleosynthesis in the wind, is due to an improved treatment of the charged-current interactions of electron flavored neutrinos and anti-neutrinos with nucleons. A comparison is also made between the results obtained using either variable Eddington factors or simple equilibrium flux-limited diffusion. The latter approximation, which has been frequently used in previous studies of proto-neutron star cooling, accurately describes the total neutrino luminosities (to within 10%) for most of the evolution, until the proto-neutron star becomes optically thin.

2.1 Introduction

A proto-neutron star (PNS) is born after the core of a massive star collapses to supra-nuclear densities, experiences core bounce due to the repulsive portion of the nuclear interaction which launches a shock wave that may eventually serve to disrupt the entire star in a supernova, and leaves behind a compact remnant. The overlying star is ejected and some portion of the mass may or may not fall back (c.f. Janka et al. 2007). In reality the mass of the PNS may increase with time due to this accretion, but a frequent assumption that is reasonable for low mass progenitors, and one adopted here, is that the PNS evolves in isolation after the shock has exited. Because of the large release of gravitational binding energy ($2 - 5 \times 10^{53}$ ergs), the PNS is initially hot and extended compared to a cold neutron star but large portions of the mass are still at supra-nuclear densities. Due to the high density and reasonably large temperature of this nuclear material, it is opaque to neutrinos of all flavors. In the outer regions of the PNS where the density is lower, the material is semi-transparent to neutrinos. This hot extended object undergoes Kelvin-Helmholtz cooling by emitting neutrinos of all flavors

over a period of up to a minute (Burrows & Lattimer 1986), at which time it transitions to a phase of optically thin neutrino cooling.

This qualitative description was confirmed when about twenty neutrinos were observed from SN 1987A (Bionta *et al.* 1987, Hirata *et al.* 1987). There were not enough events, however, to determine much detail of the cooling process (Lattimer & Yahil 1989, Loredo & Lamb 2002), though limits were placed on the properties of weakly interacting particles (Keil et al. 1997). If a similar core collapse supernova were to occur today, modern neutrino detectors would see thousands of events. Detailed modeling of the neutrino emission is needed if we are to learn about the central engine of core collapse supernovae from a nearby event.

Theoretical predictions of post-bounce neutrinos have existed for more than 25 years (Burrows & Lattimer 1986, Mayle et al. 1987, Keil & Janka 1995, Sumiyoshi et al. 1995, Pons et al. 1999, Fischer *et al.* 2010, Hüdepohl *et al.* 2010, Roberts et al. 2012). Since the evolution of PNSs is described by the Kelvin-Helmholtz cooling of the collapsed, shock heated remnant of a core-collapse supernova, it is fundamentally a radiation hydrodynamics problem (although the regions important for neutrino emission are not very *dynamic* after bounce). Over time, the treatment of radiative transfer and neutrino microphysics in simulations has become increasingly sophisticated, moving from the equilibrium flux limited diffusion (EFLD) and greatly simplified neutrino physics (Burrows & Lattimer 1986) to full solutions of the Boltzmann equation (Fischer *et al.* 2010) with more realistic microphysics (Hüdepohl *et al.* 2010).

Here, a new fully implicit code is developed for calculating the detailed evolution of PNSs in spherically symmetric general relativity within a variable Eddington factor formalism. The structure of the paper is as follows: In section 2.2, the

equations of neutrino transport within the projected symmetric trace-free moment formalism of Thorne (1981) are described, and generic neutrino source terms for this formalism are derived. In section 2.3, a method for obtaining closure relations for the moment equations via a formal solution of the Boltzmann equation are described. A fully implicit numerical implementation of neutrino transport coupled to hydrodynamics/hydrostatics is described in section 2.4 (with code tests described in appendix 2.8). A fiducial model of PNS cooling is detailed in section 2.5. These results are compared with the results of an EFLD calculation of PNS cooling in section 2.6.1. The implications of these new calculations of PNS cooling on the composition of the neutrino driven wind are discussed in section 2.6.2. In section 2.6.3, the properties of the integrated neutrino emission are discussed. The convention $\hbar = c = G = 1$ is adopted in sections 2.2 through 2.4 to avoid a plethora of factors. In section 2.6.2, units with $\hbar = c = 1$ are used.

2.2 The Moment Approach to General Relativistic Radiative Transfer

The equations of radiative transfer in curved space-times were first derived by Lindquist (1966), which described the evolution of the invariant distribution function along geodesics in phase space. The general form of the general relativistic Boltzmann (or Lindquist) equation in the absence of external forces is

$$\frac{df\left(x^{\mu}, p^{\nu}(x^{\mu})\right)}{d\tau} = p^{\beta}\left(\frac{\partial f}{\partial x^{\beta}} - \Gamma^{\alpha}_{\beta\gamma} p^{\gamma} \frac{\partial f}{\partial p^{\alpha}}\right) = \left(\frac{df}{d\tau}\right)_{\mathrm{coll}}, \tag{2.1}$$

where f is the invariant distribution function, p^{β} is the neutrino four-momentum (which is constrained to be on mass shell), and $\Gamma^{\alpha}_{\beta\gamma}$ are the Christoffel symbols.

The collision term on the right hand side describes the destruction and production of neutrinos on a particular phase-space trajectory by capture processes, pair annihilation, scattering, and their inverses. In addition to describing the propagation of neutrinos along trajectories in physical space, this also encodes the evolution of the energy of neutrinos along geodesics of the spacetime. In three spatial dimensions, this is a seven dimensional equation that needs to be solved for each neutrino species.

A number of numerical strategies can be employed to solve the transport problem (Mihalas & Mihalas 1984). Foremost among these are discrete ordinate methods, where the Boltzmann equation is directly discretized in momentum space as well as in physical space (e.g. Yueh & Buchler 1977, Mezzacappa & Messer 1999, Liebendörfer et al. 2004), and moment-based approaches, where angular integrations of the Boltzmann equation in momentum space are performed (e.g. Thorne 1981, Burrows et al. 2000, Rampp & Janka 2002). These two approaches give similar results in one-dimensional models, at least in the context of core-collapse supernovae (Liebendörfer et al. 2005). An additional technique that has only been employed for solving static problems in the supernova context, but is perhaps the most capable of retaining fidelity to the underlying Boltzmann equation, is Monte Carlo neutrino transport (Janka & Hillebrandt 1989, Keil et al. 2003).

The moment approach results in an infinite hierarchy of coupled equations which needs to be truncated at some order in practice. Generally, only the zeroth and first order moment equations are retained and a closure relation is assumed between the first two moments and the higher order moments that enter the first two moment equations. Such schemes are referred to as variable Eddington factor methods (Mihalas & Mihalas 1984). When only the first two moments are used,

the number of equations relative to discrete ordinate methods is significantly reduced, easing the computational burden (especially in an implicit scheme like the one described below). Of course, this gain in computational efficiency is useful only if reasonable closures can be obtained. The closure relations only encode information about the angular distribution of neutrinos, so that the approximations involved in solving a linearized Boltzmann equation do not severely impact the fidelity of numerical calculations to the true solution (Mihalas & Mihalas 1984, Ensman 1994).

Here a variable Eddington factor approach to radiative transfer is employed, with the closure relations being obtained from a formal solution of the static relativistic Boltzmann equation. This approach is similar to that used by Burrows et al. (2000) and Rampp & Janka (2002), except for being fully general relativistic, incorporating both inelastic scattering and pair production (in contrast to only the former), using energy integrated groups rather than energy "pickets", and in the specific method of finding the closure relations. The formalism for this method is described below.

The moments of the Boltzmann equation also most naturally give the various forms of the diffusion approximation, which has been used in the majority of PNS studies (Burrows & Lattimer 1986, Keil & Janka 1995, Pons et al. 1999, Roberts et al. 2012) and in a significant fraction of studies of the early core-collapse and bounce phases(Bruenn 1985, Wilson & Mayle 1993). The formalism is connected to EFLD in appendix 2.9.

2.2.1 General Relativistic Generalities

In spherical symmetry, it is simplest to work in a coordinate system that anticipates a Lagrangian frame for the fluid. The metric for such a space-time is given by (Misner & Sharp 1964)

$$ds^2 = -e^{2\phi}dt^2 + \left(\frac{r'}{\Gamma}\right)^2 da^2 + r^2 d\Omega^2, \tag{2.2}$$

where ds is the invariant interval, t is the time measured at infinity, r is the areal radius, Ω is the solid angle, and Γ and ϕ are metric potentials. Coordinate freedom can be exploited to choose this frame to be the rest-frame of the fluid, which demands (Liebendörfer et al. 2001a)

$$\frac{\partial r}{\partial a} = \frac{\Gamma}{4\pi r^2 n_B}. \tag{2.3}$$

Here, n_B is the baryon number density and

$$\Gamma = \sqrt{1 + u^2 - \frac{2m}{r}} \tag{2.4}$$

where u and m are defined below. With this choice, the orthonormal frame associated with the coordinate frame is just the rest frame of the fluid and da is just the change in enclosed baryon number with the physical volume. Therefore, this formulation is working in the Lagrangian frame, as claimed.

The equations of spherically symmetric general relativistic hydrodynamics and the Einstein equation are recorded for convenience (Misner & Sharp 1964). Most of these results are nicely presented and detailed in similar form by Liebendörfer et al. (2001a). The time evolution of the areal radius is given by,

$$\frac{\partial r}{\partial t} = e^{\phi} u \tag{2.5}$$

which defines u. The evolution of u is given by

$$\frac{\partial u}{\partial t} = \Gamma^2 \frac{\partial e^{\phi}}{\partial r} - e^{\phi} \frac{m + 4\pi r^3 (p + Q)}{r^2}, \tag{2.6}$$

where Q is the viscosity and p is the pressure of the fluid. This gives the equation of hydrostatic balance when the left hand side equals zero (i.e. the Tolman-Oppenheimer-Volkov equation (Oppenheimer & Volkoff 1939)). The enclosed gravitational mass, m, is defined by

$$\frac{\partial m}{\partial a} = \Gamma \left(\frac{E}{n_B} + \epsilon \right) + u \frac{H}{n_B}, \tag{2.7}$$

where ϵ is the internal energy per baryon, E is the total neutrino energy density in the rest frame, and H is the net radial energy flux from neutrinos. The constraint equation for the metric potential ϕ is

$$\frac{\epsilon}{e^{\phi}} \frac{\partial e^{\phi}}{\partial a} + \frac{1}{n_B e^{\phi}} \frac{\partial (e^{\phi} p)}{\partial a} + \frac{1}{r^3 n_B e^{\phi}} \frac{\partial (r^3 e^{\phi} Q)}{\partial a} = 0, \tag{2.8}$$

where a small time dependent term has been neglected.

The transport equations described in the next section are formulated in a congruence corresponding to the four-velocity field of the PNS (clearly, this is not a geodesic congruence). The behavior of this congruence is best described by expanding the covariant derivative of the four-velocity as

$$U_{\mu;\nu} = -a_{\nu} U_{\mu} + \frac{\Theta}{3} P_{\mu\nu} + \sigma_{\mu\nu} + \omega_{\mu\nu}, \tag{2.9}$$

where U_{μ} is the tangent four-vector field of the congruence, $P_{\mu\nu}$ is the projection tensor (which projects into the vector subspace orthogonal to U^{μ}) $a^{\nu} = U^{\alpha} U^{\nu}_{;\alpha}$ is the acceleration, $\Theta = U^{\mu}_{;\mu}$ is the expansion, $\sigma_{\mu\nu}$ is the shear, and $\omega_{\mu\nu}$ is the rotation. Using the continuity equation, the expansion of the congruence becomes

$$\Theta = -D_{\hat{t}} \ln(n_B). \tag{2.10}$$

In spherical symmetry, the acceleration four-vector is parallel to the radial orthonormal basis vector, so that only the scalar acceleration is needed

$$a = \Gamma \frac{\partial \phi}{\partial r}. \tag{2.11}$$

In spherical symmetry, the shear is characterized by a single component, the scalar shear

$$\sigma = -\frac{2u}{r} - \frac{2}{3}\Theta. \tag{2.12}$$

Additionally, such a spherically symmetric congruence possesses no rotation, so that $\omega_{\mu\nu} = 0$. The quantity

$$b = \frac{\Gamma}{r} \tag{2.13}$$

will also be required, which is related to the extrinsic curvature (Thorne 1981). The orthonormal frame temporal and radial derivative operators are

$$D_{\hat{t}} = e^{-\phi} \frac{\partial}{\partial t} \tag{2.14}$$

and

$$D_{\hat{r}} = 4\pi r^2 n_B \frac{\partial}{\partial a} = \Gamma \frac{\partial}{\partial r}. \tag{2.15}$$

2.2.2 Variable Eddington Factor Transport Equations

Here, the evolution equations for the neutrino number density, energy density, number flux and energy flux are derived from the zeroth and first order moments of the relativistic Boltzmann equation. The basic results are taken from the spherically symmetric version of the projected symmetric trace-free moment formalism of Thorne (1981). This formalism reduces to an expansion of the neutrino distribution function in terms of Legendre polynomials in a flat space-time.

The moments of the distribution function are defined in spherical symmetry as

$$w^n = \frac{\omega^3}{(2\pi)^2} B_n \int_{-1}^{1} d\mu P_n(\mu) f(\omega, \mu) \tag{2.16}$$

where

$$B_n = \frac{n!(2n+1)}{(2n+1)!!}, \tag{2.17}$$

P_n are the Legendre polynomials, and ω is the neutrino energy in the fluids rest frame. The first two moment equations in spherical symmetry can be read off from equation 5.10 of Thorne (1981)

$$\begin{aligned} & w^0_{,\hat{t}} + \frac{4}{3}\Theta w^0 + \frac{3}{2}\sigma w^2 + w^1_{,\hat{r}} \\ 2(a+b)w^1 - \frac{\partial}{\partial\omega}\omega & \left[a w^1 + \frac{\Theta}{3} w^0 + \frac{3}{2}\sigma w^2 \right] \quad = \quad s^0 \end{aligned} \tag{2.18}$$

and

$$\begin{aligned} & w^2_{,\hat{r}} + (a+3b)w^2 + w^1_{,\hat{t}} + \left[\frac{4}{3}\Theta + \sigma \right] w^1 + \frac{1}{3} w^0_{,\hat{r}} + \frac{4}{3} a w^0 \\ & -\frac{\partial}{\partial\omega}\omega \left[a w^2 + \left(\frac{\Theta}{3} + \frac{2}{5}\sigma \right) w^1 + \frac{1}{3} a w^0 + \frac{3}{2}\sigma w^3 \right] = s^1, \end{aligned} \tag{2.19}$$

where s^l are the neutrino source terms defined in section 2.2.3. To close this system, define the Eddington like factors

$$g_2 = w^2/w^0 \tag{2.20}$$

$$g_3 = w^3/w^1 \tag{2.21}$$

which both go to zero in the limit $f(\mu) = f_0 + \mu f_1$, which corresponds to the diffusion regime. Note that these differ from the standard definition of the Eddington factors (Rampp & Janka 2002), which is due to how I have chosen to calculate the moments. For free streaming radiation in a flat background $g_2 = 2/3$, and these

equations reduce to the linear wave equation for $h = h(r \pm t) \equiv r^2 w_0$. A method for approximating these Eddington factors is detailed in section 2.3.

For problems that are close to being static on the radiation timescale, it is useful to switch the independent variable ω, the energy in the fluid rest frame, of w^i to the energy at infinity, ν (c.f. Schinder & Bludman 1989). In the case of PNS cooling, the energy at infinity is much closer to being a constant of the motion and therefore a more natural variable. Additionally, this choice simplifies the formal solution of the Boltzmann equation. The moments of the distribution function are then

$$w^i = w^i(r, \nu(\omega, r, t)) \tag{2.22}$$

where the energy at infinity is defined as $\nu = e^{\phi(r,t)}\omega$. This means that the replacement

$$\frac{\partial w^i}{\partial x} \rightarrow \frac{\partial w^i}{\partial x} + \frac{\partial \nu}{\partial x}\frac{\partial w^i}{\partial \nu} \tag{2.23}$$

needs to be made for all radial and time derivatives, resulting in

$$\begin{aligned} &\frac{\partial w^0/n_B}{\partial t} + \frac{w^0}{n_B}e^{\phi}\left(\frac{\Theta}{3} + g_2\frac{3}{2}\sigma\right) + \frac{\partial}{\partial a}\left(4\pi r^2 e^{\phi} w^1\right) \\ &-\frac{e^{\phi}}{n_B}\frac{\partial}{\partial \nu}\nu\left[\left(\frac{\Theta}{3} + g_2\frac{3}{2}\sigma\right)w^0\right] + \frac{\nu}{n}\frac{\partial \phi}{\partial t}\frac{\partial w^0}{\partial \nu} = e^{\phi}\frac{s^0}{n_B} \end{aligned} \tag{2.24}$$

and

$$\begin{aligned} e^{-\phi}\frac{\partial w^1}{\partial t} + \left[\frac{4}{3}\Theta + \sigma\right]w^1 + n_B e^{-\phi}\frac{\partial}{\partial a}\left[4\pi r^2 e^{\phi}\left(\frac{1}{3} + g_2\right)w^0\right] \\ + \left(\frac{2}{3} - g_2\right)(a-b)\,w^0 - \frac{\partial}{\partial \nu}\nu\left[\left(\frac{\Theta}{3} + \frac{2}{5}\sigma + \frac{3}{2}\sigma g_3\right)w^1\right] \\ + e^{-\phi}\frac{\partial \phi}{\partial t}\nu\frac{\partial w^1}{\partial \nu} = s^1. \end{aligned} \tag{2.25}$$

To easily deal with optically thick regions where the distribution function may possess a sharp Fermi surface, energy integrated groups are used rather than

discrete energy "pickets". The group numbers, energies, number fluxes, energy fluxes, and source terms in group g are defined by

$$\begin{aligned}
N_g &= \int_{\omega_{g,L}}^{\omega_{g,U}} \frac{d\omega}{\omega} w^0, \qquad F_g = \int_{\omega_{g,L}}^{\omega_{g,U}} \frac{d\omega}{\omega} w^1, \\
S_g^0 &= \int_{\omega_{g,L}}^{\omega_{g,U}} \frac{d\omega}{\omega} s^0, \qquad S_g^1 = \int_{\omega_{g,L}}^{\omega_{g,U}} \frac{d\omega}{\omega} s^1, \\
E_g &= \int_{\omega_{g,L}}^{\omega_{g,U}} d\omega w^0, \qquad H_g = \int_{\omega_{g,L}}^{\omega_{g,U}} d\omega w^1, \\
Q_g^0 &= \int_{\omega_{g,L}}^{\omega_{g,U}} d\omega s^0, \qquad \text{and } Q_g^1 = \int_{\omega_{g,L}}^{\omega_{g,U}} d\omega s^1.
\end{aligned} \tag{2.26}$$

Here, $\omega_{g,L}$ is the lower energy bound of an energy group and $\omega_{g,U}$ is the upper bound. Integrating over energy at infinity within groups gives

$$N_g = \int_{\nu_{L,g}}^{\nu_{U,g}} \frac{d\nu}{\nu} w^0 \text{ and } E_g = e^{-\phi} \int_{\nu_{L,g}}^{\nu_{U,g}} d\nu w^0 \tag{2.27}$$

and similar expressions for F_g, H_g, and the source terms. The operators $\int d\nu/\nu$ and $\int d\nu$ can then be applied to the "red shifted" equations. The evolution the neutrino group number densities are described by

$$\begin{aligned}
&\frac{\partial}{\partial t}\left(\frac{N_g}{n_B}\right) + \frac{\partial}{\partial a}\left(4\pi r^2 e^{\phi} F_g\right) \\
&-\frac{e^{\phi}}{n_B}\left(\frac{\Theta}{3} + g_2 \frac{3}{2}\sigma - e^{-\phi}\frac{\partial \phi}{\partial t}\right) w^0 \Big|_{\nu_L}^{\nu_U} = e^{\phi}\frac{S_g^0}{n_B}.
\end{aligned} \tag{2.28}$$

The last term on the left hand side describes the red or blue shifting of neutrinos to other groups via compression and time variation of the metric potential ϕ. If the group comprises energies from zero to infinity, the red shifting terms drop out and one is left with the standard number transport equation given in Pons et al.

(1999). Applying the number operator to equation 2.25 and simplifying gives

$$\begin{aligned} e^{-\phi}\frac{\partial F_g}{\partial t} + \left[\Theta + \left(\frac{3}{5} - \frac{3}{2}g_2\right)\sigma\right] F_g \\ + \frac{r^2 n_B}{3e^{3\phi}}\frac{\partial}{\partial a}\left(4\pi e^{3\phi} N_g\right) + \frac{n_B}{r}\frac{\partial}{\partial a}\left(4\pi r^3 g_2 E_g\right) \\ - \left[\frac{\Theta}{3} + \left(\frac{2}{5} + \frac{3}{2}g_2\right)\sigma - e^{-\phi}\frac{\partial \phi}{\partial t}\right] w^1\Big|_{\nu_L}^{\nu_U} &= S_g^1. \end{aligned} \tag{2.29}$$

This includes similar terms to equation 2.28, plus a term that includes the effects of compression on the total number flux. The energy group evolution equations are

$$\begin{aligned} \frac{\partial}{\partial t}\left(\frac{E_g}{n_B}\right) + e^{\phi}\left(\frac{\Theta}{3} + g_2\frac{3}{2}\sigma\right)\frac{E_g}{n_B} + e^{-\phi}\frac{\partial}{\partial a}\left(4\pi r^2 e^{2\phi} H_g\right) \\ - \frac{1}{n_B}\left(\frac{\Theta}{3} + g_2\frac{3}{2}\sigma - e^{-\phi}\frac{\partial \phi}{\partial t}\right)\left(\nu w^0\right)\Big|_{\nu_L}^{\nu_U} = e^{\phi}\frac{Q_g^0}{n_B}. \end{aligned} \tag{2.30}$$

Aside from the addition of a compression term and different factors of e^{ϕ}, this is identical to equation 2.28. The energy flux group evolution equations are

$$\begin{aligned} e^{-\phi}\frac{\partial H_g}{\partial t} + \left[\frac{4}{3}\Theta + \sigma\right] H_g \\ + \frac{r^2 n_B}{3e^{4\phi}}\frac{\partial}{\partial a}\left(4\pi e^{4\phi} E_g\right) + \frac{n_B}{re^{\phi}}\frac{\partial}{\partial a}\left(4\pi r^3 e^{\phi} g_2 E_g\right) \\ - \left(\frac{\Theta}{3} + \frac{2}{5}\sigma + g_3\frac{3}{2}\sigma - e^{-\phi}\frac{\partial \phi}{\partial t}\right)\left(\nu w^1\right)\Big|_{\nu_L}^{\nu_U} &= Q_g^1. \end{aligned} \tag{2.31}$$

The numerical implementation of the red-shifting terms is described in section 2.4.6.

Additionally, neutrinos have a back-reaction on the matter they are propagating through by exchanging energy, lepton number, and momentum with the background medium. Assuming that the background possesses a thermal state, the first law of thermodynamics for the medium can be combined with the sum

of equations 2.30 over all groups to find an equation for the conservation of total internal energy

$$\begin{aligned} \frac{\partial}{\partial t}\left(\epsilon + \sum_{g,s}\frac{E_{g,s}}{n}\right) + e^{\phi}\Theta\left(\frac{p}{n} + \sum_{g,s}\frac{E_{g,s}}{3n}\right) \\ + \frac{3e^{\phi}}{2}\sigma\sum_{g,s} g_{2,g}\frac{E_{g,s}}{n} + e^{-\phi}\frac{\partial}{\partial a}\left(4\pi r^2 e^{2\phi}\sum_{g,s} H_{g,s}\right) &= 0 \end{aligned} \tag{2.32}$$

where the sums are over groups and species. Obviously, the neutrino energy source terms have exactly canceled with the source terms for the medium.

In the absence of neutrinos, the electron fraction of the background medium is fixed, i.e. $e^{-\phi}\dot{Y}_e = 0$. When neutrinos are included, interactions of electron flavored neutrinos exchange lepton number with the background, yielding $e^{-\phi}\dot{Y}_e = -\sum_g S_g^0/n_B$. The total lepton number of the medium is given by $Y_L = Y_e + \sum_g \left[N_{g,\nu_e} - N_{g,\bar{\nu}_e}\right]/n_B$. Combining the evolution equation for Y_e with equations 2.28 gives the lepton number evolution equation

$$\begin{aligned} \frac{\partial}{\partial t}\left(Y_e + \sum_g\left[\frac{N_{g,\nu_e}}{n_B} - \frac{N_{g,\bar{\nu}_e}}{n_B}\right]\right) \\ + \frac{\partial}{\partial a}\left(4\pi r^2 e^{\phi}\sum_g\left[F_{g,\nu_e} - F_{g,\bar{\nu}_e}\right]\right) &= 0. \end{aligned} \tag{2.33}$$

This constitutes the full set of evolution equations for the state of the medium including non-thermal neutrinos of all flavors, when the Eddington factors g_2 and g_3 are specified.

2.2.3 Neutrino Source Terms

The collision term in equation 2.1 describes how neutrinos move from one trajectory to another via scattering and how they are created and destroyed by the underlying medium. For the PNS problem these processes include neutral current

scattering off of electrons, nucleons, and nuclei (Reddy et al. 1998), neutrino pair production via nucleon-nucleon bremsstrahlung (Hannestad & Raffelt 1998) and electron-positron annihilation (Bruenn 1985), and charged current processes involving electron and anti-electron flavor neutrinos and neutrons and protons, respectively (Reddy et al. 1998).

The details of these microphysical processes are eschewed by assuming that the differential cross-sections for these processes are known and referring the reader to the papers cited above, as well as the review Burrows et al. (2006). The exact details of the microphysics used in the code will be reported in a future publication, although certain aspects are discussed in sections 2.5 and 2.6.2. Many of the results in this section are well known (e.g. Bruenn 1985, Pons et al. 1999), and are included here for completeness and to make clear the details of the exact implementation within the integrated energy group formalism described above. Explicit detailed balancing (independent of the choice of underlying scattering kernels) is emphasized.

The source function for a particular moment is given by

$$s^l = \tfrac{\omega^3}{(2\pi)^2} B_l \int_{-1}^{1} d\mu \, P_l(\mu) \times \left(j_a(1-f) - \tfrac{f}{\lambda_a} + j_s(1-f) - \tfrac{f}{\lambda_s} + j_p(1-f) - \tfrac{f}{\lambda_p} \right), \tag{2.34}$$

which includes contributions from absorption ($1/\lambda_a$), scattering ($1/\lambda_s$), pair-annihilation ($1/\lambda_p$), and their inverses (j_a, j_s, and j_p). The choice of metric and reference frame implies that the scattering kernels should be evaluated in the rest frame of the fluid, simplifying things compared to hybrid frame approaches (Hubeny & Burrows 2007).

For the absorption part, using the standard detailed balance relations gives

$$j_a(1-f) - \frac{f}{\lambda_a} = \frac{1}{\lambda_a^*}\left(f_{eq}(\omega, T, \mu_{\rm eq}) - f(\omega,\mu)\right), \tag{2.35}$$

where $\lambda_a^{*-1} = [1+\exp\{-(\omega-\mu_{\rm eq})/T\})]\lambda_a^{-1}$ and f_{eq} is a Fermi-Dirac distribution. The scattering contributions are

$$j_s = \int \frac{d\omega'}{(2\pi)^3}\omega'^2 \int_{-1}^{1} d\mu' \int_0^{2\pi} d\phi'\, R^s(\omega', \omega, \mu') f(\omega', \mu_{out}) \tag{2.36}$$

and

$$\lambda_s = \int \frac{d\omega'}{(2\pi)^3}\omega'^2 \int_{-1}^{1} d\mu' \int_0^{2\pi} d\phi'\, R^s(\omega, \omega', \mu')(1 - f(\omega', \mu_{out})), \tag{2.37}$$

and the pair-annihilation contributions are

$$j_p = \int \frac{d\omega'}{(2\pi)^3}\omega'^2 \int_{-1}^{1} d\mu' \int_0^{2\pi} d\phi'\, R^p_{in}(\omega, \omega', \mu')(1 - \bar{f}(\omega', \mu_{out})) \tag{2.38}$$

and

$$\lambda_p = \int \frac{d\omega'}{(2\pi)^3}\omega'^2 \int_{-1}^{1} d\mu' \int_0^{2\pi} d\phi'\, R^p_{out}(\omega, \omega', \mu')\bar{f}(\omega', \mu_{out}). \tag{2.39}$$

The outgoing cosine is given by $\mu_{out} = \mu\mu' - \sqrt{1-\mu^2}\sqrt{1-\mu'^2}\cos\phi'$. The R_{out} functions are related to the differential cross-section by

$$R(\omega, \omega', \mu) = \frac{(2\pi)^2}{\omega'^2}\frac{1}{V}\frac{d\sigma}{d\omega' d\mu}, \tag{2.40}$$

with no phase space blocking term for the final neutrinos in the differential cross-section. The R functions obey the detailed balance relations for scattering

$$R^s(\omega, \omega', \mu) = R^s(\omega', \omega, \mu)e^{(\omega-\omega')/T}. \tag{2.41}$$

and annihilation

$$R^p_{out}(\omega, \omega', \mu) = R^p_{in}(\omega, \omega', \mu)e^{(\omega+\omega')/T} \equiv R^p(\omega, \omega', \mu). \tag{2.42}$$

For use in the moment formalism, R must be expanded in terms of the Legendre polynomials as

$$R(\omega, \omega', \mu') = \sum_{l=0}^{\infty} R_l(\omega, \omega') P_l(\mu'). \tag{2.43}$$

The distribution function, f, is also expanded in a similar way. In general, this results in integrals of the form

$$\begin{aligned} F_{klmn} = & \int_{-1}^{1} d\mu \int_{-1}^{1} d\mu' \int_{0}^{2\pi} d\phi' P_k(\mu') P_l(\mu) P_m(\mu) \\ & \times P_n(\mu\mu' - \sqrt{1-\mu^2}\sqrt{1-\mu'^2}\cos\phi') \\ = & \ 2\pi \tfrac{\delta_{kn}}{2n+1} I_{lmn}. \end{aligned} \tag{2.44}$$

where $I_{lmn} = \int_{-1}^{1} d\mu P_l(\mu) P_m(\mu) P_n(\mu)$. For a more detailed description of such an expansion, see Mezzacappa & Bruenn (1993).

Using this expansion, the scattering contribution to the source term is given by

$$\begin{aligned} s_s^l = & \ \frac{4\omega^3}{(2\pi)^4} B_l \int d\omega' \omega'^2 \\ & \times \left\{ \frac{R_l^s f_l'}{(2l+1)^2} e^{-(\omega-\omega')/T} - \frac{R_0^s f_l}{2l+1} \right. \\ & \left. + \frac{1}{2} \sum_{m,n=0}^{\infty} R_n^s f_n' f_m \frac{I_{lmn}}{2n+1} \left(1 - e^{-(\omega-\omega')/T}\right) \right\}, \end{aligned} \tag{2.45}$$

and the pair annihilation contribution is given by

$$\begin{aligned} s_p^l = & \ \frac{4\omega^3}{(2\pi)^4} B_l \int d\omega' \omega'^2 e^{-(\omega+\omega')/T} \\ & \times \left\{ R_0^p \delta_{0l} - \frac{R_0^p f_l}{2l+1} - \frac{R_l^p \bar{f}_l'}{(2l+1)^2} \right. \\ & \left. + \frac{1}{2} \sum_{m,n=0}^{\infty} R_n^p f_m \bar{f}_n' \frac{I_{lmn}}{2n+1} \left(1 - e^{(\omega+\omega')/T}\right) \right\}. \end{aligned} \tag{2.46}$$

Clearly, all of the moments are coupled to all of the other moments by the source terms in addition to the coupling present on the LHS of the moment equations. Practically, this series must be truncated at some finite order. It is standard to use only the zeroth and first moment (Burrows et al. 2006). This convention is followed, but with the caveat that this may not be a good approximation for the annihilation terms near the free streaming regime (Pons et al. 1998).

2.2.3.1 Zeroth Order Source Function

Now the three contributions to the source functions for the number and energy group equations are considered separately. Special attention is given to assuring that the chosen forms for the source terms *explicitly* push the neutrinos towards equilibrium, independent of the chosen opacity functions.

The absorption part of the source function is given by

$$S^0_{a,g} = \left\langle \frac{1}{\lambda^*_a} \right\rangle_g [G_g - N_g] \,, \tag{2.47}$$

and

$$Q^0_{a,g} = \left\langle \frac{1}{\lambda^*_a} \right\rangle_g [B_g - E_g] \,, \tag{2.48}$$

where

$$B_g = \int_{\omega^g_L}^{\omega^g_U} d\omega \frac{2\omega^3}{(2\pi)^2} \frac{1}{e^{(\omega-\mu_{\rm eq})/T}+1}, \tag{2.49}$$

and

$$G_g = \int_{\omega^g_L}^{\omega^g_U} d\omega \frac{2\omega^2}{(2\pi)^2} \frac{1}{e^{(\omega-\mu_{\rm eq})/T}+1}. \tag{2.50}$$

The average over the inverse absorption mean free path can be performed in a number of ways. For small enough energy intervals for groups, the mean free path for the central energy of the group can be taken. It can also be assumed that the energy within a group is distributed as in a blackbody, but renormalized

to the total energy within the group. Then the averaged inverse mean free path is analogous to the Planck mean opacity, but using a Fermi-Dirac distribution instead of a Planck distribution. Independent of the averaging procedure chosen, this term serves to push the neutrino energy density towards equilibrium with the background medium.

To find the scattering contribution to the zero order moment equation, it is assumed that the distribution of energy within a particular energy group is proportional to the blackbody distribution. Using this ansatz in equation 2.45 and then averaging over group energies gives scattering term

$$\begin{aligned} S^0_{s,g} = \sum_{g'} & \Phi^s_{0,gg'} N_{g'} \left(\frac{D_{g'}}{G_{g'}} - 1 \right) (D_g - N_g) \\ & - \Phi^s_{0,gg'} N_g \left(\frac{D_g}{G_g} - 1 \right) (D_{g'} - N_{g'}) \\ & + \Phi^s_{1,gg'} F_g F_{g'} \left(\frac{D_g}{G_g} - \frac{D_{g'}}{G_{g'}} \right), \end{aligned} \tag{2.51}$$

and

$$\begin{aligned} Q^0_{s,g} = \sum_{g'} & \Phi^s_{0,gg'} N_{g'} \left(\frac{D_{g'}}{G_{g'}} - 1 \right) (C_g - E_g) \\ & - \Phi^s_{0,gg'} E_g \left(\frac{C_g}{B_g} - 1 \right) (D_{g'} - N_{g'}) \\ & + \Phi^s_{1,gg'} H_g F_{g'} \left(\frac{C_g}{B_g} - \frac{D_{g'}}{G_{g'}} \right), \end{aligned} \tag{2.52}$$

where

$$C_g = \int_{\omega^g_L}^{\omega^g_U} d\omega \frac{2\omega^3}{(2\pi)^2}, \text{ and } D_g = \int_{\omega^g_L}^{\omega^g_U} d\omega \frac{2\omega^2}{(2\pi)^2}.$$

The averaged scattering kernel is defined as

$$\Phi^s_{l,gg'} = \left\langle R_l(\omega, \omega') e^{-(\omega - \mu_{\nu,\mathrm{eq}})/T} \right\rangle_{\Delta E_g, \Delta E_{g'}}, \tag{2.53}$$

where the average is taken over the energies of the incoming and outgoing groups. This has the useful property $\Phi^s_{l,gg'} = \Phi^s_{l,g'g}$, which derives from the detailed balance criterion given above. This form of the scattering source term naturally conserves neutrino number, although it does not push the neutrino numbers toward the expected distribution for a purely scattering process. Both source terms go to zero when neutrinos are in both chemical and energy equilibrium with the medium. The energy exchange expression does not go to zero when $g' = g$. Although it might be naively assumed that this corresponds to elastic scattering and therefore not contribute to the evolution of the group energy, there are in fact contributions from small energy transfer scatterings to this term as well. Although these will conserve neutrino number within the group, they can result in energy exchange with the medium. This allows the formalism to somewhat naturally deal with energy transfer due to scattering off nucleons, which generally exchanges energy on a scale that is smaller than the group spacing. The weighting function for the average over the groups necessarily involves some level of approximation. The natural incorporation of equilibrium far outweighs the small error introduced due to the approximate weighting of the scattering kernel.

Using a similar procedure to the one used for the scattering source term, the energy integrated pair production/annihilation source term is given by

$$\begin{aligned} S^0_{p,g} = &\sum_{g'} \Phi^p_{0,gg'} \left(D^0_{g'} - \bar{N}_{g'}\right)\left(D^0_g - N_g\right) \\ -&\Phi^p_{0,gg'} N_g \bar{N}_{g'} \left(D^0_{g'}/\bar{G}_{g'} - 1\right)\left(D^0_g/G_g - 1\right) \\ &+\Phi^p_{1,gg'} F_g \bar{F}_{g'} \left(1 - e^{(\omega+\omega')/T}\right), \end{aligned} \tag{2.54}$$

where the over bar denotes the energy density and flux of a neutrinos anti-species. This term once again naturally goes to zero when thermal equilibrium is reached

(i.e. when $N_g = G_g$ and $F_g = 0$). Here,

$$\Phi^p_{i,gg'} = \left\langle e^{-(\omega+\omega')/T} R^p_i(\omega,\omega') \right\rangle_{\Delta E_g, \Delta E_{g'}}. \tag{2.55}$$

The source term Q^1_p can be obtained from the above equation by the replacements $F_g \rightarrow H_g$, $N_g \rightarrow E_g$, $D_g \rightarrow C_g$, and $G_g \rightarrow B_g$, while leaving the g' terms unchanged.

2.2.3.2 First Order Source Function

For the first order source function terms, one does not need to be as careful about getting forms that explicitly go to zero in equilibrium as all terms end up being proportional to the first order distribution function and therefore satisfy this constraint automatically.

The absorption contribution to the first order source function is

$$S^1_a = -F_g \left\langle \frac{1}{\lambda^*_a} \right\rangle_g, \tag{2.56}$$

and

$$Q^1_a = -H_g \left\langle \frac{1}{\lambda^*_a} \right\rangle_g. \tag{2.57}$$

The scattering source term in equation 2.28 is

$$\begin{aligned} S^1_s = \sum_{g'} \Phi^s_{0,gg'} F_g \left[N_{g'} \left(\frac{D_g}{G_g} - \frac{D_{g'}}{G_{g'}} \right) - D_{g'} \left(\frac{D_g}{G_g} - 1 \right) \right] \\ + \frac{\Phi^s_{1,gg'}}{3} F_{g'} \left[N_g \left(\frac{D_g}{G_g} - \frac{D_{g'}}{G_{g'}} \right) + D_g \left(\frac{D_{g'}}{G_{g'}} - 1 \right) \right]. \end{aligned} \tag{2.58}$$

The source term Q^1_s can be obtained from the above equation by the replacements $F_g \rightarrow H_g$, $N_g \rightarrow E_g$, $D_g \rightarrow C_g$, and $G_g \rightarrow B_g$, while leaving the g' terms unchanged. When scattering is iso-energetic, this reduces to

$$\begin{aligned} S^1_{s,\text{iso-en}} &= -F_g \frac{2\omega^2}{(2\pi)^2} \left[\tilde{R}^s_0(\omega) - \tilde{R}^s_1(\omega)/3 \right] \\ &\equiv -H_g \left[\chi^s_0(\omega) - \chi^s_1(\omega)/3 \right] \end{aligned} \tag{2.59}$$

where $\tilde{R}_l^s$ is the iso-energetic scattering kernel.

The first order moment equation pair annihilation source term is

$$S_p^1 = \sum_{g'} \Phi_{0,gg'}^p F_g \left[\bar{N}_{g'} \left(1 - e^{\beta(\omega+\omega')} \right) - D_{g'}^0 \right] + \frac{\Phi_{1,gg'}^s}{3} \bar{F}_{g'} \left[N_g \left(1 - e^{\beta(\omega+\omega')} \right) - D_g^0 \right], \tag{2.60}$$

and Q_p^1 can be found the same replacement required to find S_s^1 from Q_s^1.

2.3 Formal Solution of the Boltzmann Equation

To get the factors g_2 and g_3, an angle dependent version of the Boltzmann equation needs to be solved. First, note that the outer layers of the PNS are in tight radiative equilibrium throughout the duration of the simulation. Therefore, all time dependence can be reasonably dropped in the equation of radiative transfer if one is only interested in the ratios of various moments. Of course, such an approximation breaks down in highly dynamical situations. For such circumstances, a closure scheme like the one described in Rampp & Janka (2002) is more appropriate. This time-independent formulation of the formal solution, which makes calculation of the Eddington factors significantly easier, is similar to the approach advocated by Ensman (1994), except that it incorporates general relativistic affects, such as the bending of geodesics. Schinder & Bludman (1989) describe a similar, but time-dependent formulation.

In a spherically symmetric static spacetime, the equation of radiative transfer

is (Lindquist 1966)

$$\Gamma\left[\mu\frac{\partial}{\partial r}+(1-\mu^2)\left\{\frac{1}{r}-\frac{\partial\phi}{\partial r}\right\}\frac{\partial}{\partial\mu}\right]f(\nu,\mu,r)$$
$$=\frac{1}{\lambda_a^*}\left[f_{eq}(r)-f(\nu,\mu,r)\right]$$
$$+j_s[f](1-f(\nu,\mu,r))-\lambda_s^{-1}[f]f(\nu,\mu,r). \tag{2.61}$$

Here, the neutrino distribution function, f, has been written in terms of the energy of the neutrinos at infinity, ν, and μ is the cosine of the angle of neutrino propagation relative to the radial vector.

A formal solution to equation 2.61 can easily be found using the method of characteristics. The characteristic equations are

$$d\lambda\equiv\frac{dr}{\Gamma\mu}=\frac{d\mu}{\Gamma(1-\mu^2)(1/r-\frac{\partial\phi}{\partial r})}=df\Big/\left(\frac{df}{d\lambda}\right)_{coll} \tag{2.62}$$

where λ is the physical path length. The second equality is easily integrated to find a relationship between r and μ along a geodesic. Any geodesic can be characterized by the radius at which $\mu=0$. First, define the quantity

$$\beta=r_m e^{-\phi_m}, \tag{2.63}$$

where the subscript m denotes the minimum radius of propagation. This is just the impact parameter of the trajectory. Then, for a given β and r, the angle of propagation along a geodesic is given by

$$\mu=\pm\sqrt{1-\left(\frac{\beta e^{\phi}}{r}\right)^2}. \tag{2.64}$$

The first equality in the characteristic equations can be integrated to find the physical path length between any two radii for a particular characteristic if Γ and ϕ are assumed constant over this distance, giving

$$\Delta\lambda\approx\pm\Gamma^{-1}\left[\sqrt{r_f^2-e^{2\phi}\beta^2}-\sqrt{r_i^2-e^{2\phi}\beta^2}\right], \tag{2.65}$$

where the plus sign is for $r_f > r_i$ and the minus sign otherwise. This form is consistent with the assumption of constant metric functions across zones (as is used in the actual code), but it can introduce difficulties when a trajectory moves from one zone to another near the radius of minimum propagation.

Clearly, equation 2.61 is a non-linear integro-differential equation due to the functional dependence of the scattering terms on the local distribution function. An approximate solution to the Lindquist equation is desired were the solutions along characteristics are decoupled and the formal solution can be directly integrated. The simplest approximation is to just to make the replacement $f \rightarrow f_{eq}$ in the scattering terms. This approximation will only be valid at high optical depth and is therefore suspect for use in the decoupling region. The next order approximation is to use a distribution function inferred from our knowledge of E_g and H_g. Assuming that the energy is distributed within a group as within a blackbody gives

$$\begin{aligned} \hat{f}_0(\nu, r) &= f_{\rm eq}(\nu, r)\frac{E_g}{B_g}, \\ \hat{f}_1(\nu, r) &= 3 f_{\rm eq}(\nu, r)\frac{H_g}{B_g}. \end{aligned} \tag{2.66}$$

Employing the Legendre expansion of the scattering kernel, integrating over outgoing neutrino angle, and only including the elastic scattering contribution gives the scattering source and sink terms

$$\begin{aligned} j_s(\omega, \mu) &= \frac{2\omega^2}{(2\pi)^2}\sum_{l=0}^{\infty}\frac{1}{2l+1}P_l(\mu)\tilde{R}^s_l(\omega)\hat{f}_l(\omega) \\ &\approx f_{\rm eq}(\omega)\left\{\chi^s_0(\omega)\frac{E_g}{B_g} + \mu\chi^s_1(\omega)\frac{H_g}{B_g}\right\} \end{aligned} \tag{2.67}$$

and

$$\lambda_s^{-1}(\omega, \mu) = \chi^s_0(\omega) - j_s(\omega, \mu). \tag{2.68}$$

Using the last characteristic equation, the solution of the linearized Boltzmann equation is

$$\begin{aligned} f(\nu,\beta,r_f) \quad &= f(\nu,\beta,r_i)e^{-\tau(r_i,r_f)} \\ &+e^{-\tau(r_i,r_f)}\int_{r_i}^{r_f}\frac{dr}{\Gamma\mu}e^{\tau(r_i,r)}\left\{j_s+f_{eq}/\lambda_a^*\right\}, \end{aligned} \tag{2.69}$$

where the optical depth is

$$\tau(r_i,r_f)=\int_{r_1}^{r_2}\frac{dr}{\Gamma\mu}(1/\lambda_a^*+\chi_0^s). \tag{2.70}$$

This has the appealing property that there is no coupling between different βs and νs, so the evolution of the distribution function along each path in phase space can be solved for independently.

2.4 Numerical Implementation

Aside from the equation of state and neutrino opacities for dense matter, PNS evolution is described by the transport equations 2.28, 2.29, 2.30, 2.31, 2.32, and 2.33 and the structure equations 2.5, 2.6, 2.7, 2.3, and 2.8. These describe the evolution of the dependent variables $y(a,t)=\{r,u,m,\phi,n_B,T,Y_e,F_g,N_g,E_g,H_g\}$. To solve these equations numerically, the variables $\{a_{i+1/2},r_{i+1/2},u_{i+1/2},m_{i+1/2},F_{g,i+1/2},H_{g,i+1/2}\}$ are discretized on zone edges while the variables $\{\phi_i,n_{B,i},T_i,Y_{e,i},N_{g,i},E_{g,i}\}$ are discretized on zone centers. The derivatives in the PNS evolution equations are then finite differenced, turning them to algebraic equations for the above dependent variables. This is the most natural choice for discretizing the above equations, because the thermodynamic quantities, neutrino number density, and neutrino energy density are defined on zone centers while the neutrino number and energy

fluxes are defined across zone edges which results in internal energy and lepton number conservation being made explicit in the discretized equations.

The general form of these algebraic equations is then

$$\mathcal{G}\left(y_{i-1}^{n,n+1}, y_i^{n,n+1}, y_{i+1}^{n,n+1}\right) = \mathcal{T}(y_i^n, y_i^{n+1})$$
$$+(1-\theta)\,\mathcal{Y}\left(y_{i-1}^n, y_i^n, y_{i+1}^n\right) + \theta\,\mathcal{Y}\left(y_{i-1}^{n+1}, y_i^{n+1}, y_{i+1}^{n+1}\right) = 0, \tag{2.71}$$

where n is the current time, at which the dependent variables are known, and $n+1$ is the next time step at which the dependent variables are desired. Here, $\mathcal{T}$ denotes the differenced time derivatives and $\mathcal{Y}$ denotes the rest of the terms. I choose to employ a fully implicit method for solving these equations, i.e. $\theta = 1$. This leaves a set of non-linear algebraic equations that must be solved to find the values of the dependent variables at time step $n+1$.

These equations are solved by standard high-dimensional Newton-Raphson (NR) techniques (Press et al. 1992). This requires calculating derivatives of all the functions g with respect to y. These derivatives are calculated analytically. Due to the number of derivatives, such an undertaking is prone to error. Therefore, all derivative functions are checked against numerical derivatives by automated software before they are included in the actual evolution code. The NR updates are given by the solution of an $N_z \times (6+2N_gN_s)$ -by-$N_z \times (6+2N_gN_s)$ matrix, where N_z is the number of radial zones, N_g is the number of neutrino energy groups, and N_s is the number of included neutrino species. This can rapidly become quite large for reasonable zoning and number of energy groups, and become too slow for dense matrix techniques. Luckily, the matrix involved is in fact block-diagonal, as each zone is only coupled to its neighboring zones, which significantly reduces computational time compared to solving a general dense matrix.

Although the equations are formally non-linear, they are sufficiently close to

linear that NR iteration results in good convergence after a small number of iterations. It is generally demanded that the average relative deviation of the solution from zero is at least less than one part in a thousand. Often, the solution found by NR iteration satisfies the equations to close to machine precision. This scheme has been implemented using object-oriented `FORTRAN2003`. The block diagonal matrix equations are solved using the software package `LAPACK` (Anderson et al. 1999).

To save computational time, the equations are solved using only the neutrino number equations and approximating the neutrino energy densities and fluxes using $E_g \approx \langle\omega\rangle_g N_g$. Once this set of equations is satisfied, a correction step is taken using the energy groups instead of the number groups. This approximation does not seem to introduce any significant error into the calculation. It is found that the total neutrino energy loss calculated using the approximation $E_g \approx \langle\omega\rangle_g N_g$ differs from the actual neutrino energy loss by around one part in a thousand when thirty energy groups are used. The code conserves lepton number to machine precision because lepton number conservation is explicitly enforced by equation 2.33. Conservation of total energy is not explicitly enforced. It is found that the total change in rest mass over the simulation agrees with the total neutrino energy lost to within a few percent. A series of test problems are performed with the code in Appendix 2.8.

2.4.1 Equation of State

To close the transport and structure equations described above, an equation of state is required relating the pressure, energy density, and equilibrium neutrino chemical potential to n_B, T, and Y_e. Additionally, accurate derivatives of these

quantities are required for calculation of the Jacobian matrix for NR iteration. Calls to the equation of state must also be computationally efficient. To meet these requirements, the equation of state is implemented in a tabular form. The Helmholtz free energy per baryon, $F = \epsilon - sT$, is tabulated as a function of n_B, T, and Y_e, as well as derivatives with respect to these variables up to second order. A bi-quintic interpolation is then used to get values of the free energy and its derivatives between grid points (Timmes & Swesty 2000). This guarantees that the thermodynamic functions will be smooth in the independent variables, thermodynamically consistent (Swesty 1996), and does not introduce problems in the calculation of the NR corrections.

The differential of the Helmholtz free energy is

$$\begin{aligned} dF &= -sdT + \frac{p}{n_B^2} dn_B + \sum_i \mu_i dY_i \\ &= -sdT + \frac{p}{n_B^2} dn_B + (\mu_e + \mu_p - \mu_n) dY_e. \end{aligned} \tag{2.72}$$

From this, the required thermodynamic quantities can be read off:

$$\begin{aligned} p = n_B^2 \left(\frac{\partial F}{\partial n_B} \right)_{T,Y_e}, \; s = -\left(\frac{\partial F}{\partial T} \right)_{n_B,Y_e}, \\ \text{and } \mu_{\nu_e,\text{eq}} \equiv (\mu_e + \mu_p - \mu_n) = \left(\frac{\partial F}{\partial Y_e} \right)_{n_B,T}. \end{aligned} \tag{2.73}$$

2.4.2 Neutrino Opacities

The group averaged neutrino opacities are calculated using a ten point quadrature over each group to find an effective Planck mean opacity for the absorption terms in each group. The scattering and annihilation kernels which couple the groups, $\Phi_{g,g'}$, are calculated using a five point quadrature over both the incoming and outgoing energies. Detailed balance is exploited to halve the number of

calculations required. The scattering terms are not weighted by a local thermal neutrino distribution.

2.4.3 Integration of the Formal Solution

The formal solution to the static Boltzmann equation is calculated at the beginning of every time step and the Eddington factors enter the moment transport equations explicitly. Because time independent transport is assumed, no previous knowledge of the distribution functions is required and a new grid of impact parameters can be chosen at any time step, without having to worry about remapping old solutions as in Rampp & Janka (2002).

If all quantities are assumed to be constant across zones, the formal solution (equation 2.69) can easily be integrated, giving

$$f(\nu, \mu_s, r_{i+1/2}) = f(\nu, \mu_s, r_{i-1/2})e^{-\Delta\tau_i} + \Delta f_0 + \Delta f_1 \tag{2.74}$$

for the change in f across zone i.

The physical path length across the zone, $\Delta\lambda_i$, is given by equation 2.65 and the optical depth across the zone is

$$\Delta\tau_i = \Delta\lambda_i(1/\lambda_a^* + \chi_0^s). \tag{2.75}$$

The additions to the neutrino beam from the medium and scattering from other beams are given by

$$\Delta f_0 = f_{\rm eq}\frac{1/\lambda_a^* + \frac{E_g}{B_g}\chi_0^s}{1/\lambda_a^* + \chi_0^s}(1 - e^{-\Delta\tau_i}), \tag{2.76}$$

and

$$\Delta f_1 = f_{\rm eq}\chi_1^s\frac{H_g}{B_g}e^{-\Delta\tau_i}\int_0^{\Delta\lambda_i} d\lambda\mu(\lambda)e^{\lambda(1/\lambda_a^* + \chi_0^s)}. \tag{2.77}$$

The integral required for Δf_1 cannot be calculated analytically because $\mu(\lambda)$ is a fairly complicated function. As this is a subdominant term, an "average" μ can be pulled out of the integral (which is allowable if μ does not change much across the zone). This gives the approximation

$$\Delta f_1 \approx \mu(r_i, \beta) f_{\rm eq} \chi_1^s \frac{H_g}{B_g} \frac{1 - e^{\Delta\tau_i}}{1/\lambda_a^* + 1/\lambda_s^*}. \tag{2.78}$$

Note that μ changes most rapidly when it is close to zero, but this term contributes the least in that region so the error from this approximation should not be too large.

Numerically, there is a problem with this formulation as it stands. Assume that a trajectory in zone i is close to its minimum radius of propagation, $\mu > 0$, and that it is close to a zone boundary. It then propagates to the zone boundary and is considered to be in zone $i+1$. Because ϕ is increasing with radius, $\phi_{i+1} > \phi_i$. The new radius is taken to be $r_{L,i+1}$, so that the new angle of propagation is

$$\mu_n = \sqrt{1 - \left(\frac{r_m e^{\phi_{i+1} - \phi i}}{r_{L,i+1}}\right)^2}, \tag{2.79}$$

$e^{\phi_{i+1}-\phi i} > 1$, and $r_m \approx r_{L,i+1}$. Since, μ_n must be real, it becomes ill defined. In practice this problem is overcome setting μ to zero if it would have been imaginary.

Starting from the outer boundary of the computational grid, these equations are solved along an inward going characteristic, through the radius of minimum propagation, and then along the outward going characteristic for each tangent ray. The impact parameters of the tangent ray grid are chosen to be equally spaced in radius for the calculations described in this paper. Once the distribution function for a particular energy at infinity has been calculated along tangent rays, moments of the distribution function at radii r_i are calculated from a weighted sum that reduces to the correct limit if the distribution function is locally constant in angle.

Angular resolution is reduced at larger depths in the star. Because the distribution is extremely close to isotropy and $g_2 \approx g_3 \approx 0$, this does not pose a significant problem for PNS evolution.

2.4.4 Boundary Conditions

To close the system of transport equations, boundary conditions for the surface fluxes H_g and F_g are required. For this boundary condition, the formal solution is used to calculate the factors

$$\alpha_g = \frac{\int_{-1}^{1} d\mu \mu f(r, \mu, \nu_g)}{\int_{-1}^{1} d\mu f(r, \mu, \nu_g)}, \tag{2.80}$$

so that $F_{g,\text{bound}} = \alpha_g N_g$ and $H_{g,\text{bound}} = \alpha_g E_g$ in the final zone. At the inner edge of the computational grid, incident fluxes are specified (for PNS evolution, they are of course specified to be zero).

The boundary conditions for the radius, gravitational mass, velocity, and pressure are implemented by including a fixed ghost zone at the inner and outer boundaries. The boundary condition for the metric potential ϕ is given by matching to the Schwarzschild vacuum solution to the Einstein equations at the outer boundary. This gives $\phi_s = \log(\Gamma_s)$.

2.4.5 Rezoning

To maintain reasonable spatial resolution, conservative post time step regridding is employed. Where conservation laws do not specify the properties of a new zone, piecewise linear interpolation is used. This generally results in smooth radial dependence of the fluid quantities. The implementation is similar to the method used in `Kepler` (Weaver et al. 1978).

The re-gridding is driven by gradients in the density and radius. Generally, the radius is not allowed to vary by more than 5% between zones and the density is allowed to vary by no more than 20%. This generally results in approximately 100-150 zones being on the grid. The choice of relative density changes places high resolution in regions where neutrino decoupling is occurring.

2.4.6 Red Shifting Terms

Due to red and blue shifting between groups, equations 2.28, 2.29, 2.30 and 2.31 contain the un-integrated moments w^i. Therefore, an approximation method for these moments is required. When integrated over all energies, these terms go to zero. Therefore, any chosen numerical scheme must have terms balancing between groups for energy conservation. To move forward, something must be assumed about how energy is distributed in the groups. The simplest scheme is to assume that it is uniform. Then within a particular group $w^{0,1} = \{N_g, F_g, E_g, H_g\}/(\omega_{g,H} - \omega_{g,L})$. It could also be assumed that the internal energy is distributed as a black body, which is consistent with the assumption used in the source terms. The uniform distribution is chosen due to its simplicity. For the H_g evolution equation, this results in

$$\begin{aligned} &-\omega_{g,U}\left[\left(\tfrac{\Theta}{3}+\tfrac{2}{5}\sigma+g_3\tfrac{3}{2}\sigma-e^{-\phi}\tfrac{\partial\phi}{\partial t}\right)\left(\tfrac{H_g}{2\Delta\omega_g}+\tfrac{H_{g+1}}{2\Delta\omega_{g+1}}\right)\right] \\ &+\omega_{g,L}\left[\left(\tfrac{\Theta}{3}+\tfrac{2}{5}\sigma+g_3\tfrac{3}{2}\sigma-e^{-\phi}\tfrac{\partial\phi}{\partial t}\right)\left(\tfrac{H_{g-1}}{2\Delta\omega_{g-1}}+\tfrac{H_g}{2\Delta\omega_g}\right)\right]. \end{aligned} \tag{2.81}$$

Similar expressions result for equations 2.28, 2.29, and 2.30. It is straight forward to verify that these terms disappear when summed over groups.

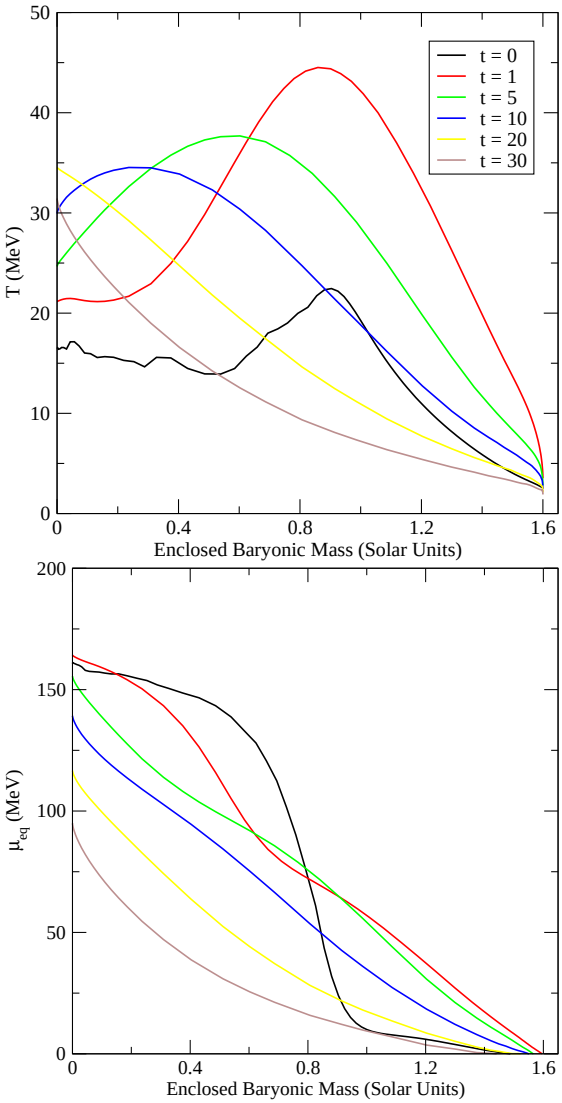
t = 0
t = 1
t = 5
t = 10
t = 20
t = 30
T (MeV)
Enclosed Baryonic Mass (Solar Units)
μeq (MeV)
Enclosed Baryonic Mass (Solar Units)

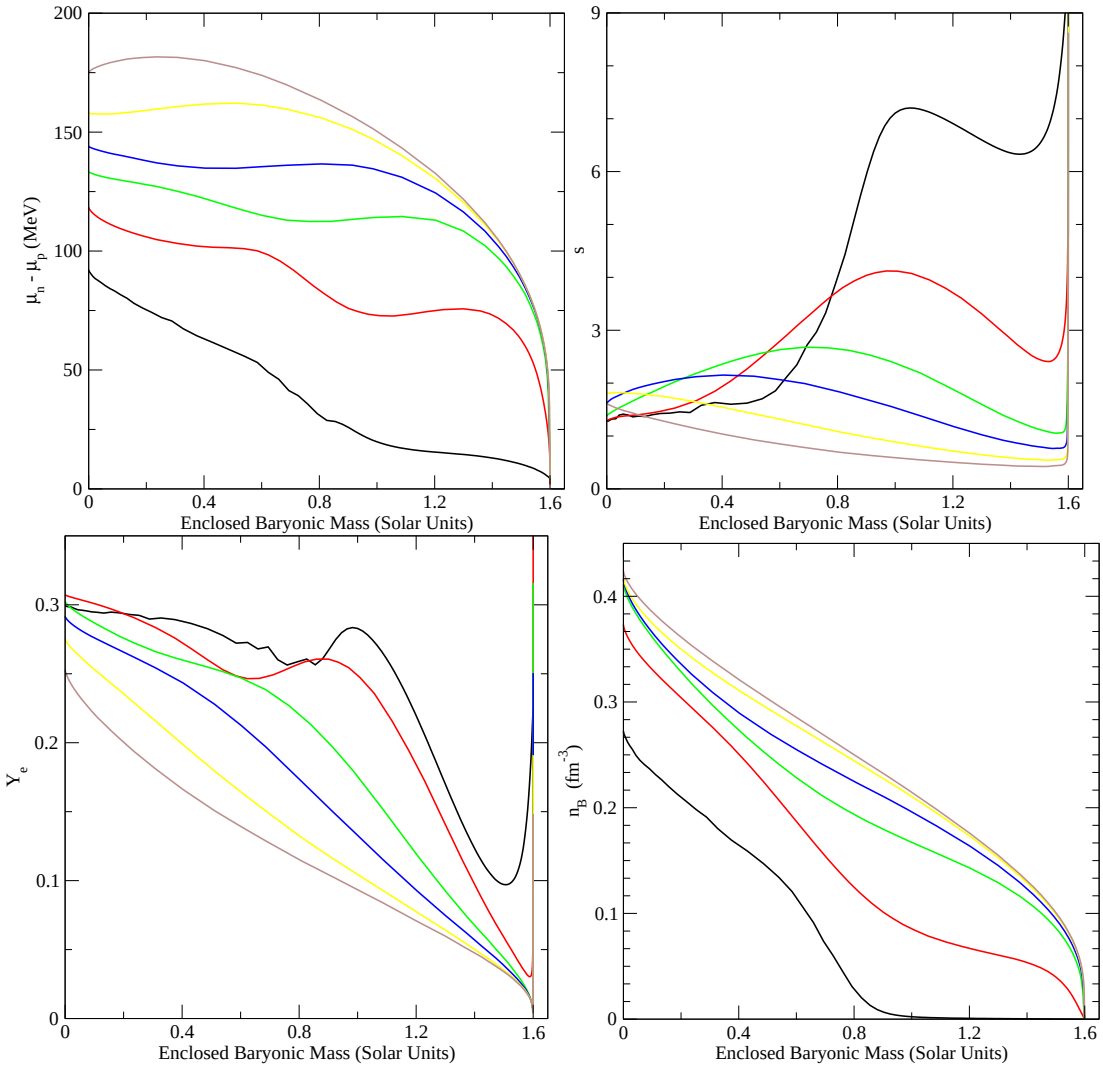

Figure 2.1: The internal structure of the PNS for selected times in the fiducial simulation. The temperature, equilibrium electron neutrino chemical potential, proton neutron chemical potential difference, dimensionless entropy per baryon, electron fraction, and baryon density are plotted at times 0 s, 1 s, 5 s, 10 s, 20 s, and 30 s, from left to right and top to bottom. The horizontal axes show the enclosed baryon number in units of the number of baryons in the sun ($N_\odot \equiv 12.04 \times 10^{56}$). This figure can be directly compared to figure 9 of Pons, et al. (1999), as it was produced using the same initial model and a very similar nuclear equation of state and neutrino opacity set.

2.5 Proto-Neutron Star Evolution

Rather than follow the collapse of a massive stellar core through bounce, the calculations here start from a separate calculation of the highly dynamic phase of initial collapse. For ease of comparison with previous work, the $1.6\,M_{\odot}$ baryonic mass initial model from Pons et al. (1999) is employed and the affects of convection are not considered. This will correspond to a $1.4\,M_{\odot}$ gravitational mass neutron star after it has cooled and can be thought of as representative of a standard neutron star (Kiziltan et al. 2010). The cooling and de-leptonization of this object is followed for 55 seconds, which is shortly after the time the PNS becomes optically thin.

2.5.1 Physical Ingredients

A relativistic mean field of equation of state consisting of only neutrons, protons, and electrons is assumed. The GM3 parameter set is used without hyperons (Glendenning & Moszkowski 1991), which is what was used in Pons et al. (1999). Neutrino opacities are also calculated in the relativistic mean field approximation using the formalism of Reddy et al. (1998). The tensor polarization is also included so that "weak magnetism" affects are included to all orders (Horowitz & Pérez-García 2003). The electron scattering rates from Yueh & Buchler (1977) are used for the inelastic scattering kernels. Nucleon scattering is assumed to occur within a single group, although the opacities are calculated using the full inelastic differential cross-sections. Bremsstrahlung is implemented using the structure function given in Hannestad & Raffelt (1998). Rather than include this in the annihilation kernels, the Bremsstrahlung mean free path has been calculated assuming a thermal distribution for the secondary neutrinos. Given the uncertainty

in the Bremsstrahlung rate itself and its large density dependence, this is a reasonable approximation. Electron positron pair annihilation (Bruenn 1985) is also included. Pure neutrino processes (i.e. $\nu_e + \bar{\nu}_e \rightarrow \nu_\tau + \bar{\nu}_\tau$) are not included. This set of rates is fully consistent with the rate set used in Pons et al. (1999), but differs significantly from the rate sets used in recent collapse simulations (Hüdepohl *et al.* 2010, Fischer et al. 2011).

The study here uses 30 logarithmically spaced energy groups from 2 MeV to 75 MeV plus one final group extending from 75 MeV to 1000 MeV to encompass the tail of the thermal distribution. This final group is only populated deep in the PNS and it is in tight thermal equilibrium due to the extremely short mean free paths for such high energy neutrinos. Minimal differences are found in the PNS evolution if only 20 groups are employed to cover the same energy range.

The adaptive radial gridding algorithm is set to keep approximately 130 zones on the grid and allow for at most a 20% change in density across a zone and a 10% change in radius across a zone. The boundary pressure is set so that the outer edge of the model has a density around $2 \times 10^9\,\mathrm{g\,cm^{-3}}$. This is a sufficiently low density that all of the neutrinos have decoupled well within the outer boundary.

2.5.2 Structural Evolution

Qualitatively, the internal structure of the PNS evolution follows the standard picture of Kelvin-Helmholtz PNS cooling as described by Burrows & Lattimer (1986), Keil & Janka (1995), and Pons et al. (1999), where the gravitational binding energy of the compact object provides energy lost to neutrino emission. After the shock produced by the supra-nuclear density bounce of the core propagates through the outer layers of the PNS, a high entropy shocked region is left on top

of a cold un-shocked PNS core, which has an entropy similar to the initial entropy of the pre-supernova iron core. The outer shocked layers have de-leptonized during the ν_e burst, but neutrinos in the core itself have been trapped since before bounce (although partial deleptonization has occurred), resulting in a large non-zero $\mu_{\nu_e,\mathrm{eq}}$ and $Y_e \approx 0.3$ (c.f. Liebendörfer et al. 2001b). This provides the initial condition for PNS cooling.

The internal structure of the PNS simulation is shown in figure 2.1 for a number of times (with time zero corresponding to the starting point of the simulations, not the time of core-bounce). The models start with a core entropy of ~ 1.2. The entropy rises from 1.6 at an enclosed baryonic mass of $\sim 0.6\,M_\odot$ to 7.4 at an enclosed mass of $1.0\,M_\odot$. This implies that the supernova shock was born at around $0.6\,M_\odot$, which is reasonably consistent with the core-collapse results of Thompson et al. (2003). The shocked mantle is at low density relative to the core and extends to large radius (material that is at a density of $10^{-5}\,\mathrm{fm}^{-3}$ is found at 99 km), mainly due to the thermal contribution to the pressure.

From this initial state, the shock heated mantle rapidly contracts over the first second or so of the simulation. This contraction is driven by the rapid loss of energy and lepton number via neutrinos, which can readily escape due to the low density of the envelope and long interaction mean free paths. The loss of lepton number and thermal energy reduces pressure support in the mantle, and the mantle responds by rapidly contracting (i.e., rapid relative to the cooling timescale of the core, not rapid compared to the dynamical timescale of the envelope). By two seconds into the simulation, material at a density of $10^{-5}\,\mathrm{fm}^{-3}$ is at 17 km. This is fairly close to the cold neutron star radius for GM3 (13.5 km). The work provided by this contraction is enough to increase the peak temperature of the mantle from

22 MeV to 45 MeV even though the entropy of the mantle has decreased from 7 to 4 over this period.

This period of the PNS evolution is most likely to be sensitive to the initial conditions for the simulations, as at later times the details of the initial structure should be washed out. The envelope of the PNS should also be convective, which significantly alters the rate of energy and lepton number transport in the PNS (c.f. Roberts et al. 2012). Additionally, there might be significant accretion luminosity over this period (although this is approximately accounted for by the mantle). Therefore, especially given the older provenance of the initial conditions, the results from this period should be taken as only qualitatively correct.

While the mantle is contracting, $\bar{\nu}_e$s and ν_xs are being transported down the positive radial temperature gradient into the core while the ν_es are being transported outwards down the large equilibrium chemical potential gradient. This results in a net heat flux into the core and a net lepton flux out of the core. This has been referred to as "Joule heating" of the core in previous work (Burrows & Lattimer 1986). Additionally, the inner regions contract over this period due to the increased boundary pressure on the un-shocked core from the cooling mantle. This contributes to the temperature increase in the core in addition to the Joule heating.

After the initial period of mantle contraction, the density structure of the PNS becomes similar to that of a cold PNS. Joule heating continues to increase the temperature of the inner most regions until the central temperature reaches its peak value of 35 MeV at 18 s in the simulation. Then, the temperature of the entire star falls with time. The entropy evolution exhibits a similar behavior. Lepton number is lost from the entire PNS core over this time and the electron

fraction evolves toward the expected value for matter in beta-equilibrium with no net electron neutrino number. After about 15 seconds, contraction slows since the PNS is nearly at the cold neutron star radius. After this, neutrino emission is powered chiefly by the loss of thermal energy from the star.

It is also worth noting that the temperature gradient and the $\mu_{\nu_e,\mathrm{eq}}$ gradient in the shocked layers of the PNS become increasingly shallow from 1 s onwards. Additionally, as the density of the outer layers rises, the neutron proton chemical potential difference $\hat{\mu} = \mu_n - \mu_p$ gets larger. The increase in $\hat{\mu}$ and the decrease in $\mu_{\nu_e,\mathrm{eq}}$ bring $\hat{\mu}$ close to the electron chemical potential $\mu_e = \hat{\mu} + \mu_{\nu_e,\mathrm{eq}}$ as time goes on. These considerations have significant consequences for the spectral evolution of the neutrinos and which are discussed in section 2.6.2.

2.5.3 Emergent Luminosity and Spectral Evolution

The total integrated energy loss in neutrinos over the duration of the simulation is $E_\nu = 2.32 \times 10^{53}\,\mathrm{erg}$, and the total lepton number radiated is $N_L = 3.2 \times 10^{56}$. The neutrino emission from the PNS is shown in figure 2.2. As is discussed above, the first couple of seconds are dominated by the contraction of the PNS mantle. Over the first second of the simulation, 38% of the total neutrino energy loss and 20% of the total lepton number loss occurs. During this period, the ν_x number luminosity is produced mainly by the un-shocked core, as the μ and τ neutrinos are mainly coupled to the envelope through scattering. Therefore, the luminosity in these flavors is lower because of the smaller emitting surface (which is not offset by the temperature of the core).

During mantle contraction, there is a high de-leptonization rate driven by the outermost layers of the star. After the first few hundred milliseconds, de-

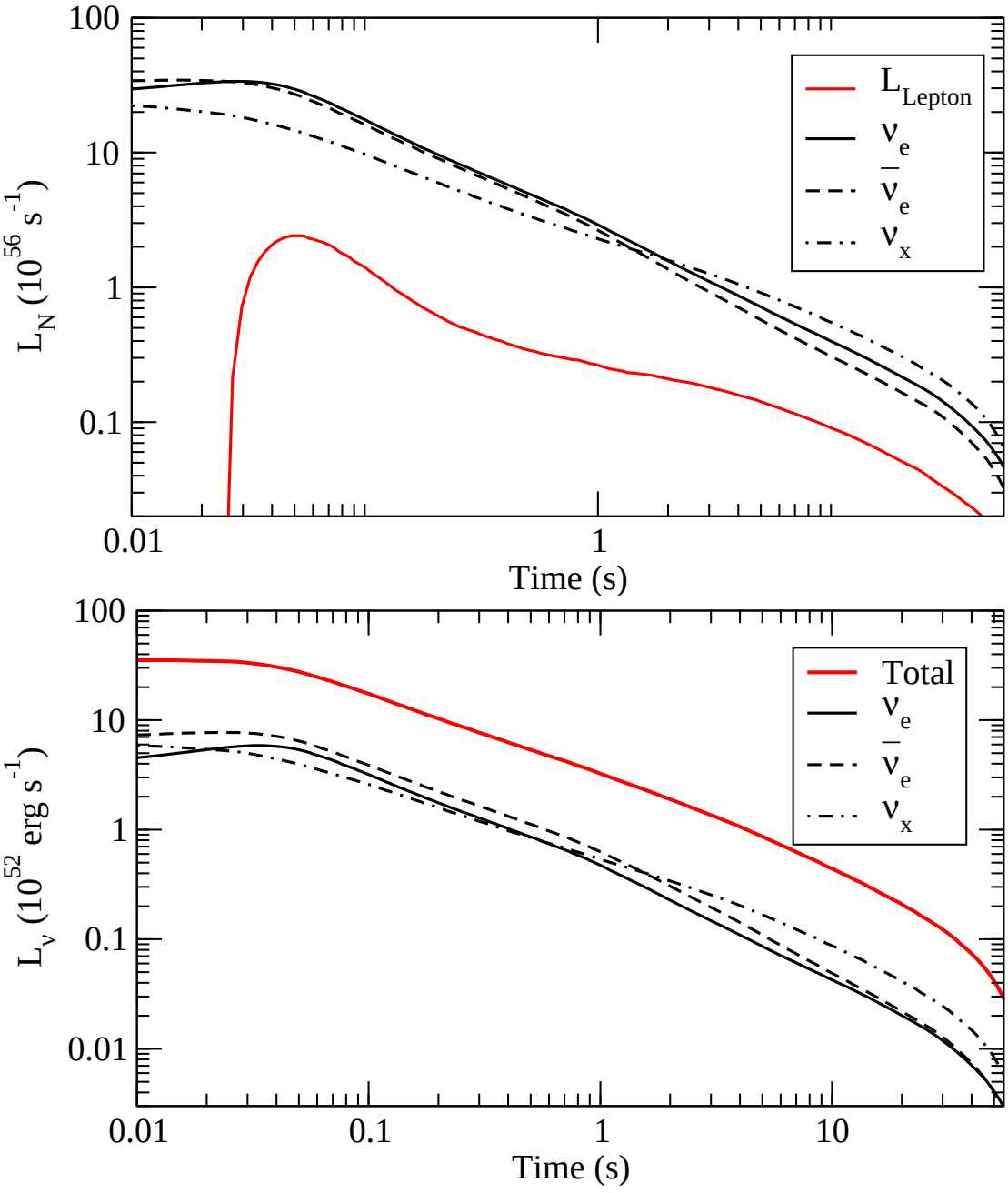

Figure 2.2: Top panel: Number luminosities as a function of time for ν_e (solid black line), $\bar{\nu}_e$ (dashed black line), ν_x (dot-dashed black line) and the de-leptonization rate, $\dot{N}_{\nu_e} - \dot{N}_{\bar{\nu}_e}$. Bottom panel: Energy luminosities as a function of time. The black lines are the same as in the top panel, but the solid red line is the total energy emitted in neutrinos per time.

leptonization slows as the outer layers go towards $\mu_{\nu_e,\mathrm{eq}} \approx 0$ and de-leptonization is driven by diffusion out of the core. The values of the de-leptonization rate before 80 ms are unrealistic, as they are determined by the relaxation of the assumed initial conditions for the neutrinos.

Over the first two seconds, the ν_x luminosities are significantly lower than the luminosities of the electron flavored neutrinos. The neutrino energy and number luminosities as a function of radius at 500 ms after the beginning of the simulation are shown in figure 2.3. First, this illustrates that the μ and τ neutrino number fluxes are being set much further inside the star (at around 18 km) than the electron neutrinos, but they exchange energy out to a significantly larger radius via scattering. Second, there is an inward directed anti-electron, μ and τ flux near the mantle core boundary. As cooling precedes, heat diffuses down the positive temperature gradient (and positive equilibrium chemical potential gradient for the anti-electron neutrinos) into the lower entropy core. This is the Joule heating discussed above. In contrast, the large negative equilibrium chemical potential gradient for the electron neutrinos overwhelms the positive radial temperature gradient and the electron neutrino flux is positive everywhere.

After the PNS has contracted to close to the cold neutron star radius, the ν_x luminosity has increased relative to the ν_e and $\bar{\nu}_e$ luminosities. In fact, the ν_x luminosity is about twice the luminosity in either of the electron neutrino species. These neutrinos decouple further inside the PNS and are therefore emitted at a higher effective temperature, resulting in a larger number and energy luminosity. Between thirty and forty seconds the PNS becomes transparent to neutrinos and the luminosity drops off significantly.

The average energies of the emitted neutrinos at infinity as a function of time

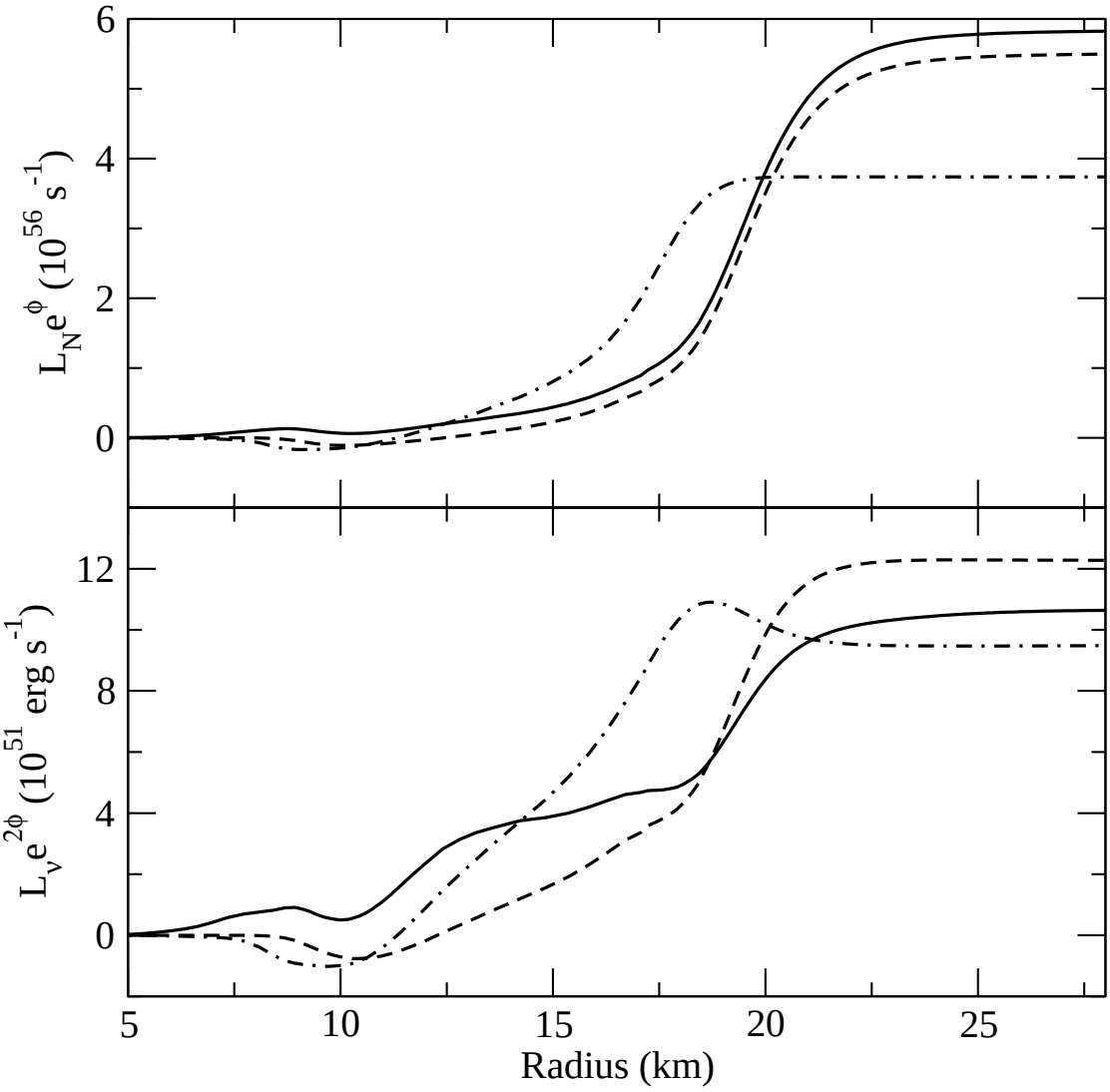

Figure 2.3: Neutrino number and energy luminosities at infinity as a function of radius at 500 ms into the simulation. The solid lines are for electron neutrinos, the dashed lines are for electron antineutrinos, and the dot-dashed lines are for μ and τ neutrinos.

are shown in figure 2.4. Within the integrated energy group formalism, the neutrino energy moments at infinity are defined as

$$\langle \epsilon^n \rangle = e^{n\phi_s} \frac{\sum_g \langle \omega \rangle_g^{n-1} H_g}{\sum_g F_g}, \tag{2.82}$$

where $\langle \omega \rangle_g$ is a group averaged energy and ϕ_s is the surface value of the metric potential.

During the mantle contraction phase, there is the standard hierarchy of neutrino average energies $\langle \epsilon_{\nu_e} \rangle < \langle \epsilon_{\bar{\nu}_e} \rangle < \langle \epsilon_{\nu_x} \rangle$. After mantle contraction has ceased, the energy decoupling radius of electron neutrinos and μ and τ neutrinos becomes similar and for the rest of the PNS evolution $\langle \epsilon_{\bar{\nu}_e} \rangle \approx \langle \epsilon_{\nu_x} \rangle$. This is in contrast to the difference between the electron neutrino and anti-neutrino average energies, which obey $\langle \epsilon_{\nu_e} \rangle < \langle \epsilon_{\bar{\nu}_e} \rangle$ for the entire calculation, although the two average energies get closer at late times. An analysis of why this is, its implications, and a comparison to other results in the literature is given in section 2.6.2.

The emitted neutrino spectra at two representative times are shown in 2.5 for reference. The ν_x neutrinos decouple further in the star than the $\bar{\nu}_e$ neutrinos at five seconds into the simulation so that they have a larger number luminosity due to the larger temperatures found there, but these flavors have a similar energy sphere due to inelastic scattering which accounts for the similar value of the peak of the luminosity as a function of neutrino energy.

2.6 Discussion

2.6.1 Comparison to EFLD

Until recently (Hüdepohl *et al.* 2010, Fischer *et al.* 2010), most studies of PNS cooling used the EFLD approximation to describe neutrino transport (Burrows &

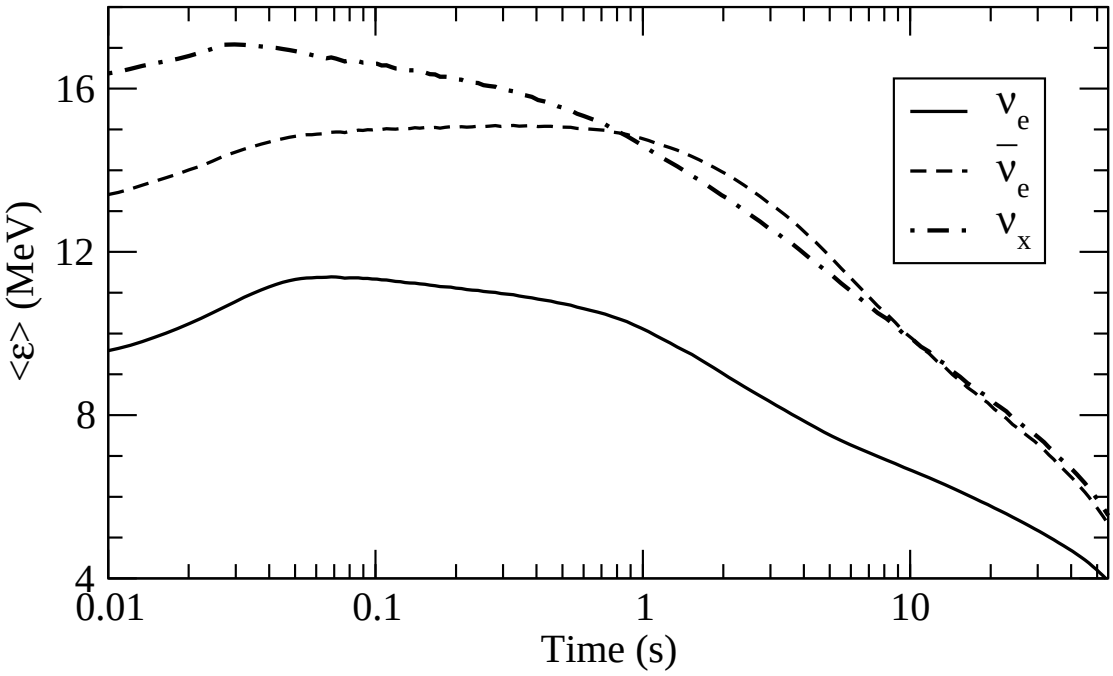

Figure 2.4: Average energies of the emitted neutrinos measured at infinity.

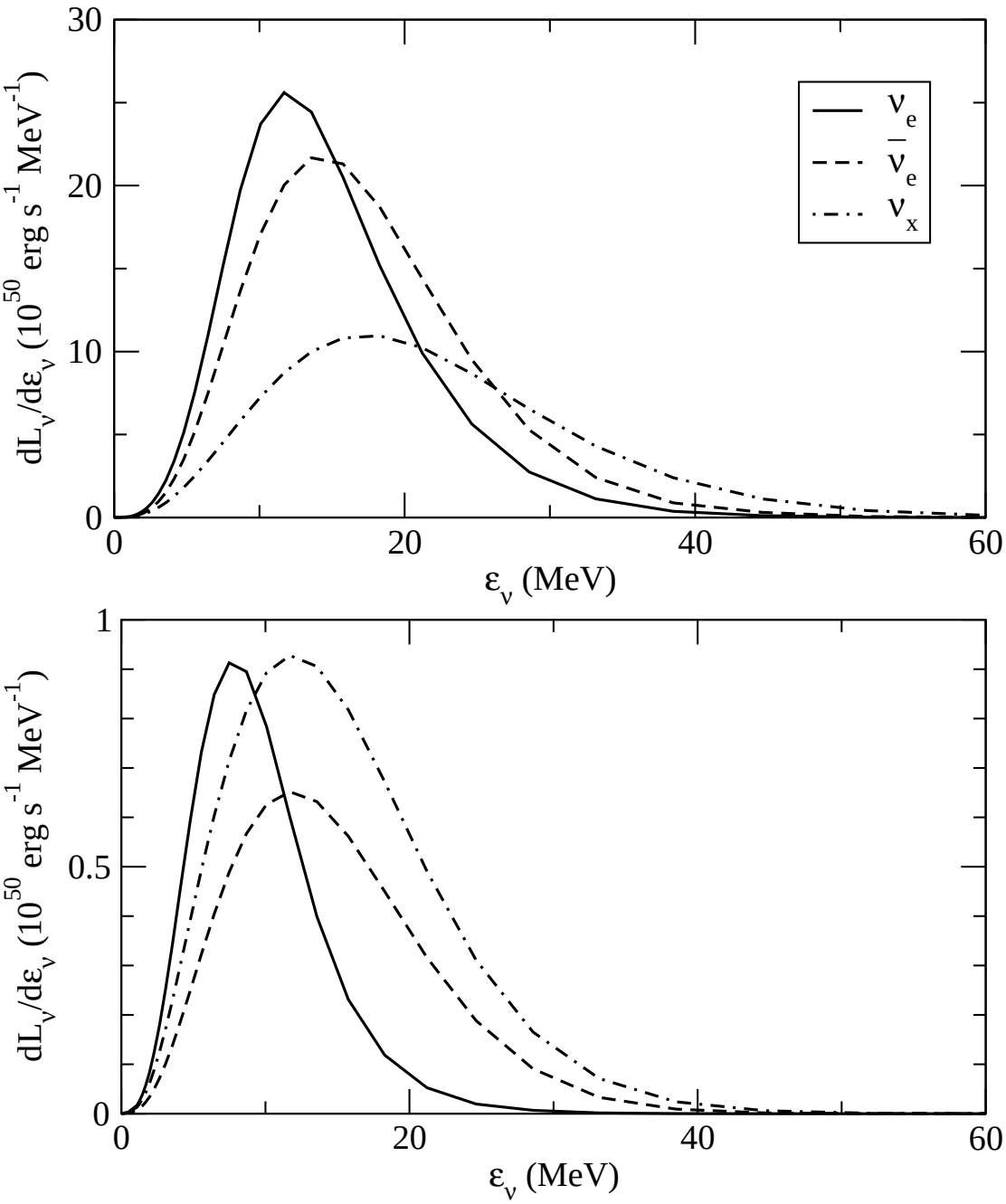

Figure 2.5: Neutrino spectra for all three flavors tracked in the simulation. The top panel is at 100 ms after the start of the simulation, the bottom panel is the spectrum at 5 seconds.

Lattimer 1986, Keil & Janka 1995, Pons et al. 1999, Roberts et al. 2012). It is thus a worthwhile exercise to compare the results obtained using EFLD and the present variable Eddington factor method for transport. No detailed comparison of the effect of different flux limiters is attempted since EFLD clearly breaks down in the decoupling regime independent of the flux limiter used. See Messer et al. (1998) and Pons et al. (2000) for discussions of the affect of different flux limiters.

Models using the identical microphysics and initial conditions described in section 2.5 were calculated using the EFLD code described in Roberts et al. (2012) with convection turned off. This code is similar to the one used in Pons et al. (1999) and is completely different from the one used in this paper. A derivation of EFLD in the context of this paper is included in Appendix 2.9. The EFLD luminosities as a function of time are shown in figure 2.6, alongside the luminosities from section 2.5. EFLD clearly does a reasonably good job of predicting the total neutrino luminosity, but poorly predicts the luminosities of each flavor.

At early times, some deviation in the total luminosity is expected because the mantle, which is driving most of the neutrino emission, is not particularly optically thick. Additionally, at late times when the whole PNS becomes optically thin, EFLD deviates from the variable Eddington factor solution. But for the bulk of the PNS evolution the deviation between the two methods is around 10%, which is surprisingly good agreement. Given that most predictions made using EFLD codes have relied only on the total neutrino luminosity, it seems that previous results can be reasonably trusted. The total luminosity emitted from the PNS is set at the neutrino spheres of each flavor, which is the last point at which EFLD can be considered reliable. The outermost layers of the PNS in which the neutrinos decouple can come into radiative equilibrium on a short timescale and therefore

rapidly adjust to the flux being pushed through them from below. As neutrinos propagate through the outer layers in the EFLD formalism, flux may be shifted between flavors unrealistically but the outer layers of the PNS will rapidly evolve to carry the right total luminosity. Therefore, it is not surprising that EFLD gets the total luminosity right but fails to predict the luminosities of specific flavors. Of course, EFLD makes no predictions regarding the spectral properties of the neutrinos.

2.6.2 Neutrino Spectra and The Composition of The Neutrino Driven Wind

The most striking difference between the present simulations and other recent studies (Hüdepohl *et al.* 2010, Fischer *et al.* 2010) is the greater difference in the present study of the electron neutrino and anti-neutrino average energies at late times. There are a number of possible reasons for this difference.

One is the initial model chosen for the PNS evolution. Rather than use an initial model from a separate calculation of core-collapse, both Hüdepohl *et al.* (2010) and Fischer *et al.* (2010) follow the entire evolution of the supernova. In so far as the initial models are similar, the two approaches should give the same answer. The initial model used here is somewhat dated and was chosen mainly to facilitate the comparison with the work of Pons et al. (1999). At early times the initial progenitor model will certainly affect the properties of the emitted neutrinos significantly, but after the first second Pons et al. (1999) found that the evolution does not depend sensitively on the initial progenitor model. Of course, the difference in the average energies of the electron and anti-electron neutrinos is a fairly subtle effect. Therefore, the effect of the progenitor model should not be

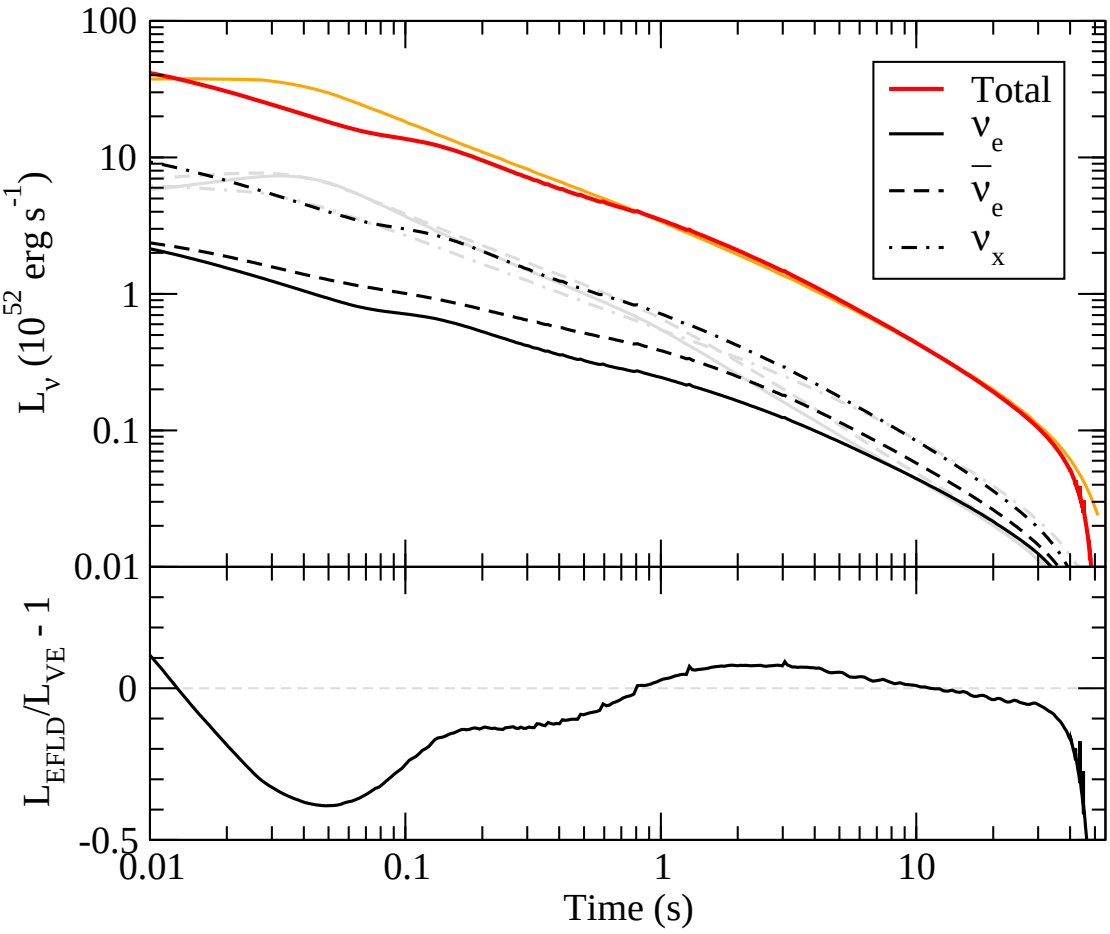

Figure 2.6: Luminosities as a function of time for ν_e (solid black line), $\bar{\nu}_e$ (dashed black line), ν_x (dot-dashed black line) of time and the total luminosity (red line) in the EFLD approximation. The gray and orange lines is the data from figure 2.2. The bottom panel shows the ratio of the total EFLD luminosity to the total luminosity calculated using the new code.

ruled out, but based on the argument below it seems unlikely that the progenitor model is the dominant factor.

It is possible that the methods used for transport differ enough to give disparate results. This also seems unlikely considering all three approaches come close to directly solving the Boltzmann equation, that the formalism described in this work is fairly similar to the formalism of Hüdepohl *et al.* (2010) (see Rampp & Janka 2002), and that the approaches of Fischer *et al.* (2010) and Hüdepohl *et al.* (2010) have been shown to yield similar results (Liebendörfer et al. 2005).

A more significant difference though may be the microphysics employed. The difference between the electron neutrino and anti-neutrino spectral temperatures is mainly set by the difference between their respective mean free paths to capture on nucleons, as the scattering mean free paths for both species are nearly equal. Due to de-leptonization, there are far more neutrons to capture electron neutrinos than protons to capture electron anti-neutrinos. Of course, it is possible for both of these reactions to have strong final state blocking (electron blocking for the neutrinos and neutron blocking for the anti-neutrinos). If it is assumed that there is no energy transfer to the nucleons, as in Fischer et al. (2011), then both reactions will be strongly blocked, the elastic interaction rates described in Bruenn (1985) go to the same value, and it is expected that average electron neutrino and anti-neutrino energies will be similar at late times due to the similar charged current mean free paths for both species.

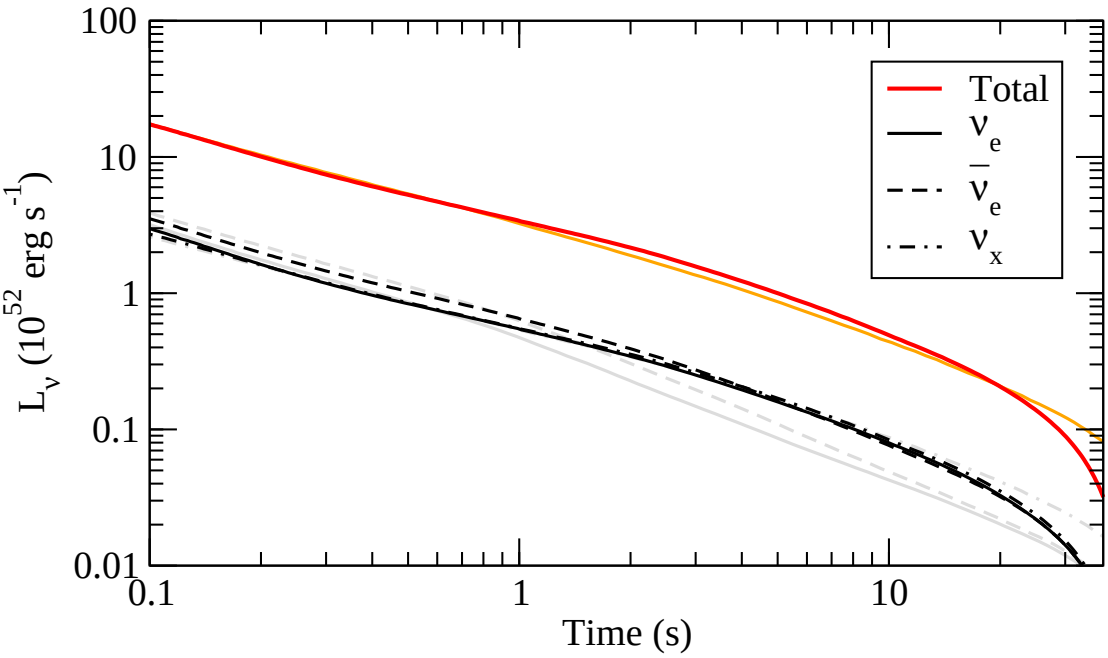
100
10
1
0.1
0.01
0.1
1
10
Time (s)
L_ν (10^{52} erg s^{-1})
Total
ν_e
$\bar{\nu}_e$
ν_x

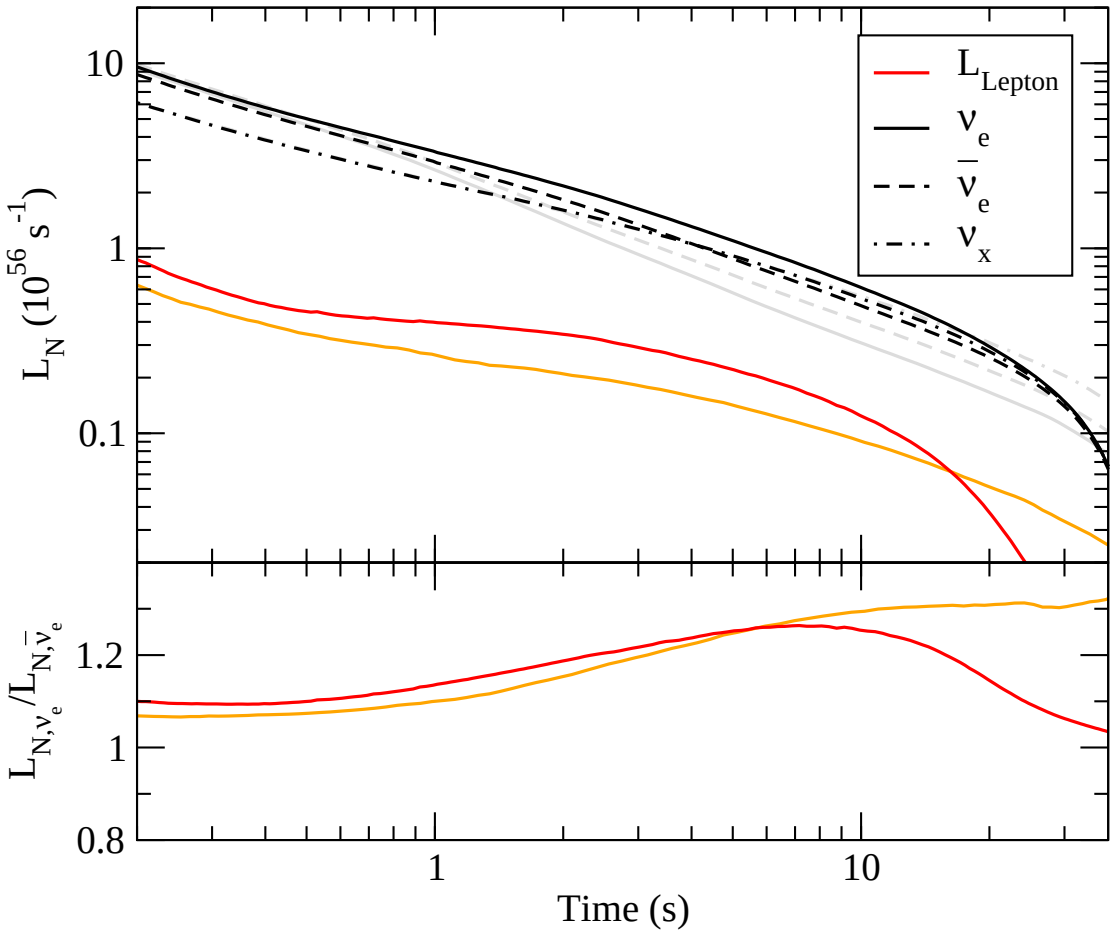

Figure 2.7: Energy and number luminosities for a model using the Bruenn (1985) nucleon capture rates compared to the fiducial model described in section 2.5. Notice the slightly increased ν_e and $\bar{\nu}_e$ cooling rates at late times and the convergence of all three luminosities. The black lines and red lines are for the model using Bruenn 1985 rates, while the gray and orange lines are for the model described in section 2.5. In the lower plot, the ratio $\dot{N}_{\nu_e}/\dot{N}_{\bar{\nu}_e}$, which is of consequence to the electron fraction in the neutrino driven wind, is shown in the bottom plot of the second panel.

The final state blocking symmetry predicted by the charged current rates of Bruenn (1985) does not agree with more detailed calculations of the electron neutrino capture rates. There is in fact a strong asymmetry between the two reactions, because there is significantly more energy available in the entrance channel for $\nu_e + n \rightarrow e^- + p$ than for $\bar{\nu}_e + p \rightarrow e^+ + n$. The difference between the energy of the entrance channels is just the difference between the fermi energies of the neutrons and protons. The Fermi energies for interacting nucleons are given by $e_{F,i} = k_{F,i}^2/2M_i + U_i$, where U_i is an isospin dependent potential energy due to strong interactions in the medium. For neutron rich conditions, the neutron potential energy is larger than the proton potential energy due to the nuclear symmetry energy. Most of the potential difference, $U_N - U_P$ is transferred to the outgoing electron in the reaction $\nu_e + n \rightarrow e^- + p$. This effect can significantly decrease the absorption mean free path for electron neutrinos. Due to the large value of the nuclear symmetry energy relative to the value expected for free nucleons, $U_N - U_P$ accounts for a significant fraction of $\hat{\mu}$. Although this amount of energy is often not enough to put the final state electron above the electron Fermi surface, it is enough to put the final state electron in a relatively less blocked portion of phase space. This effect is included in the relativistic formalism of Reddy et al. (1998), which is used to calculate the neutrino interaction rates used in the models presented in this work. The details of the importance of realistic kinematics on charged current rates will be discussed in future work.

To illustrate how more realistic rates affect the predicted neutrino properties, a model identical to the one described in section 2.5 was run, except that the nucleon capture rates were replaced with the Bruenn (1985) capture rates neglecting the nucleon potentials. The luminosities as a function of time are shown in figure 2.7.

The changes in the luminosity are relatively small. The most obvious difference is that the luminosities of all neutrino species asymptote to one another at late times, which is similar to the behavior seen in Fischer et al. (2011). From one to ten seconds, there is a significantly smaller difference between the luminosities than in the fiducial model. Cooling via electron neutrinos and anti-neutrinos is also increased at late times, but the ν_x luminosity is virtually unchanged, as expected. Before 1 s, the electron neutrino luminosity is reduced. It is unlikely that this is significant, as the first approximately hundred milliseconds of these simulations are suspect for the reasons described above. The reason for the early time decrease is less clear. It is unlikely that this is due to the effects of nuclear interactions because the region where electron neutrinos decouple is in the mantle which is at low density.

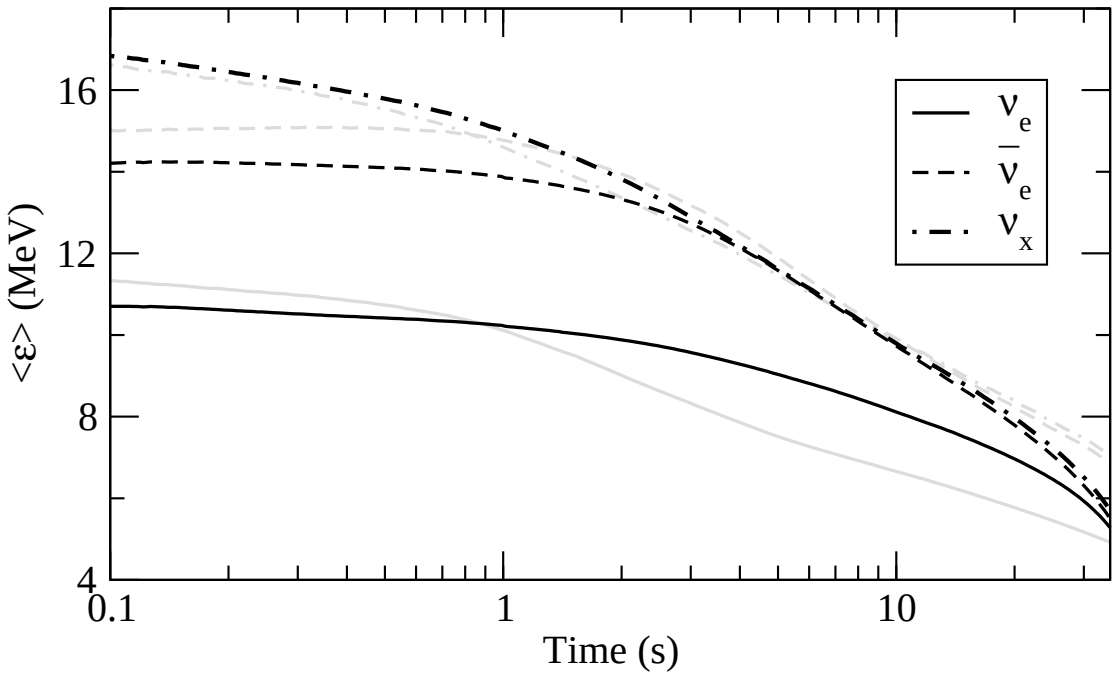

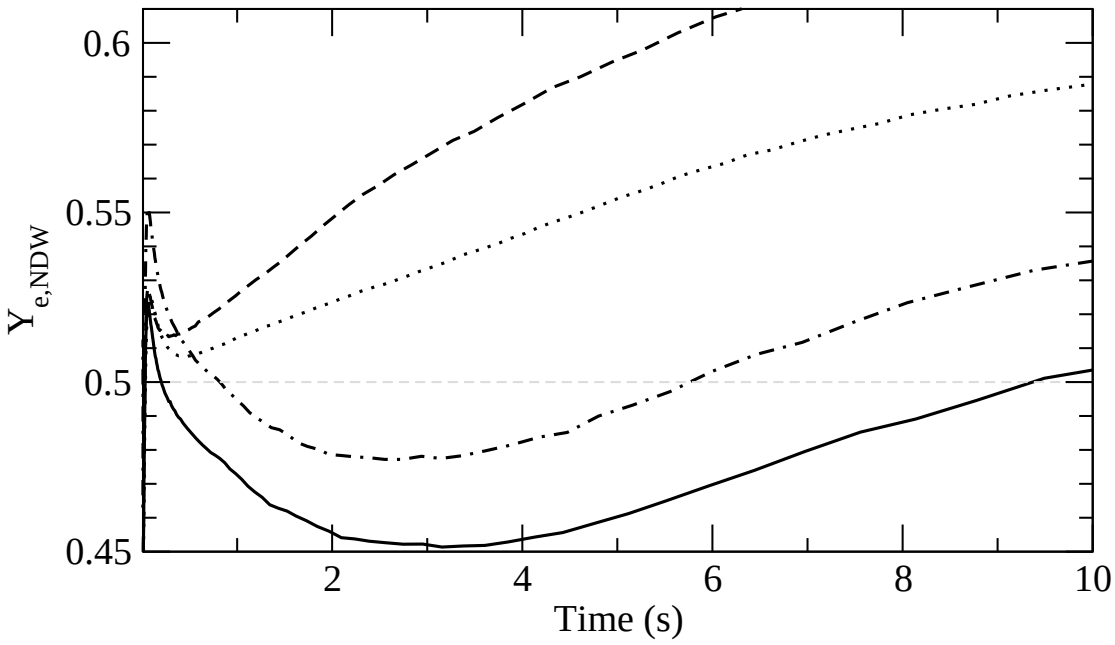

Figure 2.8: Top panel: Energy moments of the outgoing neutrino flux measured at the surface of the calculation using the Bruenn (1985) approximation for the electron neutrino and anti-neutrino capture rates on nucleons (black lines). The gray lines are for the fiducial model using the full capture cross-sections from Reddy, et al. (1998). There is little variation for the $\bar{\nu}_e$ and ν_x energies between the two cross-section prescriptions, but there is a significant change in the ν_e average energies. Bottom panel: Predicted neutrino driven wind electron fraction as a function of time. The dotted line is from a PNS model using the Bruenn (1985) rates, the solid line is for the Reddy, et al. (1998) rates including tensor polarization corrections and the mean fields Horowitz, et al. (2003), the dot-dashed line is a model using the Reddy, et al. (1998) rates without tensor polarization corrections and with mean fields, and the dashed line is a model using the Reddy, et al. (1998) rates with tensor polarization corrections but neglecting the effects of mean fields. Note that neutron richness is predicted from about 1.5 to 10 seconds when realistic kinematics is used in the capture rates, while the wind is predicted to be proton rich throughout when the effects of the neutron and proton potentials are ignored.

The evolution of the average neutrino energies are shown in figure 3.5. There is little change between the models in the electron anti-neutrino, μ, and τ neutrino average energies, but there is a significant change in the electron neutrino average energies. At early times the average energy is reduced compared to the fiducial model and at late times it is increased. The late-time convergence is easily explained by the argument given in the paragraphs above and by the arguments given in Fischer et al. (2011).

This difference is important to the composition of the neutrino driven wind. The electron fraction of the neutrino driven wind can be estimated as (Qian & Woosley 1996)

$$Y_{e,\mathrm{NDW}} \approx \left[1 + \frac{\dot{N}_{\bar{\nu}_e}\langle\sigma(\epsilon)_{p,\bar{\nu}_e}\rangle}{\dot{N}_{\nu_e}\langle\sigma(\epsilon)_{n,\nu_e}\rangle}\right]^{-1} \tag{2.83}$$

where $\langle\sigma\rangle$ are the energy averaged cross-sections for neutrino capture on nucleons, which are approximately proportional to ϵ^2. Smaller relative ν_e average energies and lower de-leptonization rates lead to a lower electron fraction in the wind.

The evolution of the electron fraction in the neutrino driven wind calculated using equation 3.17 for both models, as well as a model that does not include weak magnetism corrections and a model that does not include mean field effects, but which do include full kinematics in the structure functions, is shown in the second panel of figure 3.5. The capture rates for low densities given in Burrows et al. (2006), which include first order weak magnetism and recoil corrections, have been used. This was done to put the comparison between the models on even footing, although it is not necessarily consistent with the rates used inside the PNS itself. The alpha effect (Fuller & Meyer 1995) has also not been taken into account, which will push Y_e closer to a half in both proton and neutron rich conditions. Energy moments of the neutrino flux are taken using the values at

the surface of the computational domain, not at infinity. The $\dot{N}_{\nu_e}/\dot{N}_{\bar{\nu}_e}$ term is increasing with time in both models (see figure 2.7), which increases the electron fraction in the wind. Note that once neutrinos are free streaming, this term is invariant with radius.

With these assumptions, the fiducial model of section 2.5 actually does result in a period of neutron richness in the wind, in contrast to the results of Hüdepohl *et al.* (2010) and Fischer et al. (2011). The wind is not very neutron rich ($Y_e \gtrsim 0.45$ at all times) and this change, by itself, would not result in substantial r-process nucleosynthesis in the standard neutrino driven wind where entropies are $\lesssim 150$ (Roberts et al. 2010). If for some reason the entropy were higher though, the possibility of an r-process remains. In contrast, the model that uses the rates of Bruenn (1985) and the model using the Reddy et al. (1998) rates without isospin dependent nuclear potentials consistent with the underlying equation of state results in a wind that is always proton-rich.

To emphasize that this result is mainly due to the reaction kinematics and not the inclusion of weak magnetism, models with the tensor polarization set to zero are also shown in the bottom panel of figure 3.5. As is expected from the first order weak magnetism corrections given in Horowitz (2002), allowing for a tensor portion of the response increase the difference between the electron neutrino and anti-neutrino average energies. This results in a lower electron fraction in the case including the tensor polarization relative to the case without. Still, the change between these two models is only a fraction of the change in the electron fraction when the Bruenn (1985) rates are used.

Given the sensitivity to the neutrino interaction rates, it is possible that further improvement of the treatment of electron neutrino and anti-neutrino capture

will alter this conclusion in one direction or the other. Because the asymmetry between the electron neutrino capture rates depends on the value of the symmetry energy and the symmetry energy varies with density (Fattoyev *et al.* 2010), it may be that different nuclear equations of state alter the predicted neutron excess in the NDW. Variations of the calculation of the rates, such as incorporating the effect of correlations in the nuclear medium, can significantly change the timescale of the neutrino emission (Reddy *et al.* 1999) and possibly the spectral properties. Even if updated rates only change the rates at high density, this may affect $\dot{N}_{\nu_e}/\dot{N}_{\bar{\nu}_e}$ and thereby change the properties of the wind. Such extensions depend on the underlying equation of state, which is uncertain, and also on approximations inherent to many-body theories of strongly interacting systems. While this deserves further consideration, the results presented here seem to indicate that effects due to kinematics, degeneracy and mean fields are crucial.

It bears mentioning that the study of Hüdepohl *et al.* (2010) did allow for energy and momentum transfer between the nucleons and leptons (Buras et al. 2006), but did not account for the difference between the neutron and proton mean field potentials. Their rates were calculated within the random phase approximation of Burrows & Sawyer (1999), which is an improvement over the mean field rates used in this work. Additionally, weak magnetism corrections were approximately included in this study via the prescription of Buras et al. (2006). Their average energies were further apart than when the Bruenn (1985) rates were used, but the difference was still not great enough to result in a wind with a neutron excess. The average energies of the electron neutrinos and anti-neutrinos also asymptote to one another fairly rapidly in Hüdepohl *et al.* (2010), in contrast to the present study. This is all reasonably consistent with the affect of neglecting the mean

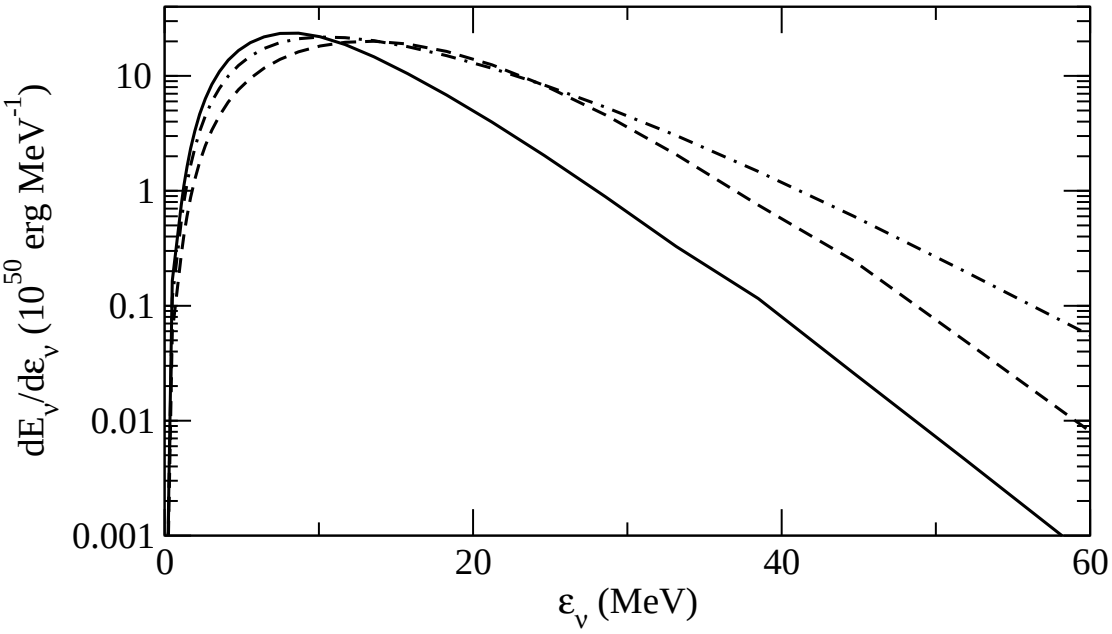

Figure 2.9: Spectrum of integrated neutrino emission over the duration of the simulation. Although the peak of the $\bar{\nu}_e$ spectrum corresponds to the peak of the ν_x spectrum, the ν_x spectrum has a significantly harder tail.

field potentials in the nucleon kinematics, but it is far from certain that this is the main source of discrepancy. Further exploration of why this work differs from the work of Hüdepohl *et al.* (2010) is surely warranted.

Even given these caveats, it is tantalizing that the wind is neutron rich in the fiducial model once again. Extensions of the standard neutrino driven wind model which include heating from a source besides neutrinos can produce the r-process even for such modest neutron excesses (Suzuki et al. 2006).

2.6.3 Time Integrated Spectra

In figure 2.9, the integrated neutrino luminosity as a function of neutrino energy at infinity is shown for the model described in section 2.5. The time

integrated average energies of the neutrinos are $\langle \epsilon_{\nu_e} \rangle = 8.3\,\mathrm{MeV}$, $\langle \epsilon_{\bar{\nu}_e} \rangle = 12.2\,\mathrm{MeV}$, and $\langle \epsilon_{\nu_x} \rangle = 11.1\,\mathrm{MeV}$. Although the μ and τ neutrinos are as hot or hotter than the electron anti-neutrinos at early times, the time integrated average is weighted more strongly towards late times so that they in fact have a somewhat lower average energy.

Time integrated neutrino spectra are interesting for both nucleosynthesis via the ν-process (Heger et al. 2005) and for predictions of the diffuse supernova neutrino background (Ando 2004). The neutrinos are non-thermal and are not easily described by an effective Fermi-Dirac distribution. Given the sensitivity of the ν-process to the energy of the emitted neutrinos (especially the energies above threshold), it seems that calculations of neutrino-induced nucleosynthesis needs to be done with more accurate neutrino spectra to check previous results in the literature. These integrated spectra are only approximate however because a substantial fraction (20%) of the neutrinos are emitted during the first second of mantle contraction, this phase of evolution contributes the majority of the high-energy tail, and the mantle contraction phase is most sensitive to the approximate initial conditions used.

2.7 Conclusions

A new code for following the evolution of PNSs has been described and some first results obtained. In section 2.2.2, a formalism for moment based neutrino transfer with variable Eddington factors has been described, based on the work of Thorne (1981) and Lindquist (1966). The framework is fully general relativistic and is formulated in the rest frame of the fluid, which simplifies calculation of the collision terms. The code employs energy integrated groups, rather than discrete

energies, for solving the radiative transfer problem. This makes it well suited for dealing with problems were thermodynamic equilibrium holds in large portions of the problem domain and the distribution functions may contain sharp Fermi surfaces. A method for finding Eddington factors from a formal solution to the static Lindquist equation was also described. Additionally, general descriptions of the source terms for absorption, scattering, and pair annihilation have been provided which are consistent with the formalism, explicitly obey detailed balance, and therefore naturally deal with the transition to equilibrium. The details of a fully implicit numerical implementation of these transport equations alongside the equations of general relativistic hydrodynamics were then described in section 2.4.

The results of a fiducial model of PNS cooling were presented in section 2.5. The evolution proceeds similarly to previous results in the literature in which a similar nuclear equation of state and neutrino opacities were used. I have focused on the spectral properties of the emitted neutrinos, which were not well described by the formalism of Pons et al. (1999). Similar behavior is found to other recent results in the literature: spectral softening as a function of time and convergence of the $\bar{\nu}_e$ and $\nu_{\tau,\mu}$ luminosities after about two seconds of evolution (Fischer *et al.* 2010, Hüdepohl *et al.* 2010).

In contrast to other recent studies (c.f. Fischer et al. 2011) however, the new studies show that the average energy of the electron neutrinos does not converge to the average energies of the other neutrino flavors at late times. Additionally, the electron neutrinos are significantly cooler than the anti-electron neutrinos for most of the simulation. This difference is likely due to the treatment of charged current neutrino interactions, where a realistic treatment of the nucleon kinematics including the nuclear potential is important (see section 2.6.2). The implications

of this result for the electron fraction in the neutrino driven wind and possible r-process nucleosynthesis in this environment were discussed and warrant further exploration.

A quantitative comparison was also made between the results of an EFLD calculation of PNS evolution and evolution with the code described in this paper in section 2.6.1. It was found that EFLD provides a good approximation to the total neutrino luminosity during periods in which the neutrino luminosity is dominated by emission from optically thick regions. This approximation does break down in the optically thin regime as expected. Additionally, it does a poor job of predicting the luminosities of individual neutrino flavors.

The most significant improvement which could be made to this work would be to improve the initial models. This could be done either by using a more realistic post-core collapse initial models or updating the code to allow it to follow collapse and bounce itself, similar to Hüdepohl *et al.* (2010) and Fischer *et al.* (2010). Such improvements will affect the early time evolution, but are probably less important to the evolution of the PNS after one second. Additionally, a more realistic equation of state that includes nuclei at low densities (Shen et al. 2011) should be employed with consistent opacities.

Of course, this work has also been limited to one dimension, which may be a gross, although necessary, oversimplification. Convection, magnetic fields, and rotation may be central players in the evolution of PNSs. Approximate mixing length convection will be included in a subsequent version of the code. In the future, this code will be applied to understanding the diffuse supernova neutrino background, predicting the affects of different prescriptions for the nuclear equation of state on PNS cooling, and investigating black hole formation.

2.8 Appendix: Code Tests

Here I consider static transport through an homogeneous sphere with unit radius, and unit optical depth. A flat space-time is assumed. The first test performed is for consistency between the formal solution of the Boltzmann equation and the moment equations. In addition to the factors g_2 and g_3, the formal Boltzmann solver can also calculate $g_1 \equiv w^1/w^0$ which should be equal to H_g/E_g. For a purely absorptive atmosphere, the formal solution is exact. A comparison of g_1 and H_g/E_g is shown in figure 2.10. For this calculation, one hundred equally spaced radially zones and a grid of 150 tangent rays with impact parameters spaced equally in radius were used. The calculation was then evolved for ten units of time. The differences between the two Eddington factors are negligible, aside from in the inner most zones. This agreement does not depend strongly on the number of tangent rays employed. The disagreement in the inner most regions is due to the small number of tangent rays which have impact parameters that are less than the radius at which the Eddington factor is calculated. The distribution function is not well resolved and is therefore in error. Such problems should not arise in the actual evolution of PNSs, as the inner most regions are generally opaque.

As a second test, a sphere which includes a scattering contribution to the opacity is considered. In this case, the formal Boltzmann solver no longer gives an exact solution of the transport equation because of the approximate treatment of the scattering terms (see section 2.3). The problem set up involves a sphere of optical depth one with 10% of the opacity coming from absorption and 90% coming from isotropic scattering. Using a similar numerical set up to the absorbing atmosphere gives the results shown in figure 2.10. Once again the deviation

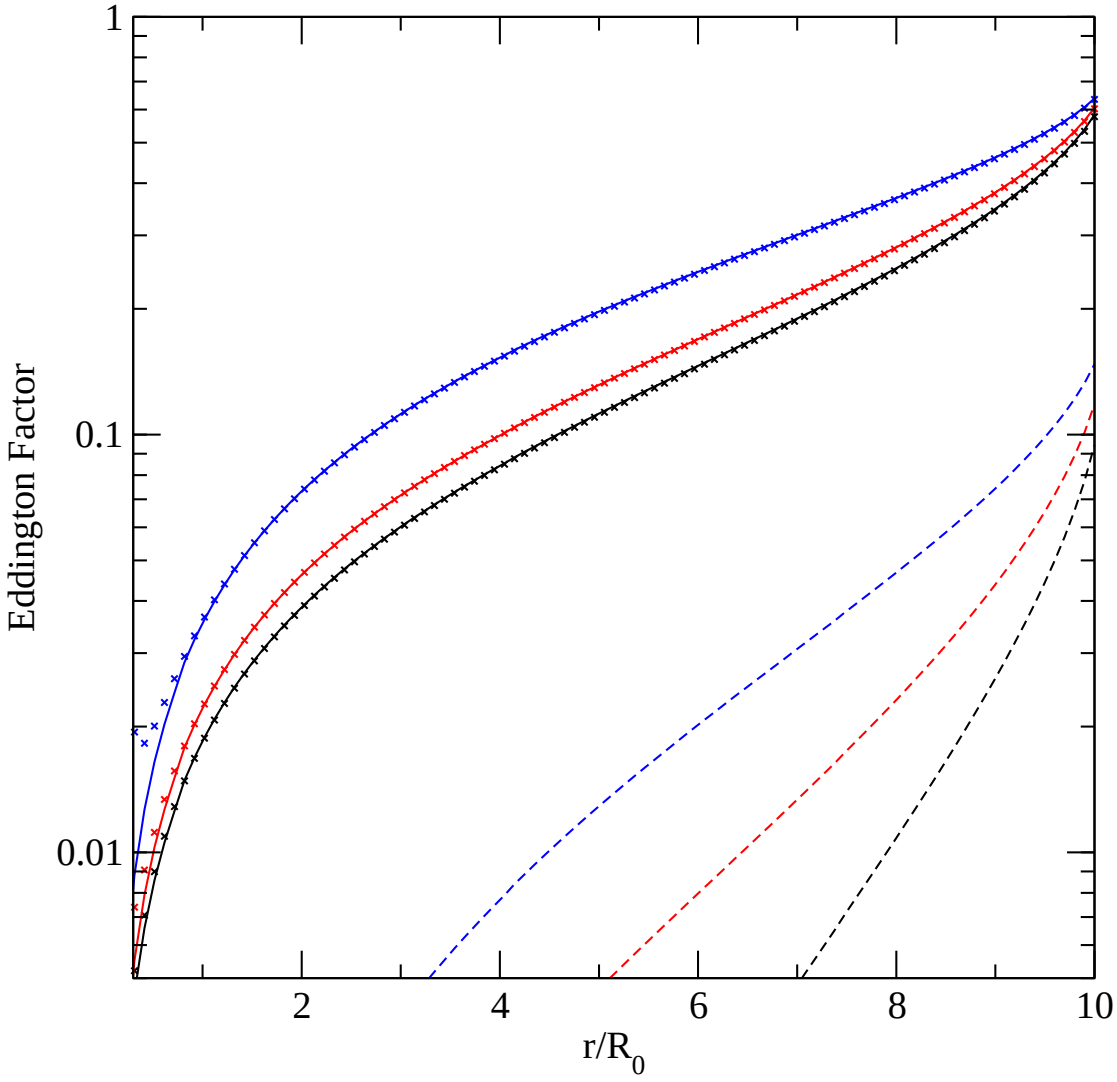

Figure 2.10: Comparison of H_g/E_g (crosses) and g_1 (solid lines) for a purely absorbing (black lines) and an isotropic scattering sphere (red lines) with total optical depth one and a first order scattering sphere (blue lines) with $\tau = 0.1$. Aside from at the center, there is excellent agreement between the formal solution and the results of the moment calculation. The dashed lines are the second Eddington factors, g_2, for the same models.

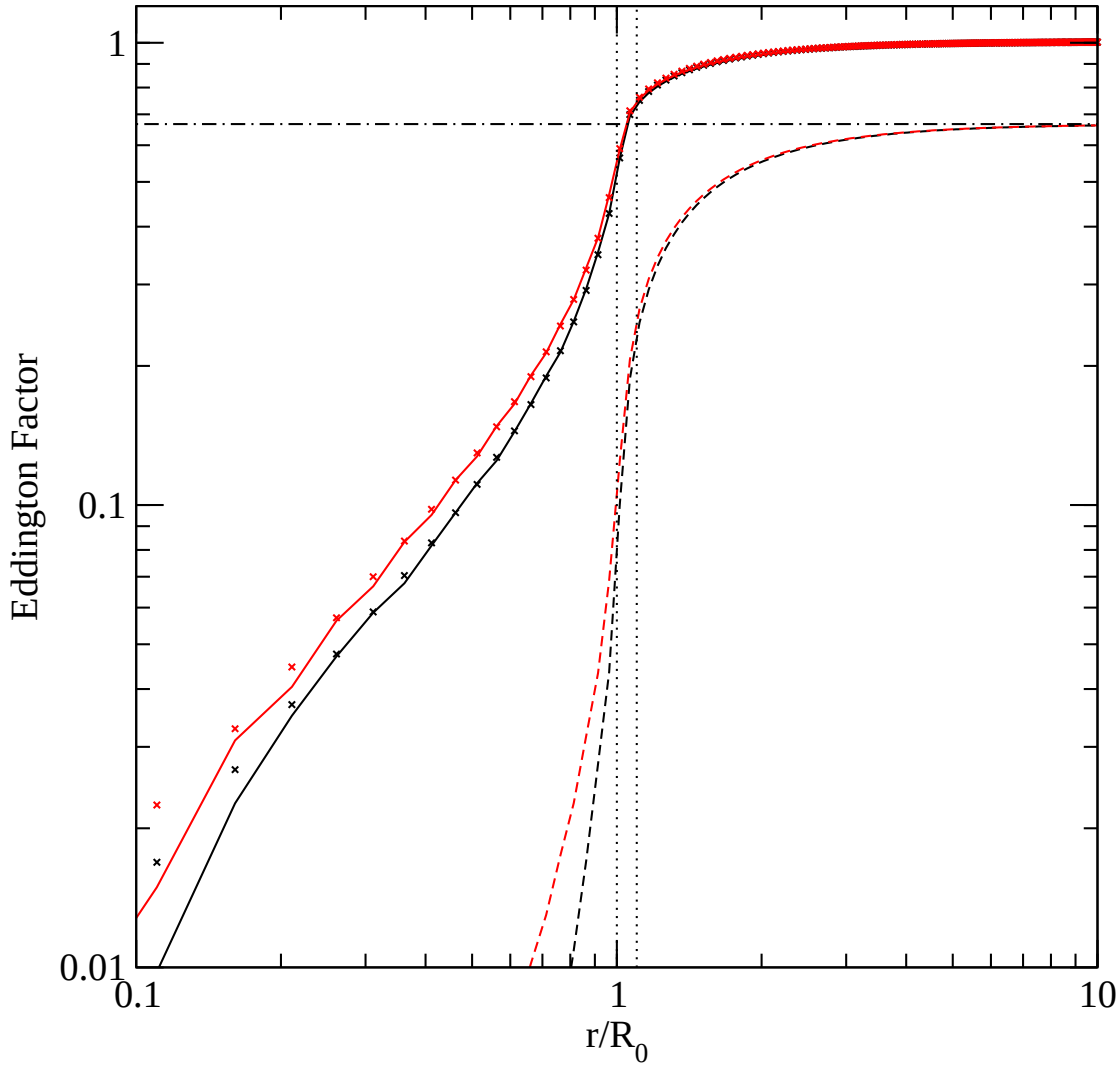
1
0.1
0.01
Eddington Factor
0.1
1
10
r/R0

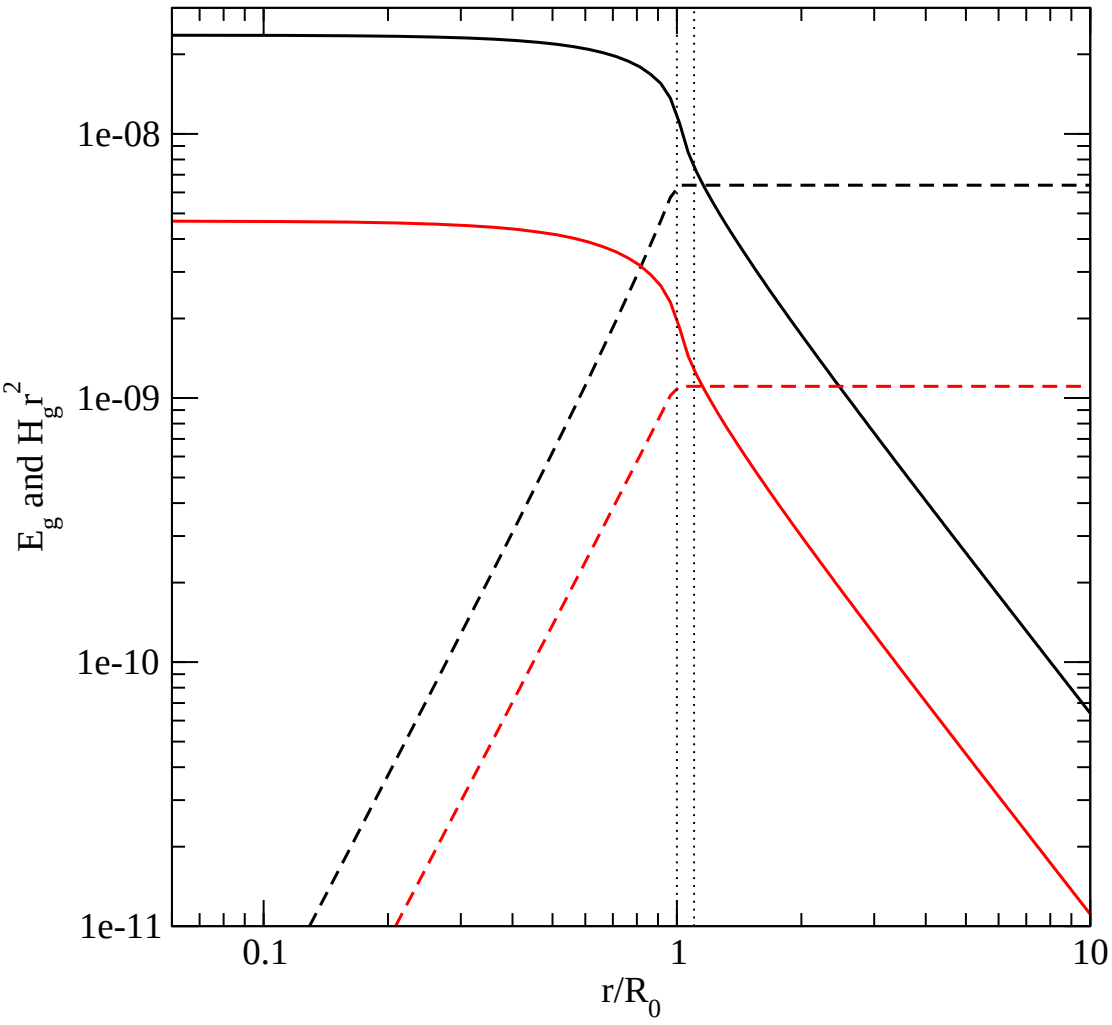

Figure 2.11: First Panel: Eddington factors for radiation streaming from a homogenous sphere into free space. The solid lines are the Eddington factors g_1 for the purely absorptive sphere (black) and the isotropic scattering sphere (red). The crosses show H_g/E_g. The dashed lines are the second Eddington factor, g_2, for the same models. The vertical dotted lines show the radii at which the opaque sphere ends. The horizontal dashed line shows the expected asymptotic value of g_2 for free streaming radiation. Second Panel: Properties of the radiation field as a function of radius. The solid lines show the radiation energy density and the dashed lines show the luminosity per steradian, $r^2 H_g$. The colors are the same as in the top panel. Once again, the vertical dotted line denotes the end of the opaque sphere.

between the formal solution and the results of the moment calculation are small. Above the two innermost zones, the maximum deviation of the two results for g_1 is less than 1%. At radii greater than 8, the deviation is less than 0.1%. A second scattering test problem was run with the isotropic scattering opacity, χ_0^s, set to zero and the first order scattering opacity, χ_1^s, set to 90% of the total opacity. The sphere was assumed to have an optical depth $\tau = 0.1$. The agreement between the moment calculation and the formal solution was found to be similar to the isotropic scattering case.

Tests similar to the homogeneous sphere tests of Rampp & Janka (2002) have also been performed. In these, a unit optical depth sphere of radius one is included inside a transparent region of radius ten, with a sharp transition region from the semi-opaque sphere to the surrounding vacuum. Such a scenario is similar to the neutrino decoupling region of PNSs, and is therefore an important test problem for any neutrino transport code for PNS evolution. The calculation domain is split up into 200 zones, equally spaced in radius and 301 a grid of 301 tangent is employed. Only the radiation density, E_g and flux, H_g, are evolved. The calculation is then run for fifty time steps, which allows the calculation to relax to steady state and forget the details of the initial conditions of the radiation field. Once again, one calculation was run with a purely absorbing opacity and a second was run with 10% absorbing opacity and 90% isotropic scattering opacity.

The final Eddington factors and radiation field for these calculations are shown in figure 2.11. For the purely absorbing calculation, the formal solution of the Boltzmann equation is exact. In the inner most zones, the distribution function is under resolved in angle due to the small number of tangent rays which pass through this region. This is not a problem for PNS simulations, as the optical

depth in the interior is always much larger than one. Therefore, the Eddington factors are close to zero and have negligible affects on the moment transport solution. The deviation of the moment solution, outside the inner most region, from the formal solution is less than 1%. In the decoupling region the agreement is excellent. Additionally both g_1 and g_2 asymptote to their expected values for free streaming radiation far from the core.

2.9 Appendix: Equilibrium Flux Limited Diffusion

In the diffusion approximation, the distribution function is approximated by $f(\omega, \mu) = f_0(\omega) + f_1(\omega)\mu$. This results in $g_2 = g_3 = 0$. The time dependence is then dropped and compression terms are then dropped from the first moment equation. Ignoring the terms containing derivatives with respect to energy (which will drop out in the end of our analysis anyway), I find

$$\Gamma \left(\frac{\partial w^0}{\partial r} + 4 \frac{\partial \phi}{\partial r} w^0 \right) = 3 s^1 \tag{2.84}$$

If the redshifted frequency is denoted as $\nu = \omega e^{\phi}$, the redshifted source function is

$$s^1 = -w_1 D^{-1}(\nu e^{-\phi}) \tag{2.85}$$

which gives the redshifted neutrino flux per energy

$$w_1 = -\Gamma \frac{D(\nu e^{-\phi})}{3} \left(\frac{\partial w^0}{\partial r} + 4 \frac{\partial \phi}{\partial r} w^0 \right) \tag{2.86}$$

where $D(\omega) = (1/\lambda_a^* + \chi_0^s - \chi_1^s/3)^{-1}$. This amounts to assuming that the neutrino flux instantaneously equilibrates to the gradients in the neutrino number density.

Because a number of terms have been dropped, this expression does not guarantee that $w_1 \leq w_0$, which means that it is possible for the neutrino fluxes to violate causality (Levermore & Pomraning 1981). This problem is usually circumvented by introducing a flux limiter, which is a correction to the diffusion coefficient which depends on $\xi = w_1/w_0$ and serves to keep the fluxes causal. In section 2.6.1, the flux limiter of Levermore & Pomraning (1981) has been used, but it was found in Pons et al. (1999) that the results of EFLD calculations are reasonably insensitive to the choice of flux limiter.

The total energy flux is given by

$$H = \int d\omega w^1 = -e^{\phi}\Gamma \int d\omega \frac{D(\nu e^{-\phi})}{3}\left[\frac{\partial w^0}{\partial r} - e^{4\phi}\frac{\partial e^{-4\phi}}{\partial r}w^0\right] \tag{2.87}$$

The equilibrium portion of the EFLD approximation constitutes assuming that $f_0(\omega) = f_{\rm eq}(\omega, T, \mu)$. Using the equilibrium expression for w_0 yields

$$H = -\frac{\Gamma}{6\pi^2}\int d\omega D(\omega)\omega^3 \frac{\partial f_{\rm eq}(\omega)}{\partial r} \tag{2.88}$$

The radial derivative is then given by

$$\frac{\partial f_{\rm eq}(\nu e^{-\phi})}{\partial r} = \left[\frac{\omega}{T}\frac{\partial T e^{\phi}}{\partial r} + T e^{\phi}\frac{\partial \eta}{\partial r}\right]\frac{f_{\rm eq}(\omega)(1 - f_{\rm eq}(\omega))}{T e^{\phi}} \tag{2.89}$$

So that the energy flux is given by

$$H = -\frac{\Gamma e^{-\phi} T^3}{6\pi^2}\left[D_4\frac{\partial T e^{\phi}}{\partial r} + D_3 T e^{\phi}\frac{\partial \eta}{\partial r}\right], \tag{2.90}$$

where the energy integrated diffusion coefficients are defined as

$$D_n = \int_0^{\infty} dx x^n D(xT) f_{\rm eq}(xT)(1 - f_{\rm eq}(xT)). \tag{2.91}$$

The number flux equation can easily be determined from the energy flux equation. This gives

$$F = -\frac{\Gamma e^{-\phi} T^2}{6\pi^2}\left[D_3\frac{\partial T e^{\phi}}{\partial r} + D_2 T e^{\phi}\frac{\partial \eta}{\partial r}\right]. \tag{2.92}$$

These expressions agree with the results of Pons et al. (1999).

Now all that is left is to describe the evolution of the underlying medium. Using equation 2.32, the evolution of the total internal energy of the medium including neutrinos is found to be

$$\frac{\partial \epsilon}{\partial t} + e^{\phi}\Theta\frac{p}{n} + e^{-\phi}\frac{\partial}{\partial a}\left(\sum_{\substack{s= \\ \{\nu_e,\cdots\}}} 4\pi r^2 e^{2\phi} H_s\right) = 0 \tag{2.93}$$

Using equation 2.33, the evolution of total lepton number is found to be

$$\frac{\partial Y_L}{\partial t} + \frac{\partial}{\partial a}\left(4\pi r^2 e^{\phi}\left[F_{\nu_e} - F_{\bar{\nu}_e}\right]\right) = 0. \tag{2.94}$$

Chapter 3

Medium Modification of the Charged Current Neutrino Opacity and Its Implications

This work was performed in collaboration with Sanjay Reddy.

Abstract

Previous work on neutrino emission from proto-neutron stars which employed full solutions of the Boltzmann equation showed that the average energies of emitted electron neutrinos and antineutrinos are closer to one another than predicted by older, more approximate work. This in turn implied that the neutrino driven wind is proton rich during its entire life, precluding r-process nucleosynthesis and the synthesis of Sr, Y, and Zr. This work relied on charged current neutrino interaction rates that are appropriate for a free nucleon gas. Here, it is shown in detail that the inclusion of the nucleon potential energies and collisional broadening of the response significantly alters this conclusion. Iso-vector interactions,

which give rise to the nuclear symmetry energy, produce a difference between neutron and proton single-particle energies $\Delta U = U_n - U_p$ and alter the kinematics of the charged current reaction. In neutron-rich matter, and for a given neutrino/antineutrino energy, the rate for $\nu_e + n \rightarrow e^- + p$ is enhanced while $\bar{\nu}_e + p \rightarrow n + e^+$ is suppressed because the Q value for these reactions is altered by $\pm\Delta U$, respectively. Collisional broadening acts to enhance both ν_e and $\bar{\nu}_e$ cross-sections, but mean field shifts have a larger effect. Therefore, electron neutrinos decouple at lower temperature than when the nucleons are assumed to be free and have lower average energies. The change is large enough to allow for a reasonable period of time when the neutrino driven wind is predicted to be neutron rich. It is also shown that the electron fraction in the wind is influenced by the nuclear symmetry energy.

3.1 Introduction

The neutrino opacity of dense matter encountered in core-collapse supernova is of paramount importance to the explosion mechanism, potential nucleosynthesis, supernova neutrino detection and to the evolution of the compact remnant left behind. Matter degeneracy, strong and electromagnetic correlations, and multi-particle excitations have all been shown to be important, especially at supra-nuclear densities (e.g. Reddy et al. 1998, Burrows & Sawyer 1998; 1999, Reddy *et al.* 1999, Hannestad & Raffelt 1998, Horowitz & Pérez-García 2003, Lykasov et al. 2008, Bacca et al. 2011). Supernova and proto-neutron star (PNS) simulations that employ some subset of these improvements to the free gas neutrino interaction rates have found that these corrections play a role in shaping the temporal and spectral aspects of neutrino emission (Pons et al. 1999, Reddy *et al.* 1999,

Hüdepohl *et al.* 2010, Roberts et al. 2012). Still, much is uncertain, especially because of the approximations one must make regarding weak interactions with the dense background medium. A specific issue of importance is the difference between the average energies of electron neutrinos and electron antineutrinos. This difference is largely determined by the charged current reactions $\nu_e + n \rightarrow p + e^-$ and $\bar{\nu}_e + p \rightarrow n + e^+$ in neutron-rich dense at a densities $\rho \simeq 10^{12} - 10^{14}$ g/cm^3.

Recently, one of the authors has shown that an accurate treatment of mean field effects in simulations of PNS cooling changes the predicted electron fraction in the neutrino driven wind (NDW) (Roberts 2012) relative to simulations which do not account for mean field potentials in nuclear matter (Fischer *et al.* 2010, Hüdepohl *et al.* 2010, Fischer et al. 2012). This difference has significant consequences for the nucleosynthesis expected in the NDW (e.g. Hoffman et al. 1997, Roberts et al. 2010, Arcones & Montes 2011) and for neutrino oscillations outside the neutrino sphere Duan et al. (2006; 2010). In this work, we discuss generic aspects of strong interactions that lead to a large asymmetry in the charged current reaction rates for electron neutrinos and antineutrinos. We also demonstrate that this difference manifests itself in potentially observable effects on neutrino spectra from supernovae and that the difference depends on the assumed density dependence of the nuclear symmetry energy. The effect of multi-particle excitations on the charged current response is also explored.

Neutron-rich matter at densities and temperatures relevant to the neutrino sphere of a PNS is characterized by degenerate relativistic electrons and non-relativistic partially degenerate neutrons and protons. Beta-equilibrium, with net electron neutrino number $Y_{\nu_e} = 0$ is a reasonably good approximation for the material near the neutrino sphere because, by definition, this material can effi-

ciently lose net electron neutrino number. At these densities, effects due to strong interactions modify the equation of state and the beta-equilibrium abundances of neutron and protons. Simple models for the nuclear equation of state predict that the nucleon potential energy is

$$U_{n/p} \approx V_{\rm is}\ (n_n + n_p) \pm V_{\rm iv}\ (n_n - n_p)\,, \tag{3.1}$$

where $V_{\rm is}$ and $V_{\rm iv}$ are the effective iso-scalar and iso-vector potentials. Empirical properties of nuclear matter and neutron-rich matter suggest that $V_{\rm is} \times n_0 \approx -50$ MeV and $V_{\rm iv} \times n_0 \approx 20$ MeV. The potential energy associated with $n \rightarrow p$ conversion in the medium is

$$\Delta U = U_n - U_p \approx 40 \times \frac{(n_n - n_p)}{n_0}\ {\rm MeV}, \tag{3.2}$$

where $n_0 = 0.16$ nucleons/fm^3 is the number density at saturation. It will be shown that ΔU changes the kinematics of charge current reactions, so that the Q-value for the reaction $\nu_e + n \rightarrow e^- + p$ is enhanced by ΔU while that for $\bar{\nu}_e + p \rightarrow e^+ + n$ is reduced by the same amount. The effect is similar to the enhancement due to the neutron-proton mass difference, but is larger when the number density $n > n_0/20$.

In section 3.2, charged current neutrino opacities in an interacting medium are discussed. We consider how mean fields affect the response of the medium in detail and how this depends on the properties of the nuclear equation of state. The affect of nuclear correlations and multi-particle hole excitations are also discussed. In section 3.3, the effect of variations of the charged current reaction rates on the properties of the emitted neutrinos is studied.

3.2 The Charged Current Response

Without medium modifications, the differential cross-section for the process $\nu_e + n \rightarrow e^- + p$ per unit volume is given by

$$\begin{aligned} \frac{1}{V}\frac{d^2\sigma}{d\cos\theta dE_e} &= \frac{G_F^2}{2\pi}\left[(1+\cos\theta) + g_A^2(3-\cos\theta)\right]\, S(q_0,q) \\ &\times \quad p_e\; E_e\,[1-f_e(E_e)]. \end{aligned} \tag{3.3}$$

where the energy transfer to the nuclear medium is $q_0 = E_\nu - E_e$, and the magnitude of the momentum transfer to the medium is $q^2 = E_\nu^2 + E_e^2 - 2E_\nu E_e\cos\theta$. The free particle response function is defined by

$$S_{\rm F}(q_0,q) = \frac{1}{2\pi^2}\int d^3p_2\,\delta(q_0+E_2-E_4)f_2(1-f_4), \tag{3.4}$$

where the particle labeled 2 is the incoming nucleon, the particle labeled 4 is the outgoing nucleon. When the dispersion relation for nucleons is given by $E(p) = M + p^2/2M$, and neglecting for simplicity the neutron-proton mass difference, the integrals in Eq. 3.4 can be performed to obtain

$$S_{\rm F}(q_0,q) = \frac{M^2T}{\pi q\,(1-e^{-z})}\ln\left\{\frac{\exp\left[(e_{\rm min}-\mu_2)/T\right]+1}{\exp\left[(e_{\rm min}-\mu_2)/T\right]+\exp\left[-z\right]}\right\}, \tag{3.5}$$

where $z \equiv (q_0+\mu_2-\mu_4)/T$, μ_2 and μ_4 are the chemical potentials of the incoming and outgoing nucleons, M is the nucleon mass, and

$$e_{\rm min} = \frac{M}{2q^2}\left(q_0 - \frac{q^2}{2M}\right)^2. \tag{3.6}$$

$e_{\rm min}$ arises from the kinematic restrictions imposed by the energy-momentum transfer and the energy conserving delta function. Physically, $e_{\rm min}$ is the minimum energy of the nucleon in the initial state that can accept momentum q and energy q_0.

3.2.1 Frustrated Kinematics

The differential cross-section of ν_e absorption is the product of the nucleon response times the available electron phase space

$$\propto p_e \; E_e \; (1 - f_e(E_e)) \approx E_e^2 \; \exp\left(\frac{E_e - \mu_e}{T}\right). \tag{3.7}$$

Due to the high electron degeneracy, the lepton phase space increases exponentially with the electron energy. To completely overcome electron blocking requires $E_e = E_{\nu_e} - q_0 \approx \mu_e$ or $q_0 \approx -\mu_e$ when $E_{\nu_e} \ll \mu_e$. However, the fermi gas response function in Eq. 3.4 is peaked at $q_0 \simeq q^2/2M \approx 0$ reflecting the fact that nucleons are heavy. At large $|q_0| \simeq q \approx \mu_e$ the response is exponentially suppressed due to kinematic restrictions imposed by Eq. 3.6 that implies only neutrons with energy

$$E_2 > e_{\min} \simeq \frac{M}{2q^2} \; q_0^2 \approx \frac{M}{2}\,, \tag{3.8}$$

can participate in the reaction. For conditions in the PNS decoupling region, and in the fermi gas approximation, the ν_e reaction proceeds at $q_0 \approx 0$ at the expense of large electron blocking. Thus effects that can shift strength to more negative q_0 can increase the electron absorption rate exponentially.

It is well known that the neutron-proton mass difference $\Delta M = M_n - M_p$ increases the Q value for this reaction and a more general expression for $S(q_0, q)$ derived in Reddy et al. (1998) includes this effect. The effect of ΔM can be understood by noting, that at leading order, it only changes the argument of the energy delta-function in Eq. 3.4 and is subsumed by the replacements $q_0 \rightarrow (q_0 + \Delta M)$ and

$$e_{\min} \rightarrow \tilde{e}_{\min} \approx \frac{M}{2q^2}\left(q_0 + \Delta M - \frac{q^2}{2M}\right)^2. \tag{3.9}$$

This shift changes the location of the peak of the response moving it to the region where E_e is larger and confirming that it increases the Q value and the final state

electron energy by $\Delta M = M_n - M_p$. From Eq. 3.7 we see that the rate for ν_e absorption is increased by roughly a factor $(1 + \Delta M/E_e)^2 \ \exp(\Delta M/T)$. By the same token, the Q value for the reaction $\bar{\nu}_e + p \rightarrow e^+ + n$ is reduced by ΔM and this acts to reduce the rate. In this case, the detailed balance factor $[1 - \exp(-z)]^{-1}$ in the response function $S(q_0, q)$ is the source of exponential suppression – simply indicating a paucity of high energy protons in the plasma. For small $q_0 \ll \mu_e$, the detailed balance factor is

$$\frac{-1}{1 - \exp(-z)} \approx \exp\left(\frac{q_0 - \mu_e}{T}\right), \tag{3.10}$$

where we have use the fact that $\mu_n - \mu_p = \mu_e$ in beta-equilibrium. Since $q_0 \rightarrow (q_0 - \Delta M)$ for the $\bar{\nu}_e$ process, ΔM will suppress this rate exponentially. In line with the expectation that ΔM increases the cross-section for ν_e absorption and decreases it for $\bar{\nu}_e$ absorption.

In the following we show that the mean field energy shift, driven by the nuclear symmetry energy, has a similar but substantially larger effect in neutron-rich matter at densities $\rho \gtrapprox 10^{12}$ g/cm^3.

3.2.2 Mean Field Effects

Interactions in the medium alter the single particle energies, and nuclear mean field theories predict a nucleon dispersion relation of the form

$$E_i(k) = \sqrt{k^2 + M^{*2}} + U_i \equiv K(k) + U_i \,, \tag{3.11}$$

where M^* is the nucleon effective mass and U_i is the mean field energy shift. For neutron-rich conditions, the neutron potential energy is larger due the iso-vector nature of the strong interactions. The difference $\Delta U = U_n - U_p$ is directly related to the nuclear symmetry energy, which is the difference between the energy

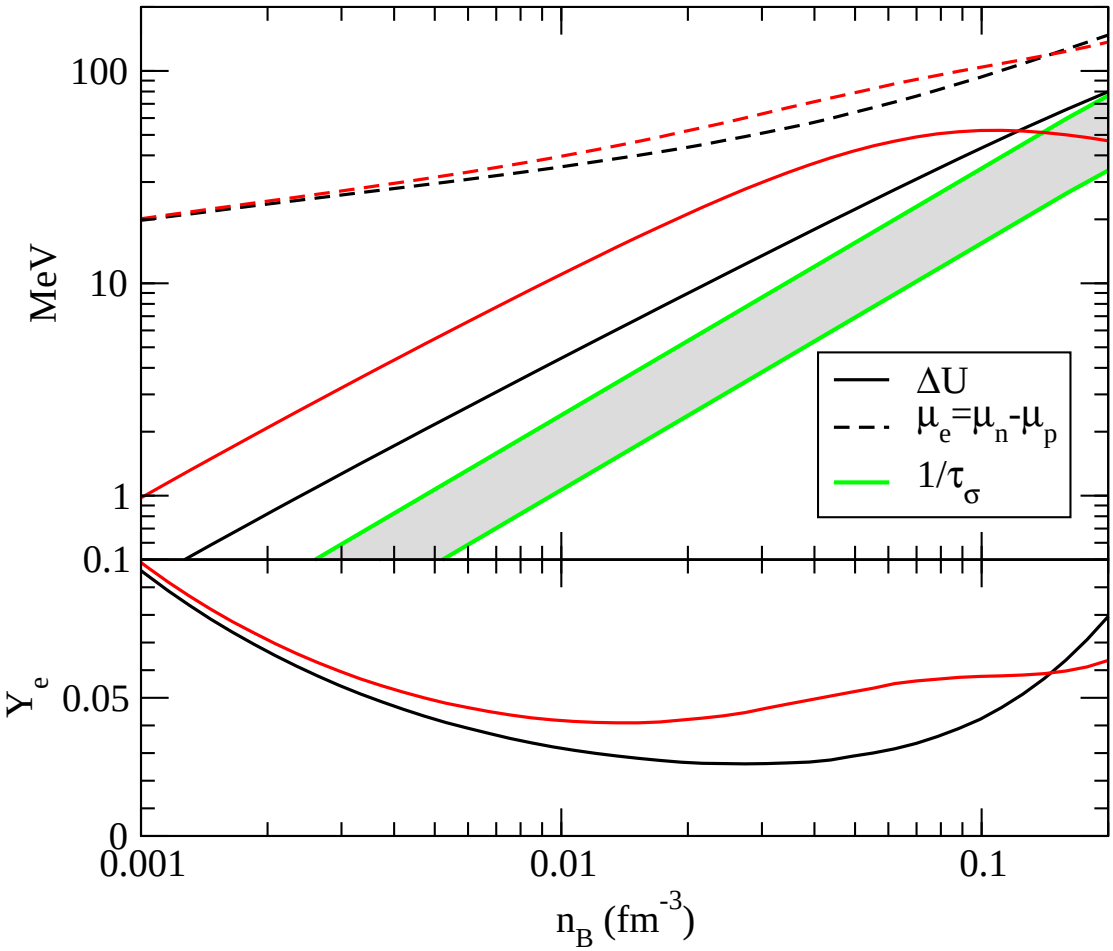

Figure 3.1: *Top Panel:* The electron chemical potential (dashed lines) and $\Delta U = U_n - U_p$ (solid lines) are shown as a function of density for the two equation of state models (IUFSU: red curves and GM3: black curves) in beta-equilibrium for $Y_\nu = 0$ and $T = 8$ MeV. The grey band shows an approximate range of values for inverse spin relaxation time calculated in Bacca, et al. (2011) and is discussed in connection with collisional broadening. *Bottom Panel:* The equilibrium electron fraction as a function of density for the two equations of state shown in the top panel.

per nucleon in neutron matter and symmetric nuclear matter. Ab-intio methods using Quantum Monte Carlo reported in Akmal et al. (1998) and Gandolfi et al. (2012), and chiral effective theory calculations of neutron matter by Hebeler & Schwenk (2010) suggest that the symmetry energy at sub-nuclear density is larger than predicted by many mean field models currently employed in supernova and neutron star studies (for a review see Steiner *et al.* (2005)). To highlight its importance we choose two models for the dense matter equation of state: (i) the GM3 relativistic mean field theory parameter set without hyperons (Glendenning & Moszkowski 1991) where the symmetry energy is linear at low density; and (ii) the IU-FSU parameter set (Fattoyev *et al.* 2010) where the symmetry energy is non-linear in the density and large at sub-nuclear density.

The electron chemical potential (dashed lines) and neutron proton potential energy difference (solid lines) for these two models are shown as a function of density in beta-equilibrium in figure 3.1. Here $Y_\nu = 0$ as a function of density with an assumed temperature of 8 MeV. At sub-nuclear densities, the IU-FSU ΔU is always larger than the GM3 ΔU value due to the larger sub-nuclear density symmetry energy in the former. The electron chemical potential as a function of density, as well as the equilibrium electron fraction, is shown in figure 3.1 for both models. In beta-equilibrium, models with a larger symmetry energy predict a larger electron fraction for a given temperature and density and therefore a larger electron chemical potential. Therefore, IU-FSU has a larger equilibrium μ_e than GM3 and $\nu_e + n \rightarrow e^- + p$ will experience relatively more final state blocking. However, as we show below, the inclusion of ΔU in the reaction kinematics is needed for consistency.

To elucidate the effects of ΔU we set $M^* = M$ and note that this assumption

can easily be relaxed (Reddy et al. 1998) and it does not change the qualitative discussion below. Because in current equation of state models the potential, U_i, is independent of the momentum, k, this form of the dispersion relation results in a free Fermi gas distribution function with single particle energies $K(k)$ for nucleons of species i, but with an effective chemical potential $\tilde{\mu}_i \equiv \mu_i - U_i$. This fact was emphasized in Burrows & Sawyer (1998), and used to show that it was unnecessary to explicitly know the values of the nucleon potentials for a given nuclear equation of state (which are often not easily available from widely used nuclear equations of state in the core-collapse supernova community) when calculating the neutral current response of the nuclear medium. Clearly, if both μ_i and $\tilde{\mu}_i$ are known, then U_i can be easily obtained. This implies that for a given temperature, density and electron fraction, the neutral current response function is unchanged in the presence of mean field effects, as the kinematics of the reaction are unaffected by a constant offset in the nucleon single particle energies. In contrast, the kinematics of the charged current reaction are affected by the difference between the neutron and proton potential and the charged current response is altered in the presence of mean field effects.

Inspecting the response function in Eq. 3.4 and the dispersion relation in Eq. 3.11 it is easily seen that the mean field response

$$S_{\rm MF}(q_0, q) = \frac{M^2 T}{\pi q \left(1 - e^{-z}\right)} \ln \left\{ \frac{\exp\left[\left(\tilde{e}_{\rm min} - \tilde{\mu}_2\right)/T\right] + 1}{\exp\left[\left(\tilde{e}_{\rm min} - \tilde{\mu}_2\right)/T\right] + \exp\left[-z\right]} \right\}, \tag{3.12}$$

where

$$\tilde{e}_{\rm min} = \frac{M}{2q^2}(q_0 + U_2 - U_4 - q^2/2M)^2\,, \tag{3.13}$$

is obtained from the free gas response by the replacements

$$\begin{aligned} \mu_i &\rightarrow \tilde{\mu}_i = \mu_i - U_i \\ q_0 &\rightarrow \tilde{q}_0 = q_0 + U_2 - U_4 \end{aligned} \tag{3.14}$$

and $q \rightarrow q$. Therefore, we see that the potential difference $\Delta U = \pm(U_2 - U_4)$ affects reaction kinematics and cannot be subsumed in the redefinition of the chemical potentials (to yield the same individual number densities).

Because $\Delta U \gtrapprox \epsilon_\nu$ for neutrino energies of interest in the decoupling region, it introduces strong asymmetry between the electron neutrino and antineutrino charged current interactions because the Q value for the reaction $\nu_e + n \rightarrow e^- + p$ is increased by $\Delta U = U_n - U_p$ and for $\bar{\nu}_e + p \rightarrow e^+ + n$ it is reduced by the same amount. Since $\Delta U < \mu_e$, this amount of energy is often not enough to put the final state electron above the Fermi surface. However, it is enough to put the final state electron in a relatively less blocked portion of phase space resulting in an exponential enhancement of the cross-section for ν_e. This is shown in figure 3.2, where the differential cross-section integrated over angle for charged current absorption is plotted as a function of the final lepton energy. The neutrino energy is set to 12 MeV and the conditions of the medium are $T = 8$ MeV, and $n_B = 0.02\,\mathrm{fm}^{-3}$ and $Y_e = 0.027$. The peak of the differential cross-section is shifted by about ΔU up (down) in ε_{e^-} (ε_{e^+}) for electron (anti-)neutrino capture. This shift significantly increases the available phase space for the final state electron in $\nu_e + n \rightarrow e^- + p$. The (arbitrarily scaled) phase space factor $p_e E_e (1 - f_e)$ is also plotted and the peak of $1/V d\sigma/dq_0$ approximately follows this relation. As was argued in section 3.2.1, the rate of $\bar{\nu}_e + p \rightarrow e^+ + n$ should also be approximately proportional to this phase space factor and be exponentially suppressed. This is seen in the figure 3.2.

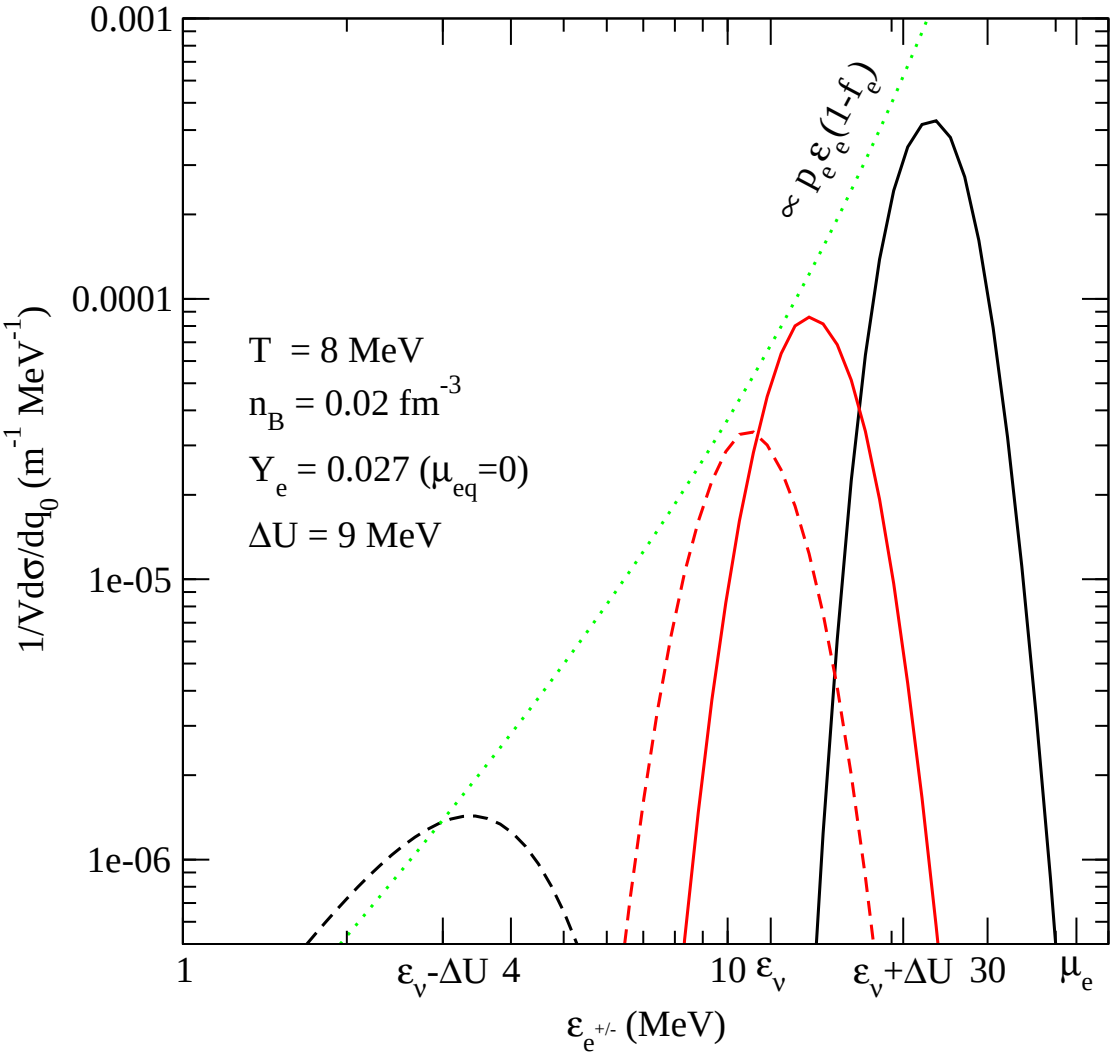

Figure 3.2: Angle integrated differential cross sections for a 12 MeV neutrino. The solid lines correspond to the reaction $\nu_e + n \rightarrow e^- + p$ and the dashed lines correspond to $\bar{\nu}_e + p \rightarrow e^+ + n$. The black lines are calculations in which mean field effects have been included, while the red lines are calculations in which the mean field effects have been ignored. The green dotted line corresponds to the available electron phase space, arbitrarily scaled. The assumed background conditions are $T = 8$ MeV, and $n_B = 0.02\,\mathrm{fm}^{-3}$. The electron fraction is 0.027, which corresponds to beta equilibrium for the given temperature, density, and the assumed nuclear interactions. The nucleon potential difference is $U_n - U_p = \Delta U = 9\,\mathrm{MeV}$. All cross-sections are for the same baryon density and electron fraction (i.e. all assume the same $\tilde{\mu}$ for the neutrons and protons).

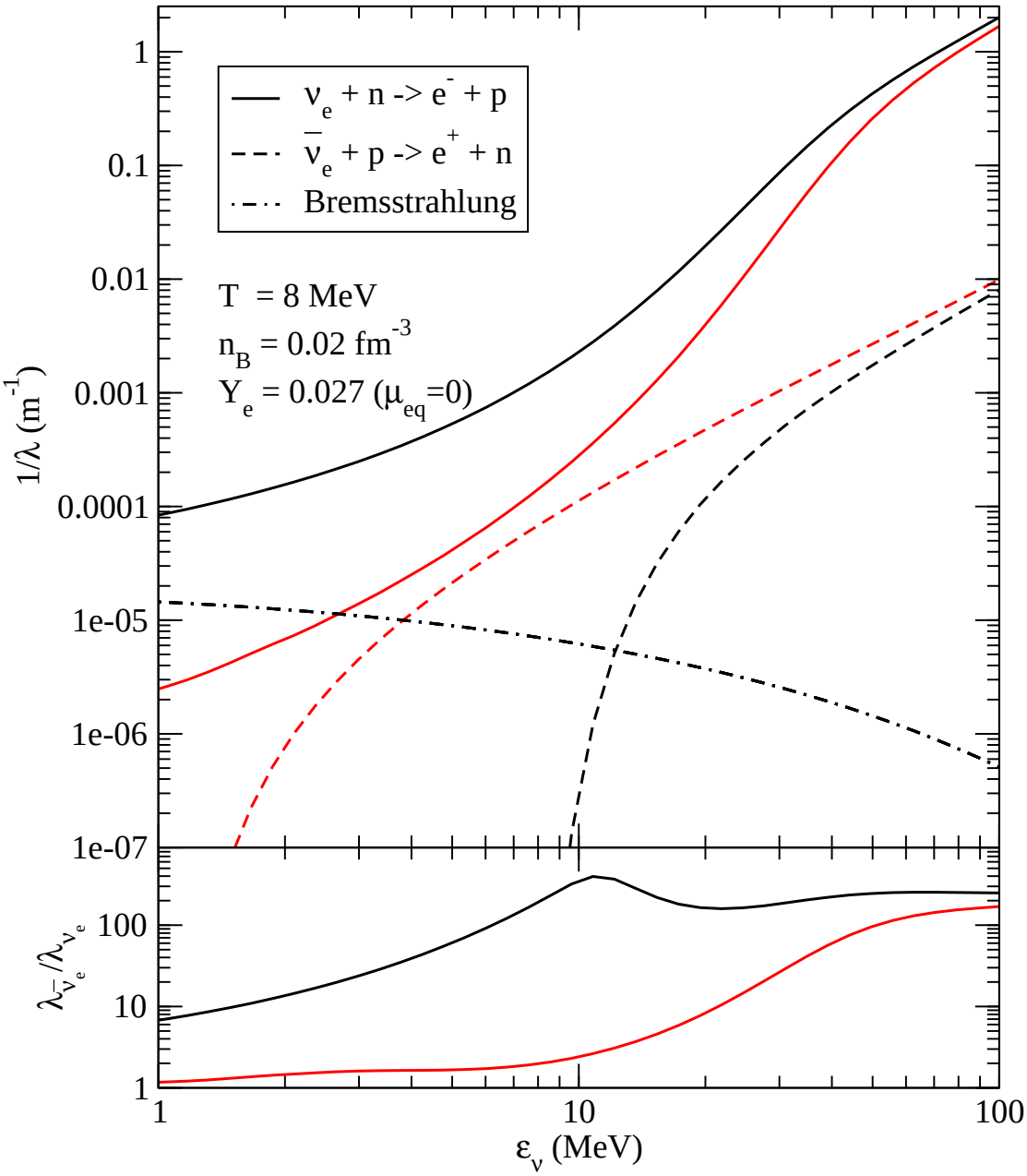

Figure 3.3: The top panel shows the total absorption inverse mean free path as a function of incoming neutrino energy for electron neutrinos (solid lines) and electron antineutrinos (dashed lines). The dot-dashed line shows the effective bremsstrahlung inverse mean free path. In both panels the black lines include mean field effects and the red lines assume a free gas response function. The bottom panel shows the ratio of the total electron neutrino capture rate to the total electron antineutrino capture rate. Beta-equilibrium has been assumed and the temperature has been fixed at 8 MeV.

In figure 3.3, the inverse mean free path ($\lambda^{-1} = \sigma/V$) is shown as a function of neutrino energy for the same conditions considered in figure 3.2. At low energies the electron neutrino mean free path is reduced when mean fields are correctly incorporated, but at larger neutrino energies the presence of mean fields becomes less important and the mean free paths with and without mean fields asymptote to each other. The electron antineutrino mean free path is reduced relative to the free gas result and the presence of a threshold at the potential difference ΔU is evident in the mean field calculation. The effective bremsstrahlung mean free path is also plotted. This is calculated assuming the secondary neutrinos are in thermal equilibrium with the background, which is a good approximation for electron antineutrino destruction. For electron antineutrinos at low energies, bremsstrahlung dominates the capture rate. Mean field effects push the energy region were bremsstrahlung is dominant to larger neutrino energies. This suggests that varying the assumed bremsstrahlung rate will also affect the spectrum of the electron antineutrinos. In the bottom panel, the ratio of the electron antineutrino mean free path to the electron neutrino mean free path is shown as a function of energy with and without the affect of mean fields. The large asymmetry induced between electron neutrino and antineutrino charged current interactions when mean fields are properly included is plainly visible.

The formalism of Reddy et al. (1998) includes this effect, and was used to calculate the neutrino interaction rates employed in the models presented in (Roberts et al. 2012) and in section 3.3 of this work. However, the formulae in Bruenn (1985) and Burrows & Sawyer (1999) for charged current rates neglect the potential energy difference in the nucleon kinematics. In Burrows & Sawyer (1999) procedure is advocated for including mean fields in which the effective chemical

potential, $\tilde{\mu}_i$ of each species is calculated from the given number density and temperature by inverting the free Fermi gas relation, then the response is assumed to be the free gas response but with the effective chemical potentials in place of the actual chemical potentials. This prescription is incorrect because while it accounts for the location of the Fermi surface of the nucleons it fails to account for the presence of a potential energy difference between incoming and outgoing nucleon states. This amounts to assuming $\mu \rightarrow \tilde{\mu}$, so that in Eq. 3.4 $\tilde{q}_0 \rightarrow q_0$ and the response becomes the non-interacting response for the given density and electron fraction. When the potential energies of the incoming and outgoing nucleons states are equal, as in symmetric matter, or for neutral current reactions this prescription results in the correct expression, but in asymmetric matter and for charged current reactions it is in error. To obtain the correct expression for the mean field polarization function from the free gas results of Burrows & Sawyer (1999) it is necessary to make *both* replacements given in equation 3.14.

3.2.3 Correlations and Collisional Broadening

In addition to the mean field energy shift, interactions correlate and scatter nucleons in the medium. Effects due correlations have been investigated in the Random Phase Approximation (RPA), where specific long-range correlations are included by summing single-pair "bubble" or particle-hole diagrams. This ensures consistency between the response functions and the underlying equation of state in the long wavelength limit. For charged currents, calculations reported in Burrows & Sawyer (1999) and Reddy *et al.* (1999) indicate that the suppression is density and temperature dependent. It can be as large as a factor of 2 at supra nuclear density, but at densities of relevance to the neutrino sphere where $\rho \lessapprox 10^{13}$ g/cm^3

the corrections are $\approx 20\%$. More importantly, the suppression found in Burrows & Sawyer (1999) and Reddy *et al.* (1999) for the charged current rate is a weak function of reaction kinematics and can viewed as a overall shift of the response in Fig. 3.2. The energy and momentum restrictions discussed previously apply also to the RPA response, and the mean field energy shift is important to include in the calculation of the particle-hole diagrams. They were included in Reddy *et al.* (1999) but omitted in Burrows & Sawyer (1999).

The excitation of two or more nucleons by processes such as $\nu_e + n + n \rightarrow n + p + e^-$ and $\nu_e + n + p \rightarrow p + p + e^-$ alter the kinematics of the charged current reaction. Typically, these two-particle reactions introduce modest corrections to the single-particle response when the quasi-particle life-time is large. However, they can dominate when: (i) energy-momentum requirements are not fulfilled by the single particle reaction; (ii) final state Pauli blocking requires large energy and momentum transfer; (iii) or both. Such circumstances are encountered in neutron star cooling, where the reaction $n \rightarrow e^- + p + \bar{\nu}_e$ is kinematically forbidden at the Fermi surface under extreme degeneracy unless the proton fractions $x_p \gtrapprox 10\%$ (Lattimer et al. 1991, Pethick 1992). Instead, the two-particle reaction $n + n \rightarrow e^- + p + \bar{\nu}_e$, called the modified URCA reaction, is the main source of neutrino production (Friman & Maxwell 1979). At temperatures encountered in PNS energy-momentum restrictions do not forbid, but instead as discussed earlier, frustrate the single-particle reactions due to final state blocking.

The excitation of two particle states in neutral current reactions has been included in a unified approach described in Lykasov et al. (2008) and incorporated into the total response function by introducing a finite quasi-particle life-time. This naturally leads to collisional broadening allowing the response to access

multi-particle kinematics and alters both the overall shape and magnitude of the response function (Hannestad & Raffelt 1998, Lykasov et al. 2008). Here, as a first step, we adapt the general structure of the response function from Lykasov et al. (2008) to show that two-particle excitations play an important role in the charged current process.

Our ansatz for the charged current response function with collisional broadening is

$$S(q_o, q) = \frac{T\ z}{1 - \exp(-z)} \int \frac{d^3p}{(2\pi)^3} \frac{f_4(\epsilon_{p+q}) - f_2(\epsilon_p)}{\Delta\epsilon_{p+q} + \hat{\mu}} I(\Gamma) \tag{3.15}$$

$$I(\Gamma) = \frac{1}{\pi} \frac{\Gamma}{(\tilde{q}_0 - \Delta\epsilon_{p+q})^2 + \Gamma^2}\,, \tag{3.16}$$

where as before $z = (q_0 + \hat{\mu})/T$ and $\Delta\epsilon_{p+q} = \epsilon_{p+q} - \epsilon_p$, and $\Gamma = 1/\tau$ where τ is the neutron quasi-particle lifetime. Effectively, the response in Eq. 3.16 relaxes the kinematic constraint for the single-nucleon excitation $q_0 = E_2(p) - E_4(|\vec{p}+\vec{q}|)$, and smears the response over a width $\propto \Gamma$. The Lorentzian form of the smearing is obtained in the relaxation time approximation discussed in Lykasov et al. (2008) and is valid when $q_0\tau \ll 1$. The quasiparticle τ is a function of the quasi-particle momentum, q, q_0 and the ambient conditions. Its magnitude and functional form at long-wavelength is constrained by conservation laws. For the vector-response, $\tau \to \infty$ in the limit $q \to 0$ due to vector current conservation. However, since spin is not conserved by strong tensor and spin-orbit interactions, the nucleon spin fluctuations occur even at $q \to 0$ and the associated spin relaxation time τ_σ is finite (Hannestad & Raffelt 1998). Further, because the spin response dominates the charged current reaction, we shall use the form in Eq. 3.16 only to modify the spin part of the charged current response.

Calculations in Bacca et al. (2011) of the spin relaxation time τ_σ in the long-

wavelength $q \to 0$ limit indicate it decreases rapidly with both density and temperature. The typical range of values of $1/\tau_\sigma$ obtained from Bacca et al. (2011) but including a 50% variation over their quoted values is shown in figure 3.1 for conditions in the neutrino sphere region. Using these values as a guide we study the effects of collisional broadening on the ν_e and $\bar{\nu}_e$ cross-sections. The differential cross-section for the axial portion of the process $\nu_e + n \to p + e^-$ is shown in figure 3.4 for $T = 8$ MeV, $n_B = 0.02\,\mathrm{fm}^{-3}$, and $Y_e = 0.027$. The initial neutrino energy is $E_{\nu_e} = 12$ MeV. As before the differential cross-section is a plotted as function of the outgoing electron energy. The result with $\Gamma \to 0$ recovers the single-particle response with the mean field energy shift included. Representative values of $\Gamma = 1, 2, 4$ MeV where chosen to approximately reflect the findings of Bacca et al. (2011) for these ambient conditions. The collisional broadening seen in figure 3.4 is quite significant. It increases the the axial portion of the cross-section by approximately $20\%, 44\%$ and 80%, for $\Gamma = 1, 2, 4$ MeV, respectively. Together, the mean field energy shift and collisional broadening push strength to regions where electron final state blocking is smaller resulting in an overall increase in the electron neutrino absorption rate.

While mean field effects reduce the $\bar{\nu}_e$ cross-section, collision broadening will tend to increase it by accessing kinematics where $-q_0$ is larger. This is shown in the inset of figure 3.4 where the $\bar{\nu}_e$ cross-section for the same ambient conditions and for $E_{\bar{\nu}_e} = 12$ MeV is plotted as a function of the positron energy $E_e^+ = E_\nu - q_0$. The units are arbitrary and the plots only serve to illustrate the relative effect of multi-pair excitations. We choose the same values of Γ as for the ν_e case. Here broadening due to multi-pair excitations has a a more significant effect than for ν_e absorption. However, despite this enhancement, the response that includes the

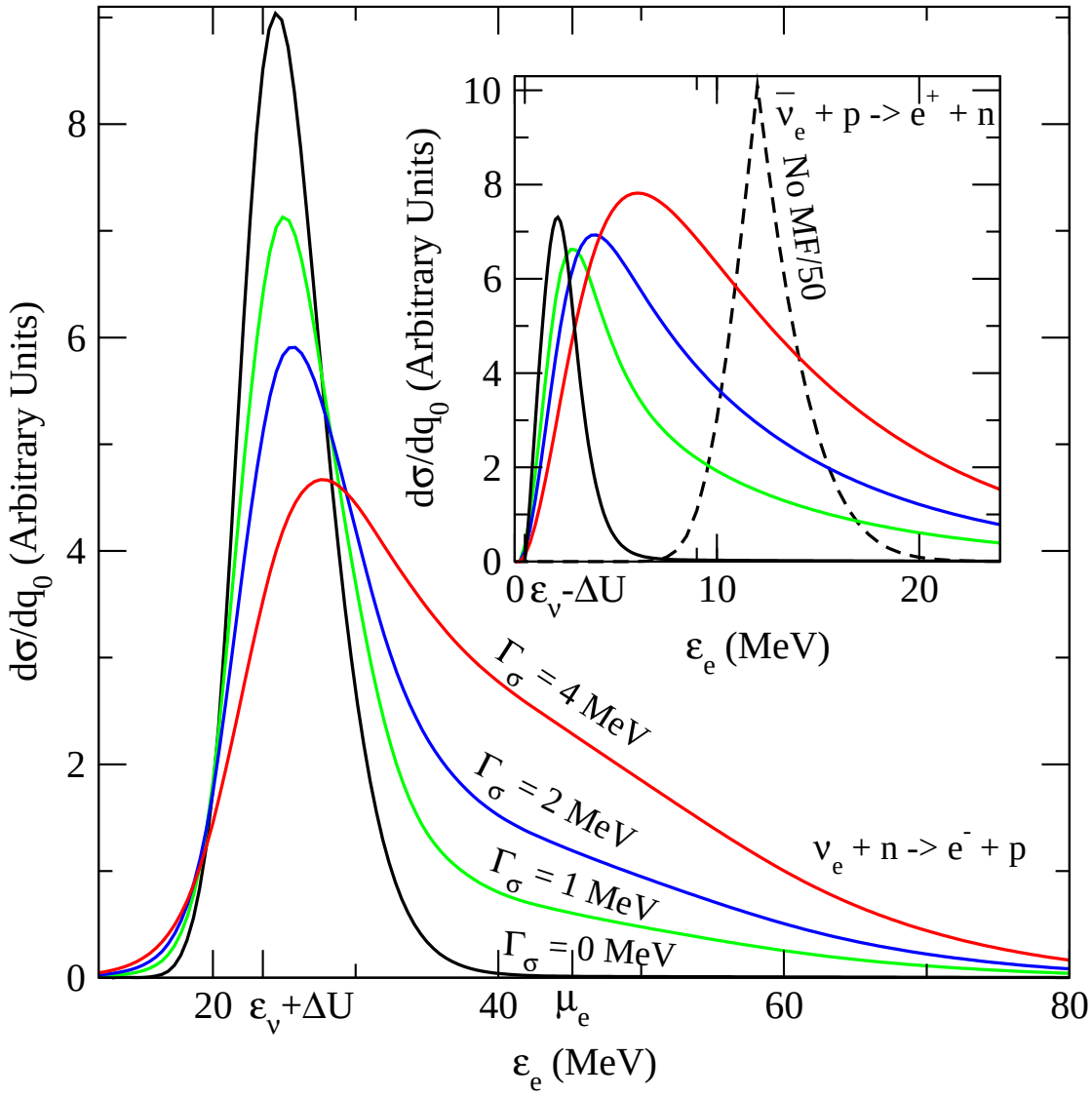

Figure 3.4: The axial portion of the ν_e (main panel) and $\bar{\nu}_e$ (inset) absorption cross-section including collisional broadening. This shifts a significant fraction of the response to larger E_e where there is larger lepton phase space available. The ambient conditions and neutrino energy are the same as those in figure 3.2.

mean field energy shift and the collisional broadening is still much smaller than the free gas response.

We extend the ansatz in Eq. 3.16 to include correlations between particle-hole excitations due to residual interactions in the spin-isospin channel using the RPA. As a first step, we employ a simple interaction in the particle-hole channel. towards determining the strength distribution of the charged current response function, we refrain from making more quantitative estimates for the change in the ν_e and $\bar{\nu}_e$ cross-sections. Qualitatively, its seems clear that collisional broadening will increase both cross-sections. For ν_e, the mean field energy shift and collisional broadening both act to enhance absorption rate. For $\bar{\nu}_e$, collisional broadening is unlikely to overcome the suppression due to the mean field energy shift.

To obtain quantitative results, we include RPA correlations by summing the and multi-particle excitations by current process and we hope to address these issues in a separate publication. In the following discussion of PNS evolution and neutrino spectra, we set aside these effects due to collisional broadening and calculate the neutrino interactions only including the mean field energy shifts calculated as described in Reddy et al. (1998).

3.3 Proto-Neutron Star Evolution

To illustrate the affect of the correct inclusion of mean field effects in charged current interaction rates, as well as the importance of the nuclear symmetry energy, three PNS cooling models are described here. The models have been evolved using the multi-group, multi-flavor, general relativistic variable Eddington factor code described in Roberts (2012) which follows the contraction and neutrino losses of a PNS over the first ~ 45 seconds of its life. These start from the same post

core bounce model considered in Roberts (2012) and follow densities down to about $10^9\,\mathrm{gcm}^{-3}$. Therefore, they do not simulate the NDW itself but they do encompass the full neutrino decoupling region.

One model was run using neutrino interaction rates that ignore the presence of mean fields, but were appropriate to the local nucleon number densities (i.e. the re-normalized chemical potentials, $\tilde{\mu}_i$, were used but we set $\Delta U = 0$). The equation of state used was GM3. This model was briefly presented in Roberts (2012). Another model was calculated that incorporated mean field effects in the neutrino interaction rates and used the GM3 equation of state. Additionally, the bremsstrahlung rates of Hannestad & Raffelt (1998) were reduced by a factor of 4 as suggested by Hanhart et al. (2001). A third model was run using the IU-FSU equation of state and including mean field effects but with everything else the same as the GM3 model. The neutrino interaction rates in all three models were calculated using the relativistic polarization tensors given in Reddy et al. (1998) with the weak magnetism corrections given in Horowitz & Pérez-García (2003).

In the top panel of figure 3.5, the average electron neutrino and antineutrino energies are shown as a function of time for the three models. As was described in Roberts (2012), including mean field effects in the charged current interaction rates significantly reduces the average electron neutrino energies because the decreased mean free paths (relative to the free gas case) cause the electron neutrinos to decouple at a larger radius in the PNS and therefore at a lower temperature. Conversely, for the electron antineutrinos the mean free path is increased, they decouple at a smaller radius and higher temperature, and the average energies are larger. The antineutrino energies are also slightly larger than the values reported in Roberts (2012) because of the reduced bremsstrahlung rate.

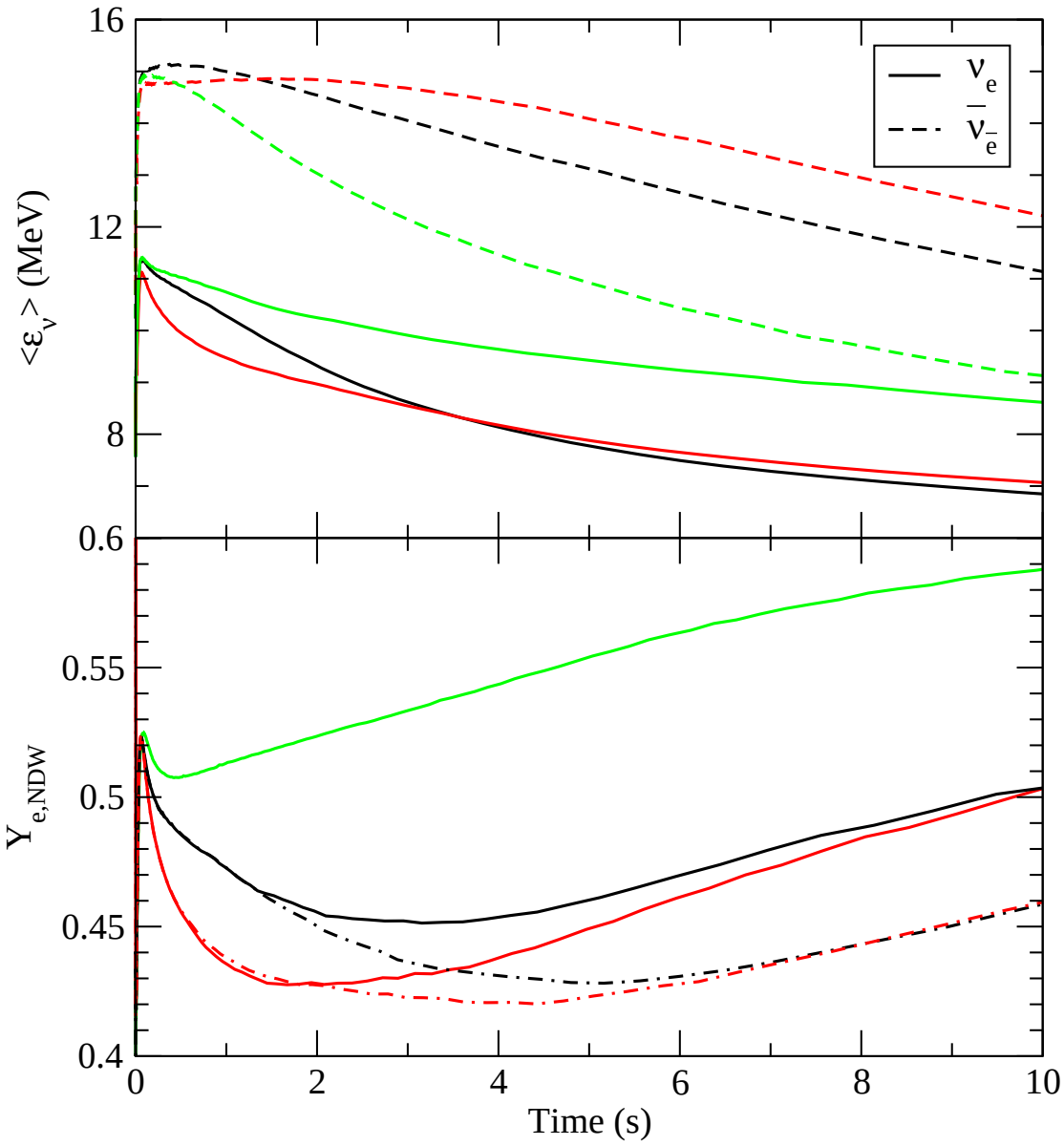

Figure 3.5: *Top panel*: First energy moment of the outgoing electron neutrino and antineutrino as a function of time in three PNS cooling simulations. The solid lines are the average energies of the electron neutrinos and the dashed lines are for electron antineutrinos. The black lines correspond to a model which employed the GM3 equation of state, the red lines to a model which employed the IU-FSU equation of state, and the green lines to a model which ignored mean field effects on the neutrino opacities (but used the GM3 equation of state). *Bottom panel*: Predicted neutrino driven wind electron fraction as a function of time for the three models shown in the top panel (solid lines), as well as two models with the bremsstrahlung rate reduced by a factor of four (dot-dashed lines). The colors are the same as in the top panel.

Additionally, there are significant differences between the two models which include mean field effects but use different equations of state. As was described above, the GM3 equation of state has a smaller symmetry energy than the IU-FSU equation of state at sub-nuclear densities and therefore has a smaller ΔU in the neutrino decoupling region. This suggests that GM3 should have slightly larger electron neutrino average energies and slightly lower average electron antineutrino energies. The results of self-consistent PNS simulations are somewhat more complicated than this simple picture, mainly because the equilibrium electron fraction near the neutrino sphere also depends on the nuclear symmetry energy which affects the charged current rates (see figure 3.1). Still, there is a larger difference between the average electron neutrino and antineutrino energies throughout the simulation (relative to GM3) when the IU-FSU equation of state is used, as expected.

The moments of the escaping neutrino distribution along with the electron neutrino number luminosities can be used to calculate an approximate NDW electron fraction (Qian & Woosley 1996)

$$Y_{e,\mathrm{NDW}} \approx \left[1 + \frac{\dot{N}_{\bar{\nu}_e}\langle\sigma(\epsilon)_{p,\bar{\nu}_e}\rangle}{\dot{N}_{\nu_e}\langle\sigma(\epsilon)_{n,\nu_e}\rangle}\right]^{-1}, \tag{3.17}$$

where $\dot{N}$ are the neutrino number luminosities and $\langle\sigma(\epsilon)\rangle$ are the energy averaged charged current cross-sections in the wind region. The approximate NDW electron fraction as a function of time for the three models is shown in the bottom panel of figure 3.5. The low density charged current cross-sections from Burrows et al. (2006) were used. First, it is clear from this plot that mean field effects significantly decrease the electron fraction in the wind. This is mainly due to the increased difference between the electron neutrino and antineutrino average energies caused by the effective Q value induced by the mean field potentials. Second, increasing

the sub-nuclear density symmetry energy decreases the electron fraction in the wind. This in turn implies that nucleosynthesis in the NDW may depend on the nuclear symmetry energy because it is sensitive to electron fraction in the wind (e.g. Hoffman et al. 1997). Still, this affect is not particularly strong because the increase in the electron neutrino cross section for increased ΔU is partially mitigated by the larger equilibrium electron fraction predicted for models with a larger nuclear symmetry energy.

3.4 Conclusions

In this work, we have discussed the physics of charged current neutrino interactions in interacting nuclear matter at densities and temperatures characteristic of the neutrino decoupling region in PNS cooling. Additionally, models of PNS cooling have been run to assess the importance of changes in the charged current rates to the properties of the emitted neutrinos. Our main findings are:

• The mean-field shift of the nucleon energies alters the kinematics of the charged current reactions. Under neutron-rich conditions it increases the Q-value for ν_e absorption and decreases it for $\bar{\nu}_e$. Due to final state blocking (electron blocking for electron neutrino capture and neutron blocking for electron antineutrino capture), the increase in the Q value leads to an exponential ($\exp(\Delta U/T)$) increase in the ν_e cross-section absorption and reduces the $\bar{\nu}_e$ absorption cross-section by $\exp(-\Delta U/T)$.

• The formulae for the charged rates developed in Burrows & Sawyer (1999) and Bruenn (1985) neglect these effects and the prescription for incorporating mean field energy shifts outlined in Burrows & Sawyer (1999) is inconsistent.

• The nuclear symmetry energy at sub-nuclear density plays a crucial role in

determining the magnitude of the difference between the mean field neutron and proton potential energies, and through its effect on the Q-values increases the difference between the mean free paths of ν_e and $\bar{\nu}_e$.

• Our *preliminary* work indicates that multi-pair excitations favor kinematics where final state electron blocking is small because the energy/momentum constraints present when only single particle-hole excitations are considered are relaxed. This is analogous to the importance of the modified URCA process in neutron star cooling. In contrast to mean field effects, multi-pair excitations decrease the mean free paths of both electron neutrinos and electron antineutrinos. Although it is difficult to determine from the limited and approximate calculations performed for this work, it seems most likely that multi-pair excitations will bring the average electron neutrino and antineutrino energies closer to one another.

• As was shown in Roberts (2012), the changes to the charged current mean free paths induced by the correct inclusion of mean fields decreases the average energy of the electron neutrinos and increases the average energy of the anti-electron neutrinos emitted during PNS cooling. The difference is relatively large, it significantly alters the predicted electron fraction in the NDW, and may have observable effects. This result has recently been independently confirmed by Martínez-Pinedo et al. (2012).

• We have also have directly shown that increasing the value of the nuclear symmetry energy at sub-nuclear densities decreases the electron fraction in the neutrino driven wind. Therefore, NDW nucleosynthesis may put some constraint on the poorly known density dependence of the nuclear symmetry energy, or vice versa. This potential astrophysical constraint is in addition those discussed in Lattimer & Lim (2012). We emphasize that it may be hard to disentangle this

from the effects of multi-particle excitations, both on the charged current reactions themselves and on the (related) bremsstrahlung rate. This effect is also partially compensated by the symmetry energy dependence of the beta-equilibrium electron fraction.

• The reduced mean free path of ν_e is also likely to affect the de-leptonization time of the proto-neutron star and may account for differences in time-scales observed in simulations performed using equations of state with different symmetry energies.

The largest uncertainty in the work presented here is the role of multi-particle excitations in the charged current response. This warrants further study before we can make reliable predictions for the supernova neutrino spectra, especially since the difference between ν_e and $\bar{\nu}_e$ spectra affects nucleosynthesis, collective neutrino oscillations and direct detection of supernova neutrinos. The sensitivity to the symmetry energy is potentially exciting since supernova neutrino detection and nucleosynthetic yields may be able to provide useful constraints.

Chapter 4

Proto-Neutron Star Cooling with Convection: The Effect of the Symmetry Energy

This work was performed in collaboration with Gang Shen, Vincenzo Cirigliano, Jose Pons, Sanjay Reddy, and Stan Woosley. It was published in Physical Review Letters as Roberts et al. (2012).

Abstract

We model neutrino emission from a newly born neutron star subsequent to a supernova explosion to study its sensitivity to the equation of state, neutrino opacities, and convective instabilities at high baryon density. We find the time period and spatial extent over which convection operates is sensitive to the behavior of the nuclear symmetry energy at and above nuclear density. When convection ends within the proto-neutron star, there is a break in the predicted neutrino emission that may be clearly observable.

4.1 Introduction

The hot and dense proto-neutron star (PNS) born subsequent to core-collapse in a type II supernova explosion is an intense source of neutrinos of all flavors. It emits the $3-5\times10^{53}$ ergs of gravitational binding energy gained during collapse as neutrino radiation on a time scale of tens of seconds as it contracts, becomes increasingly neutron-rich and cools. Cooling of the PNS and the concomitant neutrino emission are driven by neutrino diffusion and convection along the lepton number and entropy gradients left behind within the PNS after core-bounce, where the matter density and temperature are in the range $\rho = 2-6\times10^{14}$ g/cm^3 and $T = 5-40$ MeV, respectively (Burrows & Lattimer 1986, Wilson & Mayle 1988, Keil & Janka 1995, Pons et al. 1999, Fischer *et al.* 2010, Hüdepohl *et al.* 2010). While the supernova explosion mechanism and associated fall back of material are expected to influence the neutrino emission at early time (i.e. $t \lesssim 1$ s post bounce) the late time neutrino signal is shaped by the properties of the PNS, such as the nuclear equation of state (EoS), neutrino opacities in dense matter, and other microphysical properties that affect the cooling timescale by influencing either neutrino diffusion or convection (Keil et al. 1995, Pons et al. 1999, Pons et al. 2001a;b).

Here, we present one-dimensional hydrostatic models of PNS evolution including convection out to late times for two EoSs. We include approximate convective transport via mixing length theory along with diffusive gray neutrino transport, both consistent with the underlying EoS. This allows us to gauge the importance of convection and the effect of medium modifications to the neutrino opacities in dense matter to the temporal characteristics of the neutrino signal. The basic framework for PNS evolution is similar to that described in Pons et al. (1999),

except that a treatment of convection is included. We find that the behavior of the nuclear symmetry energy (which is a measure of the energy difference between dense neutron matter and symmetric nuclear matter) at high density significantly influences convection and thereby affects the observable neutrino signal.

Large scale convective overturn of material will directly transport energy and lepton number in the PNS and alters the gradients along which neutrinos diffuse, thereby strongly affecting the neutrino signal accompanying PNS formation. It has long been recognized that the outer PNS mantle is unstable to convection soon after the passage of the supernova shock, due to negative entropy gradients (Epstein 1979). This early period of instability beneath the neutrino spheres has been studied extensively in both one and two dimensions, with the hope that it could increase the neutrino luminosities enough to lead to a successful explosion (Burrows 1987, Wilson & Mayle 1988, Keil et al. 1996, Mezzacappa *et al.* 1998, Dessart *et al.* 2006, Buras *et al.* 2006). Although the role of convection at late times was studied in Refs. (Burrows 1987, Wilson & Mayle 1988), this work is the first attempt at exploring its connection to the underlying microphysics and the interplay between modified opacities and convection in shaping the observable neutrino signal.

The early one-dimensional work of Wilson & Mayle (1988) seemed to imply that neutron fingering instabilities and convection enhanced the neutrino luminosity to successfully power a neutrino driven explosion, but this result was subject to tuning of the neutron finger diffusion coefficients. Keil et al. (1996) modeled convection in two-dimensions coupled to EFLD neutrino transport along radial rays. Convective motions extended up to the neutrino sphere, which resulted in a significant increase (a factor of 2) in the total luminosity compared to a one-

dimensional model without a prescription for convection. This work followed the evolution of the PNS out to the latest time with convection included (1.2 seconds). By the end of their simulation, the convective region encompasses almost the entire star. Additionally, there are significant regions of convective under- and over-shoot from the regions that are formally Ledoux unstable. This led them to state that "it is hardly possible to describe the convective activity with a mixing-length treatment in a one-dimensional simulation". Mezzacappa *et al.* (1998) performed similar two-dimensional simulations, but with a different treatment of neutrino transport. They assumed transport was the same along all polar angles. They found convection was significantly suppressed compared to Keil et al. (1996).

The two most recent multi-dimensional studies of PNS convection are Dessart *et al.* (2006) and Buras *et al.* (2006). They both found modest enhancements in the neutrino luminosity at early times (15-20%) and see no evidence for doubly diffusive instabilities. Both groups only follow convection for the first 300 ms of PNS evolution. During this time, the convective region does not expand significantly, in contrast to Keil et al. (1996).

4.2 Mixing Length Theory in Nuclear Matter

We model convection as a diffusive process described by standard time dependent mixing length theory Wilson & Mayle (1988). In Ref. Buras *et al.* (2006) it was shown that hydrodynamic simulations in two-dimensions were well reproduced by a simple mixing scheme in one-dimension, suggesting that this is a reasonable approximation. Further, since convection proceeds efficiently throughout our simulations, our results are not particularly sensitive to the chosen mixing length. The linear growth rates are obtained from the standard Ledoux stability analysis

as

$$\omega^2 = -\frac{g}{\gamma_{n_B}} \left(\gamma_s \nabla \ln(s) + \gamma_{Y_L} \nabla \ln(Y_L) \right), \tag{4.1}$$

where

$$\gamma_{n_B} = \left(\frac{\partial \ln P}{\partial \ln n_B} \right)_{s,Y_L} \gamma_s = \left(\frac{\partial \ln P}{\partial \ln s} \right)_{n_B,Y_L} \gamma_{Y_L} = \left(\frac{\partial \ln P}{\partial \ln Y_L} \right)_{n_B,s}$$

and g, P, s, n_B, and Y_L are the local acceleration due to gravity, the pressure, entropy per baryon, baryon number density and the fraction of leptons in dense matter, respectively. Convective instability sets in for $\omega^2 > 0$. The form of the growth rate clearly implies that there will be a strong interplay between the nuclear EoS and the patterns of convection within the PNS.

This follows Thorne (1977) fairly closely for the GR corrections. First it is useful to write the acceleration due to gravity and the pressure scale height as (which can be easily read off from the TOV equations)

$$g = \frac{G_N}{r^2} \left(m + 4\pi r^3 P/c_L^2 \right) \tag{4.2}$$

$$H_p = \frac{P}{g(\rho + P)/c_L^2} \tag{4.3}$$

If we assume that the motions of the convective blobs are sub-luminal and the local acceleration due to gravity does not change much, the average acceleration due to buoyancy over a mixing length is given by

$$f = \frac{gl}{2n_B} \left(\frac{dn_B}{dr} - \frac{dP}{dr} \left(\frac{\partial n_B}{\partial P} \right)_{s,Y_e,Y_\nu} \right) \tag{4.4}$$

which implies an average convective velocity of

$$\epsilon_C \approx \frac{1}{2} f l = \frac{1}{2} v_C^2 \tag{4.5}$$

$$v_C \approx l \sqrt{\frac{g}{2 n_B} \left(\frac{dn_B}{dr} - \frac{dP}{dr} \left(\frac{\partial n_B}{\partial P} \right)_{s,Y_e,Y_\nu} \right)} \tag{4.6}$$

$$\omega = \sqrt{\frac{g}{2 n_B} \left(\frac{dn_B}{dr} - \frac{dP}{dr} \left(\frac{\partial n_B}{\partial P} \right)_{s,Y_e,Y_\nu} \right)} \tag{4.7}$$

Clearly, ω is just the growth rate of the linear Ledoux instability given above. If the convective element travels a pressure scale height, then comes in to equilibrium with the surrounding medium, we can model this as a diffusive process with a convective "diffusion" coefficient

$$D_C = \frac{V_c l}{3} = \frac{\omega l^2}{3} \tag{4.8}$$

$$\tag{4.9}$$

which gives the convective fluxes as

$$H_c = -\Lambda_h^2 D_C n_B \frac{de}{dr} \tag{4.10}$$

$$F_{e,c} = -\Lambda_e^2 D_C n_B \frac{dY_e}{dr} \tag{4.11}$$

$$F_{\nu,c} = -\Lambda_\nu^2 D_C n_B \frac{dY_\nu}{dr} \tag{4.12}$$

where the Λs are multipliers on the pressure scale height that determine the mixing length. The EFLD energy, neutrino, and electron fraction transport equations are then

$$\frac{dY_\nu}{dt} + \frac{\partial \left(4\pi r^2 e^\phi \left[F_\nu + F_{\nu,c} \right] \right)}{\partial a} = e^\phi S_n \tag{4.13}$$

$$\frac{dY_e}{dt} + \frac{\partial \left(4\pi r^2 e^\phi F_{e,c} \right)}{\partial a} = -e^\phi S_n \tag{4.14}$$

$$\frac{dE}{dt} - \frac{p}{n_b^2} \frac{dn_b}{dt} + e^{-\phi} \frac{\partial \left(4\pi r^2 e^{2\phi} \left[H_\nu + H_c \right] \right)}{\partial a} = 0. \tag{4.15}$$

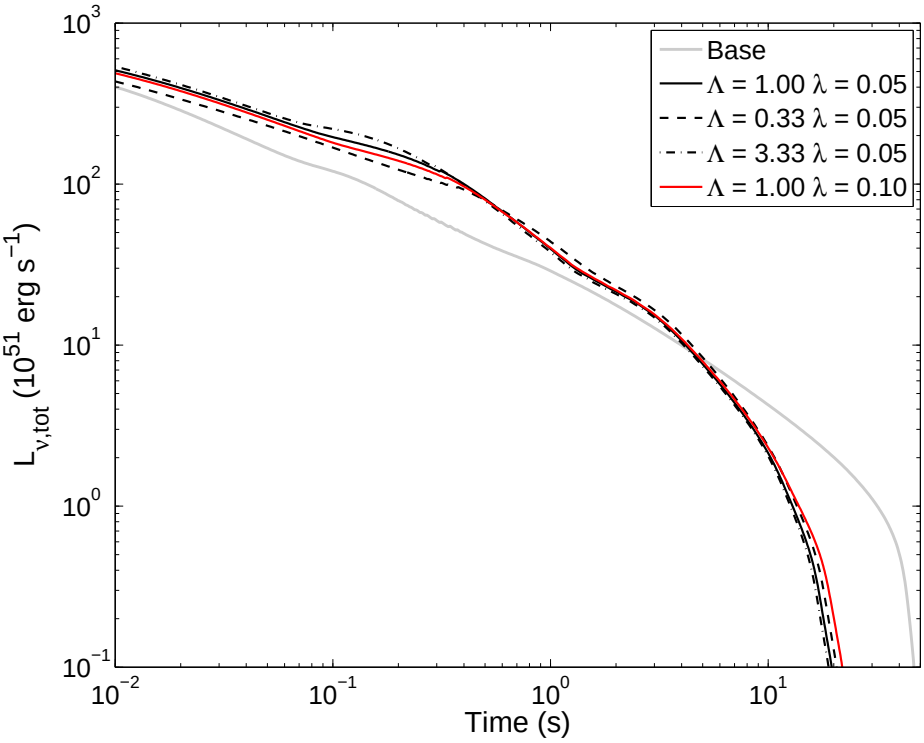

Figure 4.1: Effect of mixing length and convective suppression variation on the neutrino emission from a $1.6M_{\odot}$ PNS. The gray line is the base model which neglects convection. The black and red lines show models including convection where the mixing length parameter Λ is varied. The red line shows a model where the convergence parameter α ($= \lambda$ in the plot) has been varied.

For numerical implementation, these convective quantities must be finite differenced. The zone boundary values will be given by

$$\begin{aligned}
\tilde{v}_{i+1/2} &= \sqrt{\frac{\Delta n_B g_{i+1/2}}{\Delta r(n_{i+1}+n_i)}\left(1-\frac{\Delta P}{2\Delta n_B}\left[\left(\frac{\partial n_B}{\partial P}\right)_{i+1}+\left(\frac{\partial n_B}{\partial P}\right)_i\right]\right)} \\
&\quad \times \exp\left(-\lambda/\alpha\right) \\
&= \sqrt{-\frac{\Delta n_B g_{i+1/2}}{\Delta r(n_{i+1}+n_i)}}\sqrt{\alpha}\exp\left(-\lambda/\alpha\right) \qquad (4.16) \\
\alpha &= -1+\frac{\Delta P}{2\Delta n_B}\left[\left(\frac{\partial n_B}{\partial P}\right)_{i+1}+\left(\frac{\partial n_B}{\partial P}\right)_i\right] \qquad (4.17) \\
&= -1+\frac{\Delta P}{2\Delta n_B}\left[\frac{n_{i+1}}{P_{i+1}}\Gamma^{-1}_{i+1}+\frac{n_i}{P_i}\Gamma^{-1}_i\right] \qquad (4.18)
\end{aligned}$$

In the second equation for $\tilde{v}$, the first square root is constant during the transport solve. The adiabatic exponent is defined as $\Gamma = \left(\frac{\partial \ln P}{\partial \ln n_B}\right)_{s,Y}$. We have added an exponential to suppress convection near the edges of convective regions. The parameter λ determines how strong this suppression is. For implementation in the implicit code, derivatives of the fluxes are required (after the fluxes have been finite differenced), which in turn require derivatives of H_p, v_C, etc. with respect to Y_e, Y_ν, and T. In the adiabatic convection picture these can be obtained analytically.

In figure 4.1, we show the effect of varying the mixing length and the parameter λ. The luminosity seems to be fairly insensitive to the variations in these parameters, implying that convection is efficient and giving us hope that our approximate mixing length theory might be fairly parameter independent. The variations in Λ correspond to a difference of two orders of magnitude in the diffusion coefficients. We also note that the energy and number conservation properties of the code are not altered altered when convection is added. Energy conservation can be tuned to be better than the percent level, depending on the time stepping criteria. Number conservation is generally two orders of magnitude better.

In addition to the Ledoux instability, the PNS may be subject to doubly diffusive instabilities due to the lateral transport of composition and energy by neutrinos (Wilson & Mayle 1988, Bruenn & Dineva 1996, Miralles et al. 2000). Early one-dimensional work (Wilson & Mayle 1988) suggested that neutron fingering instabilities and convection significantly enhanced the neutrino luminosity, which powered a successful neutrino driven explosion. It is also possible to extend this MLT for adiabatic convection to doubly diffusive instabilities by just replacing the Ledoux growth rate with the growth rate predicted for the doubly diffusive instability. This would be a more general form of what Wilson & Mayle (1988) did to model neutron fingers. Because the form of the growth rates is more complicated in the doubly diffusive regime (see Miralles et al. (2000)), their derivatives cannot be easily taken analytically. This makes it challenging to put in an implicit code. This has been tried, but for models to run successfully the instability growth rate had to be suppressed when it was smaller than the dynamical timescale. This may not be so inaccurate ,but the models were still numerically unstable after a few seconds of evolution. Accounting for diffusive effects suppressed mantle convection early on slightly when the neutrino mean free path is large due to the low densities, as one would expect. At later times, the convective extent was similar to the Ledoux case. However, more recent two dimensional studies found no evidence of these doubly diffusive instabilities (Buras *et al.* 2006, Dessart *et al.* 2006). Because of this and the increased complexity of treating the doubly diffusive instabilities, we do not include them explicitly in our study.

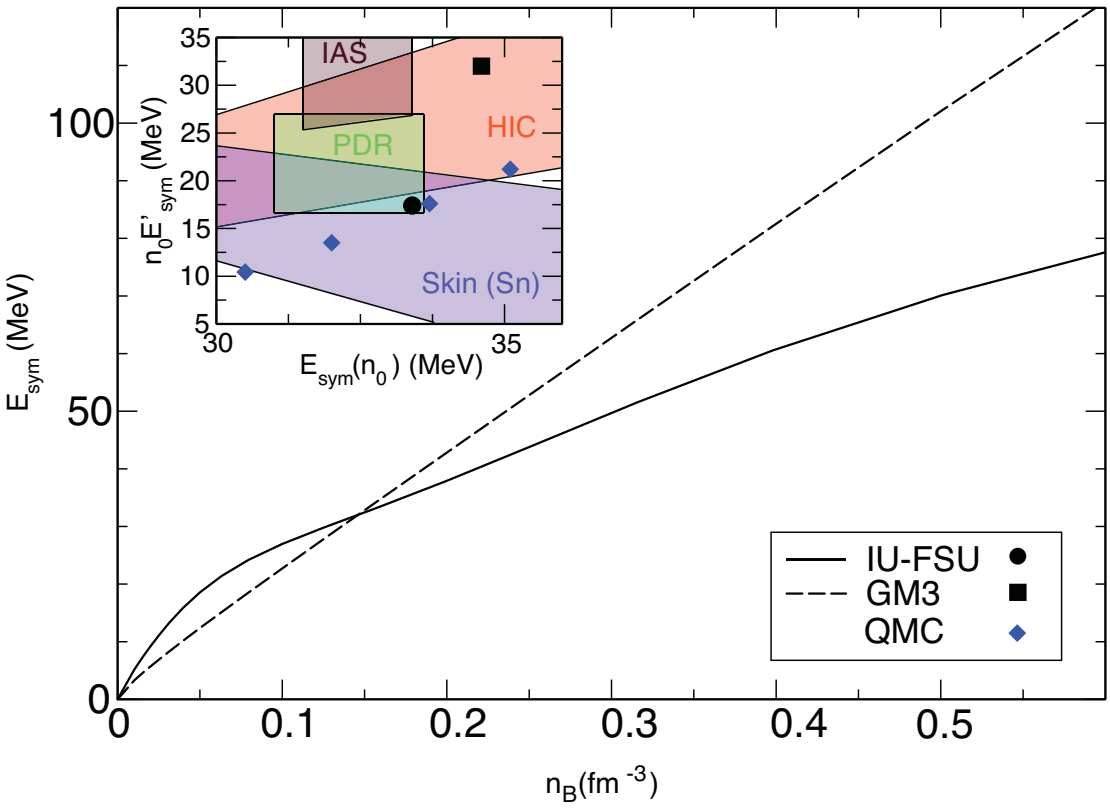

Figure 4.2: The symmetry energy as function of density for the IU-FSU and GM3 EoSs. Inset: $n_0 E'_{\rm sym}$ versus $E_{\rm sym}$ at nuclear saturation density, for IU-FSU (circle), GM3 (square), and QMC (diamonds). The shaded regions correspond to various experimental constraints taken from Ref. Tsang et al. (2011).

4.3 Microphysics and the Nuclear Symmetry Energy

The EoS and neutrino interaction rates are modeled using a relativistic mean field (RMF) model of nuclear interactions. We adopt a non-linear generalization of the original Walecka model described in Fattoyev *et al.* (2010). Here, the nucleon-nucleon interaction energy is calculated in the mean field approximation using effective interactions, which are tuned to reproduce gross observed proper-

ties of nuclei and empirical properties of symmetric nuclear matter at saturation density. Although these empirical constraints provide valuable guidance to constrain aspects of the symmetric nuclear EoS at nuclear densities, the experimental constraints on the properties of neutron-rich matter are relatively weak. The difference between the energy of symmetric matter (equal numbers of neutrons and protons) and pure neutron matter is called the symmetry energy, $E_{\rm sym}(n_B)$, and is defined by $E(n_B, x_p) = E(n_B, x_p = 1/2) + E_{\rm sym}(n_B)\delta^2 + \cdots$. Here, $\delta = (1-2x_p)$ and $E(n_B, x_p)$ is the energy per particle of uniform matter composed of neutrons and protons with total baryon density n_B and proton fraction x_p. In charge neutral matter $x_p = Y_e$ where Y_e is the electron fraction. Various experimental probes of the nuclear symmetry energy and its density dependence in nuclei and heavy-ion collisions are actively being pursued in terrestrial experiments, but are yet to yield strong constraints. These constraints are shown in the inset in Fig. 4.2 and are discussed in Refs. Fattoyev *et al.* (2010), Tsang *et al.* (2011). Quantum Monte Carlo (QMC) results are also shown in the inset in Fig. 4.2. The linear correlation between $E_{\rm sym}$ and $E'_{\rm sym}$ in the QMC results is obtained by varying values of the poorly known three-neutron interaction Gandolfi et al. (2011).

Recent work has shown that the derivative of the symmetry energy with respect to density, denoted as $E'_{\rm sym} = \partial E_{\rm sym}/\partial n_B$, plays a crucial role both in the terrestrial context where it affects the neutron density distribution in neutron-rich nuclei and in astrophysics where it affects the structure and thermal evolution of neutron stars (for a recent review see Ref. Steiner *et al.* (2005)). The pressure of neutron matter at saturation density, $P_{\rm neutron}(n_0) = n_0^2 E'_{\rm sym}$, influences the radii of cold neutron stars Lattimer & Prakash (2001). In neutron-rich nuclei, the neutron-skin thickness is also sensitive to $E'_{\rm sym}(\rho_0)$, so that there exists a linear

correlation between the neutron-skin thickness and neutron star radius Horowitz & Piekarewicz (2001).

To study the sensitivity of PNS evolution to the nuclear symmetry energy we employ two RMF models with different predictions for $E'_{\rm sym}(\rho_0)$. The first EoS is the IU-FSU EoS taken from Fattoyev *et al.* (2010), which includes a non-linear coupling between the vector and iso-vector mesons that allows the symmetry energy to be tuned at high density. The second EoS employed is the GM3 parameter set, where non-linear coupling of the vector meson fields is neglected (Glendenning & Moszkowski 1991). The symmetry energy as a function of density is shown in Fig. 4.2 for the two EoS. The inset in Fig. 4.2 shows current theoretical estimates and experimental constraints on $E_{\rm sym}$ and $n_0 E'_{\rm sym}$ at nuclear density.

In the rest of this letter, we demonstrate that $E'_{\rm sym}(\rho_0)$ plays a role in stabilizing PNS convection at late times and thereby directly affects the PNS neutrino signal. The logarithmic derivatives γ_s and γ_{n_B} are always positive, so that negative entropy gradients always provide a destabilizing influence. For given entropy and lepton gradients, stability is then determined by the ratio γ_{Y_L}/γ_s. The sign and magnitude of γ_{Y_L} is strongly influenced by the density dependence of the nuclear asymmetry energy, so that negative gradients in lepton number can be either stabilizing or destabilizing and the degree to which they are stabilizing varies from EoS to EoS. To clarify this we note that at $T = 0$ and when the neutrino contribution to the pressure is small

$$\left(\frac{\partial P}{\partial Y_L}\right)_{n_B} \simeq n_B^{4/3} Y_e^{1/3} - 4 n_B^2 E'_{\rm sym}(1 - 2Y_e), \tag{4.19}$$

which is a reasonable approximation to the finite temperature result. The first term comes from the electron contribution to the pressure, while the second term is due to nucleons and is negative since both the Fermi and interaction energies

favor a symmetric state. For high densities and low electron fractions, for realistic values of $E'_{\rm sym}$, this leads to negative γ_{Y_L}. Therefore, a larger $E'_{\rm sym}$ leads to negative lepton gradients in the PNS providing a larger stabilizing influence. $E'_{\rm sym}$ also partially determines the equilibrium value of Y_e, which can alter the value of γ_{Y_L}, but this is a smaller effect.

To demonstrate this simply we note that in the vicinity of nuclear saturation density at T=0 and $Y_\nu = 0$ the electron fraction in beta-equilibrium

$$Y_e \simeq 0.05\ S_{30}^3\ \left(1 + \frac{5}{9}\frac{L_{50}}{S_{30}}\ \frac{n_B - n_0}{n_0}\right)$$

where $S_{30} = E_{sym}(n_0)/(30\mathrm{MeV})$ and $L_{50} = 3n_0\ E'_{\rm sym}(n_0)/(50\mathrm{MeV})$ (Steiner *et al.* 2005). Plugging this in to our approximate zero temperature expression for $\partial P/\partial Y_L$ and expanding in L_{50}, we can write

$$\begin{aligned}\left(\frac{\partial P}{\partial Y_L}\right)_{n_B} \approx\ & 0.026\,\mathrm{fm}^{-4}\,\mathrm{u}^2\Big[1.25\mathrm{u}^{-2/3}\mathrm{S}_{30} + \left\{0.23(\mathrm{u}^{1/3} - \mathrm{u}^{-2/3}) + 0.21\mathrm{S}_{30}^3 - 2.1\right\}\mathrm{L}_{50} \\ & + \left\{0.12S_{30}^2(u-1) - 0.042\frac{(u-1)^2}{S_{30}u^{2/3}}\right\}L_{50}^2 + O(L_{50}^3)\Big]\end{aligned}$$

where $u = n_B/n_0$. We have confirmed numerically that terms of higher than first order in L_{50} provide only a small contribution for $L_{50} < 3$ and for reasonable densities. The equation above indicates the smaller size of the corrections arising from the $E'_{\rm sym}$ dependence of Y_e. The first two terms in the coefficient of the first order term represent this correction, while the third term comes from the explicit dependence on $E'_{\rm sym}$. In our numerical PNS simulations this effect is accounted for. In contrast, the properties of zero temperature nuclear matter should have significantly less effect on the behavior of γ_s. We find the variation of γ_s to be significantly less than that of γ_{Y_L} in the two EoSs considered here, which is consistent with expectations.

Medium modifications of the neutrino interaction rates also influence PNS evolution. These effects have been investigated in earlier work where neutrino scattering and absorption rates on nucleons and leptons were calculated within the relativistic random phase approximation (RPA) (Reddy *et al.* 1999). Here, the effects due to strong and electromagnetic correlations, degeneracy, and relativistic currents are included in a similar way. Further, the effective interactions we employ in the RPA are obtained from the underlying model for the EoS to ensure that the correlation functions which determine the neutrino scattering kernels satisfy the generalized compressibility sum-rules consistent with the EoS. Because the axial portion of the response accounts for the majority of the neutrino scattering cross-section, the presence of an axial interaction can strongly affect the total neutrino mean free path. To take this into account, we introduce an effective short-range interaction in the spin channel through the Migdal parameter, g' (Kim et al. 1995). The strength of this interaction is tuned to reproduce the spin-susceptibility of neutron matter obtained from microscopic calculations Fantoni et al. (2001). For densities above nuclear saturation, the RPA causes a significant enhancement of the mean free path relative to the mean field approximation due to the repulsive nature of the nuclear interaction at high density.

4.4 PNS Evolution

We now consider the evolution of the internal structure of the PNS with convection and varying prescriptions for the opacities. In Fig. 4.3, the evolutions of the entropy and lepton fraction for the two equations of state are shown. Over the first second in both models, convection smoothes the entropy and lepton gradients in the outer regions to a state close to neutral buoyancy. GM3 has a slightly

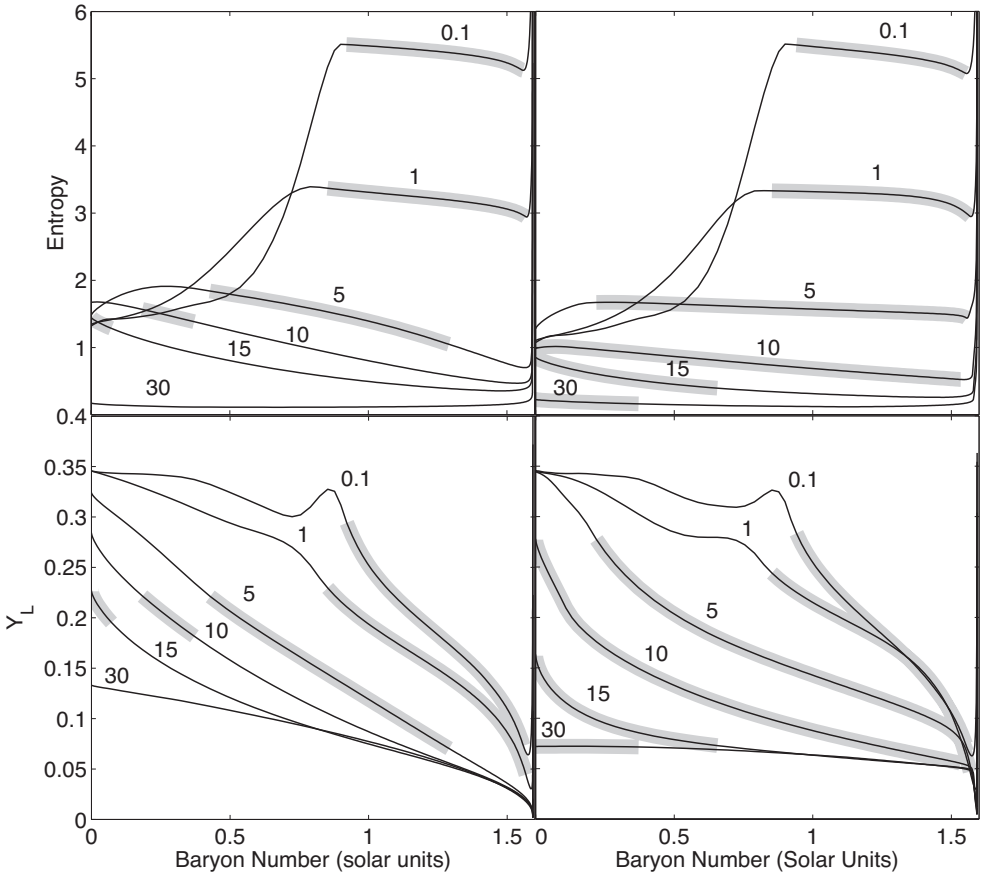

Figure 4.3: Evolution of the entropy (top panels) and lepton fraction (bottom panels) in a $1.6M_{\odot}$ rest mass PNS for the GM3 EoS (left panels) and the IU-FSU EoS (right panels). The grayed regions are convectively unstable. The labels correspond to the model times in seconds.

steeper entropy gradient, in part due to its larger $E'_{\rm sym}$, than IU-FSU. This partially accounts for the slightly larger neutrino luminosity at early times for GM3. As time progresses, convection steadily digs deeper into the core of the PNS. For both EoSs, convection proceeds all the way to the core by 15 seconds into the simulation, but it lasts in the interior regions for a much longer period of time for IU-FSU resulting in more rapid lepton depletion in the core. The exact details of how convection proceeds depend on the initial conditions of the PNS and the behavior of γ_s and γ_{Y_L} for a given EoS. For the conditions encountered in the PNS, the variation in γ_{Y_L} between the two EoSs we employ is significantly larger than the variation of γ_s. More important to the neutrino signal accompanying PNS formation, in GM3 convection ceases in the mantle by ~ 5 seconds, whereas convection in the mantle proceeds until ~ 12 seconds in IU-FSU. This difference is mainly driven by the difference in $E'_{\rm sym}$ between the two EoSs. As the mantle contracts, the second term in Eq.(4.19) becomes increasingly dominant and is eventually able to stabilize convection. Qualitatively, increasing $E'_{\rm sym}$ will shut-off convection at an earlier time.

The depth to which convection penetrates in the core and how long convection proceeds in the core are dependent upon the opacities as well as the EoS. When only mean field effects on the opacities are considered (i.e. when the neutrino mean free path is shorter), convection does not proceed all the way to the center of the PNS in the GM3 models. When RPA effects are included, convection does proceed to the central regions of the core. An increased diffusion rate allows the core to heat up and deleptonize more rapidly, thereby decreasing the stabilizing lepton gradients and increasing the de-stabilizing entropy gradients.

Of course, variations in the convective evolution of the PNS are only interesting

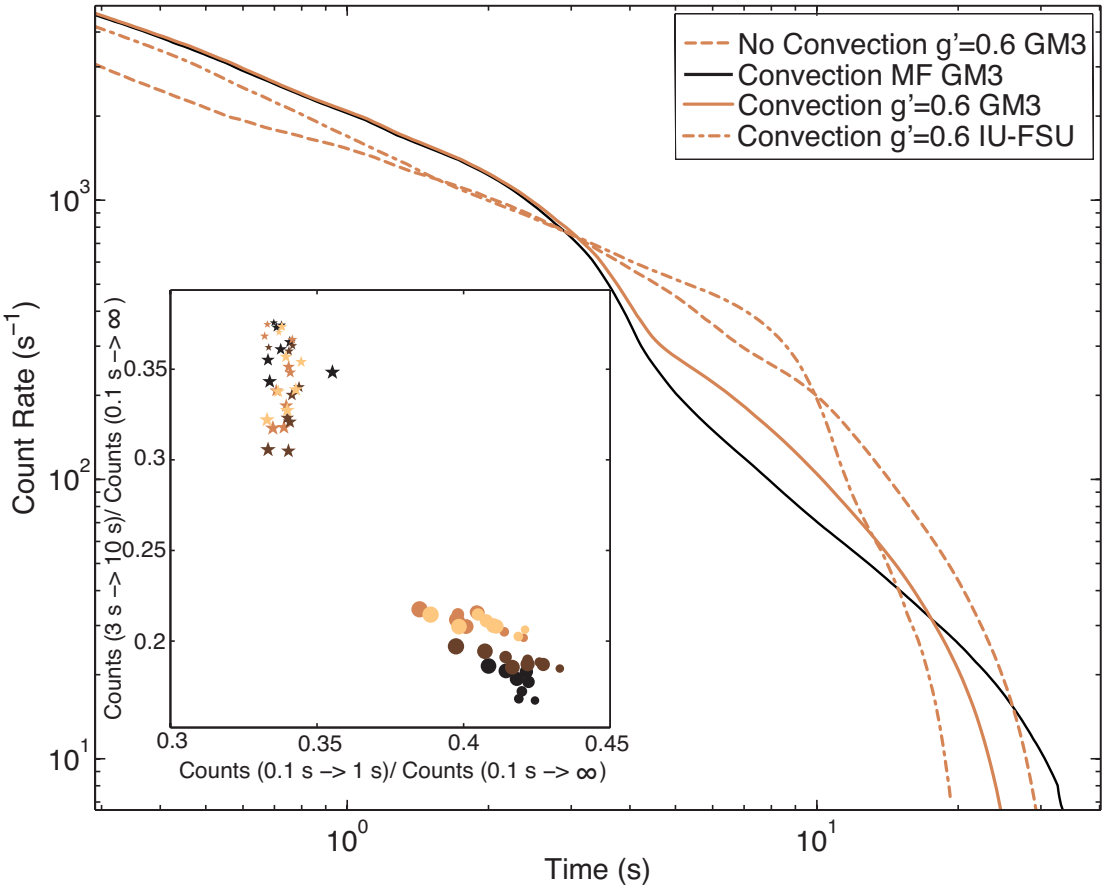

Figure 4.4: Count rates as a function of time for a number of $1.6M_\odot$ PNS models with and without convection. The black line is for neutrino opacities calculated in the mean field approximation, while all the other lines are for models that use RPA opacities with $g' = 0.6$. The inset plot shows the integrated number of counts from 0.1 s to 1 s divided by the total number of counts for $t > 0.1$ second on the horizontal axis, and the number of counts for $t > 3$ seconds on divided by the total number of counts for $t > 0.1$ second. The stars correspond to the IU-FSU EoS and the circles to the GM3 EoS. Symbol sizes correspond to various neutron star rest masses ranging from $1.2M_\odot$ to $2.1M_\odot$. Colors correspond to different values of the Migdal parameter, g'.

to the extent they are potentially observable in the neutrino emission from a nearby supernova. In Fig. 4.4 the expected neutrino count rates for a detector similar to Super Kamiokande-III are shown for a number of PNS cooling models. To determine the expected detector signal, we assume the signal is dominated by the interaction $\bar{\nu}_e + p \rightarrow e^- + n$ Ikeda *et al.* (2007) and that the detector is composed of pure water. The detector count rate is then given by

$$\begin{aligned} \frac{dN}{dt} &= 47.8 \left(\frac{L_\nu}{10^{51}\text{erg s}^{-1}}\right) \left(\frac{D}{10\text{kpc}}\right)^{-2} \\ &\quad \times \left(\frac{T_\nu}{5\text{MeV}}\right) \left(\frac{M_{det}}{50\text{kt}}\right) \frac{G(T_\nu, E_{th})}{20} \text{ s}^{-1}, \end{aligned} \tag{4.20}$$

where

$$\begin{aligned} G(T_\nu, E_{th}) &= \\ &\int_{E_{th}/T_\nu}^{\infty} dx \quad \frac{x(x+\Delta/T_\nu)^2\sqrt{x^2 - m_e^2/T_\nu^2}}{\exp(x+\Delta/T_\nu)+1} W(xT), \end{aligned} \tag{4.21}$$

L_ν is the total neutrino luminosity, T_ν is the neutrino spectral temperature (assuming a zero chemical potential), D is the distance from earth to the supernova, M_{det} is the detector mass, $W(E)$ is the detector efficiency at energy E, and E_{th} is the detector energy threshold. We have assumed a threshold energy of 7.5 MeV, a detector mass of 50 kt, a detector efficiency above threshold of unity Ikeda *et al.* (2007), and a distance of 10 kpc to the supernova. Equipartition has been assumed between neutrino flavors and the spectral temperatures are calculated from the average radius of neutrino decoupling in the PNS. The neutrino luminosities and average energies for two models are included as supplemental data.

Both the GM3 and IU-FSU EoSs show enhanced luminosities at early times relative to the models not including convection. There is only a small difference between the two equations of state at low (sub-nuclear) density, so differences

prior to one second are small. The neutrino count rate is increased by about 30% relative to the models that do not include convection. This is reasonably consistent with the early time enhancement seen in multi-dimensional models Buras *et al.* (2006). After a second, the count rates between the two EoSs begin to diverge. The most obvious feature in the count rate for GM3 appears at ~ 3 seconds, which is coincident with the end of convection in the mantle. For the IU-FSU EoS, the break is also at the time at which mantle convection ends (~ 10 seconds), although it is hard to distinguish from the point at which the PNS becomes optically thin. As was argued previously, the position of this break reflects the density dependence of the nuclear symmetry energy at $n_B > n_0$ and therefore provides a direct observable of the properties of nuclear matter in the PNS neutrino signal. Although core convection does not seem to affect the break, it may impact the subsequent cooling timescale.

In the inset in Fig. 4.4, integrated neutrino counts over two time windows are shown for a number of PNS masses. There is a clear separation between the two EoSs independent of mass. The time of the convective break creates this separation. This illustrates that this diagnostic of the symmetry energy does not require an accurate determination of the PNS mass.

4.5 Conclusions

The inclusion of nucleon correlations through the RPA begins to significantly affect the neutrino emission after about three seconds. Initially, the luminosities are increased as energy and lepton number are able to more rapidly diffuse out of the core, but at later times the neutrino signal is significantly reduced and drops below the detectable threshold at an earlier time.

In summary, using a self-consistent model for the PNS core physics, we find that the late time neutrino signal from a core collapse supernova is likely to contain a direct diagnostic of the nuclear symmetry energy at high density. With current neutrino detectors, these effects should be readily discernible in the neutrino light curve of a single nearby supernova.

Chapter 5

Integrated Nucleosynthesis from Neutrino Driven Winds

This work was performed in collaboration with Stan Woosley and Rob Hoffman. It was published in the Astrophysical Journal as Roberts et al. (2010).

Abstract

Although they are but a small fraction of the mass ejected in core-collapse supernovae, neutrino-driven winds (NDWs) from nascent proto-neutron stars (PNSs) have the potential to contribute significantly to supernova nucleosynthesis. In previous works, the NDW has been implicated as a possible source of r-process and light p-process isotopes. In this paper we present time-dependent hydrodynamic calculations of nucleosynthesis in the NDW which include accurate weak interaction physics coupled to a full nuclear reaction network. Using two published models of PNS neutrino luminosities, we predict the contribution of the NDW to the integrated nucleosynthetic yield of the entire supernova. For the neutrino luminosity histories considered, no true r-process occurs in the most basic scenario.

The wind driven from an older $1.4M_{\odot}$ model for a PNS is moderately neutron-rich at late times however, and produces ^{87}Rb, ^{88}Sr, ^{89}Y, and ^{90}Zr in near solar proportions relative to oxygen. The wind from a more recently studied $1.27M_{\odot}$ PNS is proton-rich throughout its entire evolution and does not contribute significantly to the abundance of any element. It thus seems very unlikely that the simplest model of the NDW can produce the r-process. At most, it contributes to the production of the N = 50 closed shell elements and some light p-nuclei. In doing so, it may have left a distinctive signature on the abundances in metal poor stars, but the results are sensitive to both uncertain models for the explosion and the masses of the neutron stars involved.

5.1 Introduction

The site where r-process nuclei above A=90 have been synthesized remains a major unsolved problem in nucleosynthesis theory (e.g., Arnould et al. 2007). Historically, many possibilities have been proposed (see Meyer 1994), but today, there are two principal contenders - neutron star mergers (Lattimer et al. 1977, Freiburghaus et al. 1999) and the NDW (e.g. Woosley et al. 1994, Witti et al. 1994a, Thompson et al. 2001, Wanajo et al. 2001, Arcones et al. 2007). Observations of ultra-metal-poor stars suggest that many r-process isotopes were already quite abundant at early times in the galaxy (Cowan et al. 1995, Sneden et al. 1996, Frebel et al. 2007), suggesting both a primary origin for the r-process and an association with massive stars. NDWs would have accompanied the first supernovae that made neutron stars and, depending upon what is assumed about their birth rate and orbital parameters, the first merging neutron stars could also have occurred quite early.

Both the merging neutron star model and the NDW have problems though. In the simplest version of galactic chemical evolution, merging neutron stars might be capable of providing the necessary integrated yield of the r-process in the sun, but they make it too rarely in large doses and possibly too late to be consistent with observations (Argast et al. 2004). On the other hand, making the r-process in NDWs requires higher entropies, shorter time-scales, or lower electron mole numbers, Y_e, than have been demonstrated in any realistic, modern model for a supernova explosion (though see Burrows et al. 2006).

Many previous papers and models of the neutrino driven wind have either focused on the production of nuclei heavier than iron using either greatly simplified dynamics (Beun et al. 2008, Farouqi et al. 2009) or focused on the dynamics while not including detailed nuclear physics (Qian & Woosley 1996, Otsuki *et al.* 2000, Arcones et al. 2007, Fischer *et al.* 2010, Hüdepohl *et al.* 2010). Post processing nuclear network calculations have been performed using thermal histories from accurate models of the dynamics, but the calculations sampled only a limited set of trajectories in the ejecta (Witti et al. 1994a, Woosley et al. 1994, Hoffman et al. 1997, Thompson et al. 2001) or did not include detailed weak interaction physics that sets the electron fraction in the ejecta (Wanajo et al. 2001, Wanajo 2006). No one has yet calculated the complete synthesis of a realistic NDW and combined it with the yields from the rest of the supernova.

To address this situation, and to develop a framework for testing the nucleosynthesis of future explosion models, we have calculated nucleosynthesis using neutrino luminosity histories taken from two PNS calculations found in the literature (Woosley et al. 1994, Hüdepohl *et al.* 2010). This was done using a modified version of the implicit one-dimensional hydrodynamics code Kepler, which in-

cludes an adaptive nuclear network of arbitrary size. This network allows for the production of both r-process nuclei during neutron-rich phases of the wind and production of light p-elements during proton-rich phases. Since the results of wind nucleosynthesis depend sensitively on the neutrino luminosities and interaction rates (Qian & Woosley 1996, Horowitz 2002), we have included accurate neutrino interaction rates that contain both general relativistic and weak magnetism corrections.

The synthesis of all nuclei from carbon through lead is integrated over the history of the NDW and combined with the yield from the rest of the supernova, and the result is compared with a solar distribution. If a nucleus produced in the NDW is greatly overproduced relative to the yields of abundant elements in the rest of the supernova, there is a problem. If it is greatly underproduced, its synthesis in the NDW is unimportant. If it is co-produced, the NDW may be responsible for the galactic inventory of this element. An important outcome of this study are the yields expected from a "plain vanilla" model for the NDW. Are there any elements that are robustly produced and thus might be used as diagnostics of the wind in an early generation of stars?

In §5.2, we discuss the general physics of neutrino driven winds and analytically delineate the regions in neutrino temperature space were different modes of nucleosynthesis occur. We then discuss our numerical model in §5.3. In §5.4, the results of the time dependent models are presented. We conclude with a discussion of how the NDW might affect galactic chemical evolution and consider if this allows the strontium abundance in low metallicity halo stars to be used as a tracer of supernova fallback at low metallicity. Finally, we discuss some possible modifications of the basic model that might improve the r-process production.

These ideas will be explored more thoroughly in a subsequent paper.

5.2 General Concepts and Relevant Physics

After collapse and bounce in a core collapse supernova, a condition of near hydrostatic equilibrium exists in the vicinity of the neutrinospheres. The temperature of the outer layers is changing on a time scale determined by the Kelvin-Helmholtz time of the PNS, $\tau_{KH} \approx 10s$ (Burrows & Lattimer 1986, Pons et al. 1999). Heating and cooling in this atmosphere are dominated by the charged current processes $(\nu_e + n) \rightleftharpoons (e^- + p)$ and $(\bar{\nu}_e + p) \rightleftharpoons (e^+ + n)$ (Qian & Woosley 1996). Equating these rates, while neglecting the neutron-proton mass difference and weak magnetism corrections and assuming the geometry can be approximated as close to plane-parallel gives the temperature structure of the neutron star atmosphere as a function of radius, $T_{atm} \approx 1.01\,\mathrm{MeV}\, R_{\nu,6}^{-1/3} L_{\nu,51}^{1/6} \epsilon_{\nu,MeV}^{1/3} \left(y_\nu/y\right)^{1/3}$, where $L_{\nu,51}$ and $\epsilon_{\nu,MeV}$ are the electron neutrino luminosity and average neutrino energy at the neutrino sphere in units of $10^{51}\,\mathrm{ergs\ s^{-1}}$ and MeV, respectively. The gravitational redshift factor is $y = \sqrt{1 - 2GM_{NS}/rc^2}$ which, when evaluated at the neutrino sphere, R_ν, is y_ν. Notice that the only dependence on radius is carried in the redshift factor, so that the atmosphere is close to isothermal.

At the radius, r_c, where the pressure in the envelope becomes radiation dominated, the material becomes unstable to outflow (Duncan et al. 1986). The density at which this wind begins can be found approximately by equating the radiation pressure to the baryonic pressure. This results in a critical density, $\rho_c \approx 8.3 \times 10^7\,\mathrm{g\,cm^{-3}}\, R_{\nu,6}^{-1} L_{\nu,51}^{1/2} \epsilon_{\nu,MeV} \left(y_\nu/y\right)$, at which significant outflow begins and the kinetic equilibrium of weak interactions ceases to hold. Under these conditions, nuclear statistical equilibrium is maintained on a time scale much shorter

than the dynamical time scale and, for these temperatures and densities, there will be no bound nuclei present. Since the electron fraction is set by kinetic equilibrium, the composition of the wind does not depend on any previous nuclear processing, so any nucleosynthesis from the wind will be primary.

Assuming that most neutrino heating occurs near r_c, the entropy is constant once the temperature cools to the nucleon recombination temperature, $kT \approx 0.5$ MeV. Therefore, the final nuclear abundances in the wind depend mainly on the wind entropy, electron fraction, and the dynamical timescale at the radius where alpha combination occurs (Qian & Woosley 1996). To determine the contribution of the wind to the nucleosynthesis of the entire supernova, the mass loss rate must also be known. Estimates for these quantities are given in the Appendix along with a discussion of the effect of general relativistic corrections.

Integrating the mass loss rate (equation 5.20) for a typical neutrino luminosity history implies that the wind will eject approximately $10^{-3}\,M_\odot$ of material. This in turn means that for the wind to contribute to the integrated yields of the supernova for a particular isotope, that isotope needs to overproduced relative to its solar mass fraction by a factor of at least 10^5 in the wind, assuming the rest of the supernova ejects $\sim 10\,M_\odot$ and has over production factors of its most abundant metals of order 10.

Using the analytic results for the wind dynamics and nucleosynthesis given in the Appendix (equations 5.15, 5.17, 5.20, 5.25,5.32, 5.35, 5.41, and using the neutrino interaction rates given in §5.3.1 to fix the thermodynamic state at r_c), one can easily explore the neutrino temperature parameter space to determine the neutrino temperatures and fluxes that are most conducive to the r-process or the production of the light p-process. Figure 5.1 is a neutrino two-color plot where it is assumed

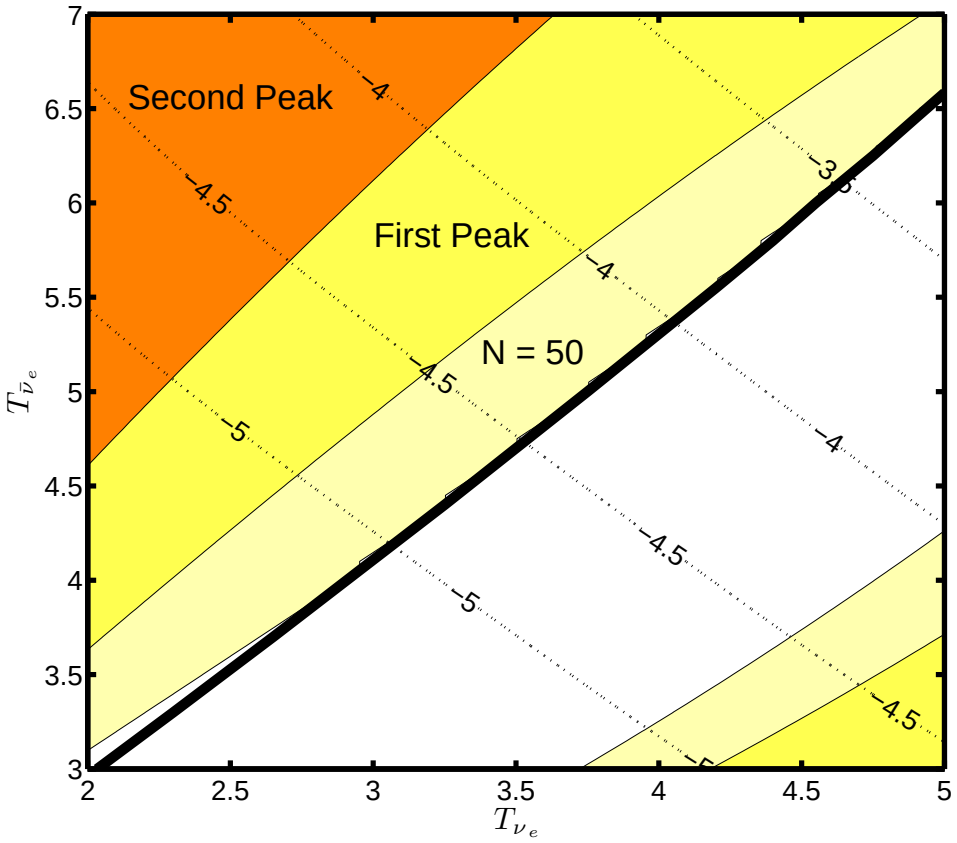

Figure 5.1: Neutrino two-color plot produced using the analytic relations in the Appendix. A neutron star with gravitational mass 1.4 $M_\odot$ has been assumed with a neutrinosphere radius of 10 km. The total neutrino luminosity is assumed to scale as $L_{\nu_e,tot} = 10^{51}(\langle T_\nu \rangle / 3.5\,\mathrm{MeV})^4\,\mathrm{ergs}^{-1}$. This luminosity is split between neutrinos and anti-neutrinos so as to ensure that the net deleptonization rate of the PNS is zero. The thick black line corresponds to an electron fraction of $Y_e = 0.5$. Above this line, neutron-rich conditions obtain and below it the matter is proton-rich. The white region is where there no free neutrons remain after charged particle reactions cease. The N = 50 (tan) region corresponds to final neutron-to-seed ratios between 0.01 and 15. The "first peak" (yellow) region corresponds to a neutron-to-seed ratio between 15 and 70, and the "second peak" (orange) region is where the neutron-to-seed ratio is greater than 70. The dashed lines correspond to the base ten logarithm of the mass loss rate in solar masses per second.

that the deleptonization rate is zero and that the neutrino luminosity scales with the temperature to the fourth power ($L_{\nu_e,tot} = 10^{51}(\langle T_\nu \rangle / 3.5\,\mathrm{MeV})^4\,\mathrm{ergs}^{-1}$). The different nucleosynthetic regions are delineated by the final calculated neutron to seed ratio. To give a feeling for how a particular point in parameter space might contribute to the integrated nucleosynthesis of the wind, the mass loss rate is also shown. The analytic models results are compared with those of our detailed numerical calculations in figures 5.4 & 5.11.

For a significant amount of material to move past the N = 50 closed shell during neutron-rich conditions, the anti-neutrino temperature must be approximately 60% higher than the neutrino temperature. For second peak r-process nucleosynthesis to occur, the asymmetry must be greater than 100%. Modern PNS cooling calculations do not give such large asymmetries (Pons et al. 1999, Hüdepohl *et al.* 2010).

Under proton-rich conditions, only a small region of the parameter space at high neutrino and low anti-neutrino temperature is favorable for the νp-process. There will be a small amount of neutron production in the white region, but it is unlikely that significant production of the light p-process elements ^{74}Se, ^{78}Kr, ^{84}Sr, and ^{92}Mo will occur. The region in neutrino temperature space where there is significant neutron production is unlikely to be reached. This region is small due to the short dynamical time scale of the wind, which reduces the time over which anti-neutrinos can capture on free neutrons. One should note that, very soon after shock formation in the supernova, a wind solution may not be appropriate and material will be entrained closer to the PNS for a longer period of time. This scenario would be similar to the the conditions used in Pruet et al. (2006).

Therefore, based upon simple principles, it seems unlikely that the standard

wind scenario will produce r-process or light p-process isotopes in solar ratios, as is required by observations of metal poor halo stars (Sneden et al. 1996). This same conclusion has been reached by other authors (Witti et al. 1994a, Hoffman et al. 1997, Thompson et al. 2001), but is repeated here in simple terms. We will find that our numerical calculations give similar results and that there is no significant r-process nucleosynthesis associated with the wind. Still, the wind can produce some isotopes that may have an observable signature. For standard PNS luminosities, the wind will spend a significant amount of time in the region of parameter space were N = 50 closed shell nucleosynthesis occurs.

5.3 Computational Method

To more accurately investigate the integrated nucleosynthesis of the NDW, we have updated the implicit Lagrangian hydrodynamics code Kepler (Weaver et al. 1978, Woosley et al. 2002) to carry out time-dependent simulations of the wind dynamics and nucleosynthesis. Kepler has been used previously to study time-independent winds(Qian & Woosley 1996), but the weak and nuclear physics employed there was rudimentary and nucleosynthesis was not tracked. Trajectories from Kepler were used for post-processing calculations of nucleosynthesis in Hoffman et al. (1997).

Kepler solves the non-relativistic hydrodynamic equations in Lagrangian coordinates assuming spherical symmetry. First order general relativistic corrections are included in the gravitational force law (cf. Shapiro & Teukolsky (1983)). All order v/c effects are neglected. This is justified since the maximum wind speeds encountered are, at most, a few percent of the speed of light. The momentum

equation is then

$$\frac{dv_r}{dt} = -4\pi r^2 \frac{\partial P}{\partial m} - \frac{Gm}{r^2}\left(1 + \frac{P}{\rho c^2} + \frac{4\pi P r^3}{mc^2}\right)\left(1 - \frac{2Gm}{rc^2}\right)^{-1} \tag{5.1}$$

where the symbols have their standard meanings. As has been shown by previous studies (Qian & Woosley 1996, Cardall & Fuller 1997, Otsuki *et al.* 2000, Thompson et al. 2001), general relativistic corrections to the gravitational force can have an appreciable effect on the entropy and dynamical time scale of the wind. The equation of state includes a Boltzmann gas of nucleons and nuclei, an arbitrarily relativistic and degenerate ideal electron gas, and photons.

5.3.1 Weak Interaction Physics

Energy deposition from electron neutrino capture on nucleons, neutrino annihilation of all neutrino flavors, and neutrino scattering of all flavors on electrons is included in the total neutrino heating rate. Neutrino "transport" is calculated in the light-bulb approximation. The energy deposition rate is dominated by neutrino captures on nucleons. The neutrino annihilation rates given in Janka (1991) are employed. For the scattering rates, the rates given in Qian & Woosley (1996) are used, but we include general relativistic corrections. Standard neutrino capture rates are employed in the limit of infinitely heavy nucleons with first order corrections. In this limit, the cross section is (Y.Z. Qian, private communication)

$$\sigma_{\substack{\nu n \\ \bar{\nu} p}} = \frac{G_F^2 cos^2(\theta_C)}{\pi(\hbar c)^4}\left[g_V^2 + 3g_A^2\right](\epsilon_\nu \pm \Delta)^2\left(1 \pm W_{M,\substack{\nu \\ \bar{\nu}}}\epsilon_\nu\right) \tag{5.2}$$

Here, G_F is the Fermi coupling constant, θ_C is the Cabibo angle, g_V and g_A are the dimensionless vector and axial-vector coupling constants for nucleons, Δ is the proton neutron mass difference, ϵ_ν is the neutrino energy, and $W_{M,\substack{\nu \\ \bar{\nu}}}$ accounts for the

weak magnetism and recoil corrections to the neutrino-nucleon cross section when the base cross section is derived in the limit of infinitely heavy nucleons (Horowitz 2002). This correction reduces the anti-neutrino cross section and increases the neutrino cross section (by about a total of 10% at the energies encountered in NDWs), which, for a given incident neutrino spectrum, significantly increases the asymptotic electron fraction. Assuming a thermal distribution, these cross sections result in the neutrino energy deposition rate for anti-electron neutrino capture

$$\begin{aligned} \dot{q}_{\bar{\nu}p} = & \ 4.2 \times 10^{18} \text{ergs s}^{-1}\text{g}^{-1} \frac{Y_p L_{\bar{\nu},51}}{\langle\mu\rangle r_6^2} \\ \times & \ \left[-W_M^{\bar{\nu}p} \frac{\langle\epsilon_{\bar{\nu}}^4\rangle}{\langle\epsilon_{\bar{\nu}}\rangle} + (1 + 2W_M^{\bar{\nu}p}\Delta) \frac{\langle\epsilon_{\bar{\nu}}^3\rangle}{\langle\epsilon_{\bar{\nu}}\rangle} \right. \\ & \left. -(2\Delta + W_M^{\bar{\nu}p}\Delta^2) \frac{\langle\epsilon_{\bar{\nu}}^2\rangle}{\langle\epsilon_{\bar{\nu}}\rangle} + \Delta^2 \right] \end{aligned} \tag{5.3}$$

and a similar expression for electron neutrino capture. The neutrino energy distributions are parameterized by assuming a Fermi-Dirac spectrum. The neutrino energy averages, $\langle\epsilon_\nu^n\rangle$, are evaluated using this distribution. The neutrino energy moments and luminosity are evaluated in the rest frame of the fluid. With general relativistic corrections for the bending of null geodesics, the average neutrino angle is given by

$$\langle\mu\rangle = \frac{1}{2} + \frac{1}{2}\sqrt{1 - \left(\frac{R_\nu y_\nu}{ry}\right)^2}. \tag{5.4}$$

Special relativistic corrections are negligible in the regions where neutrino interactions are important.

The lepton capture rates used are calculated in the limit of infinitely heavy nucleons. This results in a positron capture energy loss rate

$$\begin{aligned} \dot{q}_{e^+n} = & \ 6.9 \times 10^{15} \text{ ergs g}^{-1}\text{ s}^{-1}\, Y_n T_{10}^6 \\ \times & \ \int_0^\infty du f_e(u, -\eta) \left(u^5 + 3\delta u^4 + 3\delta^2 u^3 + \delta^3 u^2\right) \end{aligned} \tag{5.5}$$

here $f_e(u,\eta) = (\exp(u-\eta)+1)^{-1}$, η is the electron degeneracy parameter, δ is the proton neutron mass difference divided by k_bT, and Y_n is the neutron fraction. A similar rate is employed for electron capture.

For the neutrino losses, we include electron and positron capture on nucleons and include thermal losses as tabulated in Itoh et al. (1996). The energy loss rate in the wind is dominated by the electron captures.

5.3.2 Nuclear Physics

During a hydrodynamic time step in Kepler, the nuclear energy generation rate and the changing nuclear composition are calculated using a modified version of the 19-isotope network described in Weaver et al. (1978). Neutrino and electron capture rates on nucleons are coupled to the network, which are calculated under the same assumptions as the charged current energy deposition/loss rates described above. Therefore, non-equilibrium evolution of the electron fraction is accurately tracked.

Although this network is appropriate for calculating energy generation throughout the entire wind, it is not large enough to accurately track the nucleosynthesis once alpha recombination begins at $T \approx 0.5$ MeV. Therefore, for temperatures below 20GK an adaptive network is run alongside the hydrodynamics calculation. The details of this network can be found in Woosley et al. (2004) and Rauscher et al. (2002). As a fluid element passes the temperature threshold, the composition from the 19-isotope network is mapped into the adaptive network. Typically, the network contains approximately 2000 isotopes. Where available, experimental nuclear reaction rates are employed, but the vast majority of the rates employed in the network come from the statistical model calculations of Rauscher & Thiele-

mann (2000). In general, the nuclear physics employed in these calculations is the same as that used in Rauscher et al. (2002). The nucleon weak interaction rates employed in the 19-isotope network are also used in the adaptive network.

5.3.3 Problem Setup and Boundary Conditions

To start the neutrino driven wind problem, an atmosphere of mass 0.01 $M_{\odot}$ is allowed to relax to hydrostatic equilibrium on top of a fixed inner boundary at the neutron stars radius. The mass enclosed by the inner boundary is the neutron star's mass. The photon luminosity from the neutron star is assumed to be nearly Eddington, but we have found that the properties of the wind are insensitive to the the luminosity boundary condition. Once hydrostatic equilibrium is achieved, the neutrino flux is turned on and a thermal wind forms. This wind is allowed to relax to a quasi-steady state, and then the 19 isotope network is turned on and the wind is, once again, allowed to reach a quasi-steady state. After this point, the neutrino flux is allowed to vary with time, and the adaptive network is turned on.

As the calculation proceeds, the mass of the envelope being followed decreases and could eventually all be blown away. To prevent this, mass is added back to the innermost mass elements at a rate equal to the mass loss rate in the wind. The mass added to a fluid element at each time step is a small fraction of its total mass. We find that mass recycling has no effect on the properties of the wind. It is simply a way of treating a problem that is essentially Eulerian in a Lagrangian code.

For most runs, a zero outer boundary pressure and temperature are assumed. To investigate the effect of a wind termination shock, a time dependent outer

boundary condition is included in some of the simulations detailed below. The pressure of the radiation dominated region behind the supernova shock is approximately given by (Woosley et al. 2002)

$$P_{ps} \approx \frac{E_{sn}}{4\pi(v_{sn}t)^3} \tag{5.6}$$

where E_{sn} is the explosion energy of the supernova, v_{sn} is the supernova shock velocity, and t is the time elapsed since the shock was launched. As was discussed in Arcones et al. (2007), this results in a wind termination shock at a radius where the condition $\rho_w v_w^2 + P_w \approx P_{ps}$ obtains, where v_w is the wind velocity and ρ_w is the wind density. To avoid an accumulation of too many zones, mass elements are removed from the calculation once they exceed a radius of $10,000\,\mathrm{km}$. This is well outside the sonic point and nuclear burning has ceased by this radius in all calculations .

5.4 Numerical Results

To survey both low and intermediate mass core collapse supernovae, neutrino emission histories were taken from two core collapse calculations, one from a $20M_\odot$ (Woosley et al. 1994) supernova calculation and the other from a $8.8M_\odot$ (Hüdepohl *et al.* 2010) supernova calculation. Since the PNSs studied have significantly different masses and neutrino emission characteristics, one is able to get a rough picture of how integrated nucleosynthesis in the NDW varies with progenitor mass.

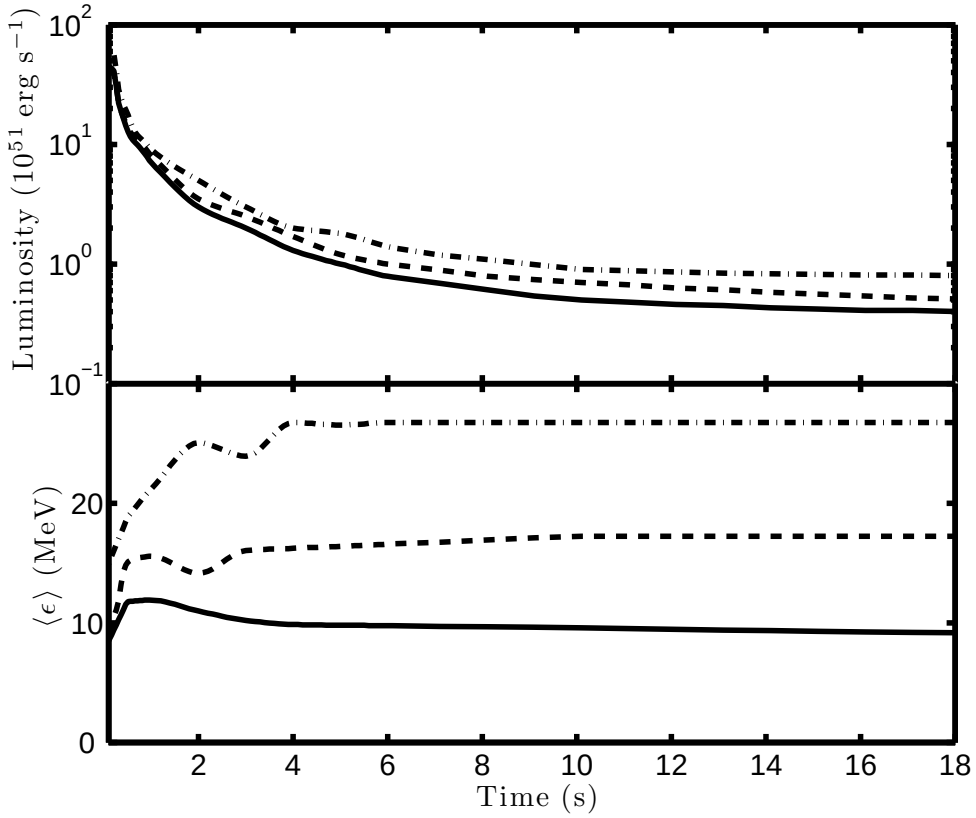

Figure 5.2: Neutrino luminosities and temperatures taken from the model of Woosley et al. (1994). The top panel is the neutrino luminosities. The bottom panel is the average neutrino energies. The solid line corresponds to ν_e, the dashed line corresponds to $\bar{\nu}_e$, the dot-dashed line corresponds to $\nu_{\mu,\tau}$.

5.4.1 Neutrino Driven Wind from a $20M_{\odot}$ Supernova

The first set of neutrino luminosities and temperatures are taken from Woosley et al. (1994). This calculation began with a $20M_{\odot}$ progenitor meant to model the progenitor of 1987A (Woosley et al. 1988). The resulting neutron star had a gravitational mass of $1.4M_{\odot}$ and the neutrino sphere was taken to be at 10 km. The neutrino luminosities and average energies as a function of time from this model are shown in figure 5.2. After about 4 seconds, the neutrino energies become constant and the large difference between the electron neutrino and anti-neutrino energies implies that the wind will be neutron rich. This supernova model had some numerical deficiencies (Sam Dalhed, Private Communication). We also note that, unlike more modern 1-D supernova models of $\sim 20M_{\odot}$ stars (e.g. Fischer *et al.* 2010), this model resulted in a successful explosion when a mixing length theory prescription for convection was included. The entropy calculated for the wind in Woosley et al. (1994) ($S/N_A k \approx 400$) were unrealistically large due to some problems with the equation of state. Here, that is not so important because the NDW is being calculated separately, but this study did rely on older neutrino interaction rates and did not include weak magnetism corrections (see §5.3.1). Therefore, the results obtained using these neutrino histories are only suggestive of what might happen in a more massive star. If weak magnetism were taken into account, the calculated electron and anti-electron neutrino temperatures would probably be somewhat further apart.

The calculation was run for a total of 18 seconds. During this time, the mass loss rate decreased by almost three orders of magnitude while a total mass of $2 \times 10^{-3} M_{\odot}$ was lost in the wind. A snapshot of the wind structure two seconds after bounce is shown in figure 5.3. Note that the wind velocity stays very sub-

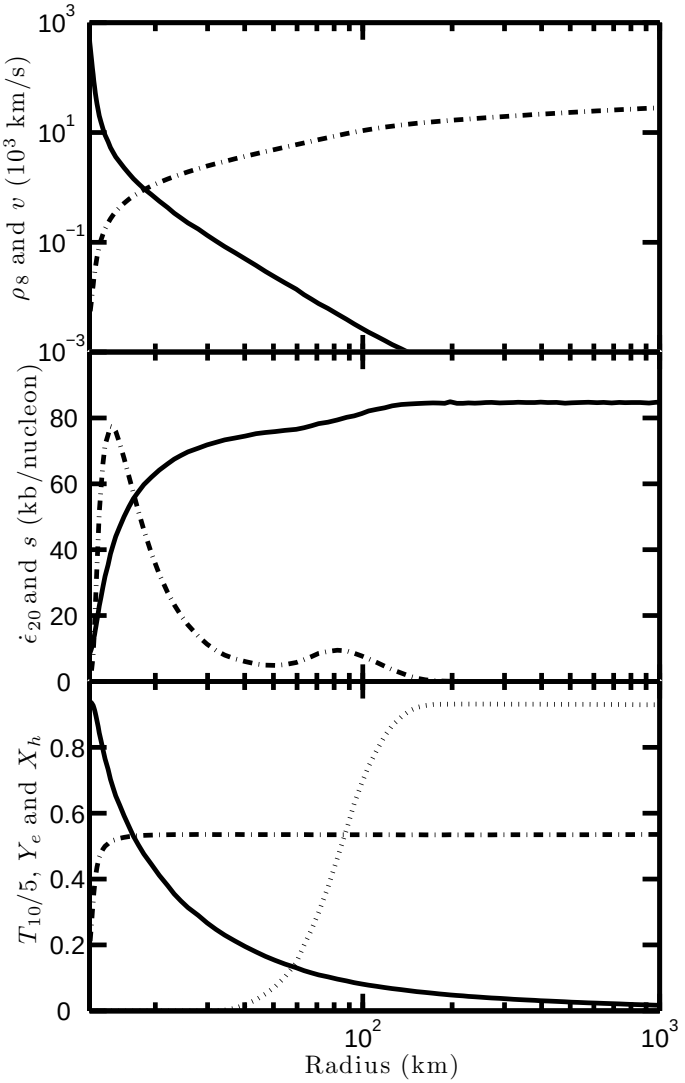

Figure 5.3: Wind structure after two seconds in the model using the neutrino luminosities from Woosley et al. (1984). The top panel shows the density in units of $10^8\,\mathrm{g\,cm^{-3}}$ (solid line) and the radial velocity in units of $10^3\,\mathrm{km\,s^{-1}}$ (dot-dashed line). The middle panel shows the net energy deposition rate from weak and strong interactions in units of $10^{20}\,\mathrm{erg\,g^{-1}\,s^{-1}}$ (dot-dashed line) and the entropy (solid line). The bottom panel shows the temperature in units of $5 \times 10^{10}\,\mathrm{K}$ (solid line), the electron fraction (dot-dahsed line), and the fraction of material contained in nuclei (dotted line).

luminal throughout the calculation. Therefore, the neglect of special relativistic effects is reasonable. The secondary bump in the energy deposition rate occurs at the same radius where nucleons and alpha-particles assemble into heavy nuclei. This increases the entropy by about 10 units. Clearly, the electron fraction is set interior to were nuclei form. The radius where nuclei form is at a large enough value that the alpha effect (Fuller & Meyer 1995) is not significant at early times in the wind. However, as the neutrino luminosity decreases with time, nucleon recombination occurs at a smaller radius, and the alpha effect becomes increasingly important.

The time evolution of the wind as calculated by Kepler is shown in figure 5.4. The increase in asymptotic entropy is mainly driven by the decrease in neutrino luminosity, since the average neutrino energies do not vary greatly. The analytic approximation (calculated using equation 5.17 and the neutrino interaction rates given in §5.3.1) to the entropy tracks the entropy calculated in Kepler fairly well. This implies that the variation in the neutrino luminosity with time does not significantly alter the dynamics from a steady state wind. In contrast to the high entropies reported in Woosley et al. (1994), the entropy here never exceeds 130. For the time scales and electron fractions also obtained, such a low value of entropy is not sufficient to give a strong r-process (see below).

The electron neutrino and anti-neutrino energies do move further apart as a function of time though, which causes the wind to evolve from proton-rich conditions at early times to neutron-rich conditions later. A transition occurs from the synthesis of proton-rich isotopes via the νp-process at early times to the $\alpha-$process mediated by the reaction sequence $\alpha(\alpha\mathrm{n},\gamma)^{9}\mathrm{Be}(\alpha,\mathrm{n})^{12}\mathrm{C}$ later. The slight difference between the analytic approximation and the Kepler calculation

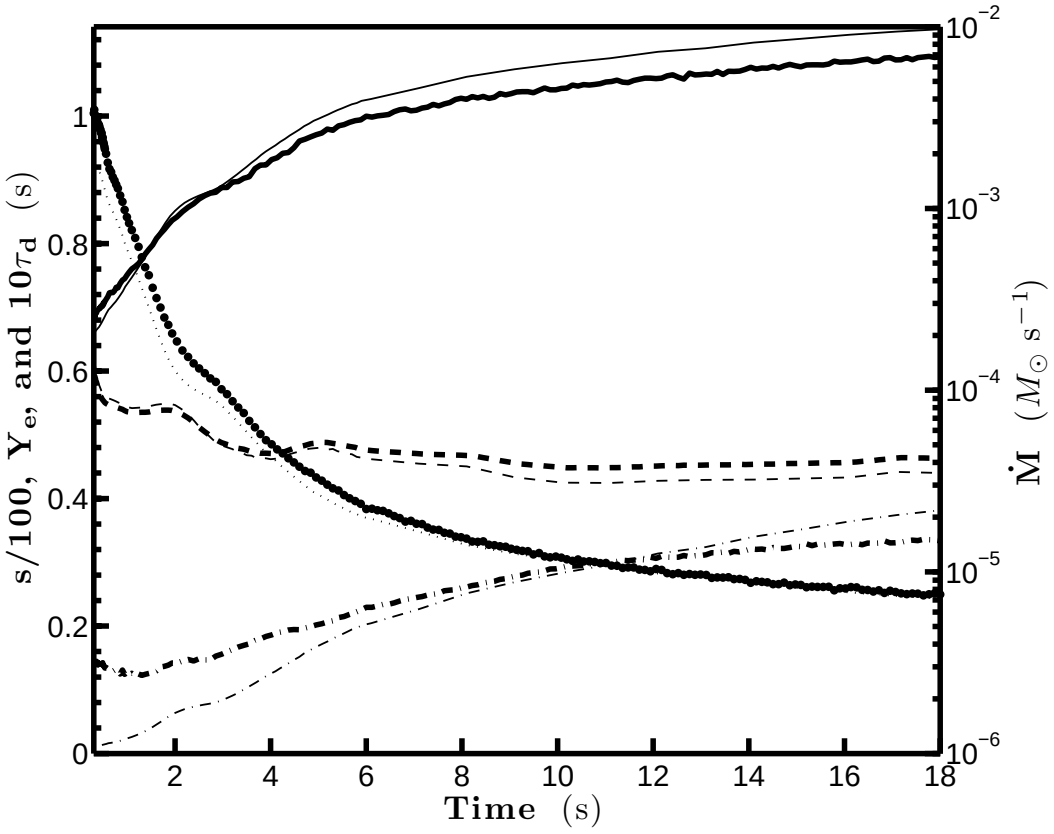

Figure 5.4: Properties of the neutrino driven wind from the Woosley et al. (1994) supernova model as a function of time. The thick lines correspond to the numerical results from Kepler and the thin lines correspond to the predictions of the analytic estimates described in the appendix. The solid line is the dimensionless entropy per baryon, the dashed line is the electron fraction, the dash dotted line is the dynamical timescale, and the dotted line is the mass loss rate. All of the quantities are taken extracted from where the wind temperature reaches 2 GK.

of Y_e is due to the alpha effect (Fuller & Meyer 1995).

Integrated production factors for the wind are shown in figure 5.5. The production factor for the species i is defined as

$$P_i = \frac{X_{i,w} M_w}{X_{i,\odot}(M_w + M_{sn})}, \tag{5.7}$$

where $X_{i,w}$ is the mass fraction of species i in the wind after all material has decayed to stable isotopes, M_w is the mass ejected in the wind, and M_{sn} is the amount of mass ejected by the entire supernova. $X_{i,\odot}$ is the mass fraction of isotope i in the sun for which the values of Lodders (2003) were used. The only isotopes that are co-produced in the wind alone are ^{87}Rb, ^{88}Sr, ^{89}Y, and ^{90}Zr, with production factor of ^{88}Sr about a factor of 3 higher than the other two N = 50 closed shell isotopes. If neutrons are exhausted at high temperatures when charged particle reactions are occurring, the wind will mainly produce the isotopes ^{88}Sr, ^{89}Y, and ^{90}Zr (Hoffman et al. 1997). This happens when the condition

$$\frac{\bar{Z}}{\bar{A}} \approx 0.42 - 0.49 = \frac{Y_e f_\alpha}{2Y_e(f_\alpha - 1) + 1} \tag{5.8}$$

is met. Here, $f_\alpha \approx 14 Y_s / Y_{\alpha,i}$ is the fraction of the initial helium abundance that gets processed into heavy nuclei.

Before eight seconds, the production factors had been much closer. After eight seconds though, the wind is dominated by ^{88}Sr because $Y_e \sim 0.45$ and only 53% of alpha particles are free after freeze out which puts $\frac{\bar{Z}}{\bar{A}} \approx 0.41$ for heavy nuclei just below the range given in equation 5.8. There are not enough free neutrons to make any significant amount of heavier nuclei, and this results in significant production of the stable N = 50 closed shell isotope with the lowest $\frac{\bar{Z}}{\bar{A}}$.

During the first four seconds, the wind is proton rich and the isotopes ^{69}Ga, ^{70,72}Ge, ^{74,76}Se, and ^{78,80,82}Kr are produced by proton captures on seed nuclei

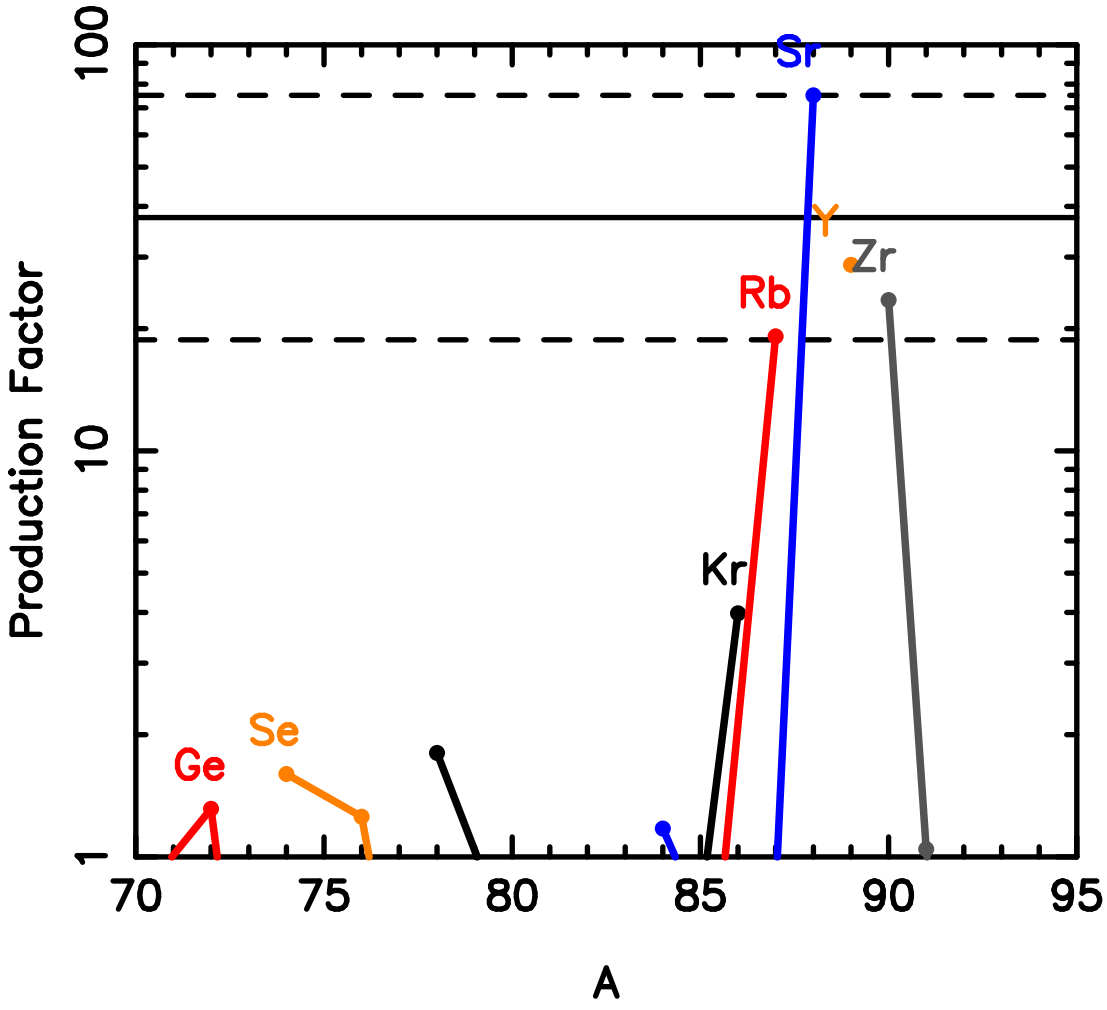

Figure 5.5: Isotopic production factors from the NDW model when the neutrino luminosities from Woosley et al. (1994) are used. The production factors are calculated assuming that 18.4 $M_{\odot}$ of material was ejected in the supernova in addition to the wind. The top dashed line corresponds to the greatest production factor in the wind, the solid line is a factor of two below that, and the bottom dashed line is a factor of two below the solid line. These lines specify an approximate coproduction band for the wind alone.

produced by the triple-alpha reaction and subsequent (α,p) reactions. Although the mass loss rate is much higher when the wind is proton rich, the alpha-fraction freezes out at 98% of its initial value, which results in significantly decreased production of heavy nuclei. The difference in final alpha fraction between the neutron- and proton-rich phases of the wind is due mainly to the difference in speed of the reaction chains $\alpha(2\alpha,\gamma)^{12}$C and $\alpha(\alpha n,\gamma)^{9}Be(\alpha,n)^{12}$C, but also to the decreased entropy at early times.

We can compare this with the analytic predictions for nucleosynthesis by plotting the neutrino temperature evolution from this model on a neutrino "two-color plot" (figure 5.6). Here we have set $L_{\bar{\nu}_e} = 1.2L_{\nu}$ which is approximately correct at late times in the calculation of Woosley et al. (1994). The wind never reaches a region in which r-process nucleosynthesis is expected, but spends a significant amount of time making nuclei in the N = 50 closed shell isotones.

5.4.1.1 Variations in Neutrino Properties

Since the neutrino temperatures from the original model were uncertain, several other models were calculated. One had a reduced (by 15%) electron antineutrino temperature; another had the weak magnetism corrections to the neutrino interaction rates turned off. A smaller antineutrino temperature is more in line with recent calculations of PNS cooling (Pons et al. 1999, Keil et al. 2003). Because the model of Woosley et al. (1994) did not include weak magnetism corrections, our model with weak magnetism corrections turned off is more consistent with the original supernova model.

The production factors for the model with a reduced electron antineutrino temperature are shown in figure 5.7. The yield of ^{88}Sr is reduced by almost a

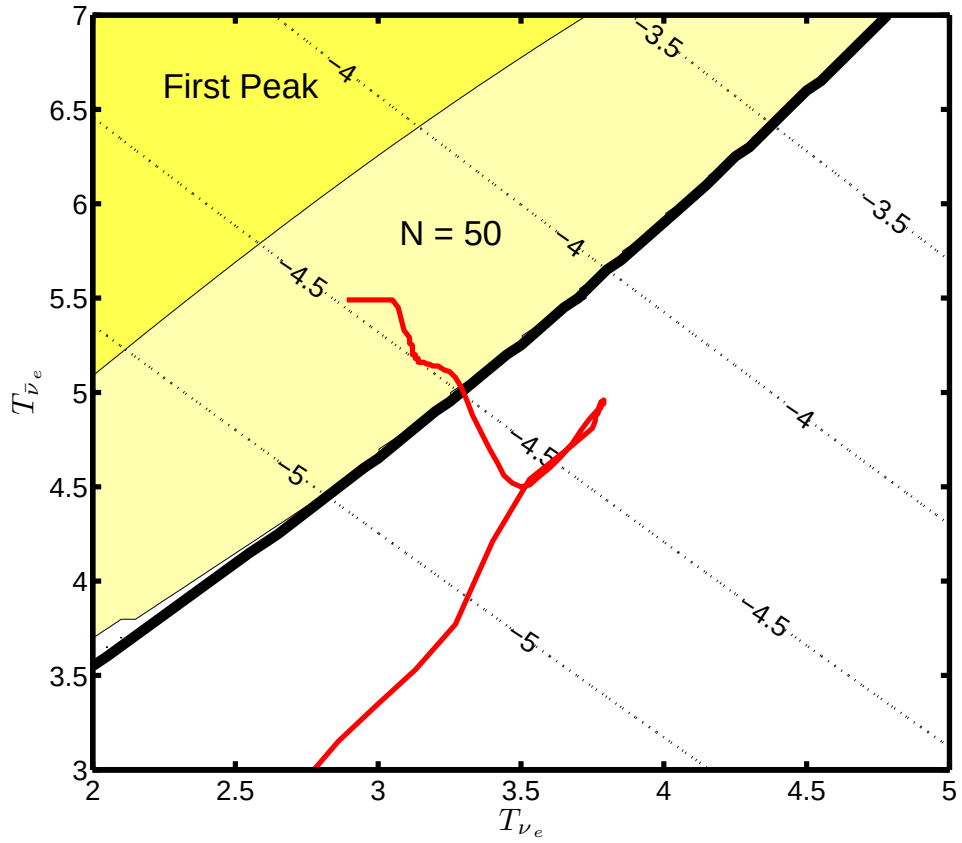

Figure 5.6: Neutrino two-color plot when the anti-neutrino luminosity is 1.2 times neutrino luminosity, and the total luminosity scales with average temperature to the fourth. Similar to figure 5.1. The red lines are the neutrino temperatures.

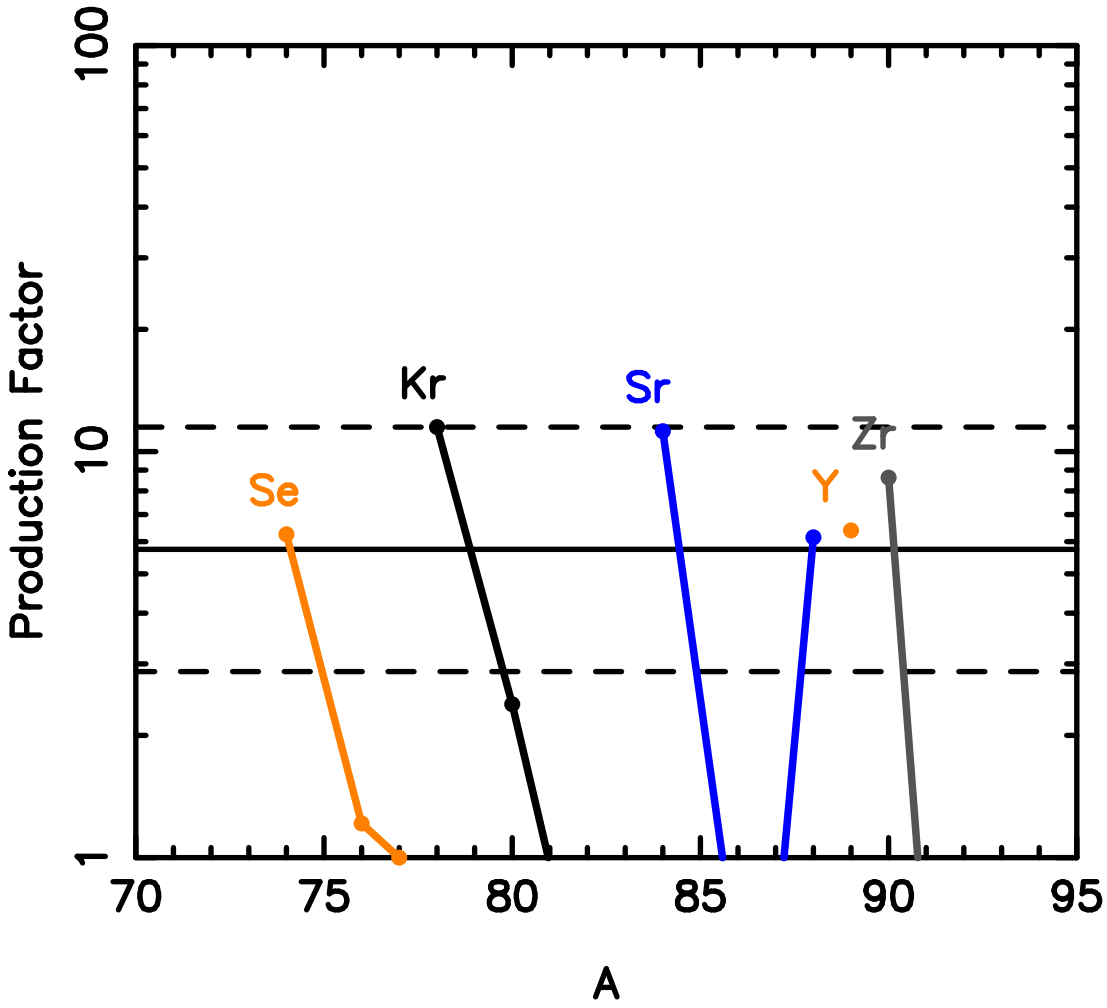

Figure 5.7: Isotopic production factors from the NDW model employing the neutrino luminosities from Woosley et al. (1994) with the anti-electron neutrino temperature reduced by 15%. The production factors are calculated assuming that 18.4 $M_{\odot}$ of material was ejected in the supernova in addition to the wind. The horizontal lines are similar to those in figure 5.5.

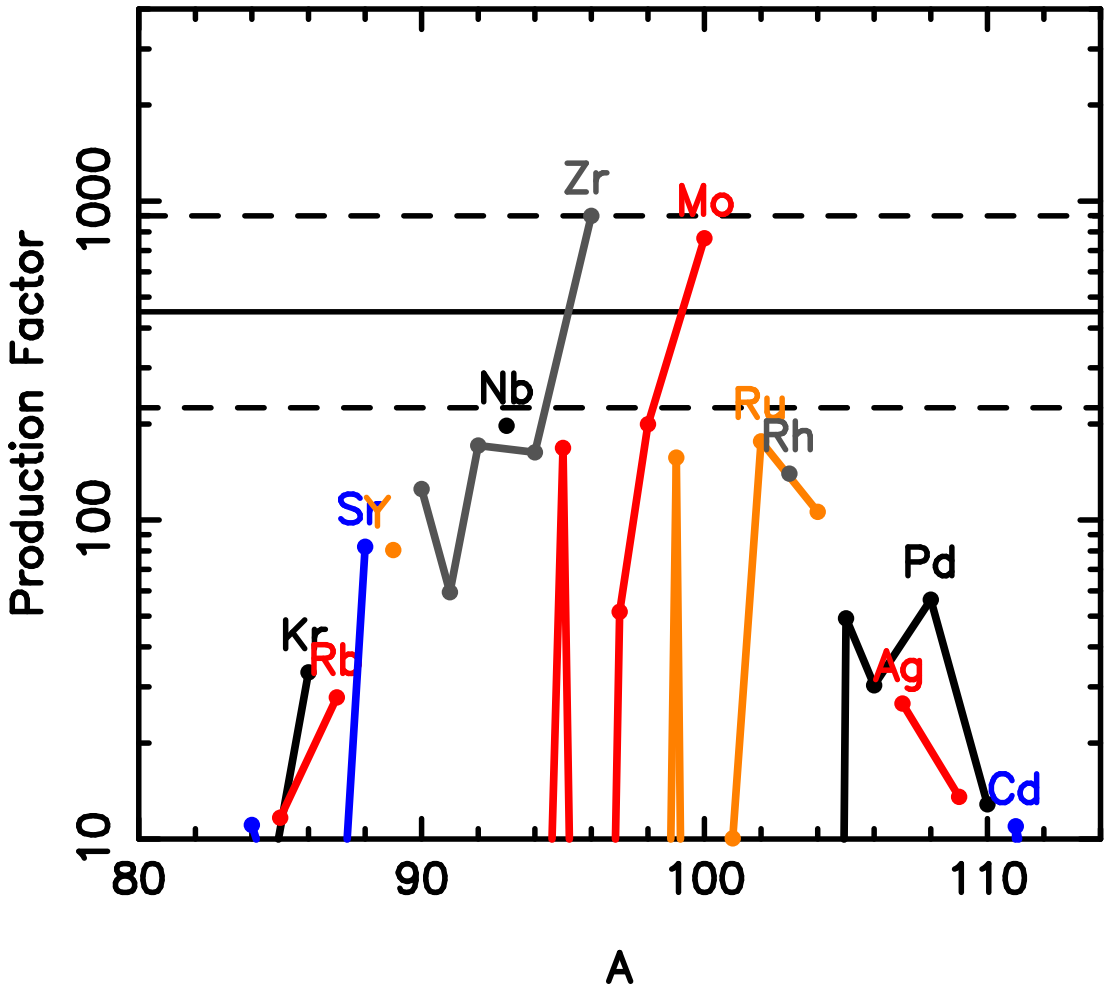

Figure 5.8: Isotopic production factors from the NDW model employing the neutrino luminosities from Woosley et al. (1994) with weak magnetism corrections turned off. The production factors are calculated assuming that 18.4 $M_{\odot}$ of material was ejected in the supernova in addition to the wind. The horizontal lines are similar to those in figure 5.5.

factor of ten from the base case, while the production factors of ^{89}Y and ^{90}Zr are reduced by a factor of three. In this case, the wind also produces the proton-rich isotopes ^{74}Se, ^{78}Kr, and ^{84}Sr. The coproduction line for lighter elements like oxygen in a $20M_{\odot}$ supernova at solar metallicity is around 18, so the wind could contribute to the total nucleosynthesis if the antineutrino temperature was reduced, but its contribution would be small.

The yields when weak magnetism corrections are ignored are shown in figure 5.8. Without weak magnetism, the electron fraction drops below 0.4 at late times when the entropy is fairly high. Equation 5.8 is no longer satisfied and material moves past the N = 50 closed shell towards A $\approx$ 110. Some r-process isotopes are produced, such as ^{96}Zr and ^{100}Mo, but not anywhere near solar ratios, and no material reaches the first r-process peak.

5.4.1.2 Effect of a Wind Termination Shock

To investigate the possible effect of a wind termination shock on nucleosynthesis, another model was run with a boundary pressure and temperature determined by equation 5.6. An explosion energy of 10^{51} erg was assumed and the shock velocity was taken as 2×10^9 cm s^{-1}. This resulted in a wind termination shock that was always at a radius greater than 10^3 km. Similar to the simulation without a wind termination shock, the N=50 closed shell elements dominate the wind's nucleosynthesis.

The main difference between the case with and without a wind termination shock is a shift in the mass of isotopes produced during the proton-rich phase. During this phase, the post shock temperature varied from 2.5 GK down to 0.8 GK and the density varied from 5×10^4 g cm^{-3} to 5×10^2 g cm^{-3}. These conditions

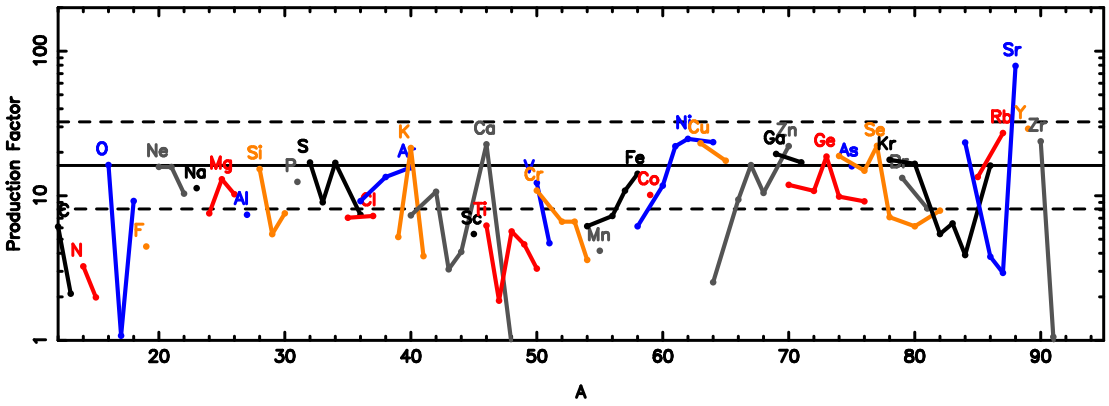

Figure 5.9: Combined isotopic production factors of the neutrino driven wind with unaltered neutrino temperatures and including weak magnetism corrections added to those of a $20M_{\odot}$ stellar model from Woosley et al. (1995). The solid black line is the coproduction line with ^{16}O. The dashed lines are a factor of two above and below the coproduction line. The neutrino driven wind is responsible for the production of ^{88}Sr, ^{89}Y, and ^{90}Zr.

are very favorable for continued proton capture once the long lived waiting point isotopes ^{56}Ni and ^{64}Ge are bypassed by (n,p) reactions. Because these conditions persist for at least a second after a fluid element passes through the wind termination shock, significantly more proton captures can occur on seed nuclei that have moved past mass ~ 64 relative to the case with no termination shock. Still, not many more neutrons are produced per seed nucleus relative to the base run. Therefore, the net number of seeds that get past the long lived waiting points remains small and the proton-rich wind does not contribute to the integrated nucleosynthesis. It should also be noted that a different treatment of the wind's interaction with the supernova shock might result in a breeze solution which may supply more favorable conditions for νp-process nucleosynthesis (Wanajo 2006).

5.4.1.3 Total Supernova Yields

In figure 5.9, the production factors from a $20M_{\odot}$ supernova model from Woosley & Weaver (1995) have been combined with the production factors we calculated in the NDW with the unaltered neutrino histories of (Woosley et al. 1994) with weak magnetism corrections included. The wind could be responsible for synthesizing the isotopes ^{87}Rb, ^{88}Sr, ^{89}Y, and ^{90}Zr. ^{88}Sr production is above the co-production band, but the rest are in agreement with the stellar yields. This overproduction of ^{88}Sr is similar to the result of Hoffman et al. (1997).

For the model with a reduced anti-electron neutrino temperature combined with the yields from the $20M_{\odot}$ supernova model, the wind contributes 28%, 42%, 35%, 75%, 75%, and 80% of the total ^{74}Se, ^{78}Kr, ^{84}Sr, ^{88}Sr, ^{89}Y, and ^{90}Zr abundances in the supernova model, respectively. This wind model does not result in any isotopes being overproduced relative to the rest of the yields of the supernova. For the case with weak magnetism turned off, the nuclei produced by the wind are overproduced relative to those made in the rest of the star by factor of nearly 100, hence this would need to be a very rare event if this model were realistic.

Since the progenitor model used in Woosley et al. (1994) was a model for SN 1987A, we have also combined the abundances calculated in the wind those predicted by Woosley et al. (1988). ^{88}Sr, produced by the NDW, dominates the elemental strontium yield. For the base NDW model, [Sr/Fe]= 0.8, if weak magnetism corrections are neglected, [Sr/Fe]= 1.6; and if the anti-neutrino temperature is reduced in the base model by 15%, [Sr/Fe]= 0.2.

Clearly, weak magnetism corrections and variations in the neutrino temperatures have a very significant effect on nucleosynthesis in the wind. Aside from the effects of an extra source of energy (5.5.2), the neutrino spectra are the largest

current theoretical uncertainty in models of the NDW.

5.4.2 Neutrino Driven Wind from a $8.8M_{\odot}$ Supernova

The second PNS model is a more modern one-dimensional calculation of an electron-capture supernova (Hüdepohl *et al.* 2010) that started from an $8.8M_{\odot}$ progenitor model (Nomoto 1984). This resulted in a PNS with a gravitational mass of $1.27M_{\odot}$ and a radius of 15 km. Together the lower mass and increased radius imply a lower gravitational potential at the neutrinosphere. This work employed neutrino interaction rates which took weak magnetism and "in-medium" effects into account. The neutrino luminosities and average energies as a function of time are shown in figure 5.10. The maximum difference between the electron and anti-electron neutrino average energies is significantly less than in the model of Woosley et al. (1994). This is likely due in part to both the decreased gravitational potential of the PNS and the more accurate neutrino interaction rates in the newer model.

The calculation was run for a total of nine seconds, at which point the mass loss rate had dropped by two orders of magnitude. The total amount of mass ejected in the wind was $3.8 \times 10^{-4}\, M_{\odot}$. In figure 5.11, the properties of the NDW calculated using Kepler are plotted as a function of time. Notice that the entropy never reaches above 100 in this model, which diminishes the likelihood of significant nucleosynthesis. For comparison, we also include the analytic estimates detailed above. There is reasonable agreement between the analytic and the numerical calculations, but not nearly as good as in the $20M_{\odot}$ model.

In contrast to the simulation run with the neutrino luminosities of Woosley et al. (1994), the electron fraction continues to increase with time. The difference

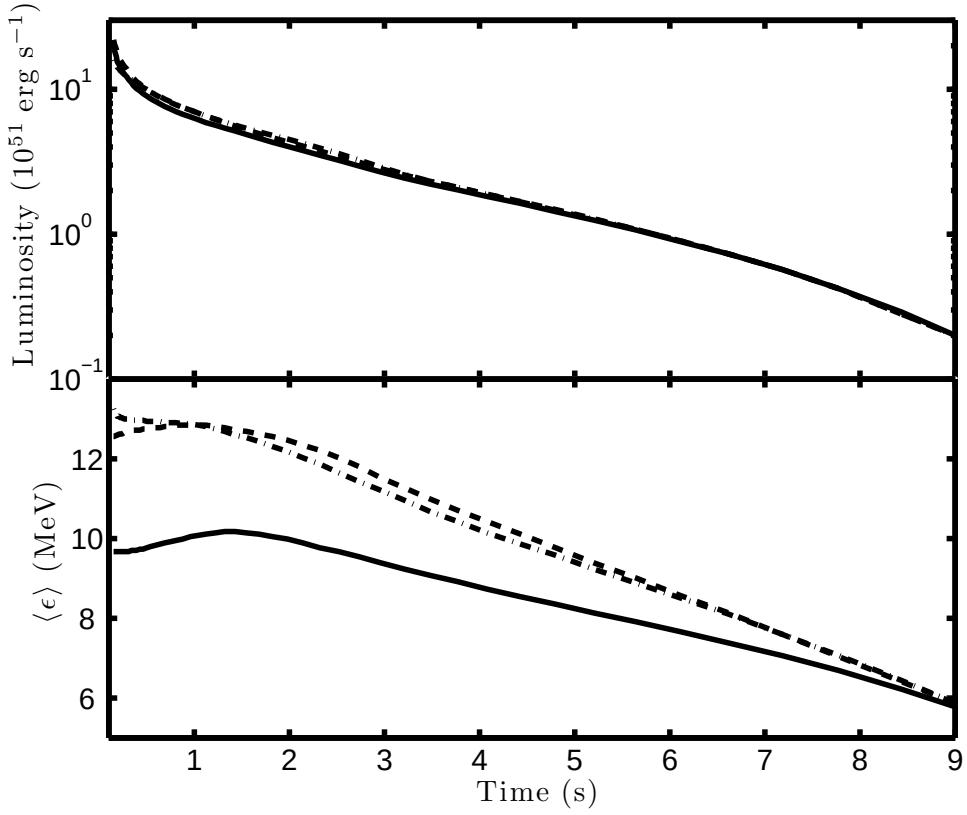

Figure 5.10: Neutrino luminosities and temperatures taken from the model of Huedepohl et al. (2010). The line styles are the same as in figure 5.2.

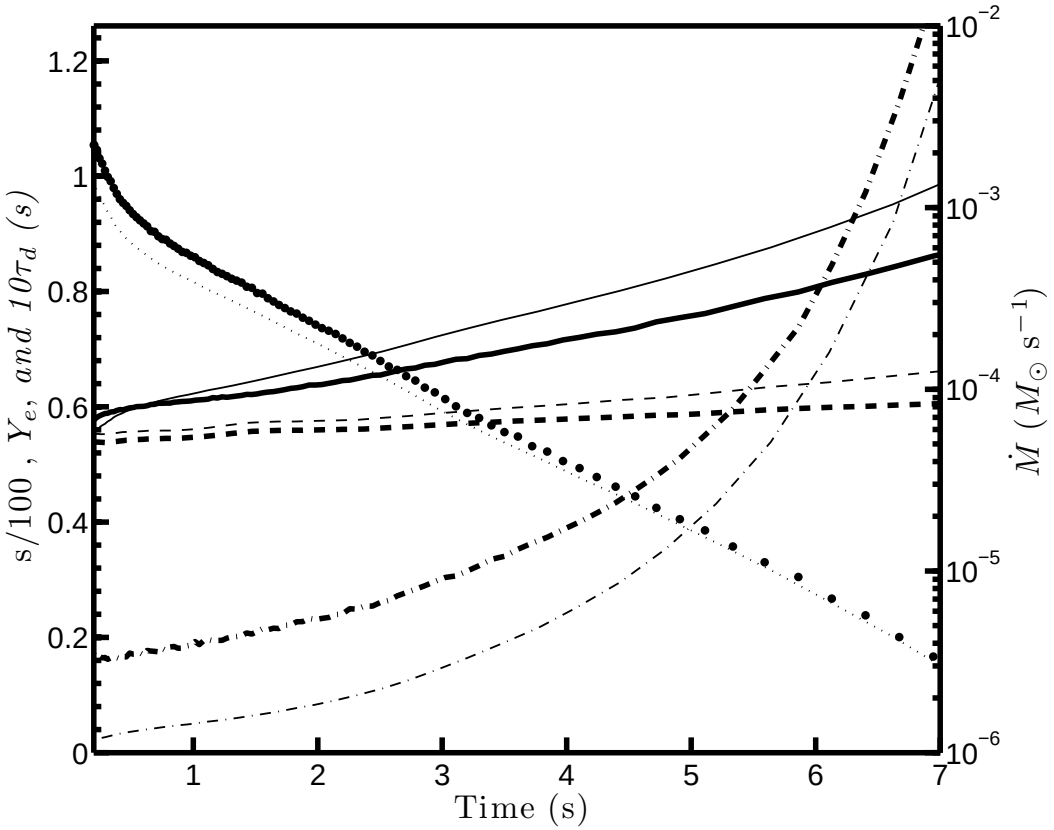

Figure 5.11: Properties of the neutrino driven wind from the Huedepohl et al. (2010) supernova model as a function of time. The lines have the same meaning as in figure 5.4.

between the average electron neutrino energy and electron anti-neutrino energy is, at most, about 3 MeV, compared to a maximum of 8 MeV in the Woosley et al. (1994) calculations. Also, the difference between the average neutrino energies decreases as a function of time, compared to an increase with time in Woosley et al. (1994). Finally, the energies of all kinds of neutrinos are lower in the Hüdepohl *et al.* (2010) calculation, so that the proton-neutron rest mass difference significantly suppresses the anti-neutrino capture rate relative to the neutrino capture rate. These differences are presumably due to both the different neutron star masses and neutrino interaction rates employed.

The conditions in this model thus preclude *any* r-process nucleosynthesis, but they are potentially favorable for production of some low mass p-process isotopes by the νp-process. The integrated isotopic production factors are shown in figure 5.12. The total ejected mass was take as 7.4 $M_\odot$, as 1.4 $M_\odot$ neutron star is left behind in the calculation of Hüdepohl *et al.* (2010). During the calculation a maximum network size of 988 isotopes is reached. The p-process elements ^{74}Se and ^{78}Kr are co-produced with ^{63}Cu, ^{67}Zn, and ^{69}Ga, but the maximum production factor for any isotope is 1 when weighted with the total mass ejected in the supernova. Therefore, in this simple model, the proton-rich wind from low mass neutron stars will not contribute significantly to galactic chemical evolution.

The entropies encountered when the mass loss rate is high are low (~ 50), so that there is more production of ^{56}Ni by triple-alpha and a subsequent αp-process. As the neutron abundance available for the νp-process is given by

$$Y_n \approx \frac{\lambda_\nu Y_p}{\rho N_A \sum_i Y_i \langle \sigma v \rangle_{i(n,p)j}}, \tag{5.9}$$

increased seed production reduces the available neutron abundance and therefore hinders production of the p-process elements ^{74}Se, ^{78}Kr, ^{84}Sr, and ^{92}Mo. Addi-

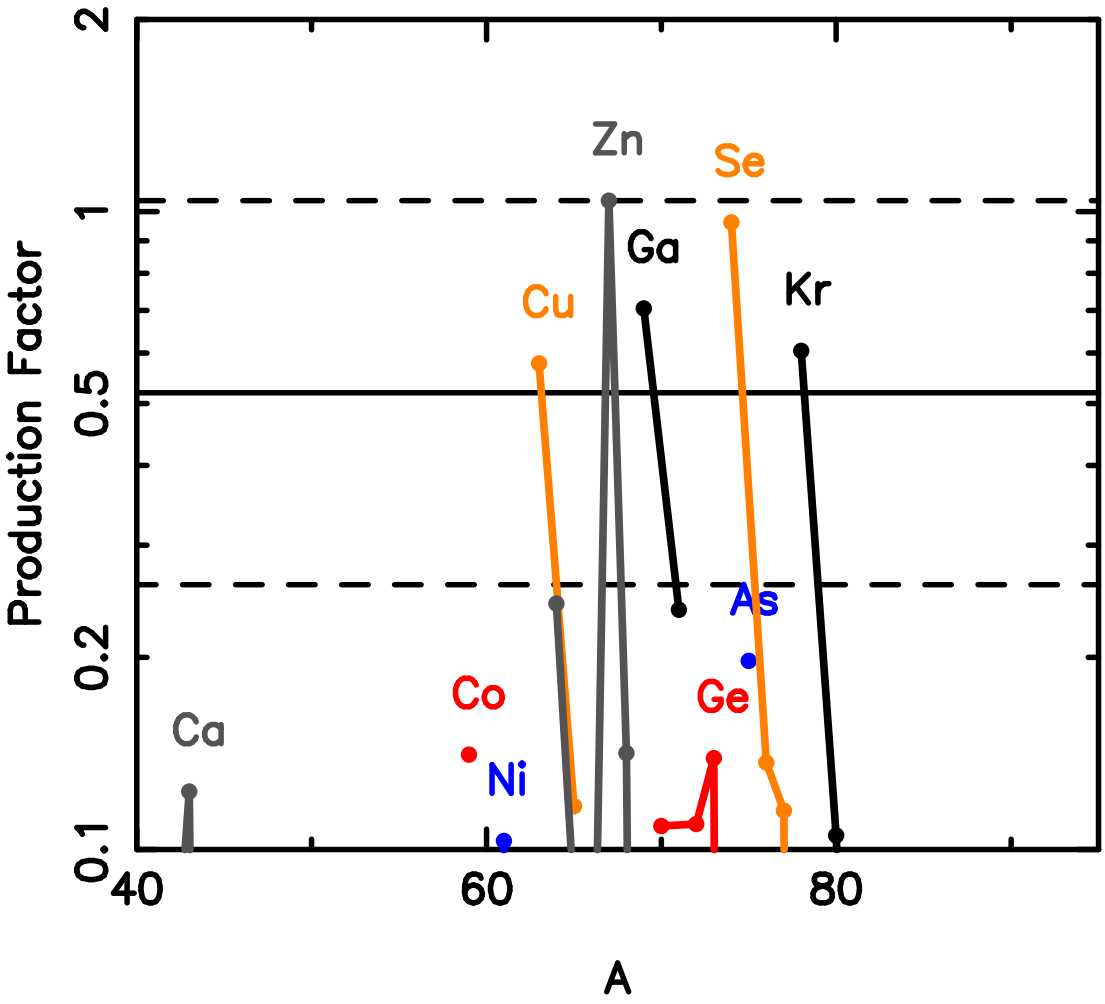

Figure 5.12: Isotopic production factors from the NDW model employing the neutrino luminosities from Huedepohl et al. (2010). The production factors are calculated assuming that 7.4 $M_{\odot}$ of material was ejected in the supernova in addition to the wind. The horizontal lines are similar to those in figure 5.5. Notice that none of the production factors are significantly greater than one.

tionally, at early times, the dynamical time scale is short which implies a smaller integrated neutron to seed ratio, Δ_n (see the appendix).

The yields of from this model cannot be combined with the yields from the rest of the supernova because they are not published. As Nomoto (1984) has discussed, the mass inside the helium burning shell was close to the mass of the neutron star that was left after the explosion. Therefore the ejecta of the supernova is expected to have small production factors. This implies that, even when the yields of the NDW are combined with the rest of the supernova, it is unlikely that these low mass core collapse supernovae will contribute significantly to galactic chemical evolution.

5.4.2.1 Effect of a Wind Termination Shock

As was mentioned above, it is very possible that a transonic wind solution may not be appropriate this early in the supernovas evolution. Fischer *et al.* (2010) have found that a wind termination shock is not present in a one-dimensional supernova model using the progenitor from Nomoto (1984). Still, it is interesting to consider the effect of a reverse shock on the wind nucleosynthesis.

A second simulation was run with a time dependent boundary pressure given by equation 5.6, with $E_{sn} = 10^{50}\,\mathrm{erg}$ and $v_{sn} = 2 \times 10^{9}\,\mathrm{cm\ s^{-1}}$. This results in a wind termination shock at a radius of approximately $3 \times 10^{8}\,\mathrm{cm}$ throughout the simulation. Inside the wind termination shock the wind dynamics are very similar to those in the run with no boundary pressure. There is almost no difference in the nucleosynthesis in the runs with and without a wind termination shock.

After 0.75 s, the post shock temperature drops below 1 GK and the wind termination shock has little effect on subsequent nucleosynthesis. Because the

post shock temperature is high for less than one second, the wind termination shock has very little effect on the integrated nucleosynthesis. A larger explosion energy would likely result in a larger effect on the nucleosynthesis, but there are still very few neutrons available to bypass the long lived waiting points and it seems unlikely that the production factors would be increased by more than a factor of a few.

5.5 Discussion

5.5.1 Strontium and Yttrium in Halo Stars

Since strontium and yttrium are abundantly produced in our models, it may be that the NDW has contributed to their production throughout cosmic history. An interesting possibility is that the abundances of these elements might trace the birth rate of neutron stars at an early time. Taking a standard r-process abundance pattern from metal poor stars with strong r-process enhancments, Travaglio et al. (2004) find that 8% and 18% of solar strontium and yttrium, respectively, are not produced by either the "standard" r-process or any component of the s-process. It therefore seems plausible that charged particle reactions in the NDW could make up this "missing" component.

Any nucleosynthesis that happens in the NDW will be primary, i.e. provided that the mass function of neutron stars at birth does not itself scale with metallicity, similar nucleosynthesis will occur for stars of any population. Below [Fe/H]~ -1.5, no component of the s-process contributes to the abundances of N = 50 closed shell isotopes (Serminato et al. 2009). If the NDW escapes the potential well of the PNS, and contributes to the galactic budget of N = 50 closed

shell isotopes, it should provide a floor to [Sr/Fe] and [Y/Fe]. Based upon the arguments of Travaglio et al. (2004), this floor would be at [Sr/Fe]≈ -0.18 and [Y/Fe]≈ -0.16. These numbers assume that when the main r-process source contributes in addition to the NDW, [Sr/Fe] and [Y/Fe] approach their solar values even though the s-process has yet to contribute. This is consistent with observations.

In defining this floor, one must assume that the abundances in a particular star sample a large number of individual supernovae. This is because the production of N=50 closed shell elements likely depends on the PNS mass and therefore the progenitor mass. As we have found, [Sr/Fe]$= 0.8$ in the $20M_{\odot}$ model with reduced anti-neutrino temperatures, but the $8.8M_{\odot}$ model produces no strontium. Observations show that below [Fe/H]~ -3, the spreads in [Sr/Fe] and [Y/Fe] increase significantly and the mean values falloff some (François et al. 2007, Cohen et al. 2008, Lai et al. 2008). Single stars have values of [Sr/Fe] below the predicted floor. This could be because, at this metallicity, the metals in a particular star come from only a handful of supernovae.

Another possible explanation of this variation is that supernova fall back varies with metallicity. Since the NDW is the innermost portion of the supernova ejecta, it will be the most susceptible to fallback. It has been found that the amount of supernova fallback depends strongly on the metallicity of the progenitor, especially going between zero and low metallicity (Zhang et al. 2008). Additionally, mixing is also greatly reduced in zero metallicity stars compared to solar metallicity stars due to the formers compact structure (Joggerst et al. 2009).

The current understanding of supernova fallback suggests that the nucleosynthetic contribution of the NDW will be suppressed at very low metallicity. Of

course, the ejection of iron by the supernova is also very susceptible to fallback, so the effect of fallback on the evolution of [Sr,Y/Fe] is complicated and may require fine tuning to give the observed decrease. A somewhat different explanation was offered by Qian & Wasserburg (2008) who attributed the fall off of [Sr/Fe] at low metallicity to the evolution of the "hypernova" rate with metallicity. For their purposes, hypernovae were stellar explosions that contributed iron without making much strontium.

Given the sensitivity of strontium and yttrium yields to uncertain NDW characteristics, especially neutrino fluxes and temperatures, it may be some time before the complex history of these elements is even qualitatively understood. It is likely though that their abundances in halo stars will ultimately be powerful constraints upon the evolution of supernova physics as a function of metallicity.

5.5.2 Possible Modifications of the Basic Model

As is clear from figures 5.5 and 5.12, the simplest case of a non-magnetic non-rotating NDW from a neutron star without additional energy deposition does not produce r-process nuclei in significant abundances. Are there extensions to this simple scenario that *could* make the wind a site of the r-process?

As was pointed out by Metzger et al. (2007), the combination of rotation and magnetic fields can decrease the dynamical time scale by magnetic "flinging". This is not particularly effective. Adding a non-thermal source of kinetic energy means that less thermal energy must be put into the wind for it to escape the potential well. Therefore, lower entropies are achieved. It seems unlikely that this mechanism, by itself, will salvage the NDW as a site for the full r-process. If there were a way to make the rotation rate of the PNS high enough, it might

be possible that there would be a centrifugally driven outflow. Then the electron fraction would be determined by kinetic equilibrium much deeper in the PNS envelope, and the material in the outflow would have an electron fraction much lower than that seen in the wind.

To test this possibility, we ran calculations with a centrifugal force term added and corotation with the PNS enforced out to 10^3 km. Unfortunately, for reasonable PNS spin rates (20 ms period), we found this had little effect on the nucleosynthesis. These calculations were in a regime were the electron fraction was still set by neutrino interactions.

Many authors have discussed the possible effects of both matter-enhanced(Qian & Fuller 1995, Sigl 1995) and collective neutrino (Pastor & Raffelt 2002, Duan et al. 2006) oscillations on NDW nucleosynthesis. If electron antineutrinos could undergo a collective oscillation near the launch radius while the electron neutrinos did not, this would increase the average energy of the antineutrinos if the μ and τ neutrinos have a significantly higher temperature, facilitating a reduction in the electron fraction. For a normal mass hierarchy however, matter enhanced neutrino oscillations would probably cause electron neutrino flavor conversion, which would *increase* the electron fraction and decrease the probability of significant r-process nucleosynthesis (Qian & Fuller 1995).

Collective neutrino oscillations can cause antineutrino oscillations in the region were the electron fraction is set, and thereby decrease the electron fraction where pure MSW oscillations would have predicted an increased electron fraction(Duan et al. 2006). Clearly, the main effect of oscillations would be on the composition of the wind, not the dynamics. As can be seen in the neutrino two color plots, oscillations would have to change the effective temperature of the anti-neutrinos by

a very large amount to move from a region where N=50 close shell nucleosynthesis occurs to a region where the second r-process peak can be produced.

These effects are based upon the assumption that μ- and τ-neutrinos are significantly more energetic than the electron neutrinos. In the calculation of Woosley et al. (1994), this is the case, as can be seen in figure 5.2. Interestingly, the μ and τ temperatures are almost the same as the electron anti-neutrino temperature in the Hüdepohl *et al.* (2010) calculation, which can be seen in figure 5.10. It is not clear wether this difference obtains because of the difference in the PNS masses or the significantly different neutrino physics employed in the calculations. A detailed study of neutrino transport in static backgrounds showed that the inclusion of all relevant neutrino interactions brings the average energies of the μ- and τ- neutrinos closer to the temperature of the anti-electron neutrinos (Keil et al. 2003). Therefore it is uncertain wether or not neutrino oscillations could effect nucleosynthesis significantly. Clearly, the uncertainties here are not in the wind itself but in the formation of the spectra in the PNS and the details of neutrino transport with neutrino oscillations.

Finally, it has been suggested (Takahashi et al. 1994a, Qian & Woosley 1996, Suzuki & Nagataki 2005b) that adding a secondary source of volumetric energy deposition can significantly increase the entropy of the wind, which results in a more alpha-rich freeze out and conditions that would be more favorable for r-process nucleosynthesis. The addition of energy to the wind also decreases the dynamical timescale. Since the important quantity to consider for the r-process is s^3/τ_d (Hoffman et al. 1997), both effects increase the chance of having a significant neutron to seed ratio after freeze out. If the NDW model is to be salvaged, this seems to us the minimal necessary extension. Of course, the physical process

contributing this extra energy is very uncertain. One possibility is that oscillations of the PNS power sound waves which produce shocks and deposit energy in the wind, similar to the supernova mechanism of Burrows et al. (2006), but smaller in magnitude. We will explore this possibility in some detail in a subsequent paper.

5.6 Conclusions

We have performed calculations of the dynamics and nucleosynthesis in time dependent neutrino driven winds. This was done for two sets of neutrino spectra calculated in one-dimensional supernova models taken from the literature. The nucleosynthesis in these models was compared with supernova yields to determine if these models were consistent with observations. Additionally, we compared the results of these numerical models to analytic models of the neutrino driven wind and found good agreement.

Similar to most of the work on the NDW after Woosley et al. (1994), we find that it is unlikely that the r-process occurs in the neutrino driven wind unless there is something that causes significant deviation from a purely neutrino driven wind. Additionally, in the simplest case, there is little production of p-process elements at early times in the wind. In our calculation that used spectra from a more massive neutron star, the wind only produces the N=50 closed shell elements ^{87}Rb, ^{88}Sr, ^{89}Y, and ^{90}Zr.

This result is sensitive to small changes in the neutrino interaction rates (i.e. the inclusion of weak magnetism) and changes to the neutrino temperature of order 10%. We also find that the effect of a wind termination shock on the wind nucleosynthesis is small.

Using neutrino spectra from an $8.8 M_{\odot}$ supernova that drives a wind which

is proton rich throughout its duration (Hüdepohl *et al.* 2010), we find that no significant νp-process occurs and the wind does not contribute to the yields of the supernova. The neutrino spectra from this model are probably more accurate than the spectra from the model of Woosley et al. (1994). We also investigated the effect of an outer boundary pressure which resulted in a wind termination shock. This had a negligible effect on the nucleosynthesis.

However, one also expects that the nucleosynthesis in the NDW will vary considerably from event to event, especially with the mass and possibly the rotation rate of the PNS. The winds from more massive PNS have greater entropy and might, in general, be expected to produce heavier elements and more of them. The neutrino spectral histories of PNS as a function of mass have yet to be determined over a wide range of parameter space. Currently, the neutrino luminosities and temperatures are the largest uncertainties in models of the NDW.

5.7 Appendix: Analytic Wind Dynamics

To understand the wind dynamics, we follow arguments similar to those of Qian & Woosley (1996) and Cardall & Fuller (1997). Conservation of the stress-energy tensor and number flux in a Schwarzschild geometry in steady state leads to the wind equations in critical form

$$\dot{M} = 4\pi r^2 m_b n \gamma y v \tag{5.10}$$

$$\gamma y v \frac{d}{dr} \ln(\gamma y h_r) = \frac{\dot{q} m_b}{c^2 h_r} \tag{5.11}$$

$$\gamma^2 \left(v^2 - c_s^2\right) \frac{dv}{dr} = \frac{v}{r}\left[2c_s^2 - \frac{GM}{ry^2}\left(1 - \frac{c_s^2}{c^2}\right)\right] - \frac{\dot{q} m_b}{3\gamma y h_r} \tag{5.12}$$

here $\dot{M}$ is the rest mass loss rate, m_b is the baryon mass, n is the baryon number density, v is the velocity measured by an observer at rest in the Schwarzschild

frame, $\gamma = (1 - v^2/c^2)^{-1/2}$, $\dot{q}$ is the neutrino heating rate per mass, c_s is the sound speed, M is the neutron star mass, $h_r = 1 + \epsilon/(m_b c^2) + P/(n m_b c^2)$, P is the pressure, and ϵ is the energy per baryon not including the rest mass. To fully describe the wind, these equations must be supplemented by a set of nuclear rate equations and an equation of state. For our analytic calculations we used a radiation-dominated non-degenerate equation of state comprised of relativistic electrons, positrons, and photons.

First, we estimate where the critical radius (i.e. the radius where radiation pressure equals the nucleon gas pressure) sits in relation to the neutrino sphere. Neglecting the temperature gradient in the equation of hydrostatic balance gives the density structure of the atmosphere,

$$\log(n(r)/n_c) \approx -\int_{r_l}^{r} dr \frac{GMm_b}{r^2 y^2 T(r)} \tag{5.13}$$

The optical depth of this atmosphere for neutrinos is

$$\tau = \sigma_\nu(\epsilon_\nu) \int_r^\infty \frac{n}{y} \approx \sigma_\nu(\epsilon_\nu) n_c \int_r^\infty \frac{dr}{y} \exp\left(-\int_{r_l}^{r} dr' \frac{GMm_b}{r'^2 y'^2 T(r')}\right) \tag{5.14}$$

Taking the neutrinosphere to be at an optical depth of 2/3, the gas pressure equal to the radiation pressure at the critical radius, and approximating gravity as constant throughout the envelope, we arrive at an equation for the critical radius

$$r_c \approx R_\nu \left[1 + \frac{T_c}{g m_b R_\nu} \ln\left(\frac{2}{3\tau_0} y_\nu\right)\right] \tag{5.15}$$

where $\tau_0 = \sigma_\nu(\epsilon_\nu) n_c T_c / g m_b$. For characteristic values of L_ν, ϵ_ν, R_ν, and M, r_c is only a few percent larger than R_ν. This implies that the GR corrections to the neutrino interaction rates at r_c will be at most a few percent. For characteristic values, the GR correction to gravity will be $y(r_l)^{-2} \approx y_\nu^{-2} \approx 1.5$. This agrees

with the observation made by previous authors that GR corrections to gravity dominate over corrections to the neutrino interaction rates (Cardall & Fuller 1997, Thompson et al. 2001).

Assuming that most neutrino heating occurs near r_c, the entropy can be considered constant once the temperature cools to the nucleon recombination temperature ($T \approx 0.5$ MeV). Therefore, the final nuclear abundances in the wind depend mainly on the wind entropy, electron fraction, and the timescale for outflow (Qian & Woosley 1996, Hoffman et al. 1997). To determine the contribution of the wind to the nucleosynthesis of the entire supernova, the mass loss rate must also be known. We now find estimates for these quantities and for the transonic radius of the wind.

To determine the asymptotic entropy, the total energy deposition per baryon needs to be estimated. Using equation 5.11 and assuming the asymptotic velocity is small, the total energy deposited per baryon is

$$\ln(\gamma_f) - \ln(y_c h_c) \approx -\ln(y_c h_c) \approx \int_{r_\nu}^{\infty} dr \frac{\dot{q} m_b}{\gamma y v c^2 h_r} \approx \int_{r_c}^{\infty} dr \frac{\dot{q}_\nu m_b}{\gamma y v c^2 h_r} = Q/(m_b c^2) \tag{5.16}$$

Considering that most of the neutrino energy is deposited near the hydrostatic atmosphere, the final entropy per baryon is approximately

$$s_f = \int_{r_\nu}^{\infty} dr \frac{\dot{q} m_b}{\gamma y v T} \approx \int_{r_c}^{\infty} dr \frac{\dot{q}_\nu m_b}{\gamma y v T} + s_c \approx -\frac{m_b c^2 \ln(h_c y_c) h_{r,c}}{T_c} + s_c \tag{5.17}$$

Assuming that the neutron-proton rest mass difference is negligible, the entropy of the envelope is negligible, and taking the relativistic enthalpy outside the logarithm to be one results in the scaling relation

$$s_f \approx 464 \ln\left(y_c^{-2}\right) R_{\nu,6}^{1/3} L_{\nu,51}^{-1/6} \epsilon_{\nu,MeV}^{-1/3} \left(\frac{y_c}{y_\nu}\right)^{1/3}. \tag{5.18}$$

Notice that all the general relativistic corrections, both due to gravity and to the neutrino interaction rates, increase the entropy from the non-relativistic case (Cardall & Fuller 1997, Otsuki *et al.* 2000). As was discussed above, the dominant correction to the newtonian case is from the GR correction to gravity.

To fix the mass loss rate, we must estimate the velocity at the critical radius. Taking the momentum equation in critical form and assuming approximate hydrostatic equilibrium and subsonic velocities gives $c_s^2 dv/dr \approx \frac{\dot{q}}{3\gamma y}$. Assuming that acceleration has occurred over a scale height, we have

$$y v_c \approx \frac{h_{eff} \dot{q}(r_c)}{6 c_s^2} \tag{5.19}$$

where the heating rate at the critical radius is divided by two to account for the fact that beneath the critical radius the net heating goes to zero over approximately a scale height so that a characteristic value of the heating rate is one half the heating rate at the critical radius. The scale height is given by $h_{eff}^{-1} = (\rho + P) GM / P r^2 y^2$. Combining these with equation 5.10 results in a mass loss rate of

$$\dot{M} \approx 4\pi r_c^4 \frac{P}{\rho + P} y_c^2 \frac{m_b n_c \dot{q}_\nu(r_c)}{3 G M c_{s,c}^2} \tag{5.20}$$

Using our result for the entropy gives a scaling relation for the mass loss rate,

$$\dot{M} \approx 7.4 \times 10^{-11}\, \mathrm{M_\odot\, s^{-1}} \frac{r_{l,6}^4 L_{\nu,51}^{5/3} \epsilon_{\nu,MeV}^{10/3}}{R_{\nu,6}^{10/3} \left(M/M_\odot\right) \ln\left(y_l^{-2}\right)} y_l^2 \left(\frac{y_\nu}{y_l}\right)^{10/3}. \tag{5.21}$$

Notice that GR corrections reduce the mass loss rate significantly, by about a factor of 2. Only including GR effects on neutrino propagation and energies decreases the mass loss rate by about 10%. The reduced mass loss rate due to GR corrections does effect the integrated nucleosynthetic yields, although the effect is not as great as the effect of the GR corrections on the entropy.

Given the entropy and the mass loss rate, we can solve for the evolution of temperature with radius outside of the heating region where the velocity is still small using the relation $\ln(h_r y) = \ln(y_c h_{r,c}) + Q \approx 0$, which gives

$$r \approx \frac{2GM}{c^2}\left[1 - (1 + Ts_f/m_b)^{-2}\right]^{-1} \tag{5.22}$$

The dynamical timescale of the wind is defined by $\tau_d^{-1} = v\gamma y/n\,|dn/dr|$. Steady state baryon number conservation yields

$$\frac{1}{n}\left|\frac{dn}{dr}\right| = \frac{2}{r} + \frac{\gamma^2}{v}\frac{dv}{dr} + \frac{GM}{r^2 y^2} \tag{5.23}$$

Neutrino energy deposition will no longer dominate the momentum equation when nucleons reform, but the velocity will be subsonic. In this limit, the momentum equation yields

$$\frac{\gamma^2}{v}\frac{dv}{dr} = \frac{GM}{r^2 y^2 c_s^2}\left(1 - c_s^2\right) - \frac{2}{r} \tag{5.24}$$

which results in an estimate for the dynamical timescale far inside the sonic point,

$$\tau_d^{-1} \approx \frac{G\dot{M}M}{4\pi r^4 n m_b y^2 c_s^2} \tag{5.25}$$

For seed formation we are interested in the dynamical timescale around 2 MeV. Combining with our result for the temperature structure of the atmosphere we have

$$\tau_{d,2} \approx \frac{16\pi(GMm_b)^3 m_b K}{9 s_f^4 \dot{M}} y^2 \tag{5.26}$$

$$\approx 8.2\,\mathrm{ms}\left(\frac{M}{1.4M_\odot}\right)^3\left(\frac{s_f}{100}\right)^{-4}\left(\frac{\dot{M}}{10^{-5}M_\odot\,\mathrm{s}^{-1}}\right)^{-1} y^2 \tag{5.27}$$

To agree with the definition of the dynamical timescale given in Qian & Woosley (1996), this should be multiplied by three as our definition of τ_d differs slightly from the one used in Qian & Woosley (1996). We note that all of the scaling relations

above are equivalent to those of Qian & Woosley (1996) in the non-relativistic limit.

From this discussion, it is unclear if a transsonic wind will obtain. A reasonable criteria for transsonic solutions is that $\rho v^2 + P$ at the sonic point is greater than the pressure behind the supernova shock, which is approximately given by equation 5.6. Equation 5.12 along with equation of state for the wind can be combined to give the temperature and sound speed at the sonic radius in terms of the sonic radius and known quantities

$$T_s = \frac{3GM_{NS}m_b}{2r_s s_f y_s^2 \left(1 + \frac{GM_{NS}}{2r_s y_s^2 c^2}\right)} \tag{5.28}$$

This results in an implicit equation for the sonic radius

$$\dot{M} \approx r_s^{-3/2} \frac{16\pi m_b^{1/2} K}{3^{3/2} s_f^{1/2}} y_s \gamma_s \left(\frac{3GM_{NS}m_b}{2s_f y_s^2 \left(1 + \frac{GM_{NS}}{2r_s y_s^2 c^2}\right)} \right)^{7/2} \tag{5.29}$$

where K is the radiation constant for photons and leptons combined. In the non-relativistic limit, the sonic radius reduces to

$$r_s \approx 860\,\mathrm{km} \left(\frac{s_f}{100}\right)^{-8/3} \left(\frac{M_{NS}}{1.4M_\odot}\right)^{7/3} \left(\frac{\dot{M}}{10^{-5}M_\odot\,\mathrm{s}^{-1}}\right)^{-2/3}. \tag{5.30}$$

The wind termination shock position is approximately given by (Arcones et al. 2007)

$$R_{rs} \approx 1.3{\times}10^3\,\mathrm{km} \left(\frac{\dot{M}}{10^{-5}M_\odot\,\mathrm{s}^{-1}}\right)^{1/2} \left(\frac{R_s}{10^9\,\mathrm{cm}}\right)^{3/2} \left(\frac{E_{sn}}{10^{51}\,\mathrm{erg}}\right)^{-1/2} \left(\frac{v_w}{10^9\,\mathrm{cm\ s}^{-1}}\right)^{1/2} \tag{5.31}$$

where E_{sn} is the supernova explosion energy, R_s is the radius of the supernova shock, and v_w is the wind velocity just inside the wind termination shock.

5.8 Appendix: Analytic Wind Nucleosynthesis

The electron fraction in the wind is given by kinetic equilibrium of neutrino interaction rates at the critical radius, as the temperature has decreased enough that lepton capture is unimportant (Qian & Woosley 1996)

$$Y_{e,f} \approx \frac{\lambda_{\nu_e}}{\lambda_{\nu_e} + \lambda_{\bar{\nu}_e}} \tag{5.32}$$

where λ_{ν_e} is the neutrino capture rate per baryon and $\lambda_{\bar{\nu}_e}$ is the anti-neutrino capture rate per baryon. After weak interactions cease and the temperature has decreased about 0.5 MeV, alpha particles form in the wind. The initial alpha number fraction is $Y_{\alpha,i} \approx Y_e/2$ for neutron-rich conditions and $Y_{\alpha,i} \approx 1/2 - Y_e/2$ for proton-rich conditions.

In both proton and neutron-rich winds, the nucleosynthesis will be characterized by the neutron to seed ratio in the wind. For winds with $Y_e >\approx 0.5$, alpha particles recombine into ^{12}C by the standard triple alpha reaction and then experience alpha particle captures up to approximately mass 56 (Woosley & Hoffman 1992). The slowest reaction in this sequence is ^{4}He$(2\alpha,\gamma)^{12}$C, so the total number of seed nuclei produced is equal to the number of ^{12}C nuclei produced. The rate of alpha destruction is given by

$$\frac{dY_\alpha}{d\tau} \approx -14\rho_0^2 Y_\alpha^3 \lambda_{3\alpha} \tag{5.33}$$

where $\rho_0 = m_b n$ is the rest mass density and $\lambda_{3\alpha}$ is the rate of triple alpha, which includes double counting factors. The factor of 14 comes from assuming alpha captures stop at ^{56}Ni. In general, we define an abundance by $n_i = nY_i$, where n_i is the number density of species i and n is the baryon density. Using our definition of the dynamical timescale, we have $d\tau \approx -\frac{\tau_d}{3T} dT$. Transforming Y_α to a function

of temperature makes the integral given above trivial to solve. Using a rate for triple-alpha from Caughlan & Fowler (1988) and assuming the reaction flow stops at ^{56}Ni results in a seed abundance at the end of the α-process given by

$$Y_s \approx \frac{1-Y_e}{28}\left(1-\left[1+1.4\times10^5\tau_d s_f^{-2}(1-Y_e)^2\right]^{-1/2}\right) \tag{5.34}$$

where s_f^{-2} enters because $\rho_0 \propto T^3/s_f$ for a radiation dominated equation of state and the density enters to the second power.

Under proton-rich conditions, the νp-process has the potential to occur. This process is similar to the rp-process, except that long lived beta-decays are by-passed by (n,p) reactions. An estimate for the integrated number of free neutrons produced is $\tau_d\lambda_{\bar{\nu}_e}(T_9\approx 2)$, so that the neutron to seed ratio is

$$\Delta_n \approx \tau_d\lambda_{\bar{\nu}_e}(T_9\approx 2)\frac{Y_p}{Y_s}. \tag{5.35}$$

Here, $\lambda_{\bar{\nu}_e}(T_9\approx 2)$ is the neutrino capture rate at the seed formation radius. A similar relation is found in Pruet et al. (2006). Although it is hard to estimate its effect, we note that the presence of a reverse shock can significantly affect the νp-process nucleosynthesis, as passage through the reverse shock slows the outward flow and rarefaction of the wind. Additionally, it increases the temperature to close to the post supernova shock temperature. At early times for characteristic explosion energies, the wind is shock heated to a temperature of a few GK. This all combines to give a longer period of time over which proton capture on heavy nuclei is efficient and allows the νp-process to continue to higher mass than it would if no wind termination shock were present.

In the neutron-rich case, seed nuclei are produced by the slightly different reaction sequence ^{4}He(αn,γ)^{9}Be(α,n)^{12}C (Woosley & Hoffman 1992). For the conditions encountered in the wind, neutron catalyzed triple-alpha proceeds about

ten times as quickly as ^{4}He(2α,γ)^{12}C. This implies that there will be a larger seed number than in proton-rich conditions. The rate of helium destruction is given by the equations (Hoffman et al. 1997)

$$\frac{dY_\alpha}{d\tau} \approx -\frac{\bar{Z}}{2}\rho_0 Y_\alpha Y_9 \lambda_{\alpha,n}(^9\mathrm{Be}) \tag{5.36}$$

$$\frac{dY_n}{dY_\alpha} \approx \frac{2(\bar{A}-2\bar{Z})}{\bar{Z}} \tag{5.37}$$

$$Y_9 = \frac{27}{32}N_a^2\left(\frac{2\pi\hbar^2}{m_b}\right)^3 Y_n Y_\alpha^2 \rho_0^2 T^{-3}\exp((B_9-2B_\alpha)/T) \tag{5.38}$$

where $\bar{Z}$ is the average proton number of the seed nuclei, $\bar{A}$ is the average nucleon number of the seed nuclei, N_a is Avogadro's number, Y_α is the alpha particle abundance, Y_n is the neutron abundance, Y_9 is the ^{9}Be abundance, $\lambda_{\alpha,n}(^9\mathrm{Be})$ is the rate of ^{9}Be destruction by (α, n), and B_α and B_9 are the binding energies of ^{4}He and ^{9}Be, respectively. For $\lambda_{\alpha,n}(^9\mathrm{Be})$, we employ the rate given in Wrean et al. (1994). This set of equations can be solved analytically by once again transforming from proper time to temperature using the dynamical timescale. The resulting implicit expression for the final alpha fraction is somewhat cumbersome, so we do not reproduce it here. The seed abundance in terms of the initial and final alpha fraction is

$$Y_s = 2\frac{Y_{\alpha,i}-Y_{\alpha,f}}{\bar{Z}} \tag{5.39}$$

the final neutron fraction is given by

$$Y_{n,f} = (1-2Y_e) - 2\frac{\bar{A}-2\bar{Z}}{\bar{Z}}\left(Y_{\alpha,i}-Y_{\alpha,f}\right) \tag{5.40}$$

so that the neutron to seed ratio is

$$\Delta_n = \frac{\bar{Z}(1/2-Y_e)}{Y_e/2-Y_{\alpha,f}} + 2\bar{Z} - \bar{A}. \tag{5.41}$$

The seed abundance at the end of charged particle reactions can be estimated by (Hoffman et al. 1997)

$$Y_s \approx \frac{1-2Y_e}{10}\left(1-\exp\left[-8\times10^8\tau_d s_f^{-3}Y_e^3\right]\right) \tag{5.42}$$

where it has been assumed that the neutron abundance is what limits the reaction. Notice that the seed abundance in the proton-rich case depends on the entropy squared because it is mediated by an effective three body reaction, but in the neutron-rich case the entropy enters to the third power because of the effective four body interaction that mediates seed production.

Chapter 6

Secondary Heating in Neutrino Driven Winds

This work was performed in collaboration with Stan Woosley.

Abstract

The neutrino driven wind (NDW) produced in core-collapse supernovae has long been considered a potential site for r-process nucleosynthesis, but there are problems with the scenario. First, the entropies found in realistic simulation of the wind are not large enough to result in an r-process. Second, recent work has shown that the wind may in fact be proton rich. One possible solution to the first problem is the inclusion of a secondary volumetric heating source. Here we explore the necessary conditions for a r-process to occur for assumed values of the electron mole number by post-processing hydrodynamic calculations with a full r-process nuclear network. We find that the secondary heating source must supply approximately the same amount of power to the wind as neutrino energy deposition to successfully produce an r-process. The conclusion is insensitive to

the electron mole fraction of the material, as long as the material is neutron rich. Acoustic power is explored as a possible source of this secondary heating. We find that acoustic power from a vibrating neutron star naturally deposits at a radius that can highly leverage the entropy in the wind. The additional heating not only raises the entropy but shortens the expansion time scale, both of which are favorable for the r-process.

6.1 Introduction

Soon after the neutrino driven wind (NDW) was suggested as a site for r-process nucleosynthesis (Woosley et al. 1994), it was realized that the entropy in the wind was too low for significant r-process nucleosynthesis to occur when only neutrino heating was included (Witti et al. 1994b, Qian & Woosley 1996, Hoffman et al. 1997). Calculations using realistic neutrino luminosities suggest that the standard NDW is, at most, responsible for producing a few isotopes near the N = 50 closed shell (e.g. Roberts et al. 2010). Previous studies that successfully created the r-process in neutrino driven outflows have either artificially increased the entropy, without considering how this increase in entropy would affect the dynamical timescale, or decreased the electron fraction to unrealistic levels (e.g. Takahashi et al. 1994b).

On the other hand, the NDW is an appealing site for the r-process from the standpoint of galactic chemical evolution. Elements generally attributed to the r-process are seen in metal poor stars, suggesting that massive stars are the site for the r-process (Sneden et al. 2008). The current galactic inventory of r-process material could be explained if only $\sim 10^{-5}\,M_{\odot}$ of r-process material was ejected by a typical supernova. The NDW ejects $\sim 10^{-4}\,M_{\odot}$ of neutron-rich material,

meaning that if all the neutron rich material were rich in r-process nuclei only a fraction of core-collapse supernovae would need to have the correct conditions for the r-process to occur to account for the galactic inventory.

A second, more recent problem with the NDW as an r-process site concerns the electron fractions encountered in the wind. With the inclusion of more accurate transport and neutrino physics, several groups have concluded that the wind is actually proton-rich throughout its evolution (Fischer et al. 2009, Huedepohl et al. 2009). But other recent work, including that presented in Chapter 2 of this thesis, suggests that the wind may be neutron rich (Roberts et al. 2012, Martínez-Pinedo et al. 2012). Given the uncertainty in the spectra of the neutrinos emitted from proto-neutron stars, it is unclear if the NDW even has a period of neutron richness. This is mostly a separate problem than the entropy and dynamical timescale of the wind. Therefore, in this work, we assume electrons fractions less than one half.

The total energy released in a core-collapse supernova is approximately equal to the binding energy of the neutron star remnant, $GM_{NS}^2/R_{NS} \sim 3 \times 10^{53}$. This energy is released over 10 to 20 s. A much smaller amount is required to drive mass loss rate $\dot{M}$ during the cooling phase, $\sim 10^{49}\,\mathrm{ergs}^{-1}$ over $\sim$ 10 seconds. Based upon this observation, secondary sources of energy input in the wind have been considered (Qian & Woosley 1996, Suzuki & Nagataki 2005a, Metzger et al. 2007). Qian & Woosley (1996), assumed an unspecified volumetric heating source and showed that it had the effect of significantly increasing the entropy and decreasing the dynamical timescale, creating conditions more favorable for r-process nucleosynthesis (Hoffman et al. 1997).

Suzuki & Nagataki (2005a) considered a magnetic mechanism for the sec-

ondary heating source - Alfven waves launched into magnetar winds and damping via non-linear processes. This mechanism requires magnetar strength magnetic fields. Metzger et al. (2007) considered this model, but also including rotation. The entropy increase both found was sensitive to the damping length parameter employed in their models. Neither calculated the detailed nucleosynthesis expected in such winds. Suzuki et al. (2006) did a preliminary study of nucleosynthesis in these Alfven wave heated winds.

Here, we explore the parameter space of extra energy deposition in the NDW to determine what conditions (energy deposition rate, damping length, and electron fraction) result in successful r-process nucleosynthesis by post-processing hydrodynamic models of the NDW with a full r-process network. Then we explore a purely hydrodynamic secondary wind heating source - acoustic energy, as suggested by (Qian & Woosley 1996). Proto-neutron star convection and oscillations (Burrows et al. 2006) are likely to excite gravito-acoustic waves that propogate outward through the envelope and into the wind. These eventually steepen into shocks and deposit their energy in the wind. We find in section 6.3.3 that these shocks naturally deposit energy at the correct radius for r-process synthesis and potentially revive the NDW as a viable site for the r-process as long as the wind is neutron rich.

6.2 General Characteristics of a Successful Secondary Heating Source

In this section we explore the necessary properties of a secondary energy source that would lead to a strong r-process, in particular the production of a second

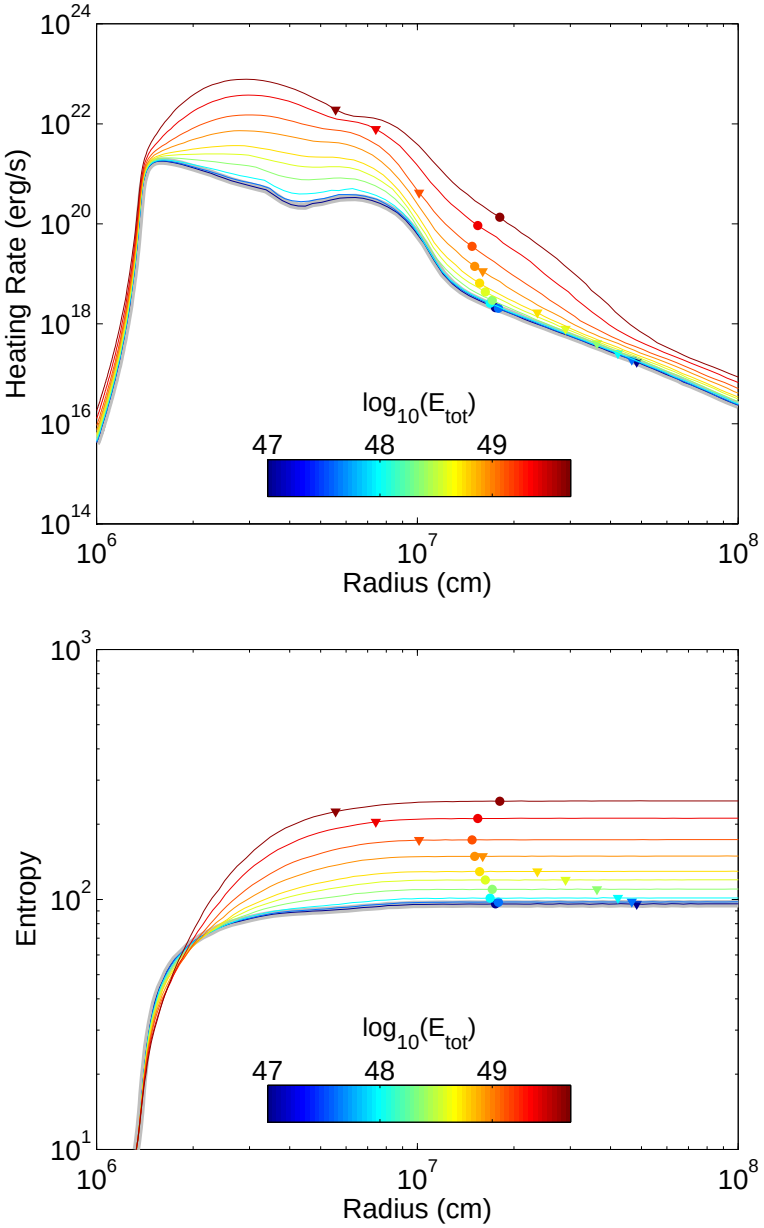

Figure 6.1: Wind properties for various secondary heating rates. $l_d = 10\,\mathrm{km}$ has been assumed. The heating rate and entropy of the wind as a function of radius are shown. The circles correspond to the radius at which the temperature is 2 GK and the triangles correspond to the sonic point.

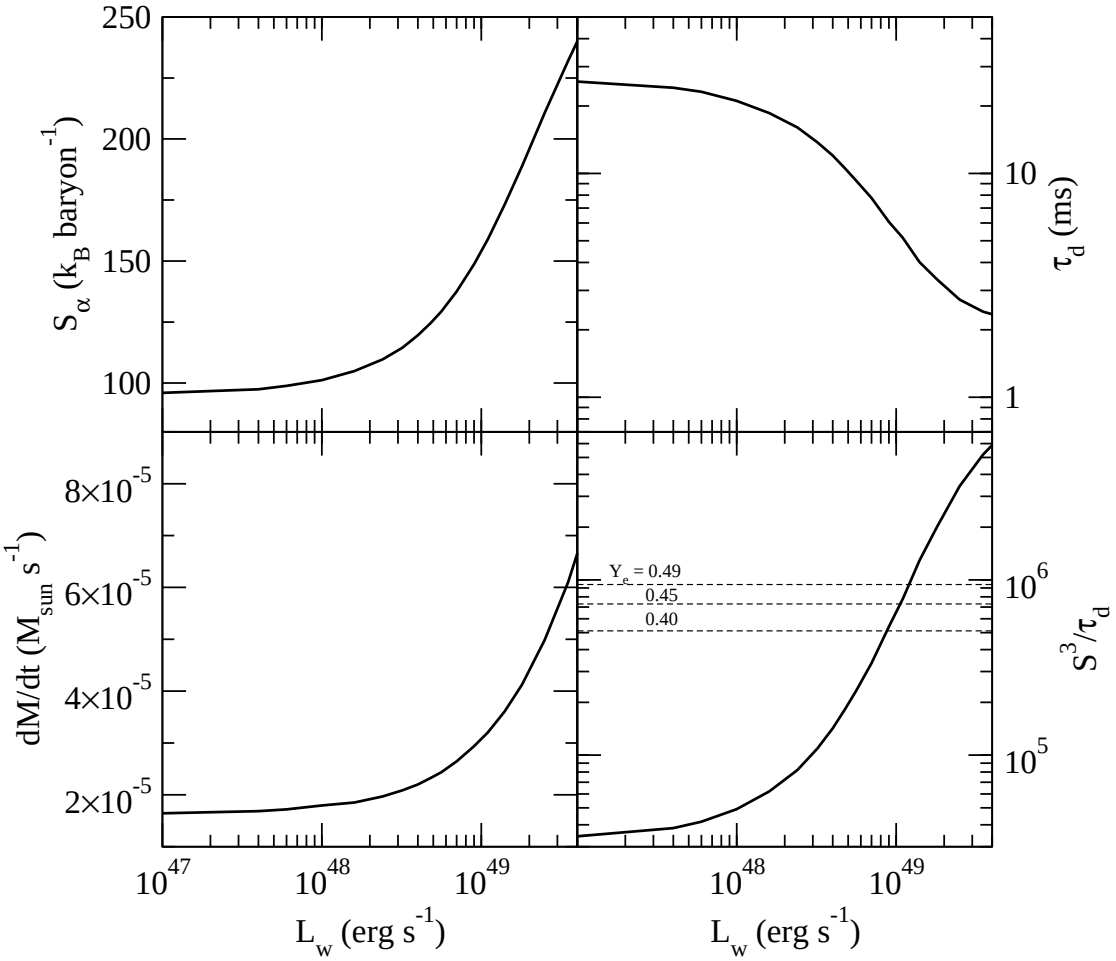

Figure 6.2: Wind properties for various secondary heating rates. $l_d = 10\,\mathrm{km}$ has been assumed. The entropy and dynamical timescale at $T = 2\mathrm{GK}$, the mass loss rate, and the nucleosynthesis condition s^3/τ_d are shown as a function of the assumed L_w. The dashed lines in the lower right plot show the threshold for r-process nucleosynthesis given by Hoffman et al. (1997) for a number of electron fractions.

r-process peak at $A \sim 190$. We first calculate the hydrodynamic structure of the wind in the presence of a secondary heating source, which is similar to the work done by Suzuki & Nagataki (2005a) and Metzger et al. (2007). We then use a full nuclear network to predict the nucleosynthetic results of these winds for a range of electron fractions to accurately assess the regions of parameter space which result in a successful r-process.

For conditions that are neutron-rich, the number of seed nuclei produced in the wind decreases with increasing s^3/τ_d, where s is the entropy where alpha recombination occurs and τ_d is the dynamical timescale. If the only energy source is neutrinos, the entropy at recombination is solely determined by the proto-neutron star atmospheric temperature (which depends on the properties of neutrinos emitted from the proto-neutron star) and the depth of the gravitational potential well. This results in the entropy of the wind decreasing with increasing neutrino luminosity and average energy. The dynamical timescale increases with luminosity and average neutrino energy, so that in a standard NDW the significant nucleosynthesis is most likely in the slow, high entropy wind, similar to the conditions found at late time in Woosley et al. (1994). These observations are mainly due to the fact that the neutrino heating rate is proportional to density, so that as the density in the wind decreases and the temperature decreases so does the net neutrino heating rate. Therefore, the bulk of the heating occurs near the radius where the wind is launched and the final entropy is just given by the amount of energy required to get out of the NS potential well divided by the temperature of the neutron star atmosphere.

Clearly, including a secondary heating source that is proportional to the density and falls off as r^{-2} will only augment the neutrino heating rate, which will

decrease the final entropy of the wind. Another option is a secondary heating source that is depends weakly on the density. It is then possible that in the high density envelope the heating rate of the secondary source per baryon will be small compared to the neutrino heating rate and it will not affect the atmospheric temperature. After the radius at which the wind is launched by neutrinos, the density falls off very sharply. At this point it is possible for the secondary heating source to dominate the heating rate per baryon. The secondary source may then increases the entropy and accelerate the flow (i.e. decrease the dynamical timescale). In tandem with neutron-rich material, this gives conditions much more favorable for r-process nucleosynthesis. In Woosley et al. (1994), it was suggested that neutrino/anti-neutrino annihilation provides such a density independent heating rate, but subsequent work has shown the net power input from neutrino annihilation to be small and not have a strong impact on the wind (c.f. Qian & Woosley 1996).

For a density independent heating rate, a simple way to parameterize the energy flux is

$$F(r) = \frac{L_w}{4\pi r^2} \exp[(r_0 - r)/l_d]. \tag{6.1}$$

Here, l_d takes into account the dissipation of the flux into the wind and sets the length scale over which this dissipation occurs. The specific energy deposition rate then becomes

$$\dot{q}_{ext} = \frac{L_w}{4\pi \rho l_d r^2} \exp[(r_0 - r)/l_d]. \tag{6.2}$$

Realistically, the dissipation length should be a function of the the properties of the wind material, as these determine the coupling of the the unspecified energy source to the material. We will argue what this should be for weak shocks in a subsequent section. This form is very similar to the form found for MHD wave

heating by Suzuki & Nagataki (2005a), which was subsequently used by Metzger et al. (2007), aside a term $v_r/(v_r + v_a)$ which accounts for the affects of a moving background on wave propagation (v_r is the radial velocity and v_a is the local Alfven velocity).

The mass loss rate due to secondary heating can be estimated as be

$$\dot{M}_w \approx \frac{L_w R_{ns}}{G M_{ns}} \approx \quad 2.7 \times 10^{-7}\, M_\odot \mathrm{s}^{-1} \times L_{w,47} R_6 \left(\tfrac{M}{1.4 M_\odot}\right)^{-1}. \tag{6.3}$$

The mass outflow rate due to neutrino heating can be linearly combined with this heating rate, as neutrino heating occurs interior to where the secondary heating mechanism becomes important. The neutrino heating induced mass flux is given by (Qian & Woosley 1996)

$$\dot{M}_\nu \quad \approx 2.5 \times 10^{-7}\, M_\odot \mathrm{s}^{-1} \times L_{\nu_e,51}^{5/3} \epsilon_{\nu_e,10\,\mathrm{MeV}}^{10/3} R_6^{5/3} M_{1.4}^2, \tag{6.4}$$

where $L_{\nu,51}$ and $\epsilon_{\nu,10\,MeV}$ are the electron neutrino luminosity and average neutrino energy at the neutrino sphere in units of 10^{51} ergs s^{-1} and ten MeV, respectively, and $M_{1.4}$ is the neutron star mass in units of 1.4 solar masses. The total mass loss rate for a fixed neutron star mass and radius is just proportional to the energy input into the wind, so that setting $\dot{M}_w \approx \dot{M}_\nu$ gives an approximate condition for dynamical heating to significantly affect the properties of the wind. This gives

$$L_{w,c} \approx 10^{47}\,\mathrm{erg\,s^{-1}} L_{\nu_e,51}^{5/3} \epsilon_{\nu_e,10\mathrm{MeV}}^{10/3} R_6^{2/3} M_{1.4}^3. \tag{6.5}$$

This is similar to the critical value found in Metzger et al. (2007). Given that L_{ν_e} and ϵ_{ν_e} decrease as cooling continues and the critical secondary heating luminosity

depends on these strongly, secondary heating is likely to be more important at later times in the NDW.

The entropy in the wind at the radius of alpha particle combination, r_α, is given by

$$\begin{aligned} s_\alpha = & \int_{R_{ns}}^{r_\alpha} \frac{dr}{vT} \left(\dot{q}_\nu + \dot{q}_w\right) \\ \approx & \frac{GM_{ns}}{R} \left\{ \frac{f_\nu}{T_{eff,\nu}} + \frac{f_w}{T_{eff,w}} \right\}, \end{aligned} \tag{6.6}$$

where $f_w = \dot{M}_w/(\dot{M}_w + \dot{M}_\nu)$, $f_\nu = 1 - f_w$, and $T_{eff,\nu} \approx 1.01\,\mathrm{MeV}\, R_{\nu,6}^{-1/3} L_{\nu,51}^{1/6} \epsilon_{\nu,MeV}^{1/3}$ is the temperature at which most of the neutrino energy is deposited (see Qian & Woosley (1996)). With the assumed heating rate given above, the effective temperature at energy is put into the wind via a secondary heating mechanism is

$$T_{eff,w} = \frac{\int_{R_{ns}}^{r_\alpha} dr e^{-r/l_d}}{\int_{R_{ns}}^{r_\alpha} dr T^{-1} e^{-r/l_d}}. \tag{6.7}$$

Assuming that $T \propto r^{-1}$ (which is true when there is no heating of the wind) and $r_\alpha \gg l_d$ gives $T_{eff,w} \approx T_{eff,\nu}/(l_d/R + 1)$. Therefore, the entropy in the wind will be

$$\begin{aligned} s \approx & 110\, L_{\nu_e,51}^{-1/6} \epsilon_{\nu_e,10MeV}^{-1/3} R_6^{-2/3} M_{1.4} \\ & \times \left\{ f_\nu + f_w \frac{R + l_d}{R} \right\}. \end{aligned} \tag{6.8}$$

The derivation of this approximate relation has not taken into account the fact that there is a finite radius at which α recombination occurs. When l_d becomes greater than r_α, the wind entropy may be increased, but this entropy increase does not help to make the freeze out more α rich. Therefore, the optimal damping length for a secondary heating mechanism is $R_{ns} \sim 10^6\,\mathrm{cm} < l_d < r_\alpha \sim 10^7\,\mathrm{cm}$. Given the approximate nature of these relations, it is useful to note that there is an upper limit that can be put on the α recombination energy. If all the energy

required to remove the material from the proto-neutron stars potential well is put in at the α recombination temperature $T \approx 0.3\,\mathrm{MeV}$, the maximum entropy is $s_{max} \approx 650 R_6^{-1} M_{1.4}$.

The argument for finding the dynamical timescale given by Qian & Woosley (1996) should still hold when secondary heating is present. This gives

$$\tau_d \equiv \left.\frac{r}{v}\right|_{T\approx 0.5\mathrm{MeV}} \approx 2.5\,\mathrm{s}\ s_{\alpha,2}^{-4} M_{1.4}^{3} \dot{M}_{-7}^{-1}, \tag{6.9}$$

where $s_{\alpha,2}$ is the entropy at α recombination in units of 100 and $\dot{M}_{-7}$ is the mass loss rate in units of $10^{-7} M_{\odot}\mathrm{s}^{-1}$. It is clear from this expression that the affect of secondary heating on the dynamical timescale will be significantly larger than its affect on the the entropy and the change in the dynamical timescale will affect the nucleosynthesis criterion s^3/τ_d even more than the change in entropy.

6.2.1 Numerical Steady State Wind Models

To explore the parameter space with more accuracy, we have calculated the hydrodynamics of the wind with an extra heating source given by equation 6.2 included in the numerical NDW models described in Roberts et al. (2010). The results presented in this sub-section are similar to those found in Metzger et al. (2007) and Suzuki & Nagataki (2005a), although we focus on the total energy deposited in the wind rather than the variation with proto-neutron star magnetic field strength in their Alfven wave heating models and use a somewhat different form for the heating rate. A total neutrino luminosity of $1 \times 10^{52}\,\mathrm{ergs}^{-1}$ has been assumed for all models. Two thirds of the total luminosity is assumed to be released as μ and τ neutrinos while the remaining third is assumed to be emitted as electron neutrinos and anti-neutrinos. The average neutrino energies are assumed

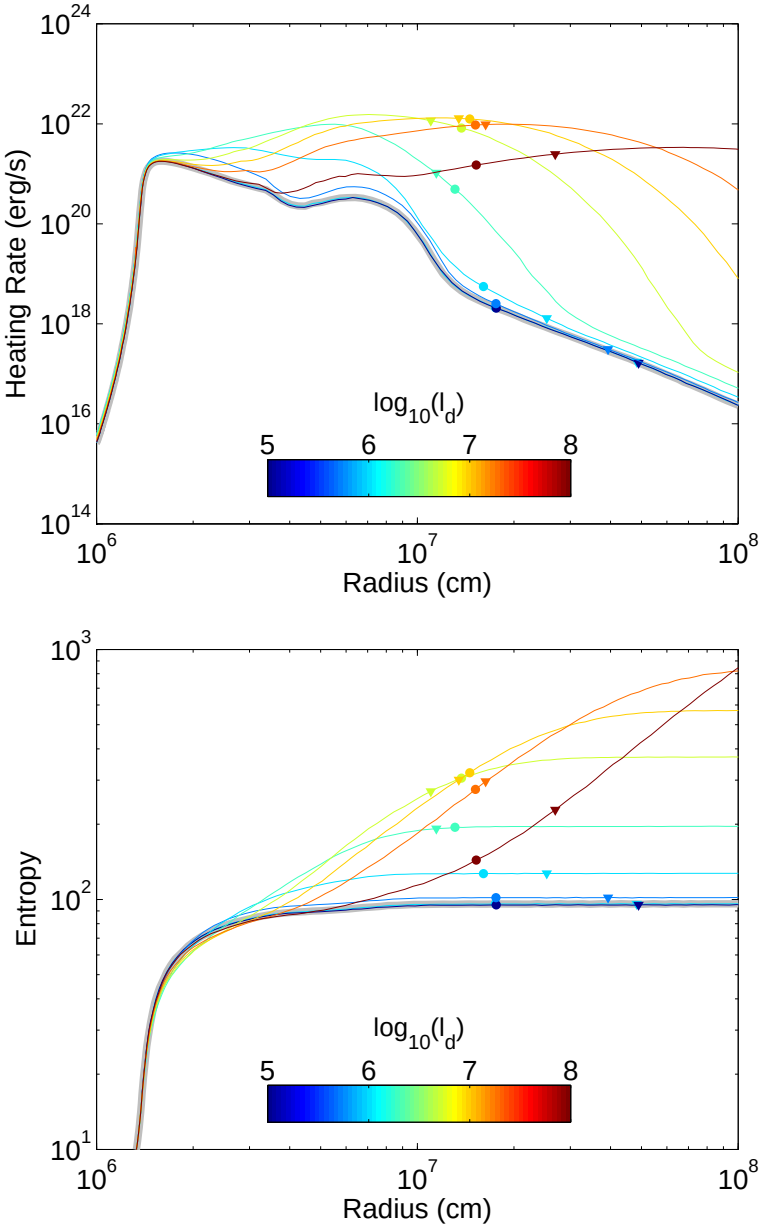

Figure 6.3: Wind properties for various energy deposition lengths. $L_{ext} = 5.2 \times 10^{48}$ km has been assumed. The heating rate and entropy of the wind as a function of radius is shown. The circles correspond to the radius at which the temperature is 2 GK and the triangles correspond to the sonic point.

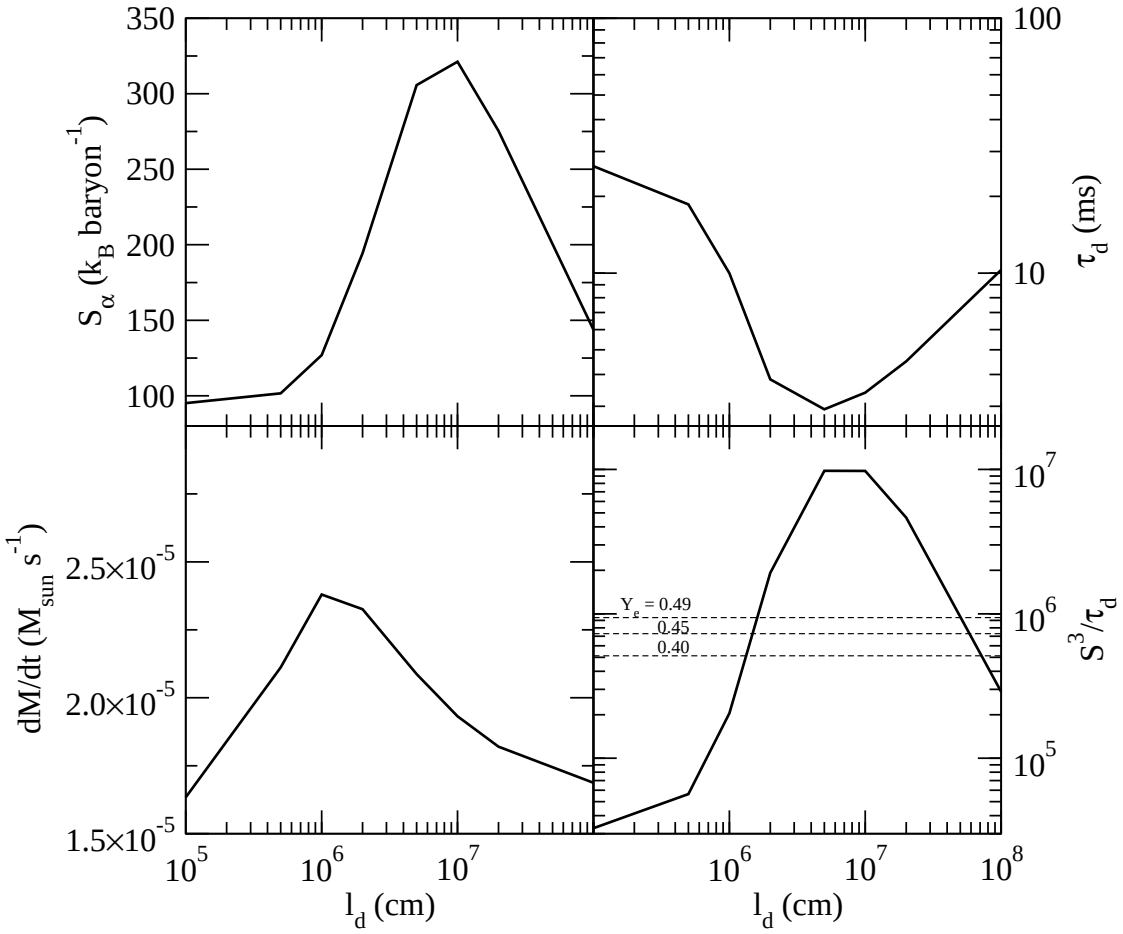

Figure 6.4: Wind properties for various energy deposition lengths. $L_{ext} = 5.2 \times 10^{48}$ km has been assumed. The entropy and dynamical timescale at $T = 2$GK, the mass loss rate, and the nucleosynthesis condition s^3/τ_d are shown as a function of the assumed l_d. The dashed lines in the lower right plot show the threshold for r-process nucleosynthesis given by Hoffman et al. (1997) for a number of electron fractions. The peak in the entropy and minima in the dynamical timescale at $l_d \sim 50$km obviously are most likely to produce r-process nucleosynthesis.

to be $\langle \epsilon_{\nu_e} \rangle = 11\,\mathrm{MeV}$, $\langle \epsilon_{\bar{\nu}_e} \rangle = 14\,\mathrm{MeV}$, and $\langle \epsilon_{\nu_x} \rangle = 19\,\mathrm{MeV}$. Because we impose the electron fraction in subsequent calculations of the wind nucleosynthesis, the relative energies of the electron neutrinos and anti-neutrinos have a very small effect on our results. The neutron star is assumed to have a mass of $1.4 M_\odot$ and a radius of 10 km. With these steady state parameters for the wind imposed, the numerical wind models are allowed to relax to a steady state over numerous dynamical timescales. When no secondary source of heating is present, the total net neutrino energy deposited in the wind is $8.6 \times 10^{48}\,\mathrm{ergs}^{-1}$. Clearly, this is of order the amount of energy required from a secondary heating source for it to significantly affect the properties of the wind.

In figure 6.2, the specific heating rate and entropy of the wind are shown for various total secondary heating rates. The entropy begins to increase significantly for energy deposition rates $>\sim 10^{48}\,\mathrm{ergs}^{-1}$ as expected. The radius at which $T = 2\,\mathrm{GK}$ stays fairly constant as the energy deposition rate is increased, while the sonic radius moves steadily inward with increased extra energy deposition. Over the range of energy inputs shown, the entropy at alpha recombination increases by a factor of two, while the dynamical timescale decreases by an order of magnitude. Given that a successful r-process depends on s^3/τ, the increase in entropy and decrease in dynamical timescale contribute equally to making conditions more favorable to r-process nucleosynthesis. This is in contradiction to most studies of r-process nucleosynthesis in the wind (c.f. Takahashi et al. 1994b, Arcones & Martinez-Pinedo 2010), where only the entropy has been artificially increased but the dynamics of the wind have been left the same. Additionally, the mass loss rate is increased meaning that secondary heating would have to persist for a shorter amount of time to provide the necessary total mass of r-process elements.

For an extra energy deposition rate of $5.2 \times 10^{48}\,\mathrm{ergs}^{-1}$, the variation of the properties of the wind with l_d is shown in figure 6.4. There is an optimal energy deposition length at $50 - 100\,\mathrm{km}$. This confirms the results of Suzuki & Nagataki (2005a) and Metzger et al. (2007). When l_d is less than this length, the extra energy is deposited closer to the atmosphere (i.e. at higher density and temperature). The higher temperature reduces the amount of entropy gained by the wind per unit energy input. Additionally, the higher density and temperature allow for increased cooling from lepton capture so that the net energy gained by the wind relative to the case of no extra heating is less than the total amount of energy deposited by the secondary heating source. For longer l_d, the energy is deposited at lower temperatures resulting in higher asymptotic energies. The problem becomes that a significant fraction of the energy is input outside the radius at which alpha recombination occurs and does not contribute to creating an alpha-rich freezeout.

6.2.2 Nucleosynthesis With Secondary Heating

Given that the entropy is changing over the region in which alpha particles are combining to form ^{12}C and the dynamical timescale is also changing significantly, the analytic estimates of the conditions necessary for r-process nucleosynthesis found in Hoffman et al. (1997) are very approximate. Therefore, to more accurately assess what heating is necessary for a successful r-process, it is necessary to use a full nuclear network. Here, the affect of a secondary heating source on wind nucleosynthesis is discussed without reference to a particular mechanism for this secondary heating. One possible mechanism for this heating is discussed in subsequent sections.

The thermodynamic trajectories described in the previous section have been

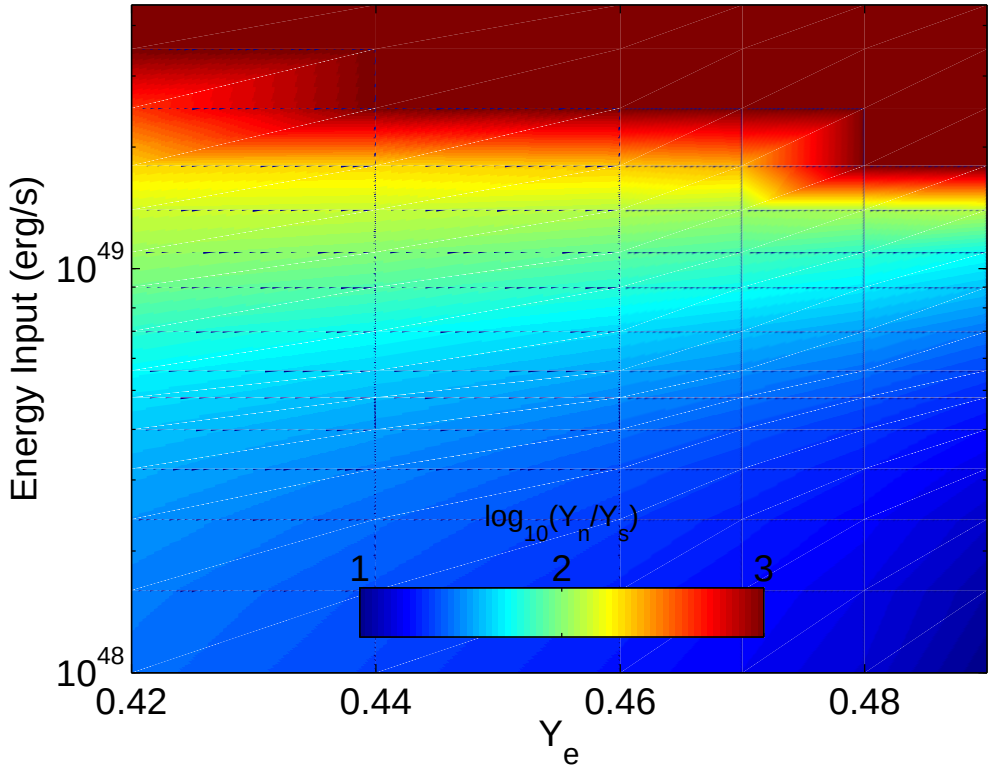

Figure 6.5: Neutron to seed ratio as a function of energy deposition rate and electron fraction. Contours are on a log scale, so that the numbers next to the colorbar denote powers of ten.

post-processed using the 6312 isotope r-process nuclear network described in Roberts et al. (2011) for various values of Y_e. The charged particle and neutron capture rates in the network up to At ($Z = 85$) are taken from Rauscher & Thielemann (2000). Past At, the neutron capture rates of Panov et al. (2010) are employed. The network terminates at $Z = 102$. Experimental values are taken for nuclear masses where available, elsewhere theoretical masses are taken from Möller et al. (2003). Neutron induced fission rates are taken from Panov et al. (2010) and the simple approximation of Frankel & Metropolis (1947) is used to calculate spontaneous fission rates. Fission barriers are taken from Mamdouh et al. (2001). For our fission fragment distributions, we employ the empirical fits of Wahl (2002).

In figure 6.5, the neutron to seed ratio as a function of L_0 and Y_e is shown. The damping length has been taken to be $l_d = 10^6\,\mathrm{cm}$. This figure was calculated assuming a total neutrino luminosity of $10^{52}\,\mathrm{erg\,s^{-1}}$. Clearly, there is a transition to a neutron to seed ratio favorable for r-process nucleosynthesis at around $7 \times 10^{48}\,\mathrm{erg\,s^{-1}}$. There is some dependence on initial electron fraction, with lower electron fractions giving a higher neutron to seed ratio. Analytically, the neutron to seed ratio is expected to decrease as Y_e^3 (Hoffman et al. 1997). The analytic result for the neutron to seed ratio when ^{12}C is produced by ^{4}He(αn,γ)^{9}Be(α,n) found in Roberts et al. (2010) is followed reasonably closely below about $10^{49}\,\mathrm{ergs^{-1}}$. For very high entropies, ^{12}C also has significant production provided by ^{4}He(2α,γ). For this reaction the neutron to seed ratio decreases as Y_e increases, which explains the behavior of the neutron to seed ratio with Y_e at very high entropies.

In figure 6.6, the final abundances versus mass number for various heating

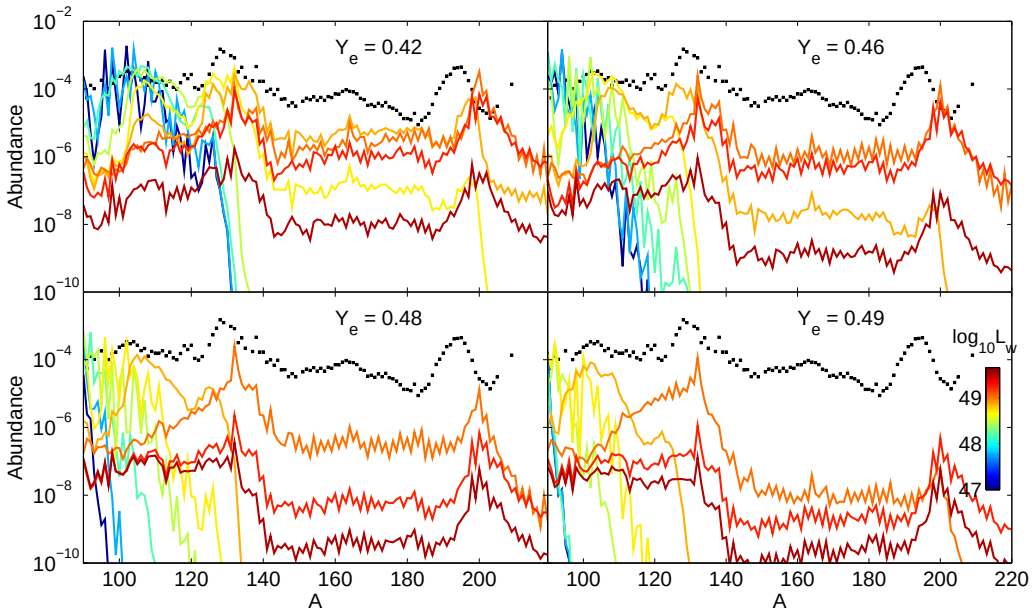

Figure 6.6: Final abundances as a function of mass number color coded by heating rate. Different panels correspond to different electron fractions.

rates and electron fractions are shown. There is a critical heating rate above $7 \times 10^{48}\,\mathrm{erg\,s^{-1}}$ for which the r-process occurs with only a small dependence on Y_e. This critical heating rate is two orders of magnitude less than the neutrino luminosity, but is similar to the total amount of energy deposited in the wind by neutrinos. For extra energy inputs where the r-process is produced, the r-process pattern is fairly invariant. Rather, increasing the energy input past the minimum value required to produce the r-process just reduces the total number of seed nuclei and shifts the r-process pattern down in total abundance. Although it is not shown in the plots, we have also run a series of models with $Y_e = 0.5$. As would be expected, these produce no r-process nucleosynthesis. Interestingly, r-process nucleosynthesis seems to occur when the 2 GK point occurs outside of the sonic radius.

Using the thermodynamic histories described in the preceding section, the variation of nucleosynthesis with l_d can be explored for an extra energy deposition rate just below the critical value for $l_d = 1$ found in the preceding paragraph. The final abundances for various l_d can be found in figure 6.7. Above $Y_e = 0.47$, there are no trajectories which produce the second r-process peak. Below this electron fraction, only the trajectories close to the optimal l_d described above produce an r-process.

6.3 Acoustic Wave Heating

Here, two mechanisms for production of acoustic waves in the wind are considered and their propagation and eventual damping in the wind is discussed.

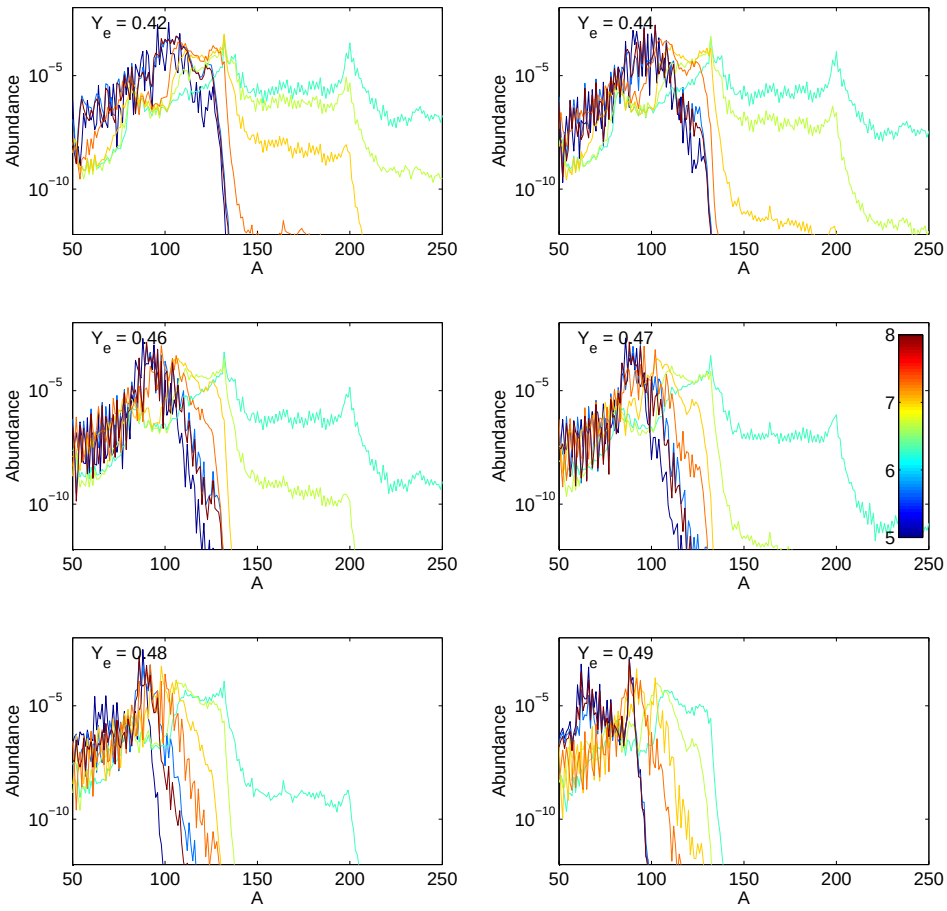

Figure 6.7: Final abundances as a function of mass number color coded by energy deposition length. Different panels correspond to different electron fractions. All trajectories have a total energy input of $5.2 \times 10^{48}\,\mathrm{ergs}^{-1}$

6.3.1 Gravity Wave Excitation and Propagation from Proto-Neutron Star Convection

It is also possible that convection in the proto-neutron star may be a significant source of wave heating (see chapter 4 for a discussion of proto-neutron star convection). This region can be crudely modeled as an isentropic region that comprises the convective region of the star connected to an isothermal atmosphere from which the wind is launched. This allows us to follow the analysis of Goldreich & Kumar (1990). Vigorous turbulent convection below the neutrino sphere will excite waves that potentially propagate from the convective region, through the isothermal atmosphere, and into the wind where they can steepen into shocks and deposit their energy. Both gravity wave modes and acoustic modes will be excited, in addition to non-propagating modes. Due to the mach number dependence of the wave excitation, the energy flux will be dominated by gravity waves. The total luminosity in gravity waves excited by convection is approximately

$$\begin{aligned} L_g \approx M_c L_c \quad &\approx 10^{50}\,\mathrm{ergs}^{-1}\,\left(\tfrac{r_c}{10^6\mathrm{cm}}\right)^2\left(\tfrac{\rho_c}{10^{14}\,\mathrm{g/cc}}\right) \\ &\times\left(\tfrac{v_c}{10^8\mathrm{cms}^{-1}}\right)^4\left(\tfrac{c_s}{10^9\mathrm{cms}^{-1}}\right)^{-1} \end{aligned} \tag{6.10}$$

which have frequencies of approximately $\omega_g \sim v_c/H_P \sim 10^2 - 10^3\mathrm{s}^{-1}$. Gravity waves of this character have been observed in two-dimensional simulations of proto-neutron star convection (Dessart *et al.* 2006).

In the outer layers of the atmosphere where the temperature has decreased (thereby increasing the pressure scale height and decreasing the acoustic cutoff frequency), gravity waves in this frequency range become evanescent. This will only persist for a few pressure scale heights until the radius were the wind is launched and the acoustic cutoff is decreased further so that the waves move into the frequency range of acoustic waves. In other words, the gravity waves will tun-

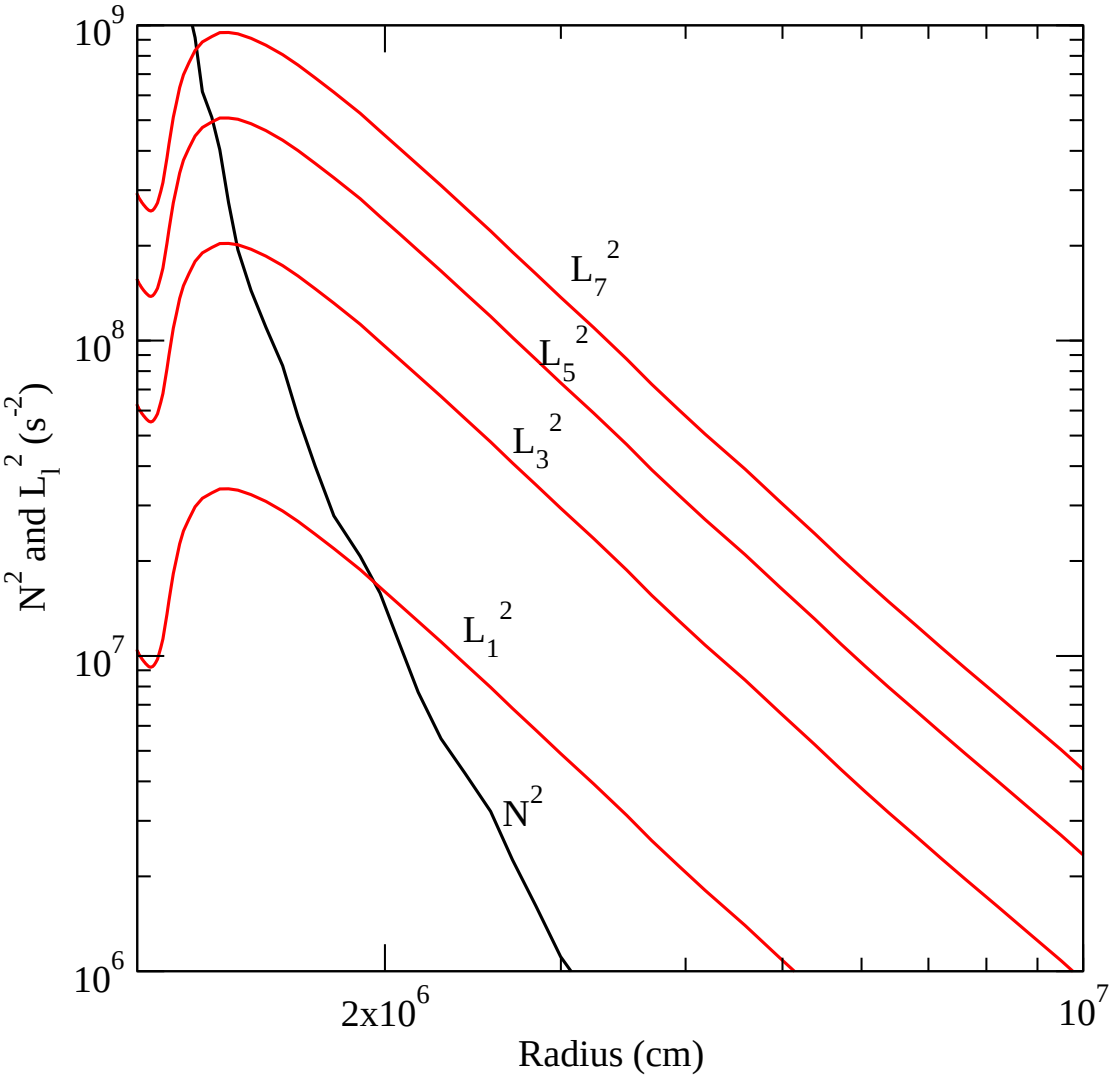

Figure 6.8: Characteristic squared wave frequencies in the outer layers of a proto-neutron star and in the NDW. The black line is the Brunt-Vaisala frequency (N^2) and the red lines are the Lamb frequencies (L_l^2) for various angular modes.

nel through the evanescent region, emerging into the wind in the acoustic branch. Although they are significantly attenuated relative to their initial amplitude, the emergent waves can still carry a significant amount of energy compared to the total amount of neutrino energy deposited in the wind, potentially affecting eventual nucleosynthesis in the wind.

In figure 6.8, the Brunt-Vaisala and Lamb frequencies are shown for the inner regions of a NDW model. The frequencies are much larger than the characteristic frequency v/r throughout this region, so it is reasonable to neglect the presence of a background velocity field. The increase in the Lamb frequency near 10 km corresponds to the region in which the envelope becomes radiation dominated, the wind is launched, and the sound speed increases rapidly. After the launching region, it the Lamb frequency falls off $\propto r^{-2}$ because there is small variation of the sound speed in the wind as the wind is radiation dominated. The Brunt-Vaisala frequency also increases rapidly in the region where the wind is launched due to the large gradient in the entropy, which cannot be seen in figure 6.8, but as the wind moves further from the launch region the entropy gradient decreases rapidly. Combining this with the $\propto r^{-2}$ fall off in the local acceleration due to gravity results in the Brunt-Vaisala frequency falling off more rapidly that the Lamb frequency.

Gravity waves are characterized by $\sigma < L_l$ and $\sigma < N$, where σ is the wave frequency. In the limit in which the WKB approximation applies, the dispersion relation for gravito-acoustic waves is

$$k_r^2 = \frac{(\sigma^2 - L_l^2)(\sigma^2 - N^2)}{c_s^2 \sigma^2}, \tag{6.11}$$

where k_r is the radial wave vector. Gravity waves emitted by the convection zone of the proto-neutron star eventually reach a radius at which $N^2 < \sigma^2 < L_l^2$,

$k_r^2 < 0$, and the waves become evanescent. At some radius after this $\sigma^2 = L_l^2$ and the evanescent wave will emerge in the acoustic branch. Convection will excite waves with angular frequencies around $10^3\,\mathrm{s}^{-1}$. So, by inspecting figure 6.8, gravity waves should transition to the acoustic branch close to the wind launch radius. Unno et al. (1989) show that, in the WKB approximation, the wave energy transmitted through the evanescent region which emerges in the acoustic branch is given by

$$L_{w,f}/L_{w,i} \approx \exp\left(-2\int_{r_a}^{r_b}\sqrt{-k_r^2}dr\right), \tag{6.12}$$

where r_a is the radius at which the waves become evanescent, r_b is the radius at which they emerge in the acoustic branch, and $L_{w,i}$ and $L_{w,f}$ are the radii are the incident and transmitted wave energy flux, respectively. When $\sigma \ll L_l$ and $N \ll \sigma$, $k_r^2 \approx l(l+1)/r^2$ and $L_{w,f}/L_{w,i} \sim (r_a/r_b)^{2\sqrt{l(l+1)}}$. Therefore, it is expected that modes of lower angular order will be transmitted more effectively through the evanescent region.

In figure 6.9, equation 6.12 has been evaluated using the wave speeds shown in figure 6.8 for a variety of wave modes. For $l = 1$ modes, the transmission efficiency is $> 40\%$ while for $l = 2$ modes the transmission efficiency is closer to 10%. The transmission efficiency falls off rapidly for higher wave numbers, as expected from the analysis above. Dessart *et al.* (2006) find that the gravity waves emitted by the proto-neutron star convection zone are dominated by the $l = 1\,\mathrm{and}\,2$ modes, so that a reasonable (somewhat conservative) estimate of the wave power transmitted through the evanescent region is $\sim 10\%$. Even if the convective energy flux in the proto-neutron star is only 10% of the total energy flux, this implies that $L_w \sim 10^{-4}\,\mathrm{to}\,10^{-3}\,L_{\nu,\mathrm{tot}}$. Comparing this with equation 6.5, it is clear that the wave energy input from convective likely exceeds the critical

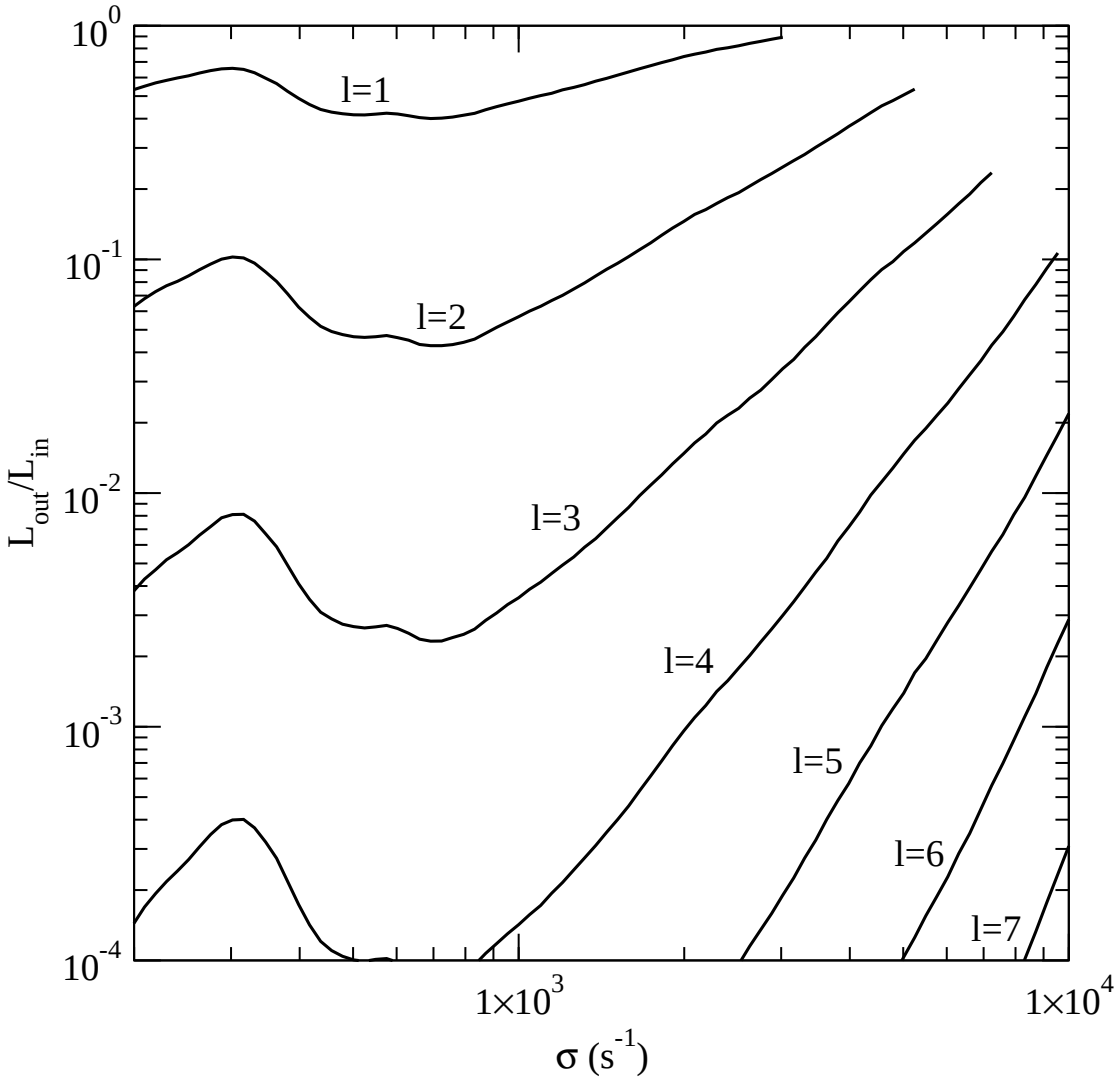

Figure 6.9: Fraction of gravito-acoustic wave energy that escapes the proto-neutron star and propagates into the NDW in the acoustic branch as a function of angular wave number l and wave frequency.

wave energy at total neutrino luminosities $\lesssim 10^{53}\mathrm{erg\,s^{-1}}$ which corresponds to times greater than about one second after core bounce. This is the time that the wind is expected to be most neutron rich (Roberts 2012). Therefore, the wave energy excited by proto-neutron star convection is likely large enough to affect the dynamics of the wind at times that have electron fractions most favorable to the r-process, if this power can be efficiently coupled to the wind.

6.3.2 Wave Excitation by G-Mode Oscillations

Core g-mode oscillations have also been suggested as a significant source of power during core-collapse supernovae (Burrows et al. 2006). In the numerical simulations of Burrows et al. (2006), accretion streams impacting the core excited low order g-modes of the inner proto-neutron star core, which in turn excited propagating acoustic waves that heated the region below the supernova shock and powered a successful, asymmetric core-collapse supernova explosion. The core effectively acted as a transducer for accretion power into acoustic power. Such acoustic power driven explosions have not been observed in the numerical simulations of other groups (e.g. Marek & Janka 2009). Additionally, Weinberg & Quataert (2008) pointed out that these lower order modes would couple effectively to higher order modes which could damp effectively by neutrino emission. These considerations seem to make it unlikely that core-collapse supernovae are powered mainly by acoustic power. Still, only a very small fraction of the neutrino energy required to power a supernova is required to significantly change the dynamics of the neutrino driven wind.

Assuming a characteristic amount of energy stored in the $l = 1$ g-mode taken from Weinberg & Quataert (2008) and taking the result for the power emitted

from a sphere oscillating in a medium from Landau & Lifshitz (1959), the energy acoustic energy emitted from g-mode oscillations should approximately be

$$\begin{aligned} L_w \sim & \quad 4 \times 10^{47}\,\mathrm{erg\,s^{-1}} \\ & \times \left(\tfrac{E_1}{10^{48}\,\mathrm{erg}}\right)\left(\tfrac{1.4M_\odot}{M_{\rm ns}}\right)\left(\tfrac{\rho}{10^{12}\,\mathrm{gcm^{-3}}}\right) \\ \times & \quad \left(\tfrac{10^9\,\mathrm{cm\,s^{-1}}}{c_s}\right)^3 \left(\tfrac{R_{\rm ns}}{10^6\,\mathrm{cm}}\right)^6 \left(\tfrac{\omega}{10^3\,hz}\right)^4 \\ & \times \tfrac{1}{1+(\omega R/c_s)^4/4}, \end{aligned} \tag{6.13}$$

where E_1 is the equilibrium energy stored in the $l = 1$ mode for a steady accretion rate, ρ is the density just outside the proto-neutron star core, and ω is the frequency of the g-mode oscillations. This mode has an angular frequency of around $2 \times 10^3\,\mathrm{s^{-1}}$ (Burrows et al. 2006). This is close to the amount of energy required to affect the dynamics of the neutrino driven wind.

There are at least one aspect that makes this mechanism less appealing than the wave production mechanism discussed in the previous section. Note that the neutrino damping is quite efficient. Weinberg & Quataert (2008) find that for modes to have equilibrium energies of $\sim 10^{48}\,\mathrm{erg}$, the neutrino damping rate is of order or larger than the rate that accretion power is being dumped into the mode. This suggests that the mode will have a $Q < 1$ and continuos accretion would be required to power the acoustic emission. Therefore, simultaneous accretion and wind outflow from the proto-neutron star would be required for this mechanism to operate.

6.3.3 Acoustic Wave Propagation and Damping in the Wind

When acoustic waves emerge into the wind region, they will propagate outward in the background flow of the wind and eventually turn in to weak shocks as the

wave peaks catch the troughs. These weak shocks will damp as they propagate through the wind and deposit their energy in the flow. Here, the region where this dissipation likely occurs in the wind is discussed using a framework similar to Stein & Schwartz (1972; 1973) and Suzuki (2002).

In a moving background the wave energy is not conserved, but the wave action is. The wave action is given by

$$S = \epsilon \frac{\omega}{\omega - kv} \tag{6.14}$$

and the evolution of the wave action is given by (Jacques 1977)

$$\partial_t S + r^{-2}\partial_r (r^2 v_g S) = \text{rest frame dissipation rate} \tag{6.15}$$

where $v_g = v + c_s$ is the group velocity of the wave, as the dispersion relation in the WKB limit is $\omega = (v + c_s)k$. This is just a statement that wave quanta are conserved (or that energy is conserved in the fluids rest frame) in the absence of dissipation.

In an isothermal atmosphere, the shock formation distance is given by (Mihalas & Mihalas 1984)

$$\Delta r_s = 2h_{\rm eff} \ln \left[\frac{c_s \lambda}{2(\gamma+1)u_0 h_{\rm eff}} + 1 \right], \tag{6.16}$$

where λ is the wavelength, u_0 is the initial amplitude of the velocity disturbance, the pressure scale height is given by

$$h_{\rm eff} \approx 5.4 \times 10^3 \,{\rm cm}\, r_6^2 c_{s,9}^2 M_{1.4}^{-1}. \tag{6.17}$$

This is significantly less than the distance over which the properties of the wind vary so that once the wave frequency is above the acoustic cutoff frequency shock will form. The acoustic cutoff frequency is given by

$$\omega_{\rm ac} = \frac{c_s}{2h_{\rm eff}} \approx 10^5 \,{\rm s}^{-1}\, r_6^{-2} c_{s,9}^{-1} M_{1.4}, \tag{6.18}$$

so that shocks are expected to form at a radius of approximately $10^6 - 10^7$ cm.

From weak shock theory, the entropy change across the shock front per gram is

$$\Delta s = \frac{2\gamma(\gamma-1)c_v}{3(\gamma+1)^2}m^3 \tag{6.19}$$

where $m = M^2 - 1$. In the weak shock limit, the propagation velocity is given by $v_s \approx c_s(1+m/2)$. This implies the shock energy evolution is governed by (Mihalas & Mihalas 1984)

$$\nabla \cdot (\mathbf{v_s}\epsilon_s) = -\frac{m}{\pi}\epsilon_s, \tag{6.20}$$

where ϵ_s is the energy density of the simple wave averaged over a wavelength. This energy deposition rate is in the rest frame of the fluid the shock is propagating through. As is well known, in a static homogenous background the propagation of a weak shock can be described by a simple wave. In the case of a spherical shock in an inhomogenous background, the propagation of finite amplitude disturbances becomes significantly more complicated. Solutions exist for plane parallel geometry with an exponential density gradient and no velocity.

Where dissipation occurs due to shock formation, another equation is required. In regions were the initial wave will have steepened into a weak shock, we can take the energy dissipation rate for a weak shock averaged over a wavelength as the rest frame dissipation rate. For a saw tooth wave, the energy per unit volume contained in a single wave period averaged over the wavelength is

$$\epsilon_s = \frac{\gamma P m^2}{3(\gamma+1)^2} \tag{6.21}$$

We take this energy as equal to the wave action, as both these quantities are defined in the rest frame and are equal to one another in the limit of an infinitely weak shock. This gives a relation between m and the wave action which closes

the set of equation with dissipation

$$m = (\gamma + 1)\sqrt{\frac{3S}{\gamma P}} \tag{6.22}$$

In steady state, the equation describing the wave action to lowest order is

$$\partial_t S + r^{-2}\partial_r(r^2 v_g S) \approx -\frac{\gamma+1}{\pi}\omega\sqrt{\frac{3S}{\gamma P}}S. \tag{6.23}$$

In the limit of a static medium, this reduces to the results of Suzuki (2004). Stein & Schwartz (1973) find that this is reasonable approximation in the static limit as long as the frequency is larger than the acoustic cutoff frequency.

This results in a local dissipation length that can be estimated as assuming a radiation dominated equation of state (in the limit of $M \ll 1$)

$$l_d \approx 2.6 \times 10^6 \,\mathrm{cm}\, \frac{c_{s,9}}{\omega_3}\left(\frac{E}{10S}\right)^{1/2}, \tag{6.24}$$

where E is the local energy density and ω_3 is the wave frequency in units of $10^3\,\mathrm{s}^{-1}$. Including the background velocity results in an increase in the dissipation length by a factor $(v+c_s)/c_s$. Clearly, smaller wave amplitudes result in longer dissipation lengths. We emphasize that this length scale is close to the optimal dissipation length found above. The radius at which shock formation occurs is also important, but this is within the optimal radius of $\sim 10^7\,\mathrm{cm}$ found above. Of course, these results rely on the WKB approximation which is only marginally valid for the wavelengths considered here. Still, this should give at least some guidance to how waves will propagate and dissipate in the wind. Therefore, it seems at least plausible that heating by weak shocks powered by gravito-acoustic energy from the proto-neutron star core could provide the secondary source of energy needed required to make the r-process in the neutrino driven wind.

6.3.4 Numerical Models with Wave Heating

In the steady state case, the wave action equation is of the form of Bernoulli's equation. Therefore, the wave action as a function of radius is given by

$$\begin{aligned} S &= S_0 \tfrac{v_{g,0}}{v_g} \left(\tfrac{r_0}{r}\right)^2 \\ &\times \left[1 + \tfrac{\gamma+1}{2\pi\sqrt{\gamma}} \sqrt{3 S_0 v_{g,0}}\, \omega \int_{r_0}^{r} \tfrac{dr}{r} \tfrac{\theta(r-r_s)}{P^{1/2} v_g^{3/2}}\right]^{-2}. \end{aligned} \tag{6.25}$$

This equation is solved, given a NDW background model, to find the local heating rate as a function of radius from weak shock energy deposition per gram,

$$\dot{q}_w = -\frac{(\gamma+1)\omega}{\pi\rho}\sqrt{\frac{3S^3}{\gamma P}}. \tag{6.26}$$

This heating rate is then fed back into the wind model. This process is iterated until a steady state wind models with secondary heating are obtained. It is assumed that the radius at which shocks are formed, r_s, is given by the radius at which $\omega < \omega_{ac}$. Because the θ function is discontinuous, wave heating is switched on exponentially to make the code stable. This just involves the replacement $\theta(r - r_s) \rightarrow \mathrm{Min}(1, \exp[\alpha(r - r_s)/r_s])$. Given the sensitivity of the nucleosynthesis to the radius at which energy is input, the choice of α will likely affect nucleosynthesis in the wind. The parameter α is chosen equal to four for the simulations described below.

The structure of one of these NDW models including wave heating is shown in 6.10. A wave frequency of $\omega = 2 \times 10^3\,\mathrm{s}^{-1}$ was assumed and the total wave energy input was $2.5 \times 10^{48}\,\mathrm{erg\,s}^{-1}$. The final asymptotic entropy in the model was 400, but a significant amount of energy is deposited around the region where α recombination occurs. Therefore, the entropy at recombination is somewhat lower than this characteristic value.

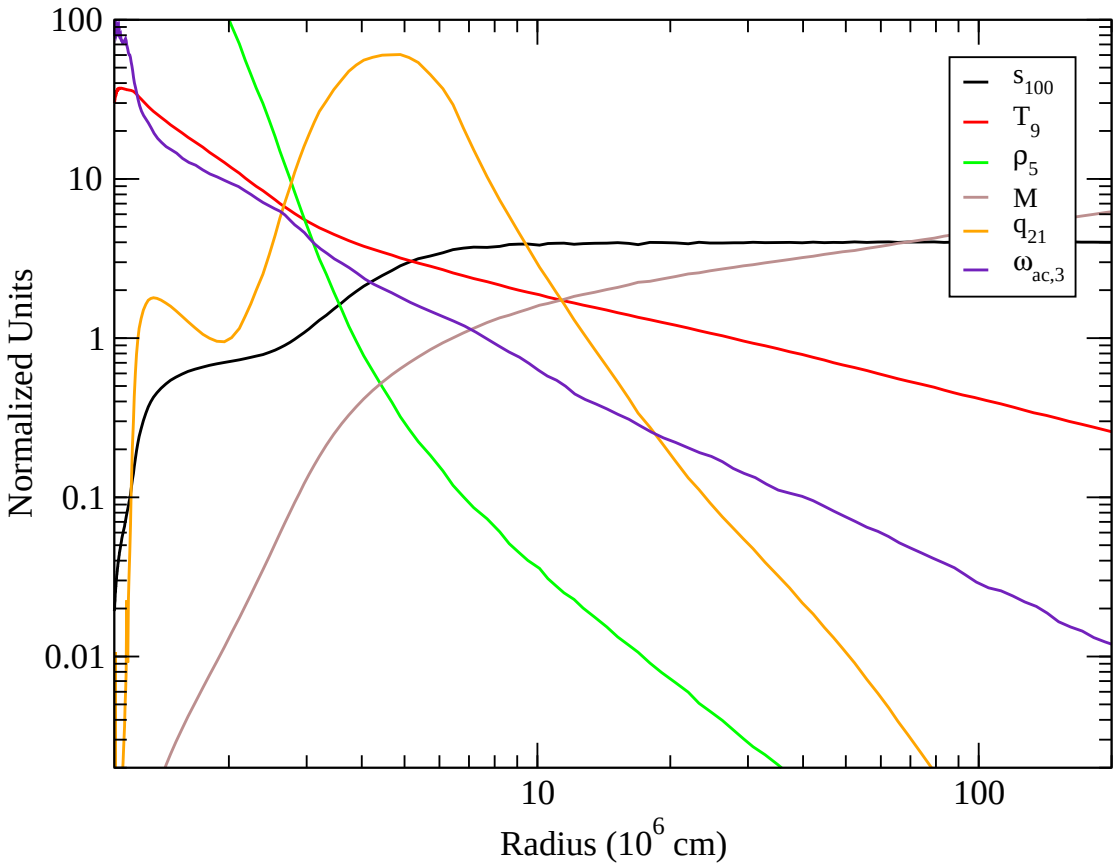

Figure 6.10: Properties of a neutrino driven outflow with a total neutrino luminosity of $7.8 \times 10^{51}\,\mathrm{erg\,s^{-1}}$ ($L_{\nu_e} = 8.1 \times 10^{50}\,\mathrm{erg\,s^{-1}}$, $L_{\bar{\nu}_e} = 1.1 \times 10^{51}\,\mathrm{erg\,s^{-1}}$, $\epsilon_{\nu_e} = 9\,\mathrm{MeV}$, and $\epsilon_{\bar{\nu}_e} = 16\,\mathrm{MeV}$). Acoustic wave heating provided a total heating rate $L_w = 2.5 \times 10^{48}\,\mathrm{erg\,s^{-1}}$ and a wave frequency $\omega = 2 \times 10^3\,\mathrm{s^{-1}}$. Various quantities characterizing the wind as a function of radius are shown: the entropy s_{100} in units of $100\,\mathrm{k_b}$/baryon, the temperature in GK, density in units of $10^5\,\mathrm{g\,cm^{-3}}$, Mach number, the total heating rate in units of $10^{21}\,\mathrm{erg\,s^{-1}\,g^{-1}}$, and the acoustic cutoff frequency in units of $10^3\,\mathrm{s^{-1}}$.

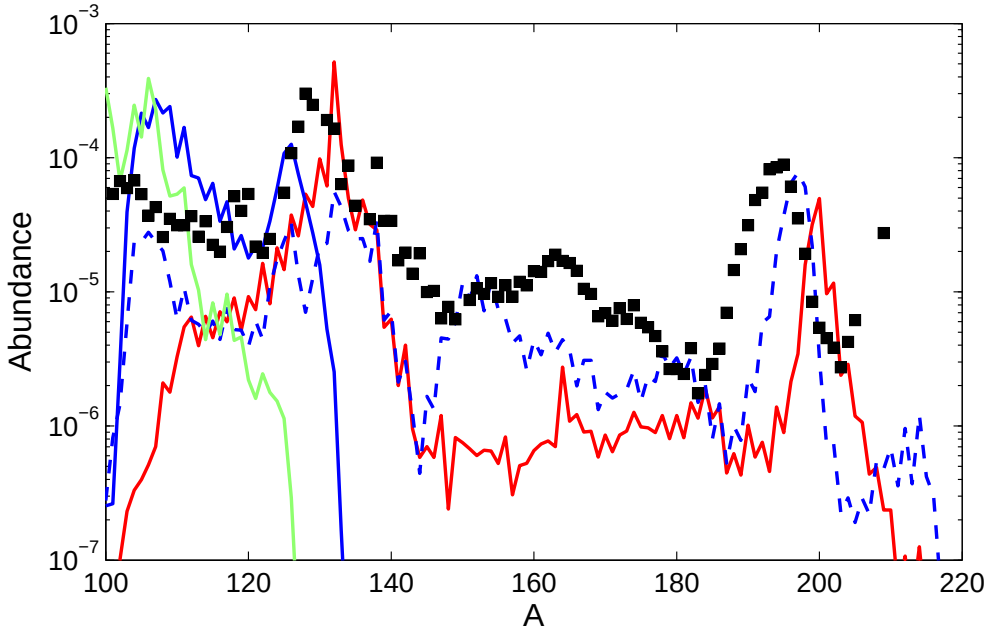

Figure 6.11: Final abundances as a function of nuclear mass number for four NDW models including wave heating. The neutrino properties assumed for the models are the same as in figure 6.10. The solid lines all assume $\omega = 10^3\,\mathrm{s}^{-1}$, while the dashed line assumes $\omega = 2 \times 10^3\,\mathrm{s}^{-1}$. The green, blue and, red lines assume $L_w = \{1\times10^{48},\ 2.5\times10^{48},\ 5\times10^{58}\}\,\mathrm{erg\,s}^{-1}$, respectively. The squares are the solar r-process abundances obtained in Arlandini et al. (1999). The electron fraction in the wind has been assumed to be $Y_e = 0.45$ in all models. The production of r-process nuclei is sensitive to the energy input in to the wind as well as the frequency of the waves, which affects the damping length and the point at which the wave frequency rises above the acoustic cutoff frequency.

In figure 6.11, temperature and density trajectories have been post-processed using the nuclear network described in section 6.2.2 with an assumed electron fraction of 0.45. As expected from the parameterized studies of secondary wind heating described above, winds including wave heating are capable of producing r-process nucleosynthesis. The nuclei produced are sensitive to the energy input and the wave frequency. It can be seen that, for an energy input of $2.5 \times 10^{48}\,\mathrm{erg\,s^{-1}}$, doubling the frequency of the waves can result in going from only making the first r-process peak to producing the third r-process peak. A similar result is found when the energy input is doubled. The final abundance patterns match the Arlandini et al. (1999) results for the solar r-process reasonably well.

6.4 Conclusions

In this chapter, it has been shown that secondary heating in NDWs is a plausible way of producing r-process nuclei in winds with marginal neutron excesses. In addition to possible heating by magnetosonic waves which has been considered in past work (Suzuki & Nagataki 2005a, Metzger et al. 2007), we have shown that purely acoustic power can also potentially provide the heating required to make NDW conditions favorable for an r-process.

First, the generic properties of a secondary heating source required to make the NDW a viable site for r-process nucleosynthesis were considered. For a secondary heating mechanism to significantly affect the entropy and dynamical timescale of the NDW – and therefore the wind nucleosynthesis – it was found that the power input into the NDW must be comparable to the power input from neutrino heating but not contribute significantly to the heating rate in the PNS atmosphere were the initial temperature of the wind is set. The second condition is easily met by

heating sources which do not strongly depend on the density because the specific heating rate due to the secondary source is then negligible in the proto-neutron star atmosphere. This power must also be deposited inside the α recombination radius, which requires that the deposition occur on a length scale of 10–100 km. Even within this range, the properties of the wind are sensitive to the characteristic radius of energy deposition. Secondary heating serves to both increase the effective entropy of the wind and decreases the dynamical timescale of the wind, both of which increase the likelihood of an *alpha*-rich freeze out.

Because the dynamics of the wind are significantly different from the parameterized constant entropy models considered in Hoffman et al. (1997) and many subsequent works, the wind trajectories including secondary heating were post-processed with a full r-process nuclear network to determine what nucleosynthesis is expected for a range of models. Production of r-process nuclei is found for even very small neutron excesses, as long as the energy input is sufficiently large. For realistic energy inputs, the required neutron excesses are consistent with the NDW wind neutron excesses predicted in chapter 3.

Second, two new mechanisms for secondary heating were considered. In the first, power is provided by weak shock heating from gravitoacoustic waves excited by proto-neutron star convection. Gravity waves excited by convection propagate into the proto-neutron star atmosphere, where they become evanescent and decrease in amplitude until they emerge in the acoustic branch in the wind. The second mechanism involves acoustic wave production by low order g-mode oscillations of the proto-neutron star. This is similar to the supernova explosion mechanism envisaged by Burrows et al. (2007), except that a much smaller amount of wave energy is required. In both cases, the acoustic waves that propagate into

the wind rapidly turn into weak shocks over a few pressure scale heights and efficiently deposit their energy. It is found that the length scale for energy deposition by weak shocks is consistent with the optimal range of length scales for energy deposition found in the first part of the study.

Both mechanisms can likely provide enough energy to significantly affect the dynamics of the wind and wind nucleosynthesis. Still, wave excitation by convection is the more promising secondary heating scenario. Because the g-mode oscillations of the proto-neutron star are powered by accretion, a non-spherical geometry where accretion and a wind occur concurrently must be imagined. Additionally, this mechanism is likely to only be operative for a short period of time after a successful supernova explosion occurs. In contrast, proto-neutron star convection proceeds for a few seconds after core bounce (see chapter 4) and the gravitoacoustic wave luminosity is correlated with the neutrino luminosity. Because the neutrino energy deposition rate scales weakly with the neutrino luminosity, the relative energy input from gravitoacoustic waves increases with time, and r-process nucleosynthesis becomes increasingly likely as time progresses.

There is still significant work required to determine if this is a truly viable mechanism for reviving the NDW r-process scenario. Although multi-dimensional simulations have shown gravity waves excited are excited by proto-neutron star convection, the amount of power emitted has not been quantitatively addressed (Dessart *et al.* 2006) and the estimates presented here have large uncertainties. Additionally, the effective entropy of the wind depends on the radius of weak shock formation which was treated in an approximate way in this work.

Bibliography

Akmal, A., Pandharipande, V. R., & Ravenhall, D. G. 1998, *Phys. Rev. C*, **58**, 1804

Anderson, E., Bai, Z., Bischof, C., Blackford, S., Demmel, J., Dongarra, J., Du Croz, J., Greenbaum, A., Hammarling, S., McKenney, A., & Sorensen, D. 1999, *LAPACK Users' Guide*, Society for Industrial and Applied Mathematics, Philadelphia, PA, third edition

Ando, S. 2004, *ApJ*, **607**, 20

Arcones, A., Janka, H., & Scheck, L. 2007, *A&A*, **467**, 1227

Arcones, A. & Martinez-Pinedo, G. 2010, *ArXiv e-prints*

Arcones, A. & Montes, F. 2011, *ApJ*, **731**, 5

Argast, D., Samland, M., Thielemann, F., & Qian, Y. 2004, *A&A*, **416**, 997

Arlandini, C., Käppeler, F., Wisshak, K., Gallino, R., Lugaro, M., Busso, M., & Straniero, O. 1999, *ApJ*, **525**, 886

Arnould, M., Goriely, S., & Takahashi, K. 2007, *Phys. Rep.*, **450**, 97

Baade, W. & Zwicky, F. 1934, *Physical Review*, **46**, 76

Bacca, S., Hally, K., Liebendörfer, M., Perego, A., Pethick, C. J., & Schwenk, A. 2011, *ArXiv e-prints*

Barbon, R., Buondi, V., Cappellaro, E., & Turatto, M. 2010, *VizieR Online Data Catalog*, **1**, 2024

Bethe, H. A. & Wilson, J. R. 1985, *ApJ*, **295**, 14

Beun, J., McLaughlin, G. C., Surman, R., & Hix, W. R. 2008, *Phys. Rev. C*, **77(3)**, 035804

Bionta *et al.*, R. M. 1987, *Physi. Rev. Lett.*, **58**, 1494

Bruenn, S. W. 1985, *ApJS*, **58**, 771

Bruenn, S. W. & Dineva, T. 1996, *ApJ*, **458**, L71+

Buras, R., Rampp, M., Janka, H.-T., & Kifonidis, K. 2006, *A&A*, **447**, 1049

Buras *et al.*, R. 2006, *A&A*, **457**, 281

Burbidge, E. M., Burbidge, G. R., Fowler, W. A., & Hoyle, F. 1957, *Reviews of Modern Physics*, **29**, 547

Burrows, A. 1987, *ApJ*, **318**, L57

Burrows, A., Dessart, L., Livne, E., Ott, C. D., & Murphy, J. 2007, *ApJ*, **664**, 416

Burrows, A. & Lattimer, J. M. 1986, *ApJ*, **307**, 178

Burrows, A., Livne, E., Dessart, L., Ott, C. D., & Murphy, J. 2006, *ApJ*, **640**, 878

Burrows, A. & Sawyer, R. F. 1998, *Phys. Rev. C*, **58**, 554

Burrows, A. & Sawyer, R. F. 1999, *Phys. Rev. C*, **59**, 510

Burrows, A., Young, T., Pinto, P., Eastman, R., & Thompson, T. A. 2000, *ApJ*, **539**, 865

Cameron, A. G. W. 1957, *Chalk River Report*

Cardall, C. Y. & Fuller, G. M. 1997, *ApJ*, **486**, L111+

Caughlan, G. R. & Fowler, W. A. 1988, *Atomic Data and Nuclear Data Tables*, **40**, 283

Cohen, J. G., Christlieb, N., McWilliam, A., Shectman, S., Thompson, I., Melendez, J., Wisotzki, L., & Reimers, D. 2008, *ApJ*, **672**, 320

Colgate, S. A. & White, R. H. 1966, *ApJ*, **143**, 626

Cowan, J. J., Burris, D. L., Sneden, C., McWilliam, A., & Preston, G. W. 1995, *ApJ*, **439**, L51

Dessart *et al.*, L. 2006, *ApJ*, **645**, 534

Duan, H., Fuller, G. M., Carlson, J., & Qian, Y. 2006, *Phys. Rev. D*, **74(10)**, 105014

Duan, H., Fuller, G. M., & Qian, Y.-Z. 2010, *Annual Review of Nuclear and Particle Science*, **60**, 569

Duncan, R. C., Shapiro, S. L., & Wasserman, I. 1986, *ApJ*, **309**, 141

Ensman, L. 1994, *ApJ*, **424**, 275

Epstein, R. I. 1979, *MNRAS*, **188**, 305

Fantoni, S., Sarsa, A., & Schmidt, K. E. 2001, *Phys. Rev. Lett.*, **87(18)**, 181101

Farouqi, K., Kratz, K., Mashonkina, L. I., Pfeiffer, B., Cowan, J. J., Thielemann, F., & Truran, J. W. 2009, *ApJ*, **694**, L49

Fattoyev *et al.*, F. J. 2010, *Phys. Rev. C*, **82(5)**, 055803

Filippenko, A. V., Li, W. D., Treffers, R. R., & Modjaz, M. 2001, in B. Paczynski, W.-P. Chen, & C. Lemme (eds.), *IAU Colloq. 183: Small Telescope Astronomy on Global Scales*, Vol. 246 of *Astronomical Society of the Pacific Conference Series*, p. 121

Fischer, T., Martínez-Pinedo, G., Hempel, M., & Liebendörfer, M. 2011, *ArXiv e-prints*

Fischer, T., Martínez-Pinedo, G., Hempel, M., & Liebendörfer, M. 2012, *Phys. Rev. D*, **85(8)**, 083003

Fischer, T., Whitehouse, S. C., Mezzacappa, A., Thielemann, F., & Liebendörfer, M. 2009, *ArXiv e-prints*

Fischer *et al.*, T. 2010, *A&A*, **517**, A80+

François, P., Depagne, E., Hill, V., Spite, M., Spite, F., Plez, B., Beers, T. C., Andersen, J., James, G., Barbuy, B., Cayrel, R., Bonifacio, P., Molaro, P., Nordström, B., & Primas, F. 2007, *A&A*, **476**, 935

Frankel, S. & Metropolis, N. 1947, *Physical Review*, **72**, 914

Frebel, A., Christlieb, N., Norris, J. E., Thom, C., Beers, T. C., & Rhee, J. 2007, *ApJ*, **660**, L117

Freiburghaus, C., Rosswog, S., & Thielemann, F. 1999, *ApJ*, **525**, L121

Friman, B. L. & Maxwell, O. V. 1979, *ApJ*, **232**, 541

Fröhlich, C., Martínez-Pinedo, G., Liebendörfer, M., Thielemann, F.-K., Bravo, E., Hix, W. R., Langanke, K., & Zinner, N. T. 2006, *Physical Review Letters*, **96(14)**, 142502

Fuller, G. M. & Meyer, B. S. 1995, *ApJ*, **453**, 792

Gandolfi, S., Carlson, J., & Reddy, S. 2011, *ArXiv e-prints*

Gandolfi, S., Carlson, J., & Reddy, S. 2012, *Phys. Rev. C*, **85(3)**, 032801

Glendenning, N. K. & Moszkowski, S. A. 1991, *Phys. Rev. Lett.*, **67**, 2414

Goldreich, P. & Kumar, P. 1990, *ApJ*, **363**, 694

Green, D. A. & Stephenson, F. R. 2003, in K. Weiler (ed.), *Supernovae and Gamma-Ray Bursters*, Vol. 598 of *Lecture Notes in Physics, Berlin Springer Verlag*, pp 7–19

Hanhart, C., Phillips, D. R., & Reddy, S. 2001, *Physics Letters B*, **499**, 9

Hannestad, S. & Raffelt, G. 1998, *ApJ*, **507**, 339

Hebeler, K. & Schwenk, A. 2010, *Phys. Rev. C*, **82**, 014314

Heger, A., Kolbe, E., Haxton, W. C., Langanke, K., Martínez-Pinedo, G., & Woosley, S. E. 2005, *Physics Letters B*, **606**, 258

Hirata *et al.*, K. 1987, *Phys. Rev. Lett.*, **58**, 1490

Hoffman, R. D., Woosley, S. E., & Qian, Y.-Z. 1997, *ApJ*, **482**, 951

Horiuchi, S., Beacom, J. F., & Dwek, E. 2009, *Phys. Rev. D*, **79(8)**, 083013

Horowitz, C. J. 2002, *Phys. Rev. D*, **65(4)**, 043001

Horowitz, C. J. & Pérez-García, M. A. 2003, *Phys. Rev. C*, **68(2)**, 025803

Horowitz, C. J. & Piekarewicz, J. 2001, *Phys. Rev. C*, **64(6)**, 062802

Hubeny, I. & Burrows, A. 2007, *ApJ*, **659**, 1458

Hüdepohl *et al.*, L. 2010, *Physi. Rev. Lett.*, **104(25)**, 251101

Huedepohl, L., Mueller, B., Janka, H., Marek, A., & Raffelt, G. G. 2009, *ArXiv e-prints*

Ikeda *et al.*, M. 2007, *ApJ*, **669**, 519

Itoh, N., Hayashi, H., Nishikawa, A., & Kohyama, Y. 1996, *ApJS*, **102**, 411

Jacques, S. A. 1977, *ApJ*, **215**, 942

Janka, H. 1991, *A&A*, **244**, 378

Janka, H.-T. 2012, *ArXiv e-prints*

Janka, H.-T. & Hillebrandt, W. 1989, *A&AS*, **78**, 375

Janka, H.-T., Langanke, K., Marek, A., Martínez-Pinedo, G., & Müller, B. 2007, *Phys. Rep.*, **442**, 38

Joggerst, C. C., Woosley, S. E., & Heger, A. 2009, *ApJ*, **693**, 1780

Keil, M. T., Raffelt, G. G., & Janka, H. 2003, *ApJ*, **590**, 971

Keil, W., Janka, H., & Mueller, E. 1996, *ApJ*, **473**, L111+

Keil, W. & Janka, H.-T. 1995, *A&A*, **296**, 145

Keil, W., Janka, H.-T., & Raffelt, G. 1995, *Phys. Rev. D*, **51**, 6635

Keil, W., Janka, H.-T., Schramm, D. N., Sigl, G., Turner, M. S., & Ellis, J. 1997, *Phys. Rev. D*, **56**, 2419

Kim, H., Piekarewicz, J., & Horowitz, C. J. 1995, *Phys. Rev. C*, **51**, 2739

Kiziltan, B., Kottas, A., & Thorsett, S. E. 2010, *ArXiv e-prints*

Lai, D. K., Bolte, M., Johnson, J. A., Lucatello, S., Heger, A., & Woosley, S. E. 2008, *ApJ*, **681**, 1524

Landau, L. D. & Lifshitz, E. M. 1959, *Fluid mechanics*

Large, M. I., Vaughan, A. E., & Mills, B. Y. 1968, *Nature*, **220**, 340

Lattimer, J. M. & Lim, Y. 2012, *ArXiv e-prints*

Lattimer, J. M., Mackie, F., Ravenhall, D. G., & Schramm, D. N. 1977, *ApJ*, **213**, 225

Lattimer, J. M. & Prakash, M. 2001, *ApJ*, **550**, 426

Lattimer, J. M., Prakash, M., Pethick, C. J., & Haensel, P. 1991, *Physical Review Letters*, **66**, 2701

Lattimer, J. M. & Yahil, A. 1989, *ApJ*, **340**, 426

Levermore, C. D. & Pomraning, G. C. 1981, *ApJ*, **248**, 321

Liebendörfer, M., Messer, O. E. B., Mezzacappa, A., Bruenn, S. W., Cardall, C. Y., & Thielemann, F.-K. 2004, *ApJS*, **150**, 263

Liebendörfer, M., Mezzacappa, A., & Thielemann, F.-K. 2001a, *Phys. Rev. D*, **63(10)**, 104003

Liebendörfer, M., Mezzacappa, A., Thielemann, F.-K., Messer, O. E., Hix, W. R., & Bruenn, S. W. 2001b, *Phys. Rev. D*, **63(10)**, 103004

Liebendörfer, M., Rampp, M., Janka, H.-T., & Mezzacappa, A. 2005, *ApJ*, **620**, 840

Lindquist, R. W. 1966, *Ann. of Phys.*, **37**, 487

Lodders, K. 2003, *ApJ*, **591**, 1220

Loredo, T. J. & Lamb, D. Q. 2002, *Phys. Rev. D*, **65(6)**, 063002

Lykasov, G. I., Pethick, C. J., & Schwenk, A. 2008, *Phys. Rev. C*, **78(4)**, 045803

Mamdouh, A., Pearson, J. M., Rayet, M., & Tondeur, F. 2001, *Nuclear Physics A*, **679**, 337

Marek, A. & Janka, H.-T. 2009, *ApJ*, **694**, 664

Martínez-Pinedo, G., Fischer, T., Lohs, A., & Huther, L. 2012, *ArXiv e-prints*

Mayle, R., Wilson, J. R., & Schramm, D. N. 1987, *ApJ*, **318**, 288

Meier, D. L., Epstein, R. I., Arnett, W. D., & Schramm, D. N. 1976, *ApJ*, **204**, 869

Messer, O. E. B., Mezzacappa, A., Bruenn, S. W., & Guidry, M. W. 1998, *ApJ*, **507**, 353

Metzger, B. D., Thompson, T. A., & Quataert, E. 2007, *ApJ*, **659**, 561

Meyer, B. S. 1994, *ARA&A*, **32**, 153

Meyer, B. S., Mathews, G. J., Howard, W. M., Woosley, S. E., & Hoffman, R. D. 1992, *ApJ*, **399**, 656

Mezzacappa, A. & Bruenn, S. W. 1993, *ApJ*, **410**, 740

Mezzacappa, A. & Messer, O. E. B. 1999, *Journal of Computational and Applied Mathematics*, **109**, 281

Mezzacappa *et al.*, A. 1998, *ApJ*, **493**, 848

Mihalas, D. & Mihalas, B. W. 1984, *Foundations of radiation hydrodynamics*

Minkowski, R. 1941, *PASP*, **53**, 224

Miralles, J. A., Pons, J. A., & Urpin, V. A. 2000, *ApJ*, **543**, 1001

Misner, C. W. & Sharp, D. H. 1964, *Physical Review*, **136**, 571

Möller, P., Pfeiffer, B., & Kratz, K. 2003, *Phys. Rev. C*, **67(5)**, 055802

Nomoto, K. 1984, *ApJ*, **277**, 791

O'Connor, E. & Ott, C. D. 2012, *ArXiv e-prints*

Oppenheimer, J. R. & Volkoff, G. M. 1939, *Physical Review*, **55**, 374

Otsuki *et al.*, K. 2000, *ApJ*, **533**, 424

Panov, I. V., Korneev, I. Y., Rauscher, T., Martínez-Pinedo, G., Kelić-Heil, A., Zinner, N. T., & Thielemann, F. 2010, *A&A*, **513**, A61+

Pastor, S. & Raffelt, G. 2002, *Physical Review Letters*, **89(19)**, 191101

Pethick, C. J. 1992, *Reviews of Modern Physics*, **64**, 1133

Pons, J. A., Ibáñez, J. M., & Miralles, J. A. 2000, *MNRAS*, **317**, 550

Pons, J. A., Miralles, J. A., & Ibanez, J. M. A. 1998, *A&AS*, **129**, 343

Pons, J. A., Reddy, S., Prakash, M., Lattimer, J. M., & Miralles, J. A. 1999, *ApJ*, **513**, 780

Pons et al., J. A. 2001a, *ApJ*, **553**, 382

Pons et al., J. A. 2001b, *Phys. Rev. Lett.*, **86**, 5223

Press, W. H., Teukolsky, S. A., Vetterling, W. T., & Flannery, B. P. 1992, *Numerical recipes in FORTRAN. The art of scientific computing*

Pruet, J., Hoffman, R. D., Woosley, S. E., Janka, H., & Buras, R. 2006, *ApJ*, **644**, 1028

Qian, Y. & Fuller, G. M. 1995, *Phys. Rev. D*, **52**, 656

Qian, Y. & Wasserburg, G. J. 2008, *ApJ*, **687**, 272

Qian, Y.-Z. & Woosley, S. E. 1996, *ApJ*, **471**, 331

Rampp, M. & Janka, H.-T. 2002, *A&A*, **396**, 361

Rauscher, T., Heger, A., Hoffman, R. D., & Woosley, S. E. 2002, *ApJ*, **576**, 323

Rauscher, T. & Thielemann, F. 2000, *Atomic Data and Nuclear Data Tables*, **75**, 1

Reddy, S., Prakash, M., & Lattimer, J. M. 1998, *Phys. Rev. D*, **58(1)**, 013009

Reddy *et al.*, S. 1999, *Phys. Rev. C*, **59**, 2888

Roberts, L. F. 2012, *ApJ*, **755**, 126

Roberts, L. F., Kasen, D., Lee, W. H., & Ramirez-Ruiz, E. 2011, *ApJ*, **736**, L21

Roberts, L. F. & Reddy, S. 2012, *ArXiv e-prints*

Roberts, L. F., Shen, G., Cirigliano, V., Pons, J. A., Reddy, S., & Woosley, S. E. 2012, *Phys. Rev. Lett.*, **108**, 061103

Roberts, L. F., Woosley, S. E., & Hoffman, R. D. 2010, *ApJ*, **722**, 954

Schinder, P. J. & Bludman, S. A. 1989, *ApJ*, **346**, 350

Serminato, A., Gallino, R., Travaglio, C., Bisterzo, S., & Straniero, O. 2009, *Publications of the Astronomical Society of Australia*, **26**, 153

Serpico, P. D., Chakraborty, S., Fischer, T., Hüdepohl, L., Janka, H.-T., & Mirizzi, A. 2012, *Phys. Rev. D*, **85(8)**, 085031

Shapiro, S. L. & Teukolsky, S. A. 1983, *Black holes, white dwarfs, and neutron stars: The physics of compact objects*

Shen, G., Horowitz, C. J., & Teige, S. 2011, *Phys. Rev. C*, **83(3)**, 035802

Sigl, G. 1995, *Phys. Rev. D*, **51**, 4035

Smartt, S. J. 2009, *ARA&A*, **47**, 63

Sneden, C., Cowan, J. J., & Gallino, R. 2008, *ARA&A*, **46**, 241

Sneden, C., McWilliam, A., Preston, G. W., Cowan, J. J., Burris, D. L., & Armosky, B. J. 1996, *ApJ*, **467**, 819

Stein, R. F. & Schwartz, R. A. 1972, *ApJ*, **177**, 807

Stein, R. F. & Schwartz, R. A. 1973, *ApJ*, **186**, 1083

Steiner, A. W., Lattimer, J. M., & Brown, E. F. 2010, *ApJ*, **722**, 33

Steiner *et al.*, A. W. 2005, *Phys. Rep.*, **411**, 325

Sumiyoshi, K., Suzuki, H., & Toki, H. 1995, *A&A*, **303**, 475

Suzuki, T., Nagataki, S., & Wanajo, S. 2006, in *International Symposium on Nuclear Astrophysics - Nuclei in the Cosmos*

Suzuki, T. K. 2002, *ApJ*, **578**, 598

Suzuki, T. K. 2004, *MNRAS*, **349**, 1227

Suzuki, T. K. & Nagataki, S. 2005a, *ApJ*, **628**, 914

Suzuki, T. K. & Nagataki, S. 2005b, *ApJ*, **628**, 914

Swesty, F. 1996, *Journal of Computational Physics*, **127**, 118

Takahashi, K., Witti, J., & Janka, H. 1994a, *A&A*, **286**, 857

Takahashi, K., Witti, J., & Janka, H. 1994b, *A&A*, **286**, 857

Thompson, T. A., Burrows, A., & Meyer, B. S. 2001, *ApJ*, **562**, 887

Thompson, T. A., Burrows, A., & Pinto, P. A. 2003, *ApJ*, **592**, 434

Thorne, K. S. 1977, *ApJ*, **212**, 825

Thorne, K. S. 1981, *MNRAS*, **194**, 439

Timmes, F. X. & Swesty, F. D. 2000, *ApJS*, **126**, 501

Timmes, F. X., Woosley, S. E., & Weaver, T. A. 1995, *ApJS*, **98**, 617

Travaglio, C., Gallino, R., Arnone, E., Cowan, J., Jordan, F., & Sneden, C. 2004, *ApJ*, **601**, 864

Tsang *et al.*, M. B. 2011, *Prog. Part. Nucl. Phys.*, **66**, 400

Unno, W., Osaki, Y., Ando, H., Saio, H., & Shibahashi, H. 1989, *Nonradial oscillations of stars*

Wahl, A. C. 2002, *Systematics of Fission-Product Yields*, Technical Report LA-13928, Los Alamos National Laboratory, Los Alamos, N.M.

Wanajo, S. 2006, *ApJ*, **647**, 1323

Wanajo, S., Kajino, T., Mathews, G. J., & Otsuki, K. 2001, *ApJ*, **554**, 578

Weaver, T. A., Zimmerman, G. B., & Woosley, S. E. 1978, *ApJ*, **225**, 1021

Weinberg, N. N. & Quataert, E. 2008, *MNRAS*, **387**, L64

Wilson, J. R. & Mayle, R. W. 1988, *Phys. Rep.*, **163**, 63

Wilson, J. R. & Mayle, R. W. 1993, *Phys. Rep.*, **227**, 97

Witti, J., Janka, H., & Takahashi, K. 1994a, *A&A*, **286**, 841

Witti, J., Janka, H., & Takahashi, K. 1994b, *A&A*, **286**, 841

Woosley, S. E., Hartmann, D. H., Hoffman, R. D., & Haxton, W. C. 1990, *ApJ*, **356**, 272

Woosley, S. E., Heger, A., Cumming, A., Hoffman, R. D., Pruet, J., Rauscher, T., Fisker, J. L., Schatz, H., Brown, B. A., & Wiescher, M. 2004, *ApJS*, **151**, 75

Woosley, S. E., Heger, A., & Weaver, T. A. 2002, *Reviews of Modern Physics*, **74**, 1015

Woosley, S. E. & Hoffman, R. D. 1992, *ApJ*, **395**, 202

Woosley, S. E., Pinto, P. A., & Weaver, T. A. 1988, *Proceedings of the Astronomical Society of Australia*, **7**, 355

Woosley, S. E. & Weaver, T. A. 1995, *ApJS*, **101**, 181

Woosley, S. E., Wilson, J. R., Mathews, G. J., Hoffman, R. D., & Meyer, B. S. 1994, *ApJ*, **433**, 229

Woosley, S. E., Wilson, J. R., & Mayle, R. 1986, *ApJ*, **302**, 19

Wrean, P. R., Brune, C. R., & Kavanagh, R. W. 1994, *Phys. Rev. C*, **49**, 1205

Yueh, W. R. & Buchler, J. R. 1977, *ApJ*, **217**, 565

Zhang, W., Woosley, S. E., & Heger, A. 2008, *ApJ*, **679**, 639